DESIGN AND SIMULATION OF A MICROWAVE POWERED MICROPLASMA SYSTEM FOR LOCAL AREA MATERIALS PROCESSING

By

Jeffri Julliarsa Narendra

A DISSERTATION

Submitted to
Michigan State University
in partial fulfillment of the requirements
for the degree of

DOCTOR OF PHILOSOPHY

Electrical Engineering

2010

ABSTRACT

DESIGN AND SIMULATION OF A MICROWAVE POWERED MICROPLASMA SYSTEM FOR LOCAL AREA MATERIALS PROCESSING

By

Jeffri Julliarsa Narendra

A microwave powered microplasma source is developed and tested for materials processing on spatially localized areas. A small diameter stream of plasma (less than 2 mm in diameter) is created by focusing microwave energy inside a discharge tube. The discharge then flows out the end of the tube onto the surface being processed delivering ions and reactive radicals. The diameter of the plasma stream from the tube to the material being processed can be controlled by an aperture mounted at the end of the tube. The spot size of the localized plasma stream ranges from 2 mm down to 10's micrometers depending on the aperture size. The discharge is created by using 2.45 GHz microwave energy that is coupled into the discharge using a small foreshortened cylindrical cavity that has a hollow inner conductor and a small capacitive gap at the end of the cavity. A processing gas mixture is fed through a 2 mm inner diameter quartz tube which is located inside the hollow inner conductor of the cavity. This tube is exposed to a high electric field at the small gap end of the cavity thus generating a surface wave plasma. The length of the surface wave discharge in the tube can be extended by increasing the microwave power to the discharge so that the plasma reaches the aperture. The operating pressures range from 0.5 Torr to 100 Torr and the microwave power utilized ranges from a few Watts to 10's Watts.

Several properties of the discharge including plasma power density, electron density and

electron temperature are measured. The power densities of argon and Ar/O_2 plasma discharges vary from 10's to over 450 W/cm^3. The plasma density and electron temperature of argon discharges are measured using a double Langmuir probe placed in the materials processing area. The plasma densities are in the range of $10^{11} – 10^{13}$ cm^{-3}.

Computational modeling of the plasma discharge and the microwave excitation of the discharge is performed using a finite element analysis. The goal of the modeling study is to complement and understand the design, development and operation of the microwave powered microplasmas. A self-consistent model of the foreshortened cylindrical cavity and plasma discharge is presented with results compared to experimental measurements.

The microplasma system is incorporated into a micromanufacturing system that integrates the plasma source with an atomic force microscope for surface measurements and nanomanipulation of the surface. Selected applications of the micromachining system demonstrated include using the microplasma as a spatially localized etcher, free radical source, and ultraviolet light source. Silicon and ultrananocrystalline (UNCD) diamond etching is performed using Ar/SF_6 and Ar/O_2 discharges, respectively, with etching rates of 0.2 – 2 µm/min and 0.6 – 2 µm/hr. Localized removal of photoresist is done by using the microplasma as a free radical source and photoresist is exposed to ultraviolet light from the microplasma source to create spatially localized patterns.

ACKNOWLEDGMENTS

I would like to begin by thanking Dr. Timothy Grotjohn, who has been my guide, my mentor that led me through the work presented here. His consultation, his suggestion, his patience, and his constant encouragement are greatly appreciated. I also would like to thank Dr. Jes Asmussen and Dr. Donnie Reinhard for their valuable suggestions and advice. Thankyou Dr. Guowei Wei for his comments and willingness to read the manuscript. The author is grateful to Jiangbo Zhang for his significant contributions to this project.

Finally I would like to thank my family for their love and their constant support for my graduate studies.

TABLE OF CONTENTS

LIST OF TABLES

LIST OF FIGURES

1 Introduction

1.1 Motivation

In the past several years, microplasmas and their applications became an emerging science and technology topic. Numerous types of microplasma sources, with operating frequency ranging from pulsed direct current (DC) to microwave, have been studied and developed. For this study, microwave power will be investigated for its use in microplasma applications, especially for material processing.

Microwave plasma sources with dimensions less than a size of a few millimeters have possible applications as miniature materials processing sources for use in spatially localized deposition applications, deposition and surface treatment on the inside of larger work pieces, formation of arrays of small plasmas for simultaneous processing of localized regions across large areas, portable low-temperature sterilization, incorporation of plasmas in micro-systems for chemical analysis, microreactors, surface treatment, and micro-thrusters for spacecraft propulsion [1][2][3].

1.2 Objective

The primary objective of this study is to develop and investigate microwave generated microplasmas to perform surface treatment of various materials. The surface treatment is conducted in a local area by exposing the area to the microplasma beam. A pattern of treated surface can be printed on the material using a microplasma beam by moving the substrate using a x-, y-, and z-axis automated motioned stage under the microplasma beam. Such a system can be controlled by a computer to obtain the desired pattern design. The size of the treated surface feature in this study are from 10's micrometers to one millimeter.

To implement this objective, two different approaches are utilized. The first approach involves system design, development and testing. The second approach develops a self-consistent simulation of the apparatus. Together, they complement each other to provide a better understanding of how the system works.

The equipment designed is called a micromachining system. In this system, material being processed is placed in a low pressure chamber. A small beam of plasma species performs a localized surface treatment of a substrate. An Atomic Force Microscope (AFM) is placed inside the processing chamber as an in-situ monitoring process. Overall, the micromachining system can do material processing and characterization in one place therefore minimizing the chance of contamination. Surface treatments of materials can be etching, deposition, surface activation, and many other applications depending on how the surface of the material reacts to species coming from the plasma. As will be described in chapter 2, microwave generated plasmas have potential applications for material processing. For this research, there are three applications of interest for microwave generated microplasmas. They are an ion source, a free radical source, and a light source.

The modeling of the experimental system provides valuable information in designing and operating the micromachining system. Electromagnetic (EM) characteristics of the microwave energy inside the plasma applicator are studied. The coupling mechanisms from the microwave energy into the plasma are simulated. In this investigation, an argon plasma is modeled. By combining the EM and plasma models, a self-consistent simulation is achieved.

1.3 Dissertation outline

The work is primarily focused on designing a local area surface processing system using a microwave powered microplasma. The approach can be divided into three parts: Design and implementation of the micromachining system (chapter 3), simulation of the system (chapter 4), and experimental results gathered using the system (chapter 5). Chapter 2 describes microplasma source design and application in the literature. Microplasma applications as ion sources, radical sources and light sources are described more thoroughly in sections 2.5 – 2.7. Various plasma simulation techniques in the literature are explained in section 2.4. Chapter 3 details the design of the micromachining system. Section 3.2 describes the microwave foreshortened coaxial cavity as the microplasma applicator. A detailed explanation for the processing area inside the processing chamber is explained in section 3.7. Chapter 4 discusses the simulation part of the proposed work. The EM model and its simulation results are described in section 4.2. The plasma model and its simulation results are discussed in section 4.3. Chapter 5 presents the results of the experimental work. Section 5.2 discusses the properties of the foreshortened coaxial cavity, followed by a discussion of the plasma behavior and characteristics. Results of the ion source, the radical source, and the light source applications are presented in section 5.3 – 5.5, respectively. Finally, chapter 6 provides a research summary and recommendations for future research.

2 Background

2.1 Introduction

For the purpose of this background review, the research literature can be divided into three categories. In the first category, microplasmas and their applications are discussed. Various types of microplasma sources are described along with their operating parameters. The second category contains a review of discharge modeling techniques. The third category is a review of different configurations of plasma systems as light sources, ion sources, and free radical sources.

2.2 Microplasma source designs in the literature

In the past, the challenge in plasma research was to develop techniques that provide high ion and free radical densities uniformly over large and ever increasing process areas. Since scale-up was usually an important issue when considering industrial applications [4][5][6][7][8], the study of very small plasmas, on the order of a few millimeters, was rare. Within the past decade there has been interest in small scale discharges due to their various potential applications. Discharges are considered as microplasmas if one of their dimension is on the order of a few millimeters or less [1]. The are many different configurations in which to build microplasma applicators. Based on different energy coupling mechanisms, microplasmas can be differentiated into several types. They are: micro-hollow cathode discharges (MHCDs), micro-inductively coupled plasmas (mICPs), micro- capacitively coupled plasmas (CCPs) which include dielectric barrier discharges (DBDs) and capillary plasma electrode (CPE) configurations, and miniature microwave-induced plasmas (mMIPs).

The breakdown of a gas, due to a dc electric potential between two electrodes a distanced apart, is heavily dependent on the pressure-distance (pd) scaling values in the Paschen curve [9] [10]. An example of a Paschen curve can be seen in figure 2.2.1. In general the curve can be divided into two regions: the left side and the right side of the minimum breakdown voltage. On the right side, as the pressure increases, the mean-free path of electrons in the gas decreases. Thus the electron is not being optimally accelerated by the electric field due to the higher number of collisions. At the left side of the Paschen minimum, the electron mean-free path can be longer than the gap distance between the electrodes. In this case, the electrons might gain a lot of energy but arrive at the anode before creating an electron avalanche. As a result, in general, the breakdown voltage of gases increases as the pd values shifting away from the Paschen minimum. However, when the electrode gap is small, on the order of 10's microns or smaller, the left hand side of the Paschen curve becomes flat because the discharge is in constricted mode. In this mode, the secondary electron yield by photons, metastables, and gas phase ionization due to fast neutrals must be take into account [10].

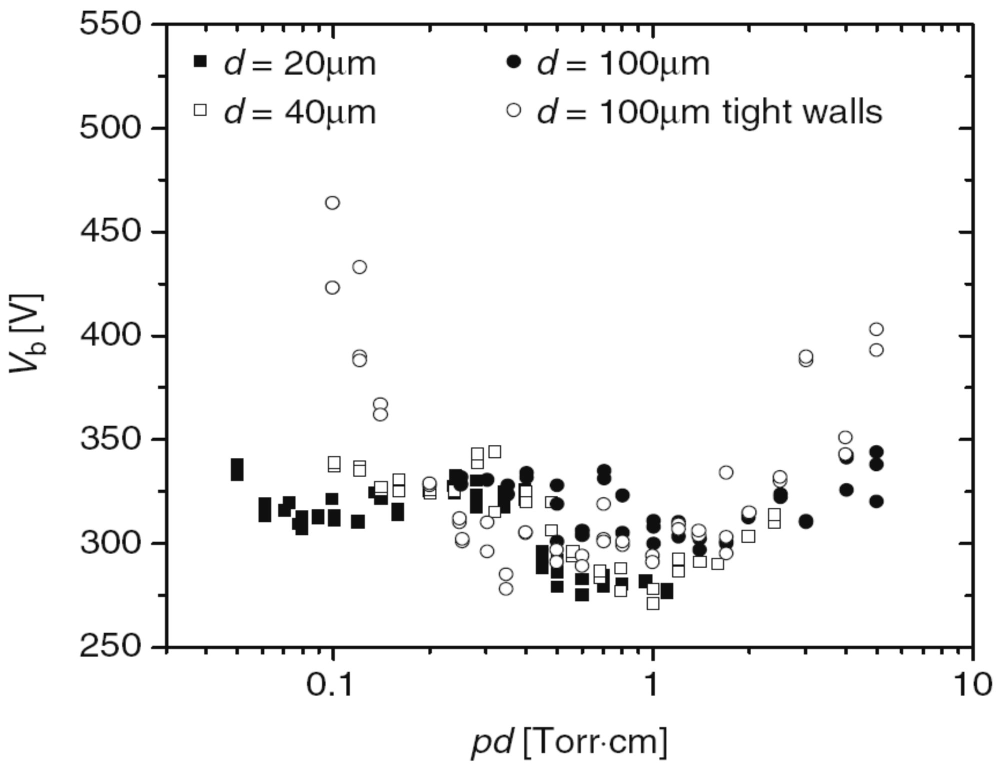

Figure 2.2.1: Voltage breakdown of argon at various gap distances between the electrodes [10].

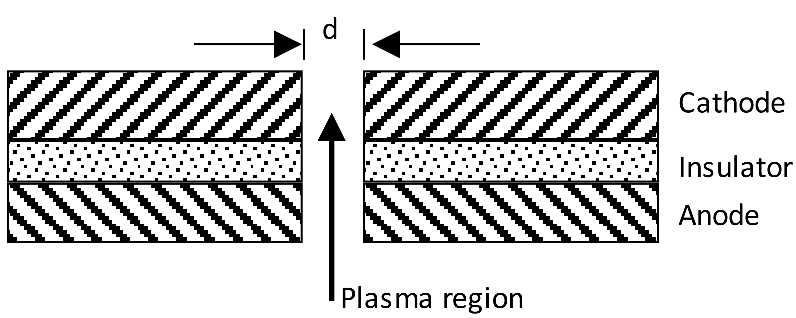

Figure 2.2.2: Illustration of a MCHD applicator. d is the gap distance between the electrodes.

MHCDs are miniaturizations of glow discharges with the cathode fall and negative glow confined in a cavity in the cathode as shown in figure 2.2.2. Studies on MHCDs were done by Schoenbach et al. [11][12][13][14] and Pitchford et al. [15] among other research groups [16] [17]. This discharge can be operated at low to atmospheric pressure and can be formed using dc or ac voltage sources. The typical discharge size is approximately the size of the hole in the electrode which ranges from 10 – 500 μm. At low current, the plasma is confined inside the hole and at higher current the plasma expands outside the hole on the cathode backside. MCHDs are known to be efficient sources of non-coherent ultraviolet (UV) and vacuum ultraviolet (VUV) radiation.

Hopwood et al. [18][19][20][21][22] has investigated a miniaturization of inductively coupled plasma (mICP) sources as illustrated in figure 2.2.3. The discharge in this ICP source is confined in a miniature aluminum vacuum chamber with a dimension of 2.5 X 2.5 X 0.6 cm. The plasma operates from 0.1 to 10 Torr, and requires less than 3 W of transmitted power at a frequency of 493 MHz. The electron temperature of the argon plasma created using this ICP source is found to vary between 3 eV and 10 eV and the charge density is in the range of 10^9-10^{10} cm^{-3}. The charge density is about an order of magnitude lower than the large scale ICP's as a result of the large surface-to-volume ratio of small discharges.

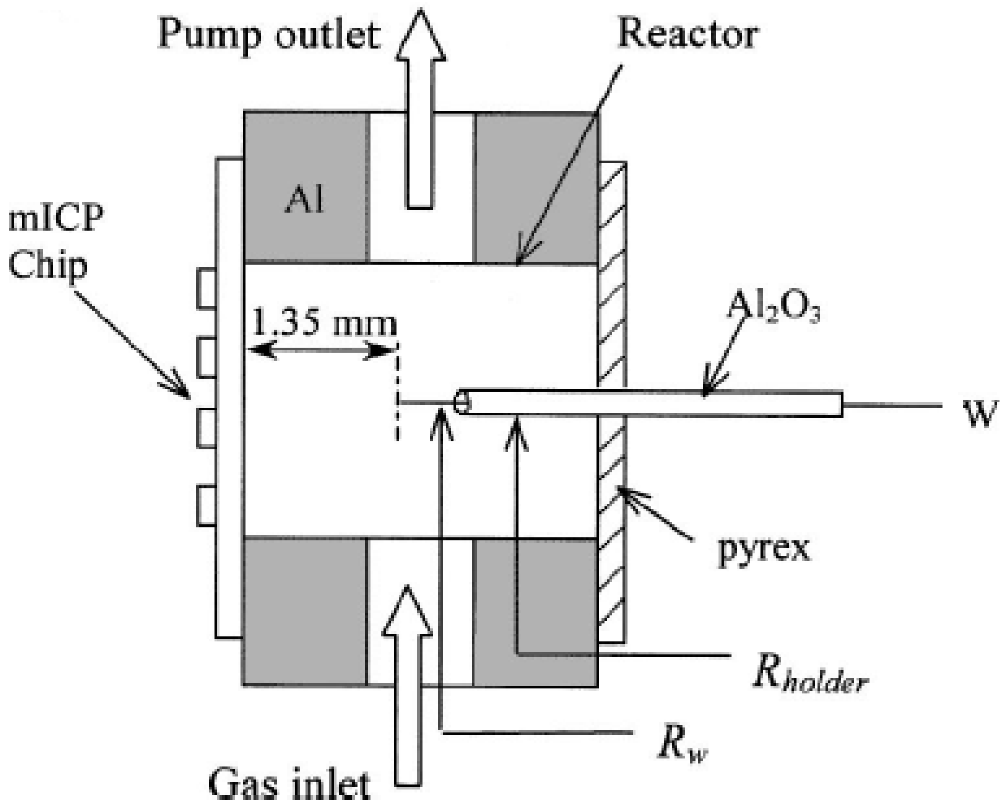

Figure 2.2.3: A cross section of the mICP system designed by Hopwood et al. with a Langmuir probe inserted in the chamber. Notes: R_{holder}: Probe holder; R_W: Probe wire tip [22].

Recently, Ichiki et al. [23] developed a microfabricated planar-type mICP source on a ceramic substrate called a microplasma jet. The device operates at atmospheric pressure and is powered with a compact VHF transmitter at 144 MHz. With an input power of 50 W, the typical plasma density is approximately 10^{15} cm^{-3} and the electronic excitation temperature of Ar was found to be 4000 – 4500 K.

Stoffels et al. [24][25][26][27][28] designed a plasma needle for fine surface treatment of bio materials. This 10 MHz radio-frequency (RF) excited plasma source operates at atmospheric pressure. Plasma appears as a small glow at the tip of a metal pin with a dimension of 5 cm long and 1 mm diameter. The characteristic dimension of a helium plasma generated using this source does not exceed 0.1 – 0.2 mm and the electron density is on the order of 10^{13} – 10^{14}

cm^{-3}.

Miniature Capacitively Coupled Plasmas (mCCP's) are another RF excited microplasmas. Yoshiki et al. [29][30] developed a self-igniting, parallel-plate, atmospheric pressure mCCP as shown in figure 2.2.4. Helium mCCP's are formed at an atmospheric pressure in a quartz channel with a depth varying between 65 and 500 μm and width varying between 500 μm and 5 mm. The excitation frequency is 13.56 MHz and the incident power ranges from 1 – 5 W.

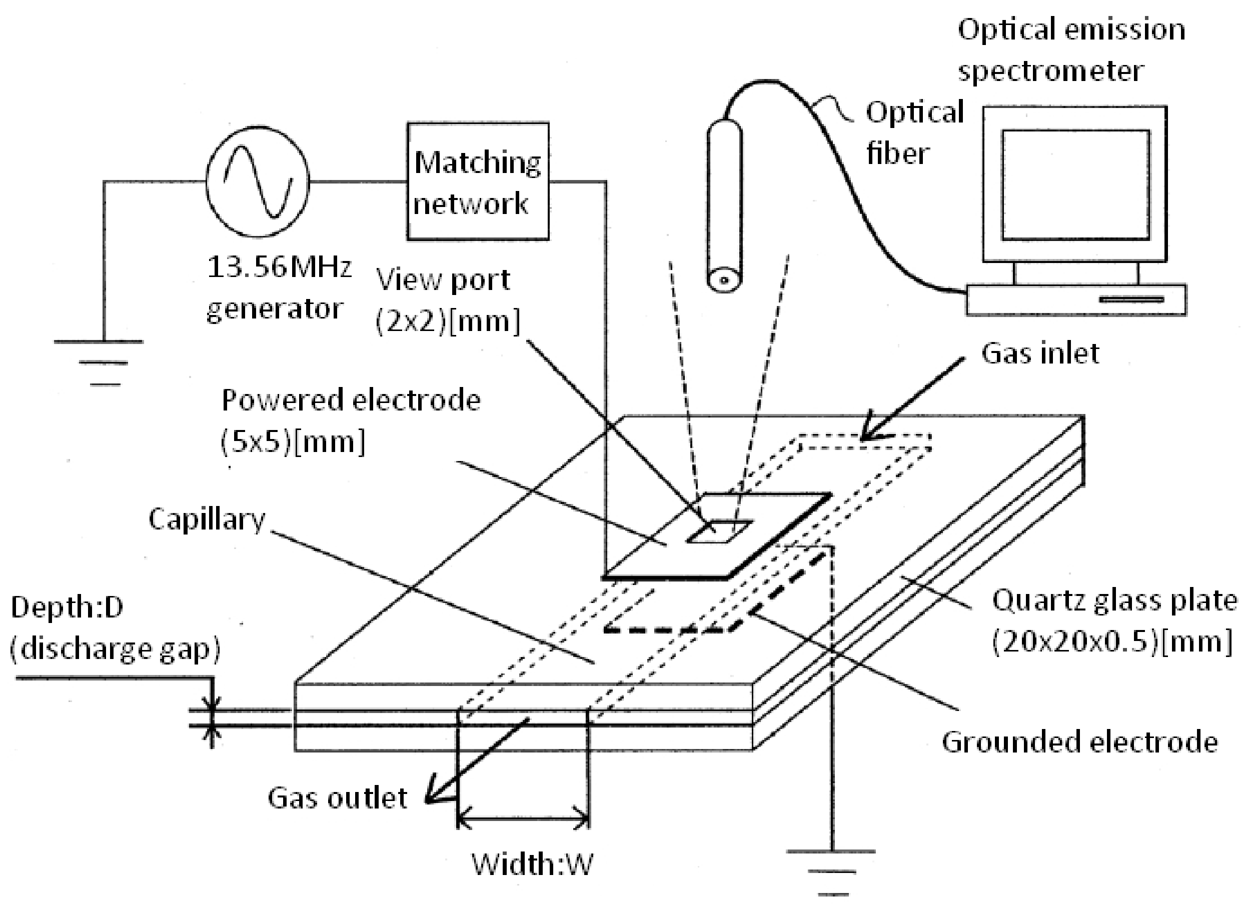

Figure 2.2.4: Schematic of mCCP designed by Yoshiki et al. [30].

The most well known design in generating mCCP's with a planar type arrangement is called a dielectric barrier discharge (DBD) as shown in figure 2.2.5. DBDs are characterized by the presence of a dielectric barrier on at least one of its electrode. The work on this type of discharge was pioneered by Okazaki et al. [31] and it has been studied by many other research groups including Niemax et al. [32][33][34][35], and Laroussi et al. [36][37]. A variant of this type of discharge was developed using a cylindrical dielectric instead of a planar one. This device is called the Capillary Plasma Electrode (CPE) applicator. The novel aspect of this CPE discharge is the electrode design in which dielectric capillaries cover one or both electrodes as seen in figure 2.2.6. This work was pioneered by Kunhardt [38] followed by others such as Becker et al. [39] and Laroussi et al. [40].

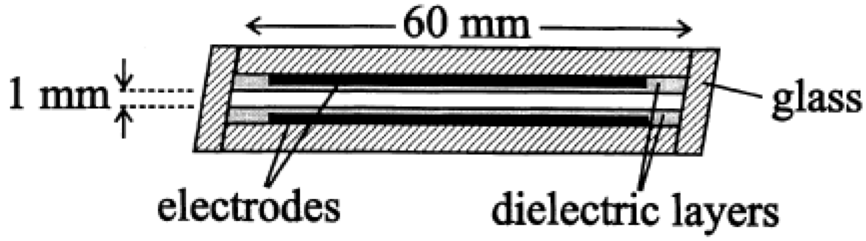

Figure 2.2.5: Schematic of DBD applicator designed by Niemax et al. [32].

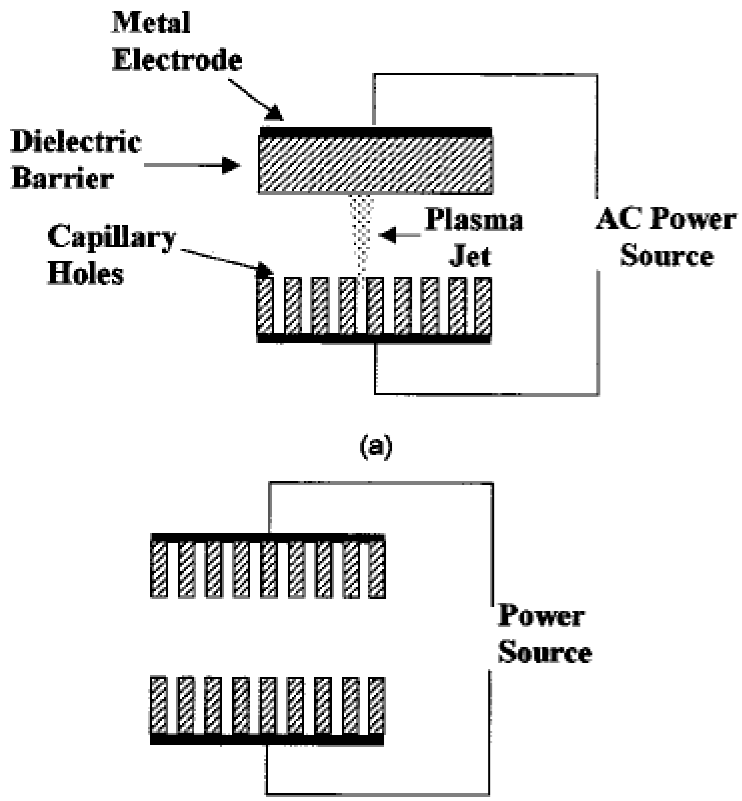

(a)

(b)

Figure 2.2.6: Schematic of CPE applicators as shown by Kunhardt [38]. (a) Modified DBD applicator with capillary electrode on one side and (b) capillary electrodes on both sides.

Development of microplasma applicators generated using microwave energy have been undertaken by several research groups. There are two principle designs for these miniature microwave induced plasmas (mMIP's). The first design employs a modified microstrip transmission line structure to couple the microwave energy. The second design uses waveguides or cavity structures.

Previous work using modified microstrip transmission lines to create microdischarges has been undertaken by Broekaert et al. [41][42][43][44][45], Moisan et al. [46], Hopwood et al.

[47][48][49][50][51], and Grotjohn et al. [52][53]. The plasma excitation in Broekaert's and Moisan's designs are done by a stripline that is parallel to the discharge tube (chamber). In the investigation by Hopwood the microdischarge is formed by a split ring resonator with the plasma formed in the high electric field region of the split. Grotjohn's design are not resonator structures, rather they operate by establishing a standing electromagnetic waves using a short at one end of the stripline. The discharge tube is located perpendicular to the stripline as seen in figure 2.2.7.

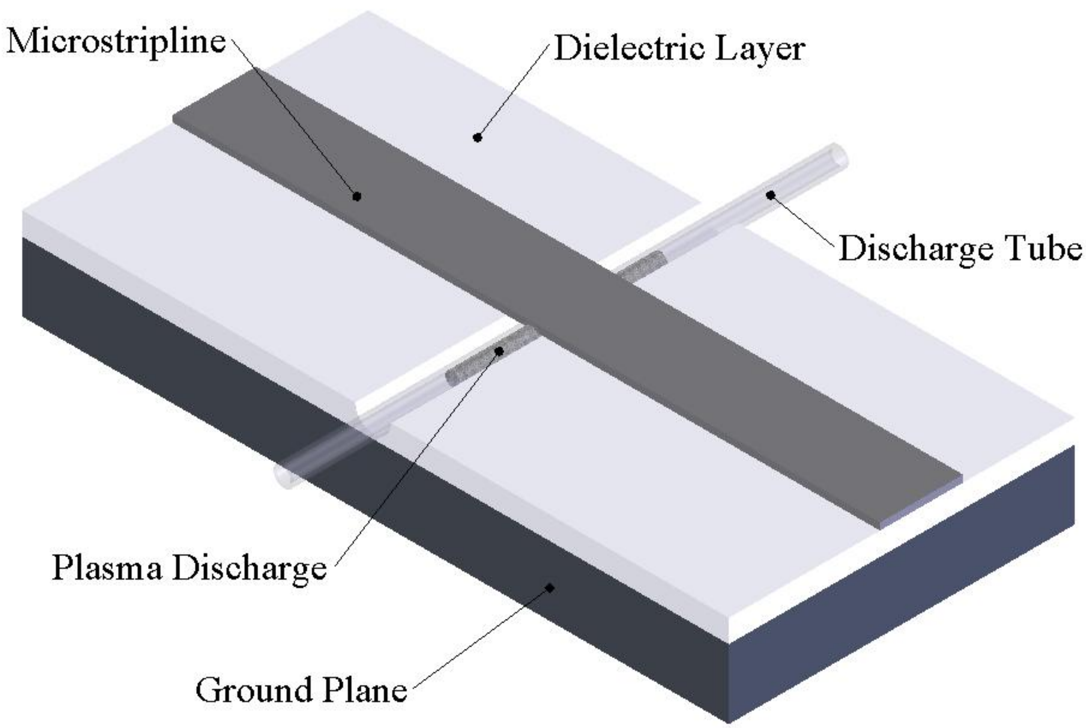

Figure 2.2.7: Illustration of microstrip applicators to generate mMIP courtesy of Grotjohn et al. [53].

At Michigan State University, small microwave discharges' characteristics have been studied since the early 1970's by Asmussen et al. [54][55][56][57][58]. Fredericks [54] studied the resonance characteristics of microwave plasmas generated using a modified coaxial cavity, called the foreshortened coaxial cavity, or the re-entrant cavity. The resonantly sustained plasmas were formed inside a quartz tube concentrically located in the cavity. Typical operating power of these plasmas was less than 30 W. Rogers [55] investigated the discharge properties of argon plasma columns with diameters of 1 – 3 mm and length up to 16 cm. The discharge was excited using a 2.45 GHz power supplied to a microwave cavity. Quartz tubes of varying diameter were used to confine the gas. The tubes ran coaxially inside the cavity. Typical electron densities for argon discharges at 1 atm were $3x10^{13}$ cm^{-3} to $3x10^{14}$ cm^{-3}. All of the above mMIP's are generated using applicators that are modified from transmission line structures or from cavity structures.

There are other research groups who have interest in designing mMIP's applicators in the similar manner. An early type of these sources was developed by Beenaker et al. [59][60] The system used a cylindrical TM_{010} cavity as the excitation source. It operates at atmospheric pressure with a typical input power of less than 200 W. Moisan et al. [61][62][63][64] developed mMIPs applicators called surfatrons. They are waveguide-based electromagnetic-surface-wave launchers that allow the generation of long plasma columns using microwaves. The design can be either based on a modified coaxial transmission line structure [61] or a rectangular waveguide structure [64]. Broekaert et al. [65][66] designed a small microwave plasma torch which generates a plasma jet up to 4 mm long. The operating power for this applicator was between 2 – 17 W. Several designs have been proposed by other research group such as Kuo et al. [67][68], Jin et al. [69] and Uhm et al. [70] to improve the generation of mMIPs.

Designs of the microplasma sources have their own advantages and disadvantages. In DC and AC microplasma sources such as MHCDs applicators, the design can be built on simple structures. In addition, the gas temperature of the plasma can be as low as room temperature. In general, the design must satisfy the pd scaling of the Paschen's curve law to sustain the plasma. Thus, the pressure condition and gap length between the electrodes have dominant influences in the design.

For plasma processing and other plasma applications, electrodeless plasmas are good candidates to avoid problems of electrode erosion and contamination. The use of high frequency as the excitation source, such as in the case of DBD's and mMIP's, allows electrodeless system design where no metal electrodes are directly touching the plasmas. In the case of mMIP's, there is another advantage compared to other systems. The plasma density of the mMIP's is generally higher as compared to the low frequency applicators, especially capacitively coupled plasmas. The disadvantage of using high frequency applicators is the need to build a matching network to increase the energy coupling efficiency. Adding the matching network may result in a more complex design.

Overall, microplasma is an emerging field because it has several advantages over the large area plasmas for some applications. It operates in a wide range of pressure conditions from high vacuum to atmospheric pressure. The surface to volume ratio is large which is promising for many potential applications. And, applications that were traditionally achieved using a large plasma can also be performed using microplasmas by creating an array of them.

2.3 Microplasma applications in the literature

Plasma sources with dimension less than a size of a few millimeters have possible applications as miniature materials processing sources for use in spatially localized deposition applications [71], deposition and surface treatment on the inside of larger work pieces, formation of arrays of small plasmas for simultaneous processing of localized regions across large areas, portable low-temperature sterilization, incorporation of plasmas in micro-systems for chemical analysis, microreactors, surface treatment, and micro-thrusters for spacecraft propulsion [1][2]. However, there are only a few studies on the potential application for mMIP's in the literature compared to other applicators.

Over the past several years, a few research groups have developed potential applications for mMIP's applicators. Hopwood et al. [72] developed a particle trapping apparatus using a microstrip split-ring resonator (MSSR) device. Micro- and nano-particles can be trapped in the MSSR microplasma because there is a high potential gradient within the microplasma. Takao et al. [73][74] investigate mMIP's application as miniature electrothermal thrusters. Typically their miniature thruster gives a thrust greater than 1 mN, with a specific impulse ~100 s and a thrust efficiency around 10% for argon plasma at a microwave power of less than 10 W. Broekaert et al. investigated the applications of their microstrip applicator for optical emission spectroscopy of gaseous species [44].

Another application of microplasmas is to observe physical phenomena such as generation of plasma bullets [75][76][40]. An atmospheric plasma jet created using a DBD applicator was observed to be a plasma bullet train traveling at hypersonic speed from 7.0 km/s to 43.1 km/s. The nature of these plasma bullets is unknown but the development of microplasma field can be seen as the enabling technologies to observe this phenomenon.

2.4 Plasma modeling in the literature

Simulation and modeling can provide a better understanding of a plasma system in addition to the experimental investigation. In general, there are two types of simulations needed to provide a self-consistent model. The first one is the coupling mechanism of the energy into the plasmas and the second one is the plasma modeling. The input parameters are set to be similar with the experimental system such as the pressure condition, the flow rates of the feed gases, and the input power or voltage. There are many different approaches for solving the system of equations of the model. The most common ones are by applying the finite-difference technique, the finite-volume technique, and the finite-element technique. These techniques will be described later in this section.

Historically, plasma modeling has been done using a number of different approximations, and the associated level of accuracy is dependent on capturing the relevance physics of the problem. The various levels include: Full kinetic models using Boltzmann's equation for multi-species [77], Particle simulation using Monte-Carlo techniques [78][79][80], Fokker-Planck approximation models [81][82], and multi-fluid models using drift-diffusion analysis [78].

Microplasma modeling has been conducted by several research groups within the last several years. Fridman et al. performed numerical simulations to characterize argon [83] and hydrogen [84] DC microplasmas. They utilized CFD-ACE+, a computational fluid dynamic software, to calculate transport of the charged particles and the electric fields by solving the partial differential equations (PDE's). The external circuit is simulated using a general purpose circuit simulator, SPICE. They also did a numerical simulation for RF discharges [85] at atmospheric pressure. For their simulation, the drift-diffusion approximation was used. The electron energy distribution function (EEDF) was obtained from the BOLSIG+ [86] software. It was noted that the RF cycle time is much smaller than a typical heat transfer time. Hence, the steady state gas heat transfer is solved during each RF cycle to obtain the temperature distribution. The entire system was computed using the finite-volume method.

Pitchford et al. simulated MHCD's [87][88], and DBD's [89][90] using BOLSIG+ software [86]. This software simulates the electron energy distribution function (EEDF) at a given reduced electric field (E/N) for various gases using spherical harmonic expansion of the EEDF with a two-term Boltzmann approximation. The deviation from Maxwellian EEDF can be calculated using this software. However, the reduced electric field is not a well posed representation in the microwave regime because the two-term approximation fails at high values of E/N since the EEDF becomes highly anisotropic.

In the case of MIP's, Grotjohn et al. [91][92][93][94][95][96][97] at Michigan State University performed numerical modeling using the finite-difference time-domain (FDTD) method. FDTD is a common modeling technique for computational electrodynamic problems. It was first introduced by Yee [98] and further developed by Taflove et al. [99][100][101]. In this technique, the time-dependent Maxwell's equations in partial differential equations (PDE's) form are discretized using central-difference approximations to the space and time partial derivatives. The resulting finite-difference equations are solved in a leapfrog manner: the electric field vector components in a volume of space are solved at a given instant in time; then the magnetic field vector components in the same spatial volume are solved at the next instant in time; and the process is repeated over and over again until the desired transient or steady-state electromagnetic field behavior is fully evolved.

Another common technique to solve a general PDE is by using the finite element method (FEM). In this technique, the complex continuous domains of the PDE are discretized into smaller sub-domains called elements which consist of solvable piecewise basis functions. By solving these elements, the approximate solution to the PDE can be found. There are several research groups who did plasma simulations using COMSOL Multiphysiscs, a FEM software. Grubert et al. [102] used a two-fluid model to simulate an argon DC glow discharge. The simulation was done in one dimension and it was performed to find the electron and ion density distribution and their flux densities under both steady-state and time-dependent conditions. Nowakowska et al. [103] examined the electric fields distributions in a waveguide-based axial-type microwave plasma source during a tuning procedure to obtain a matching condition for the microwave network. For the simulation, the plasma region was modeled with a complex dielectric permittivity. Hunyar et al. [104] performed a numerical study of surface waves in an argon plasma. The plasmas are generated using Plasmaline, a 2.45 GHz microwave plasma source. The argon discharges were simulated using a multi-fluid models approach, in this case by solving the continuity equations for the argon neutrals, electrons, and argon metastables. In addition to the continuity equations, the heat equation for the electrons was implemented.

2.5 Plasmas as light sources in the literature

The most well-known microplasma for light source applications is the plasma display panel (PDP) technology. This technology was invented in 1964 by Bitzer et. al. [105][106]. There are numerous scientific literature papers for PDP's and their development as summarized by Weber [107] and Sobel [108]. The basic principle of operation for a single unit cell of PDP's is similar to the DBD's applicators in which a gaseous species are trapped inside a cavity coated with a dielectric layer. This cavity is sandwiched between two or three electrodes. Shinoda et al. [109] reviews the structures, operations and fabrication processes of PDP technology in detail.

Eden et al. [110][111][112][113] developed a planar microcavity array of microplasmas as a light source. Their device was fabricated in a Al/Al_2O_3 structure in which the dielectric is made of a nanoporous aluminum oxide films. The principle of operation for this device is similar to the MHCD applicators described in the previous section. For a mixture of Xe/Ne gas at 400 – 800 Torr, the typical luminous efficacy for this device is around 10 – 20 lm/W.

2.6 Ion sources in the literature

Ion sources, which operate with reactive gases, have a number of applications such as polymer etching, ion implantation, reactive sputtering and thin film deposition. Grotjohn [114] reviewed the types, properties, and requirements of ion sources applied to microfabrication processes. The most common microwave ion sources operate at a frequency of 2.45 GHz under the electron cyclotron resonance (ECR) condition such as the ones developed by Asmussen et al. [115], Matsubara et al. [116] and Trassl et al. [117]. To accommodate the ECR condition, permanent or electromagnetic magnets are used to confine the charged particles. Typical ion current density for this type of applicators is in the range of 10's to 100's mA/cm^2. To get a higher ion density, a higher operating frequency can be applied. Trassl et al. increased the ion current by developing ion sources which operate at 10 GHz [118] and 14.5 GHz [119], and Sun et al. [120] proposed a 18 GHz ion source applicator. Ion source plasmas can also be excited using an RF frequency such as those designed by Hahto et al. [121] and Boonyawan et al. [122]. The plasmas generated have ion current density typically less than 100 mA/cm^2.

Another research interest for the ion source development is the ion beam extractor grid design. This extractor grid controls the energy of the ions that are delivered to the processing area. It can also be used to focus the ion beam and increase the energy by applying a voltage bias. On the other hand, to obtain more uniform ion beams in the axial direction, gridless ion source (GIS) might be preferred such as the one designed by Dawei et al. [123]. GIS can produce high quality optical coatings. However, the ion current density is in the range of 200 – 500 μA/cm^2, which is much lower than ion sources with a beam extractor grid.

2.7 Free radical sources in the literature

Plasmas also consist of free neutral radicals thus it is suitable as a free radical source. Free radicals, such as singlet oxygen, play a critical role in a variety of fields, including atmospheric chemistry [124], semiconductor fabrication [125] and surface decontamination [126]. For instance, recent research suggests [126] that atmospheric pressure plasmas can be used to decontaminate surfaces by efficiently destroying potentially harmful chemical and biological agents. These plasmas produce large quantities of O_2 ($a^1\Delta_g$), which may be one of the active agents in the decontamination process. In the semiconductor industry for example, ashing of photoresist films on semiconductor wafers involve using oxygen free radicals.

2.8 Background summary

This background chapter provides information for establishing the operating parameters for the micromachining system. Microplasmas can be generated using a number of different applicators, at various operating frequencies and using different power levels. For this work, the energy coupled into the plasma is in the form of microwave energy. Microwave excitation provides the ability to sustain high density plasmas ($n_e = 10^{11} - 10^{14} cm^{-3}$) with a power level of less than 50 W.

Different applications require different operating pressures, which can range from a few mTorr (etching) up to a few hundreds of Torr (light source). The physics of the plasma discharge changes for different operating pressure regions. Thus, the research work presented here only concentrates on plasmas that are generated in the moderate pressure region (0.1 – 100 Torr). By limiting the operating pressure, the performance of the micromachining system for various applications might not be optimal. However, it is suitable to simplify the design prototype while obtaining experimental results for each potential applications as a proof of concept.

Since one goal of this work is to study the potential applications of microplasmas, the size of the plasma beam for the material processing will be kept to be less than a few millimeters. However, the size of the plasma at the applicator can be larger than one millimeter in order to maintain a low power density. In order to generate a plasma, the smallest size of the discharge tube must be larger than the plasma sheath. The plasma sheath width can be defined as several electron Debye lengths [78], which can be expressed as:

$$\lambda_{De} = \left(\frac{\epsilon_0 T_e}{e n_0}\right)^{1/2} \qquad (2.8.1)$$

where ε_0 is the permittivity of free space, T_e is the electron temperature, e is the elementary charge and n_0 is the electron density. Assuming the electron temperature is two eV and the electron density is 10^{12} cm^3, the Debye length is 10.5 μm. Thus, this research work is aimed at creating plasma beams on the order of 10's – 100's μm.

3 Micromachining System Design

3.1 Overview of the micromachining system

The purpose of the micromachining system is to use spatially localized plasma beams to process materials. The overview of the micromachining system is illustrated in figure 3.1.1. It can be described by considering it as five sub-systems. They are the microwave network, the plasma applicator, the gas/vacuum system, the processing chamber, and the automation and characterization system. The second section of this chapter describes the foreshortened coaxial cavity, which serves as the plasma applicator. In the next sections, the overall system design is explained, including the microwave network and the gas/vacuum system. Section 3.7 describes the apparatus inside the vacuum chamber and the processing area in detail. Lastly, the automation and characterization system are presented in section 3.8.

Part of the design procedure is to decide which parts, components and type of materials are to be integrated into the overall system to achieve the goal. Thus, a brief discussion regarding the decision process to choose suitable parts, components, and materials will be presented.

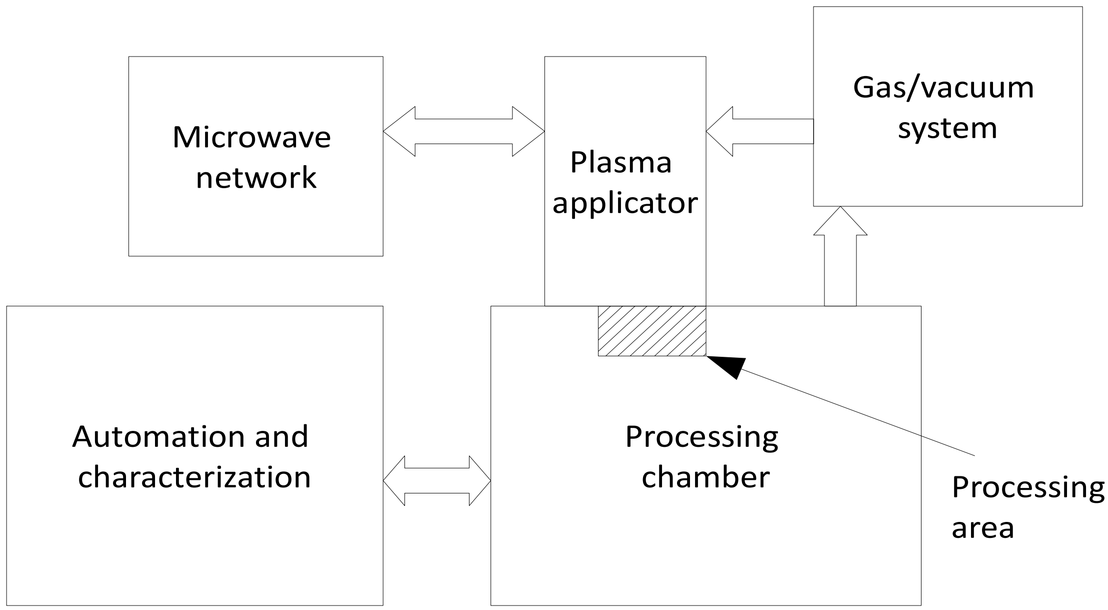

Figure 3.1.1: The schematic of the micro-machining system.

3.2 Foreshortened coaxial cavity microwave reactor

Michigan State University has developed various microwave excited microplasma applicators. To embed a microplasma applicator on top of the processing chamber the applicator needs to have a straightforward design. The most suitable candidates are the microstrip based applicator [52] and the foreshortened coaxial cavity, which is also called the re-entrant cavity [54]. The microstipline applicator, as shown in figure 2.2.7, promised a good fit for the micromachining system. The applicator could be mounted sideways so that the side of the ground plane is attached to the top of the processing chamber. The discharge tube goes in between the stripline conductor and the ground plane and into the chamber. This configuration has been tested and some issues were encountered. In order to contain the microwave radiation, a Faraday cage must be used to enclose the applicator. This makes any work on the applicator become restricted. Another issue from using this applicator was the discharge tube, which is made of quartz, breaks easily. This happened because the fragile tube is attached to the processing chamber, gas line, and trapped in between the stripline conductor and the ground plane. Any mechanical stresses that are applied to the applicator, such as adjusting the sliding short, could shattered the tube. Thus, the foreshortened coaxial cavity applicator is used because it can overcome the aforementioned issues.

The foreshortened coaxial cavity is shown in figure 3.2.1 and is a modification of a coaxial transmission line, which in this case is short-circuited at one end and has a gap at the other. That is, the inner conductor is separated from one end to form a gap region. A discharge tube is placed inside the hollow inner conductor of the cavity. Feed gas flows inside this tube at a specific flow rate and pressure. The outer diameter of the tube should be a few millimeters smaller than the inner diameter of the hollow inner conductor. This condition makes the discharge tube and the cavity independent of one another so that any cavity adjustments will not affect the tube. The cavity is mounted on a manual translational stage which acts as a cavity holder. The height of the cavity with respect to the top of the processing chamber can be adjusted by sliding the holder up or down. The gas line, which is attached to the discharge tube, is mounted on another holder so adjustment of the cavity height will not interfere with the gas line.

For the foreshortened coaxial cavity the ratio of the inner and outer conductors' radii was chosen to give the coaxial transmission line structure a characteristic impedance of 50 Ω. A quartz discharge tube with inner diameter of two millimeters and outer diameter of three millimeters was placed inside the hollow inner conductor, which has 6 millimeters inner diameter. The hollow inner conductor is tapered at the cavity gap to maximize the electric field intensity near the discharge tube. A sliding short is used to adjust the length of this cavity. The gap size between the inner conductor and the cavity gap end can be adjusted by rotating the inner conductor. A loop-ended rigid miniature coaxial transmission line delivers the microwave power into this cavity. This loop antenna can be rotated and its insertion length can also be varied. By adjusting the sliding short, gap length, coupling loop orientation and length, the cavity's resonant frequency can be tuned from less than 600 MHz to over 4 GHz for either low or high density plasma in the discharge tube [55].

A small microwave radiation leaking out from the cavity gap can be observed using a microwave survey meter for a properly tuned empty cavity. When there is a small plasma load in the cavity, the radiation leaks become negligible. However, when the plasma column gets longer, the radiation leak gets higher but it still remains below the safety limit. Thus, this applicator does not require the use of a Faraday cage.

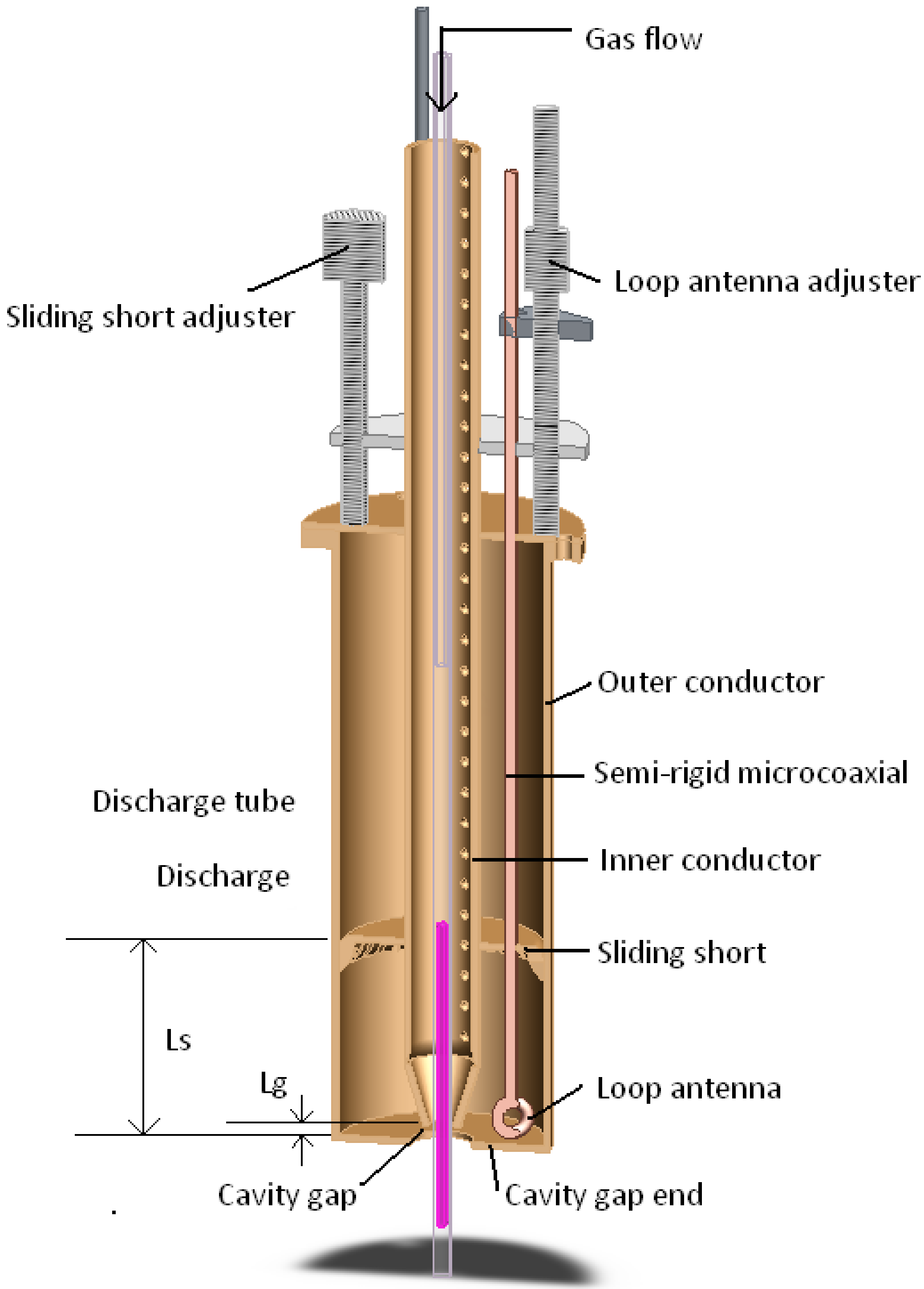

Figure 3.2.1: Schematic of the foreshortened coaxial cavity applicator. For interpretation of the references to color in this and all other figures, the reader is referred to the electronic version of this dissertation.

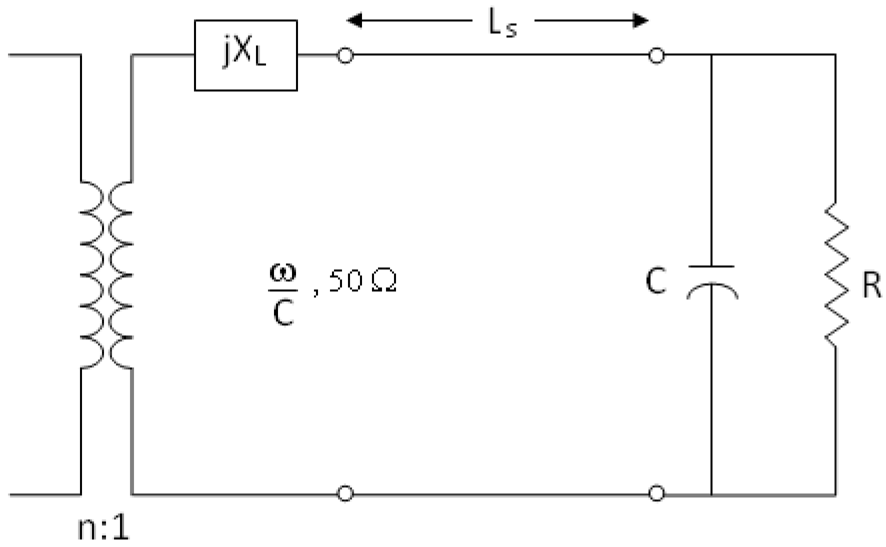

Figure 3.2.2: Equivalent circuit of the foreshortened coaxial cavity.

The equivalent circuit representation of the foreshortened coaxial cavity is shown in figure 3.2.2 On the left hand side of the equivalent circuit, the microwave energy is coupled into the cavity using a single loop antenna (n:1). jX_L is the reactance of the short circuited transmission line, L_s is the length of the transmission line and the gap region is modeled as a capacitor. Because the the gap region is small, the reactance of the gap region will be large. In order to resonate, the reactance of the short circuited transmission line must be large and inductive. To satisfy this condition, the length of the cavity should be less than, but approximately equal to, a quarter wavelength. The coupling loop antenna is orientated so that the plane of the loop is normal to the ϕ direction. In this position, microwave energy is critically coupled to the H_ϕ component of the TEM wave inside the cavity.

3.3 The microwave network

Microwave energy is supplied by a 2.45 GHz MPG-4 Opthos Instrument, Inc. microwave power supply which has an operating power range from 1 Watt to 120 Watts. The microwave circuit has a characteristic impedance of 50 Ω. The circuit includes a CT-3695-N UTE Microwave three port circulator, a 50 Ω Thermaline Coaxial resistor model 8085 as the dummy load, a Narda model 3003-10 coaxial directional coupler, STORM MFR57500 and Ecoflex15 LOW LOSS coaxial cables with N-type connectors, an Agilent E4419B power meter with Agilent 8481A power sensor, and a 30 dB attenuator.

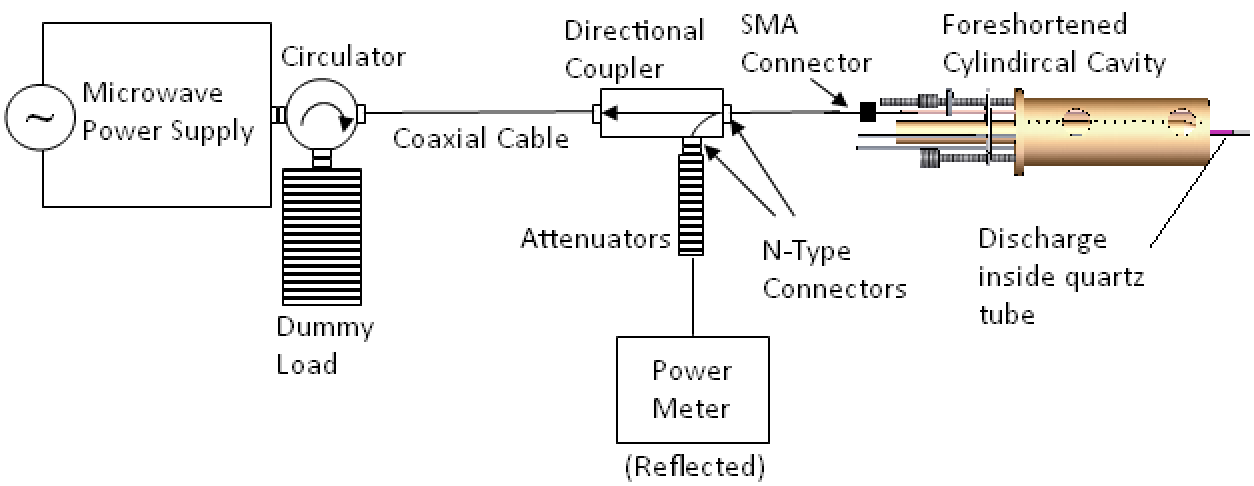

Figure 3.3.1: Schematic of the Microwave system.

The configuration of the microwave circuit is shown in figure 3.3.1. The circulator transfers the microwave energy from the microwave power source into the system. A dummy load connected to the circulator is used to protect the power supply by absorbing the reflected microwave signal from the system. A directional coupler was used in this system to measure the reflected power. The output port of the directional coupler was connected to the circulator via the STORM coaxial cable. The input port is connected to the foreshortened coaxial cavity via the Ecoflex15 coaxial cable in order to measure the reflected power from the cavity. The power meter was connected to the sampling port of the directional coupler. The Ecoflex15 cable is connected to a semi rigid coax UT085 line using an N-type to SMA adapter. The end of this microwave transmission line is a loop antenna which is located inside the foreshortened coaxial cavity. The average handling power for continuous operation for the semi rigid coaxial cable is around 70 W. Thus, the maximum input power used in the system should be lower than 70 W.

3.4 The discharge tube

Discharge tube design is an important factor in building the micromachining system. The objective of this work is to create a plasma beam with a feature size on the order of 10's to few hundred's of microns. However, as noted in the previous work [53], the smaller the tube size, the higher the power density. Conversely, the tube outer diameter must be smaller than the hollow inner conductor as noted in the previous subsection. Thus, to implement the goal of creating a sub-millimeters plasma beam from a plasma generated using the foreshortened coaxial cavity, the discharge tube used in the experiment is set to have two millimeters inner diameter and three millimeters outer diameter. To achieve the plasma beam size, the tip of discharge tube at the processing area can be modified or an aperture can be installed.

Creating a smaller inner diameter on the tip of discharge tube can be accomplished by heating the tip up to the softening point of the material. The tube needs to be rotated slowly to achieve uniform wall thickness. This method can create a tip with an opening diameter on the order of 100's microns. Another way to reduce the opening of the tube is by using a micropipette puller. The micropipette puller can fabricate an opening on the order of 10's μm. However, the discharge tube sidewall becomes tapered with a large aspect ratio compared to the diameter of the opening. A large aspect ratio should be avoided to minimize the effect of the discharge tube on the plasma such as surface wave perturbation and increased wall recombination. Material in consideration for the discharge tube is either borosilicate glass (softening point = 820 ^{O}C) or quartz glass (softening point = 1600 ^{O}C). Work involving tip modifications was performed on borosilicate tubes only since they can be softened using a regular propane torch. Softening quartz glass requires an oxygen/acetylene torch which is not available in the lab.

Reducing the diameter of the discharge tube at the tip consequently increases the pressure inside the the tube while in operation. The smaller the tip diameter the bigger the pressure differential between the processing chamber and the discharge tube. As a result, sustaining the plasma inside the tube requires a higher microwave power. By increasing the microwave power, the radiation leakage becomes significant to the point that the microwave leak can generate plasma inside the processing chamber, which is easier to generate because the pressure is lower than inside the tube. To overcome the pressure differential issue, installing a grid or an aperture a distance away from the tip of the discharge tube provides a better solution in achieving a micron size plasma beam.

A few preliminary experiments were performed using borosilicate glass as the discharge tube. Due to its low softening point temperature, borosilicate glass is not a good candidate for confining microwave plasmas especially the ones with a mixture of molecular gas, which has a gas temperature higher than the softening point of borosilicate glass. Thus, discharge tubes used in this work were made of quartz glass.

3.5 The center piece adapter

The center piece adapter, as shown in figure 3.5.1, is part of the micromachining system that holds the discharge tube and is attached to the top plate of the processing chamber. The diameter of the top part of the center piece is 38 mm and the bottom part is eight mm. The top plate of the processing chamber was machined to fit the center piece. An o-ring groove was machined on the top plate for vacuum seal (o-ring is not shown in the figure). The center piece is made of quartz glass to match the material of the discharge tube. The size of the center piece should be large enough so the vacuum seal by the o-ring is adequate. On the other hand it has to be small enough to minimize any stray microwave leaking into the processing chamber.

To provide a vacuum seal between the discharge tube and the quartz center piece two materials were considered: epoxy and Ceramabond. Epoxy provides a good vacuum seal for the intended operating pressure and only needs a relatively short time to apply and to remove. However, it is not microwave transparent and not suitable for high temperature processing. On the other hand, Ceramabond, a ceramic based bonding material, is good for high temperature processing and transparent to microwaves. The curing and removal process is very long and due to its porosity, its vacuum sealing capability might not be as good as the epoxy. The trade-off between these two materials suggests that Ceramabond is more suitable for this work. In order to make a good contact between Ceramabond and quartz, part of the quartz surface was sandblasted. The bonded piece needs to be air dried at room temperature for two hours. Then it needs to be cured in an oven at 200 ^{o}C for one hour. The removal of Ceramabond can be performed using an ultrasonic bath for approximately two hours.

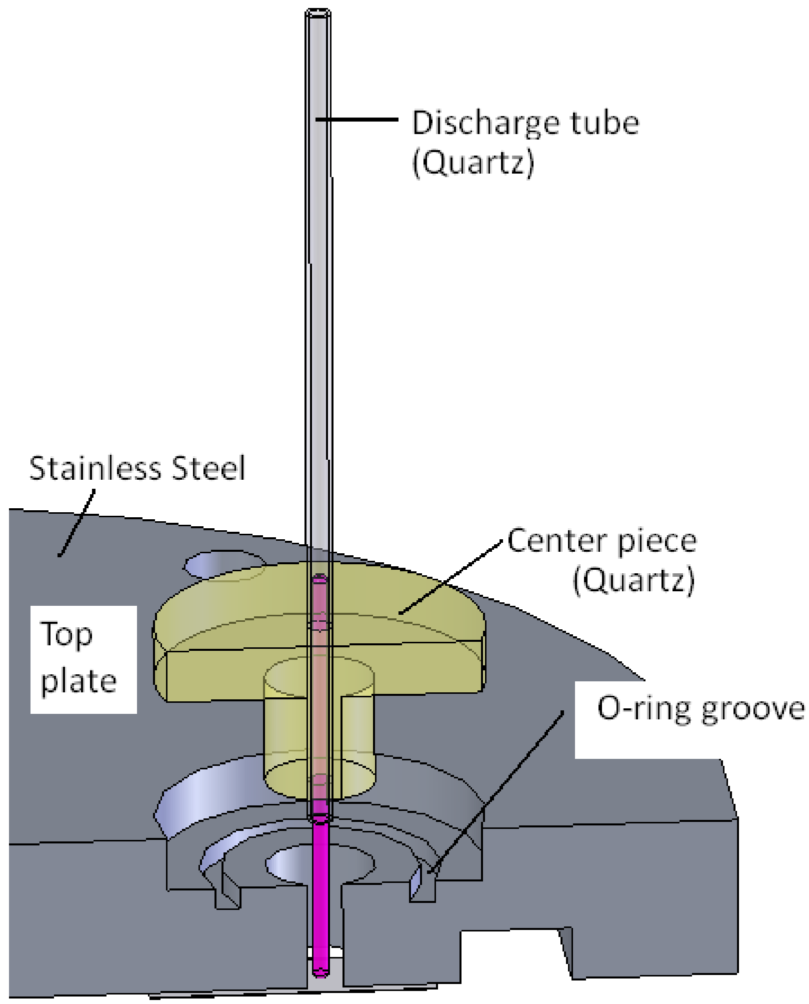

Figure 3.5.1: Drawing of the top plate of processing chamber showing the center piece.

3.6 The gas/vacuum systems

An illustration of the gas/vacuum system can be seen in figure 3.6.1. 99.999% pure argon, ultra high purity oxygen, neon, and sulfur hexafluoride (SF_6) gases are fed into the quartz tube inside the microwave cavity through mass flow controllers (MFCs) with maximum flow rate of 20 sccm for argon and 50 sccm for oxygen and SF_6. The flow rate of each feed gas can be controlled from the MKS model 247C 4-channel readout. Polyethylene tubing with a diameter of ¼ inch is used to carry the gas flow to and from the MFCs. A 4-way branch Swagelok connector is used to mix the feed gases. A smaller diameter plastic hose with an outer diameter of 1/8 inch is used to deliver the mixed gas to the quartz discharge tube. A heat shrink tubing is used to connect this small hose and the quartz tube. This heat shrink tubing does not provide a great vacuum seal, however, it is easy to replace and the vacuum leak rate is small for the operating pressure, on the order of 1 – 1.5 Torr/hr. The discharge pressure is monitored by a mechanical pressure gauge HEISE type CM-24164 with resolution range of 0 to 1500 Torr. The quartz center piece adapter is used to hold the discharge tube. This center piece adapter also vacuum seals the feed through hole at the top plate as seen in figure 3.7.1. Ceramabond type 835 from Aremco Product Inc. bonded this adapter with the quartz tube.

A rotary vane mechanical pump (Alcatel model 2020CP1) is used in this system to lower the pressure inside the processing chamber down to 300 mTorr. This mechanical pump uses 850 mL TKO-19 Ultra Hydrocarbon oil. Since feed gases used in this processing system are corrosive, such as oxygen and fluorine byproducts from SF_6, the pump oil is changed every 6 months. A 4-inch foreline trap is attached to this mechanical pump to prevent any contamination of the processing chamber from the vacuum pump oil. The pressure in the chamber is measured with a capacitive manometer MKS type 626 pressure transducer that has a measurement range from 0 to 100 Torr. The MKS 253B throttle valve is used for fine control of the chamber pressure. The pressure transducer and the throttle valve are connected to MKS type 651 pressure controller. All of the vacuum line components are based on QF-40 standard flange connectors.

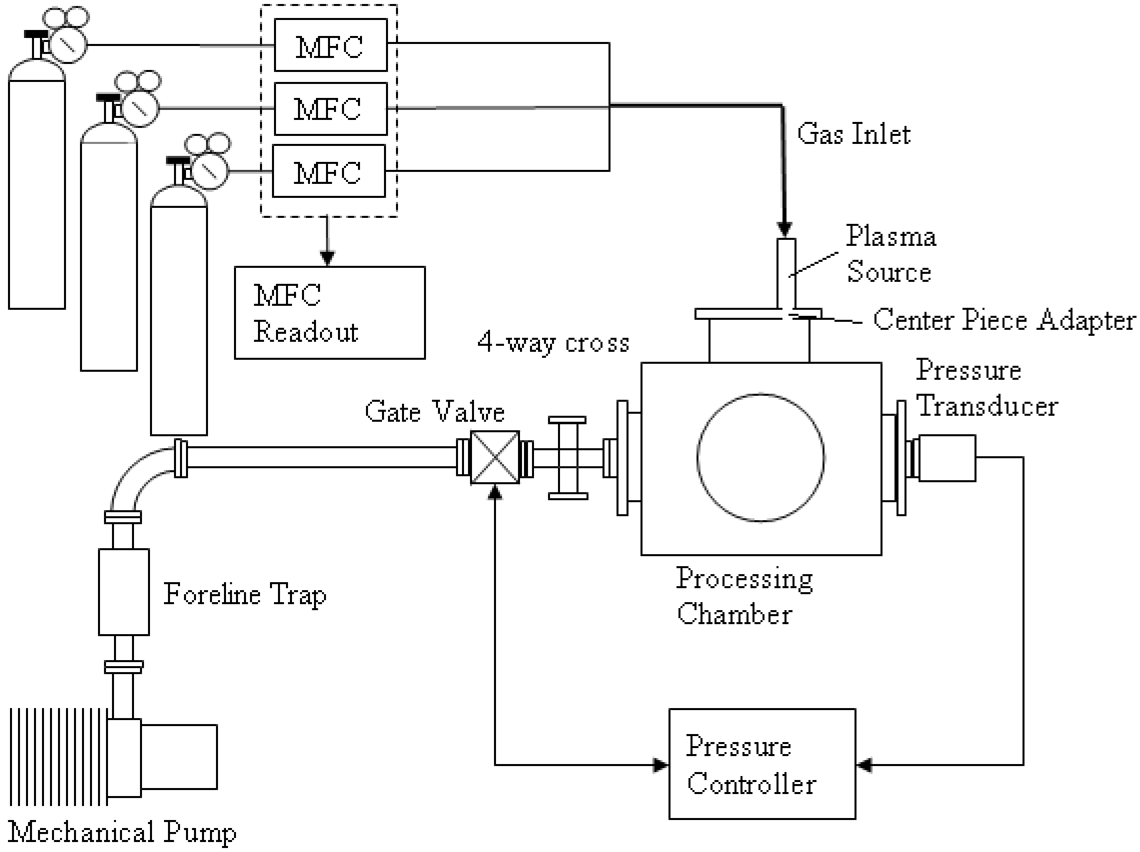

Figure 3.6.1: Schematic of the gas/vacuum system.

3.7 Vacuum chamber and processing area

The processing chamber is a 20 inch diameter cylindrical chamber with a height of 10 inch, as shown in figure 3.7.1. It is placed on top of a 2.5 by 4 feet Newport vibration isolation table. There are four main ports on the side of the chamber. The front window is used for loading the substrate. The back window is for the electrical feedthrough for the translational stage. One side window is used to connect the chamber with the throttle valve which also is connected to the vacuum pump. The other window has three smaller opening; they are for mounting the pressure transducer, inlet for additional feed gases and for venting the chamber, and one for electrical feedthrough for the RF bias circuit and/or the substrate-to-aperture distance sensing circuit.

Inside the processing chamber there are two linear stages which are connected to the substrate holder. One stage, Newport Model 562F-XYZ, has a capability to move in three directional axes with 13 mm travel range. This linear stage, which controls the location of the substrate relative to the plasma beam, is driven by actuators (Newport model LTAPPV6) with the resolution of 35 nm. This brings the micromachining system the capability to treat micro- or nano-scale patterns. All of the actuators are connected to a Newport Universal Controller/Driver model ESP300. The controller is then connected to a computer via a RS-232 cable so that the stage can be controlled using the computer and a predetermined pattern can be processed using software that has been developed by Jiangbo Zhang, a Michigan State University graduate student, in visual C++.

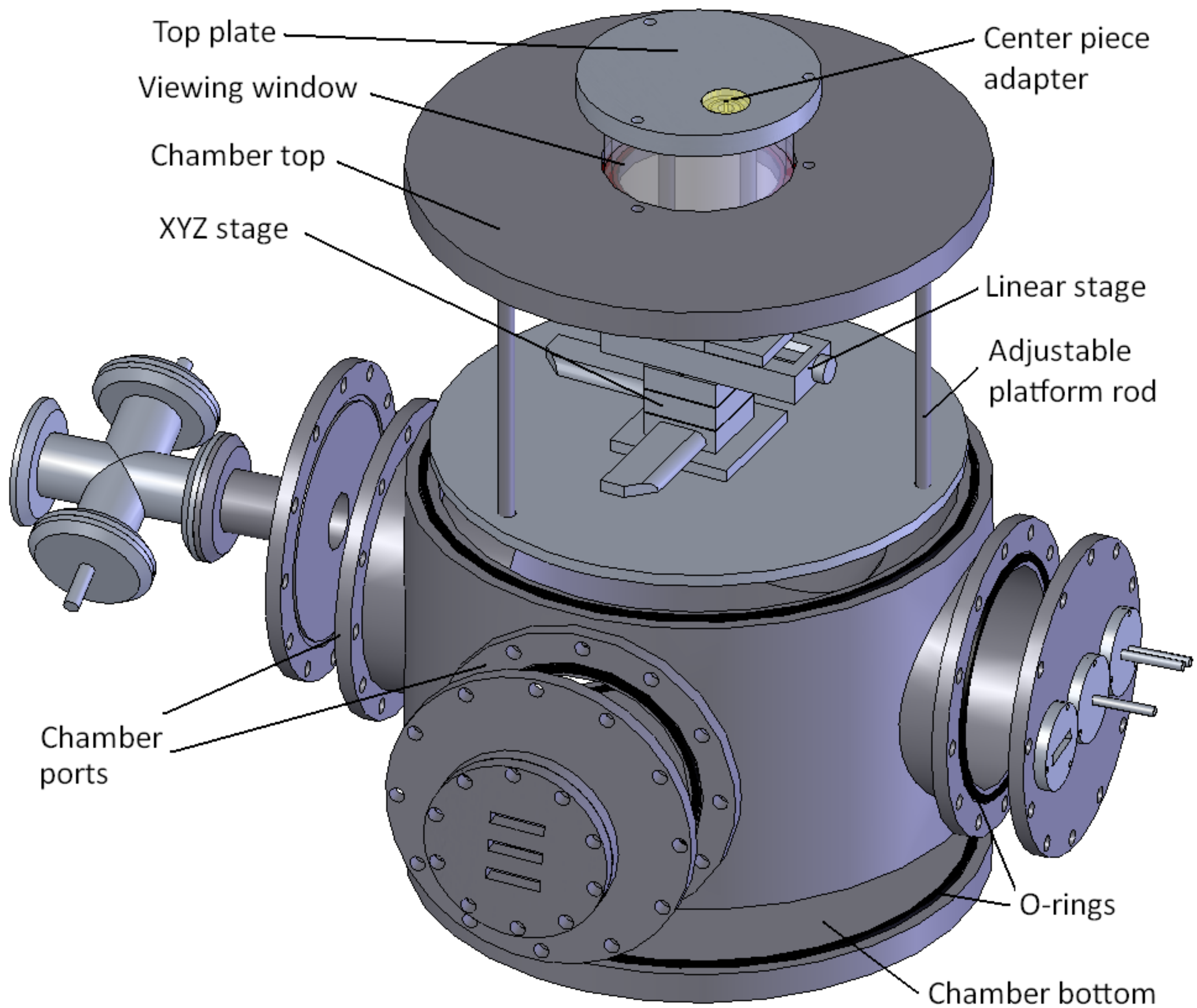

Figure 3.7.1: The exploded view of the micro-machining system processing chamber.

Another motorized linear stage, Standa Model 8MT193-100, is placed on top of the XYZ stage. It has a range of 100 mm and a resolution of 2.5 μm. It can automatically bring the sample to the Atomic Force Microscope (AFM) probe mounted at the left side of processing area.

A six inch diameter Pyrex cylindrical glass with a height of 75 mm and thickness of five mm is used as a transparent viewing window. An OPTEM optical microscope with JAI CV-S23200 color camera is used to observe the micromachining process and characterization process.

The plasma generator is located on the top of the processing chamber. The plasma column is directed into the chamber by the discharge tube. A grid or aperture can be placed at the tip of the discharge tube. This aperture can be mounted directly to the discharge tube or it can be mounted to the top plate.

Another design arrangement is provided to connect the tube to a four-way glass connector, which is shown in figure 3.7.2. An aperture is placed on the downstream of this connector. Two different methods for supplying the feed gases were used. The first method was done by pre-mixing the feed gases and flowing the mixture into the discharge tube. The second method was done by flowing the argon gas into the discharge tube and the other gas was diffused from one of the glass 4-way connector's branches. Experiments were performed using Ar/SF_6 feed gases pre-mixed in the gas line. Without applying a bias voltage to draw the fluorine ions away from the tube and into the processing chamber, the ions etched the inner wall of the tube. It was observed that the quartz discharge tube became opaque and shortly after that the plasma discharge went out.

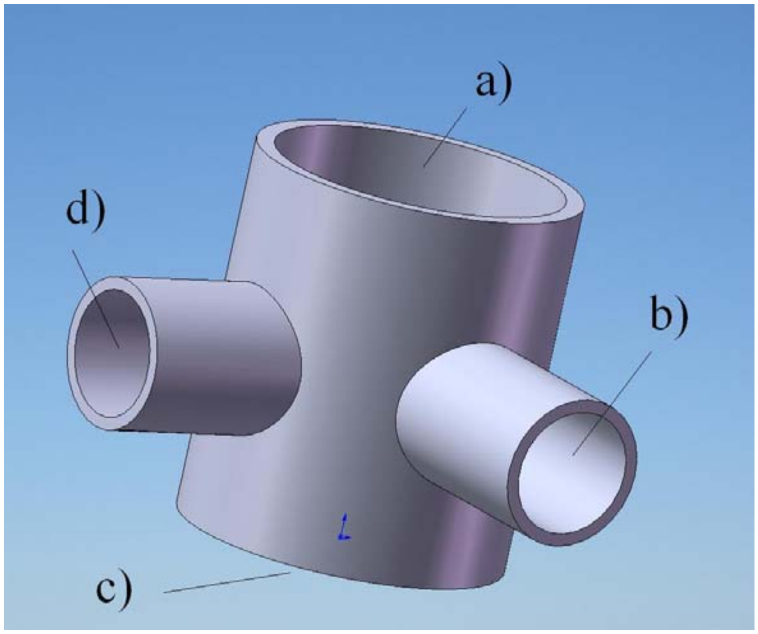

Figure 3.7.2: The 4-way glass connectors. (a) is connected to the discharge tube, (b) is for the diffused feed gas, (c) is connected to the aperture, and (d) is the exhaust line.

3.7.1 Aperture designs

There are three different materials used as the aperture that controls the spot size of the plasma. Pyrex apertures were made from round microscope slide coverslips. As seen in figure 3.7.3 a hole in the center of the Pyrex glass was created using a laser drilling technique done by Michael Becker at the Fraunhofer USA Center for Coating and Laser Applications in Plymouth, MI. The thickness of the Pyrex glass coverslips ranged from 130 - 170 μm. The opening diameter ranges were from 10's – 100's of μm. The complete set of Pyrex samples laser drilled are listed in table 3.7.1.

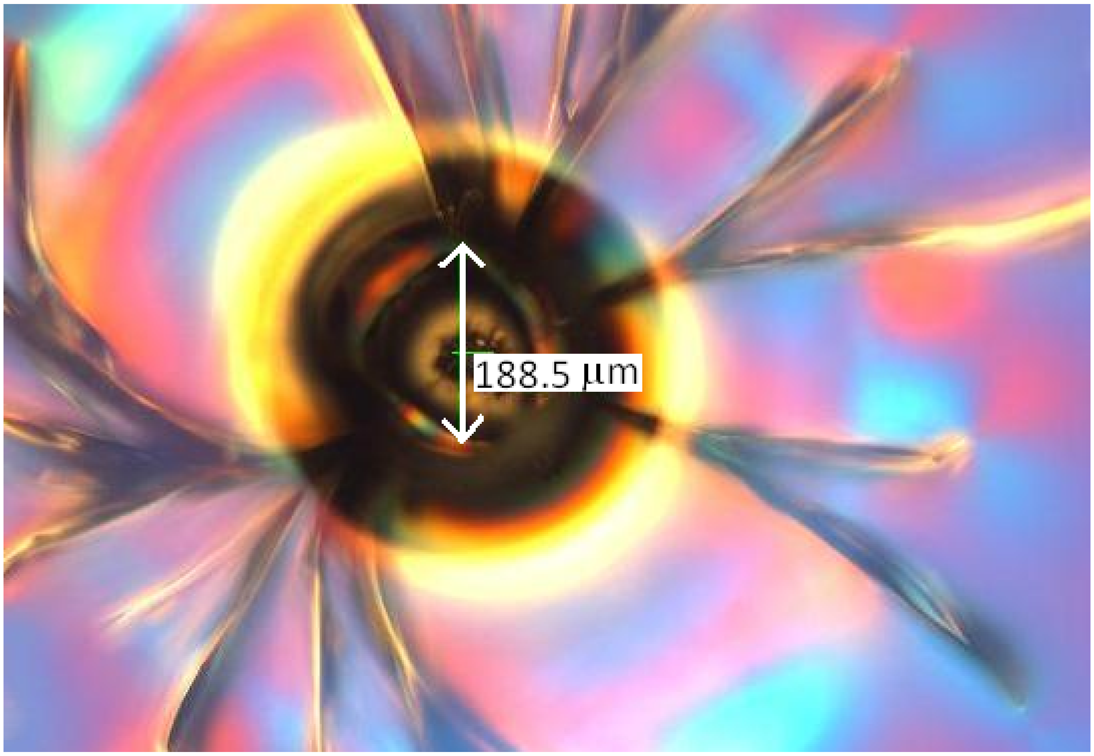

Figure 3.7.3: Optical microscope image of a Pyrex aperture. Top hole diameter is 188.5 μm and bottom hole diameter is 40.38 μm.

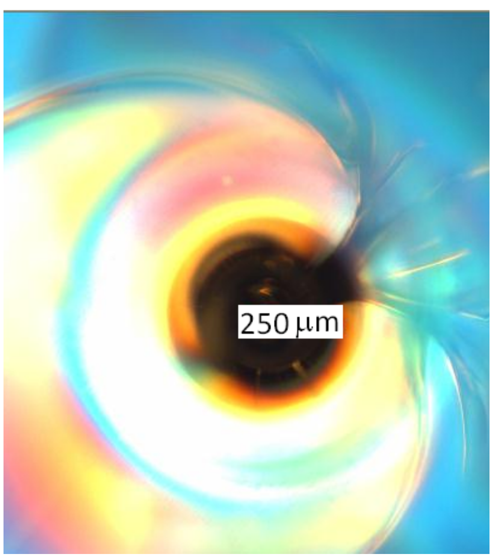

(a)

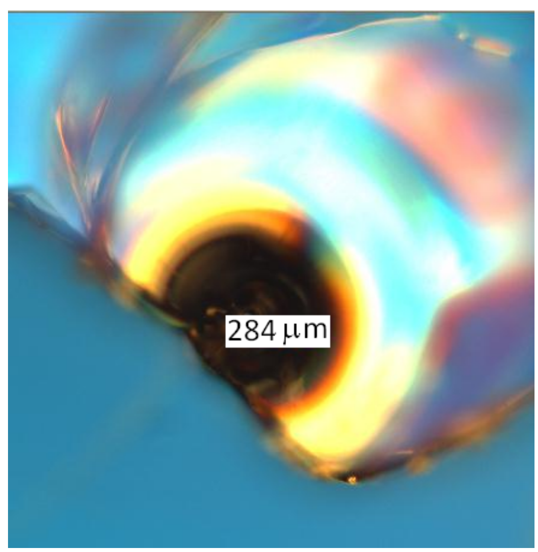

(b)

Figure 3.7.4: (a – d) Top side images of the Pyrex samples taken using an optical microscope and (e) an illustration of the Pyrex aperture.

Figure 3.7.4 (Cont'd)

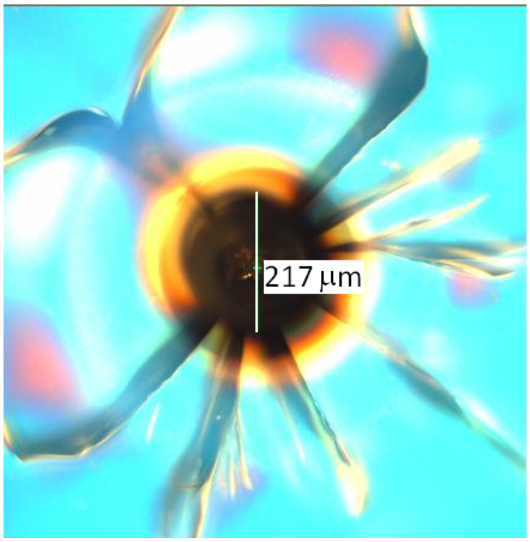

(c)

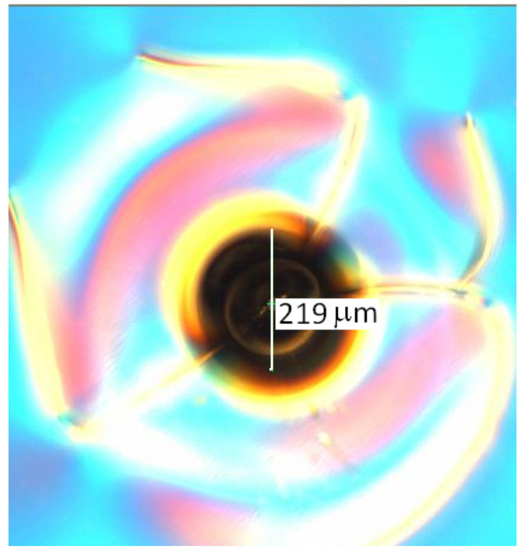

(d)

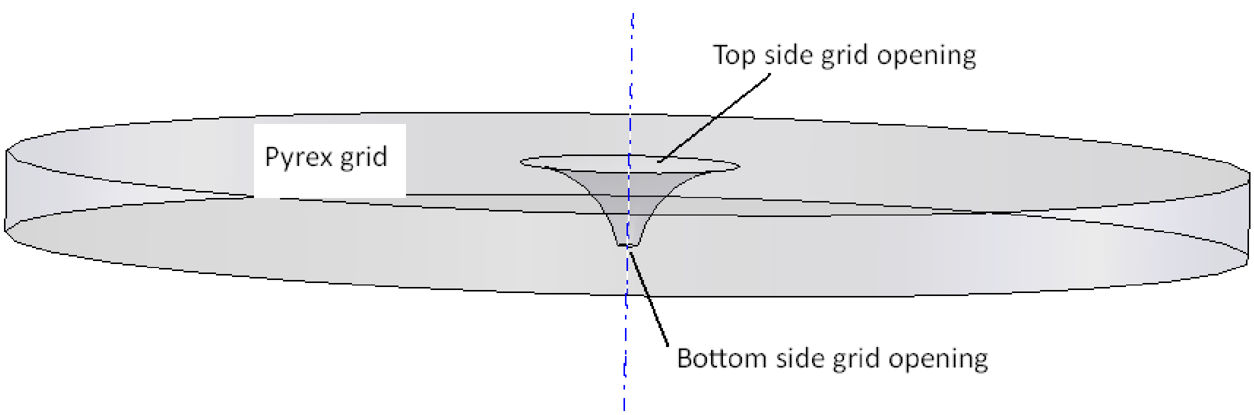

(e)

Table 3.7.1: Pyrex aperture sizes.

Sample no.	Hole diameter in μm		Figure no.
	Top side	Bottom side	
Pyrex 4	250	15.38	3.7.4 a
Pyrex 5	284	13.46	3.7.4 b
Pyrex 6	217	13.46	3.7.4 c
Pyrex 8	219	19.23	3.7.4d
Pyrex 10	188	40.38	3.7.3

As seen in figure 3.7.3 and 3.7.4 the laser drilling technique creates fractures around the aperture opening walls. The hole diameters of the top side are significantly bigger than the bottom side.

The second type of aperture was made from silicon wafers. A combination of KOH wet etching and dry etching was performed to etch a hole through a silicon wafer. Figure 3.7.5 shows the optical microscope images of a silicon wafer aperture. The square profile was obtained due to the KOH etching process.

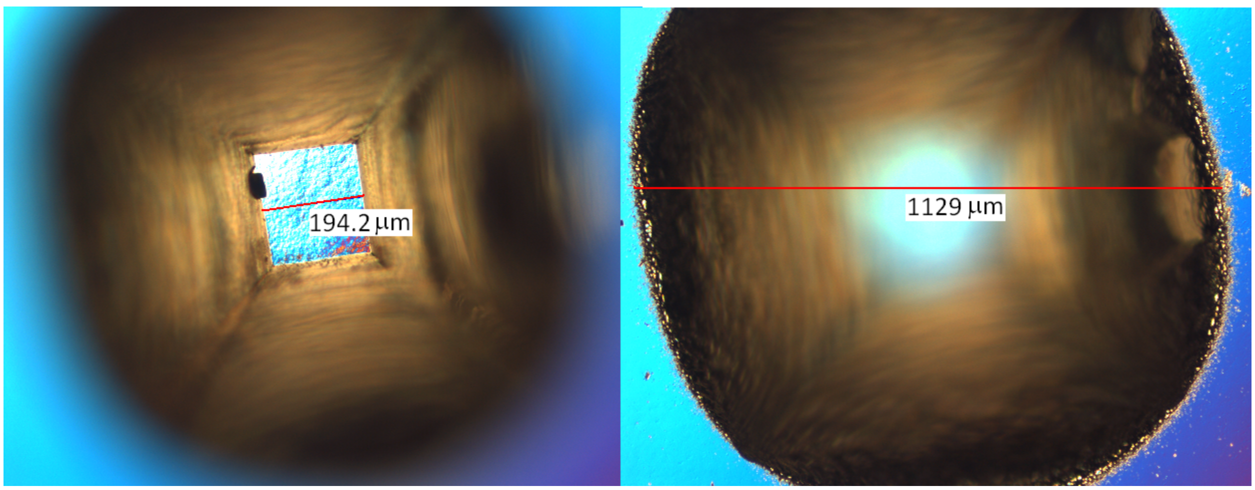

Figure 3.7.5: Optical microscope images of silicon aperture at different focus location. Hole size is 194.2 μm on the bottom (left figure) and 1.129 mm at the top (right figure).

The silicon aperture fabrication procedure starts with coating a 250 μm (100) silicon wafer with SiO_2 by an oxidation process using an oven. Next, apertures with various size are patterned on a single wafer using a lithography process. After that, the unwanted oxide layer is removed using a buffered oxide etching (BOE) procedure. Finally a KOH wet etching process is applied to remove the remaining silicon. The etching rate of this process is approximately 1 μm/min. Figure 3.7.6 shows an illustration of a silicon wafer after the KOH etching process. The KOH etching leaves an inverted pyramid profile because the etching rate of (100) silicon is faster than the (111) silicon plane.

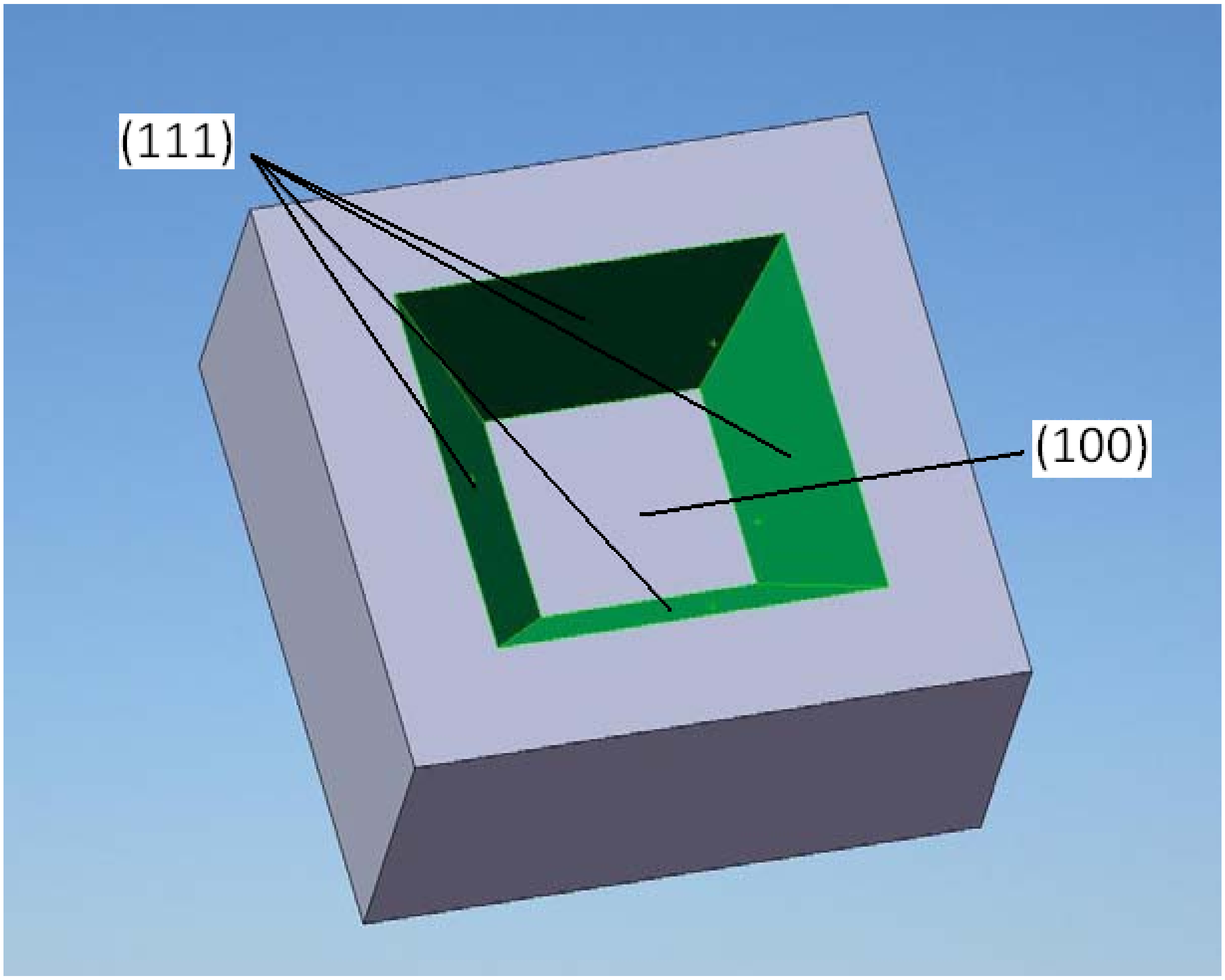

Figure 3.7.6: Illustration of silicon wafer (100) after KOH etching.

The third kind of apertures were made of stainless steel as shown in figure 3.7.7. They are Melles Griot precision pinholes. The hole diameter is 30 μm and the substrate thickness is 13 μm. All three types of the aperture are useful for different applications.

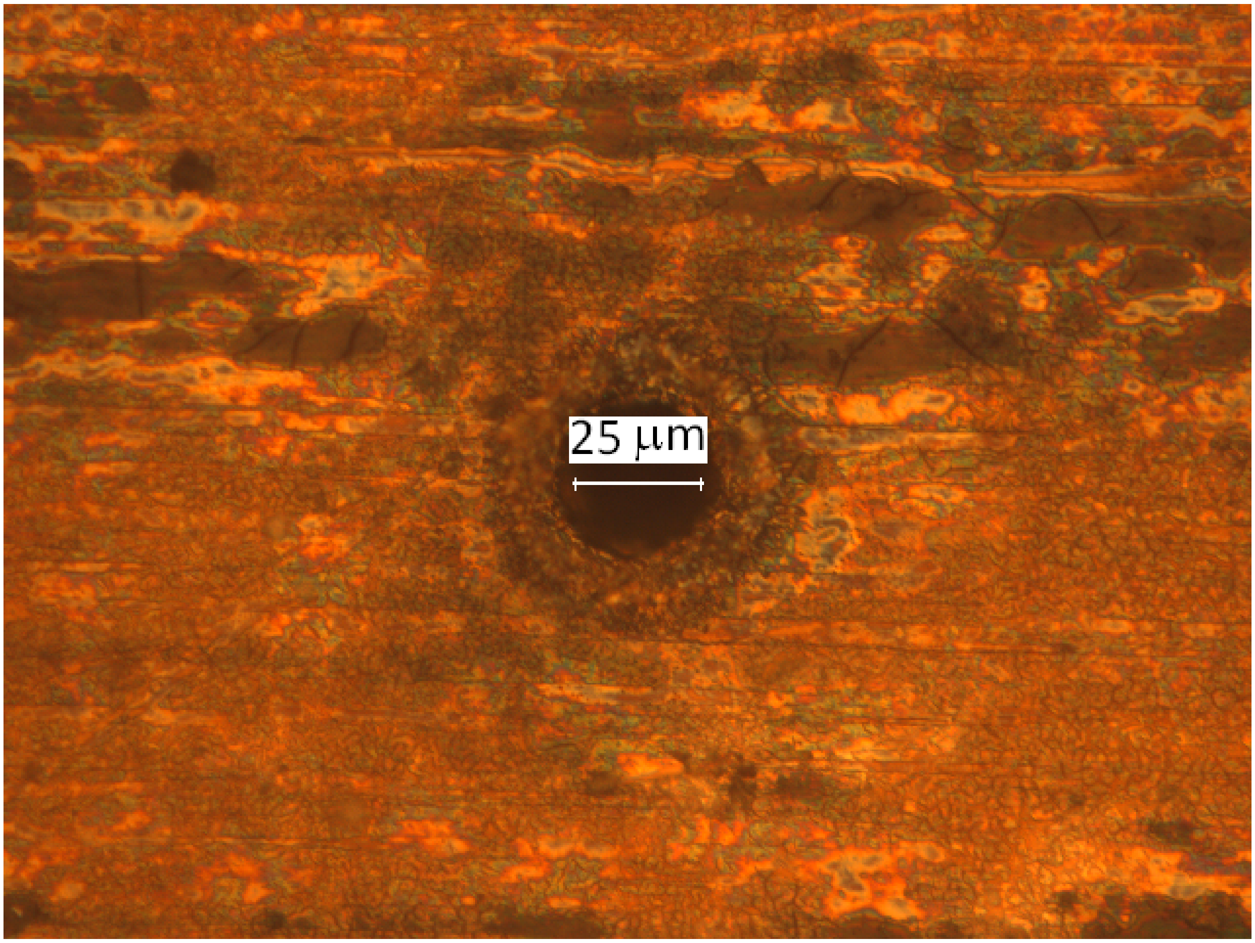

Figure 3.7.7: Optical microscope image of a Melles Griot pinhole.

3.7.2 Voltage bias designs

A bias circuit is needed to accelerate the ions from the plasma column inside the discharge tube to the substrate. The voltage source is a Wavetek function generator model 182A. This function generator is capable of operating with frequency range from 4 mHz up to 4 MHz with 20 peak-to-peak highest output voltage. Two different designs have been implemented in the micromachining system. One was intended for plasma processing without an aperture and the other was designed for plasma processing which employs a conducting aperture.

A schematic of the RF bias system connected to a conducting aperture is shown in figure

3.7.8. One electrode is connected to the aperture and the other is connected to the substrate holder. The aperture is mounted on an insulating material, in this case a Pyrex glass. The existence of plasma between the aperture and the substrate will close the circuit.

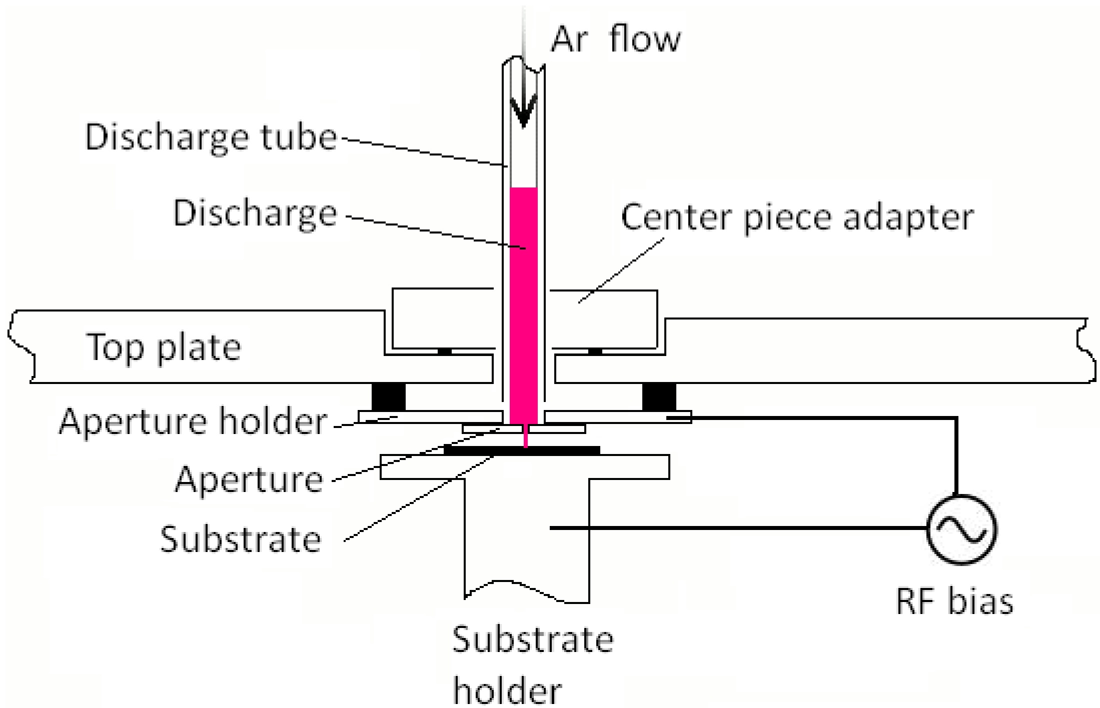

Figure 3.7.8: Schematic of the RF bias connected to an aperture.

In some experiments the aperture was not present in the system. In this case the RF bias was applied between the substrate holder and 100 μm diameter tungsten wires. The tungsten wires are placed in between the tip of the discharge tube and the substrate as shown in figure 3.7.9 or they can also be inserted through a tiny hole in the discharge tube's wall as an alternative method.

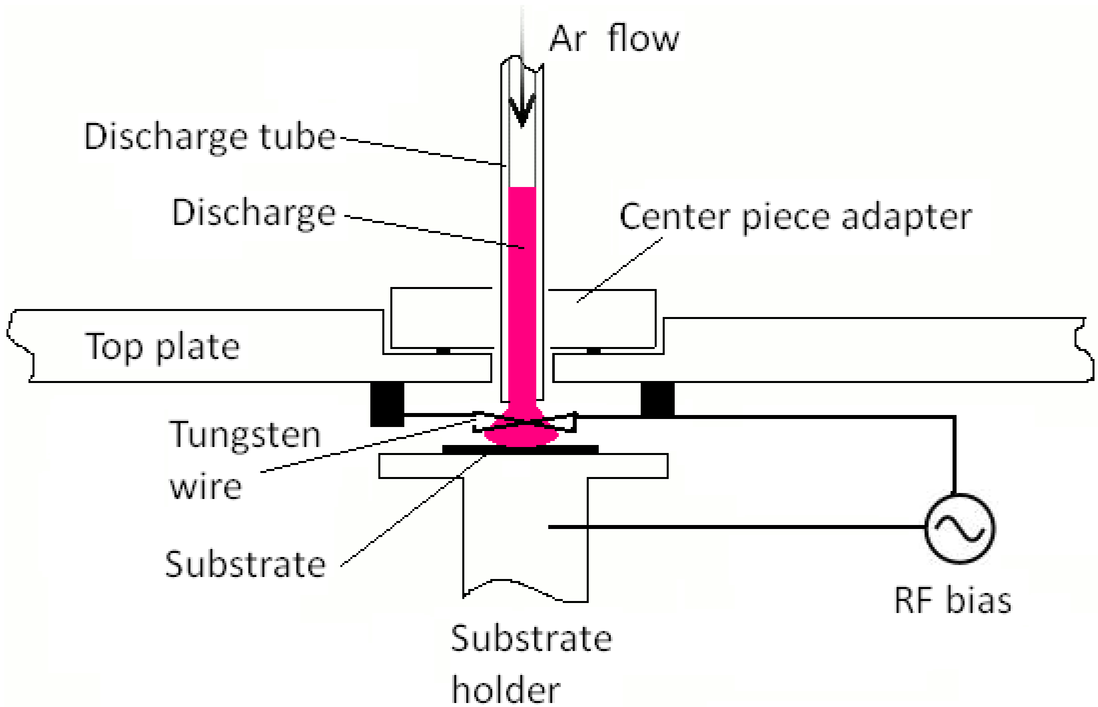

Figure 3.7.9: Schematic of the RF bias without an aperture.

3.7.3 Substrate sensing design

One of the challenges in performing localized plasma processing using the micromachining system is to control the distance between the tip of the plasma beam and the surface of the substrate. When the vacuum condition of the processing chamber changes, such as moving the substrate in and out of the chamber, this distance may change as well. Hence, a substrate sensing system is needed to monitor its location with respect to the top plate, where the tip of the discharge tube and/or the aperture is located.

The processing area of the micromachining system is shown in figure 3.7.10. A sensing block of aluminum (5 mm x 10 mm x 3 cm) was attached to the top plate of the micromachining system. Before performing the surface treatment, the substrate along with its holder is moved toward the sensing block using the moving stages. The substrate holder is made of stainless steel and is not electrically connected to any other metal parts of the chamber including the top plate. An external DC circuit is connected to the top plate and the substrate holder. The circuit has a 3 V battery source, a resistor and a LED, thus when the substrate holder touches the sensing block the circuit is closed and the LED is on. This way, the z- position of the substrate with respect to the top plate can be defined.

Another use of the sensing block is to confirm that both the top plate and the substrate are in a level position. To perform a level test, the substrate holder is placed a few μm away from the sensing block and the automated stage performs a x- and y- axis travel for the maximum range (13 mm x 13 mm). The substrate holder is 1.5 inches in diameter and one inch at the center of the holder is one millimeter deeper than at the edge. The setup of the substrate sensing has been tested using the substrate holder without a substrate on it.

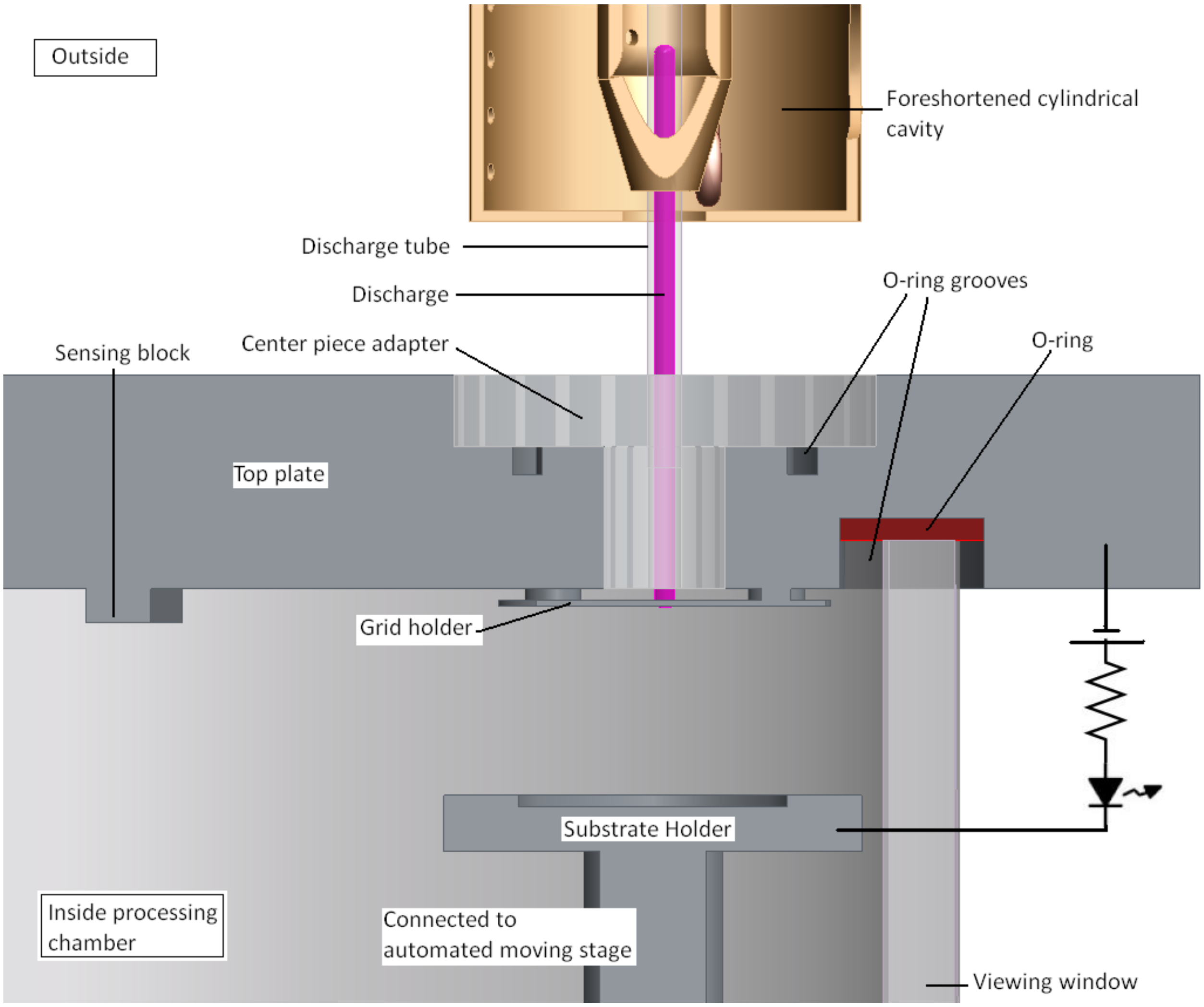

Figure 3.7.10: Schematic of the processing area of the micromachining system.

3.8 The automation and characterization system

The processing procedures of the plasma integrated micromanufacturing workcell are shown in figure 3.8.1. This part of the micromanufacturing system was primarily designed by Xi et al. [127]. Firstly, the pattern of the nanostructure is defined by a computer-aided design (CAD) model. The plasma processing tasks are performed automatically based on the input of the model. Afterward, an AFM surface topography measurement is performed to check the accuracy of the final pattern of the structure in the nanometer range. The difference is sent back to the machine and the plasma process and AFM nanomanipulation tasks are repeated until the correct and precise pattern of the structure is reached.

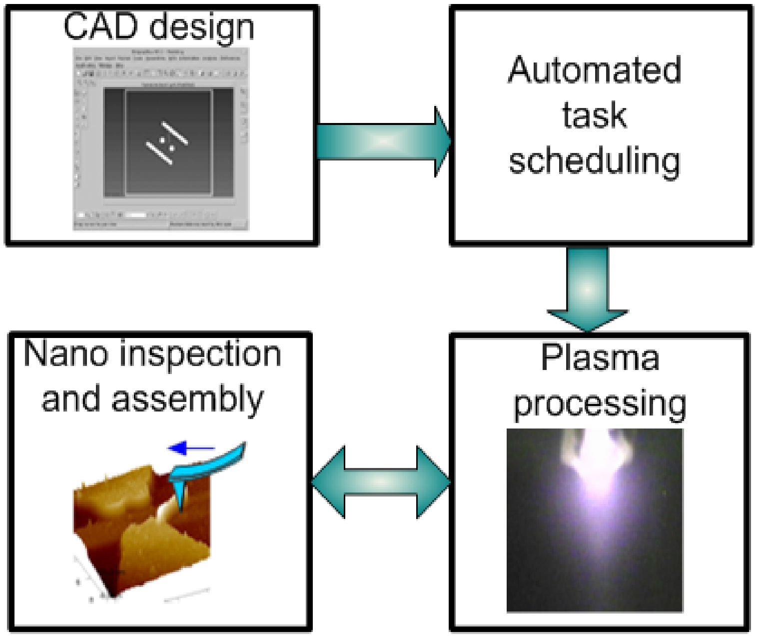

Figure 3.8.1: Flow chart of the plasma integrated micromachining system.

Conventional AFM systems detect deflection of an AFM cantilever by the reflection of a laser beam focused on the top surface of the cantilever. However, it is difficult to integrate this complicated system into the micromachining system. To solve this problem, an AFM active probe was designed and used for AFM nano-inspection and nanomanipulation inside the micromanufacturing workcell. The control diagram of the AFM active probe is illustrated in figure 3.8.2. Instead of using a reflected laser signal, the cantilever deflection is sensed by a piezoelectric material (Zinc oxide) on the AFM active probe. The active probe can also be used to measure sample surface topography by controlling the Z position of the motion stage. Since the deflection is small, the output charge from the active probe is converted to voltage through a preamplifier circuit and then the signal is feedback to the computer. By controlling the motion stage to move in the Z direction to keep the cantilever deflection at a constant value while scanning, the surface topographic data can be extracted. Moreover, the computer can also control the XYZ motion stage allowing the active probe to perform nanomanipulation.

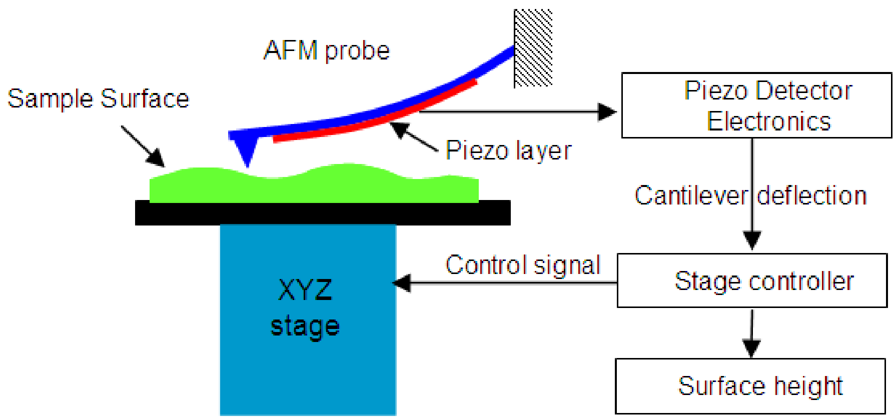

Figure 3.8.2: Control diagram of the AFM active probe.

A computer software interface was developed to control the system as shown in figure 3.8.3. The computer interface consists of two major parts: 1) plasma pattern and 2) AFM imaging. In the plasma pattern interface, the digital data from the CAD design model of the desired micropattern is converted to the position data of the moving stage. After patterning the microstructure using the plasma generator, the AFM imaging interface was implemented for the nano-inspection of the final pattern. In this interface, the active probe is directed to scan the substrate surface, and the topographic image of the surface is created based on the output voltage from the active probe.

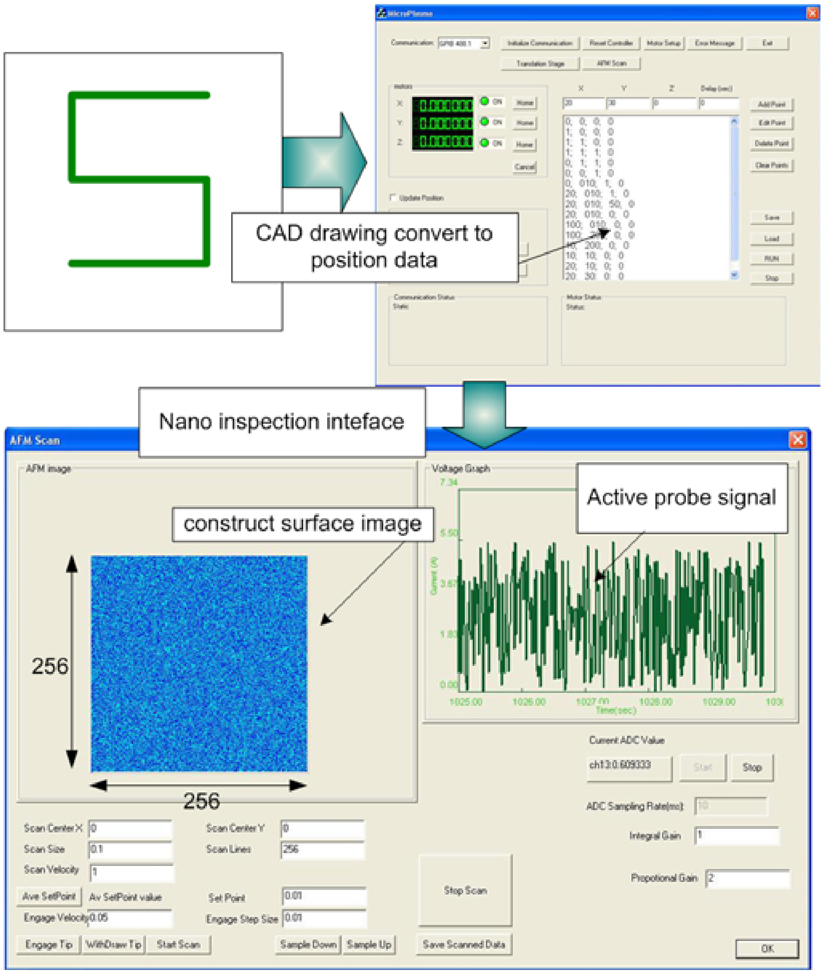

Figure 3.8.3: The computer control interface.

An experiment was conducted to detect the contact point of the active probe and the sample surface. The experimental setup is shown in figure 3.8.4. As mentioned before, the active probe was connected to a pre-amplifier circuit for charge-to-voltage signal conversion. A data acquisition card was used to provide the interface between the circuit and the computer, so that the output voltage from the circuit that indicates the deflection signal of the active probe was received and monitored in the computer. At the beginning, the sample was moved under the AFM active probe and separated by a small distance, and thus no deflection was seen at that point. When the sample was moving upwards to touch the active probe, the probe bent and a change of the voltage was detected as shown in figure 3.8.5. When the substrate moved away from the probe, the voltage was changed in the opposite direction (figure 3.8.5). This indicates that the position of the sample and the active probe can be controlled. By monitoring the active probe signal and controlling the position of the probe, a topographic image of the sample surface can be constructed and nano-inspection can be performed.

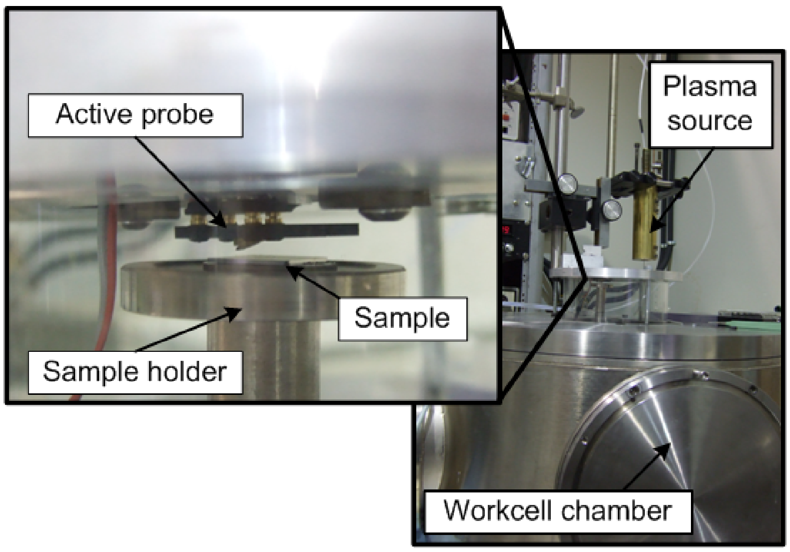

Figure 3.8.4: Photographic image of the AFM manufacturing workcell.

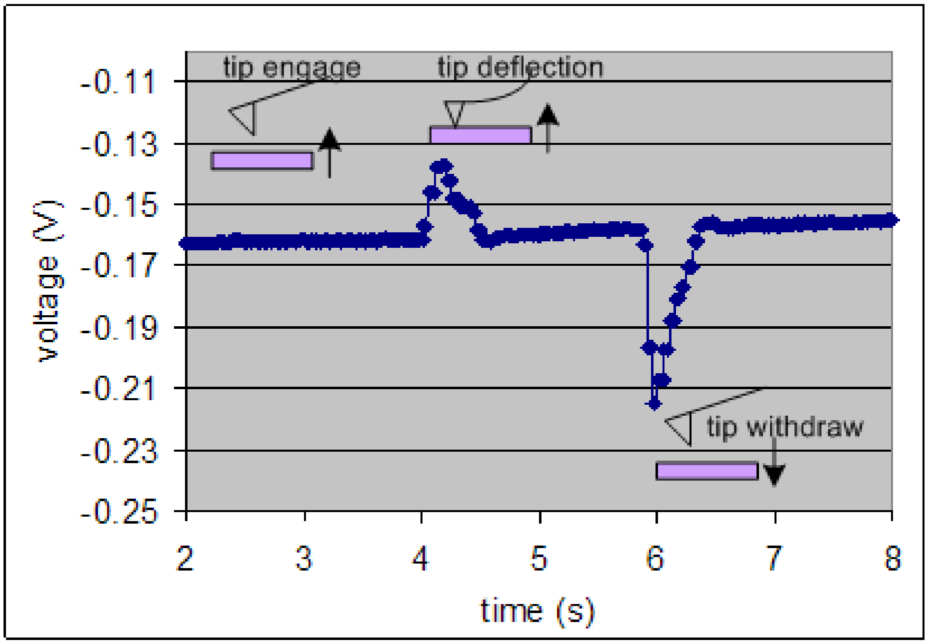

Figure 3.8.5: A typical voltage-time curve when the active probe moved towards and away from the surface.

4 Finite Element Method Simulation of the System

4.1 Introduction

Modeling the microplasma generation subsystem using computational technique provides input for the design, operation, and understanding of the micromachining system. Validation of the computational model will be done by comparing to selected experimental results.

There are two major components for the simulation of the plasma generation portion of the micromachining system. The first one is the simulation of the foreshortened coaxial cavity which provides information on the electric field distributions inside the cavity and the coupling mechanism of microwave energy heating the electron gas within the plasma. The microwave field simulations are presented in section 4.2. The second component of the plasma simulation is generation, recombination, and the transport properties of the species inside the discharge, which is presented in section 4.3. By coupling both simulations, a self-consistent modeling can be achieved as presented in section 4.4.

There are many methods to model a plasma system as previously described in section 2.4. For microwave generated plasmas, the finite-difference time-domain (FDTD) method could be used. However, the foreshortened coaxial cavity is a complicated geometry that has a thin discharge tube, small plasma load and a big cavity structure. Using the FDTD technique would require a very large computational domain. Thus, instead of modeling using FDTD, a finite element method (FEM) is used for this work because the technique can handle a complex geometry more readily. There are off the shelf software packages available at Michigan State

University to simulate electromagnetic problems. They are Ansoft HFSS and COMSOL Multiphysics. Both software packages use a FEM solver to simulate the physics of the system. This project used COMSOL since it is a multiphysics approach that has an advantage because it can be used to model a system which has multiple physical phenomenon coupled with one another.

For this study, the initial conditions are based on the experimental data. The plasma simulations are performed for argon plasma at 1 - 10 Torr with a flow rate 20 sccm. The computer used for the simulations ran Microsoft Windows XP with Intel Core 2 Duo processor at 3.00 GHz with 3.24 GB of RAM.

4.2 Electromagnetic simulations

4.2.1 Eigenfrequency analysis of empty coaxial cavities

Part of the objective of this research involves running simulations using COMSOL Multiphysics 4.0a, a finite element analysis software, to understand the plasma source behavior to direct future design improvements. The first simulations were done to establish the validity of this software. In addition, the simulation must be setup in such a way that the computational cost is minimal. The first task to accomplish this goal was to determine eigenfrequencies of an empty 2.45 GHz coaxial cavity in three dimensional (3-D) and in two dimensional (2-D) geometry. Since the expected eigenfrequencies are well known values, validity of the simulation software for this application can be established.

The cavity length of the empty coaxial cavity shown in figure 4.2.1 was set to be 6.12 cm, which is the half wavelength of the 2.45 GHz microwave operating frequency in air (

$\mu_r = 1 ; \epsilon_r = 1 ; \sigma = 0 [S/m]$). The cavity wall is assumed to be made of a good conducting material, which can be approximated as a perfect electric conductor (PEC) that has a zero tangential component of the electric field:

$$\vec{n} \times \vec{E} = 0 \tag{4.2.1}$$

The simulation domain can be seen in figure 4.2.1. Both the 2-D and 3-D simulations were conducted using the RF module in COMSOL.

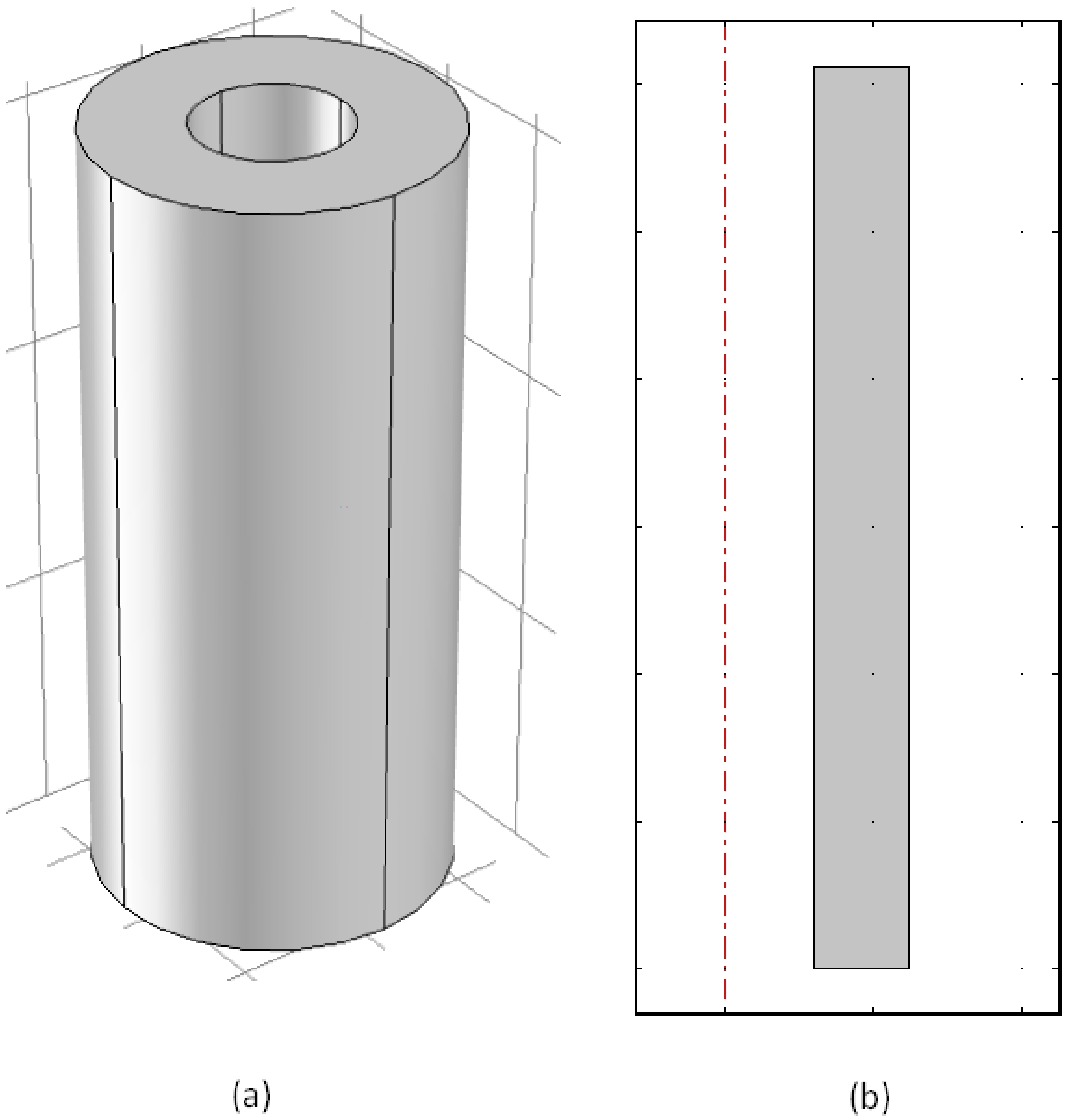

Figure 4.2.1: Simulation domain for the eigenfrequency analysis of an empty coaxial cavity in (a) 3-D and (b) 2-D. Inner diameter: 12 mm, outer diameter: 27.6 mm.

For the 3-D model the free tetrahedral mesh, which is the default mesh type for 3D simulation in COMSOL, was used. The size of each element was set to be smaller than one-fifth of the wavelength to ensure convergence. The total number of elements generated in the mesh was 2622. The simulation was set to find the first few eigenfrequencies around 2.45 GHz. The result of this simulation are shown in figure 4.2.2.

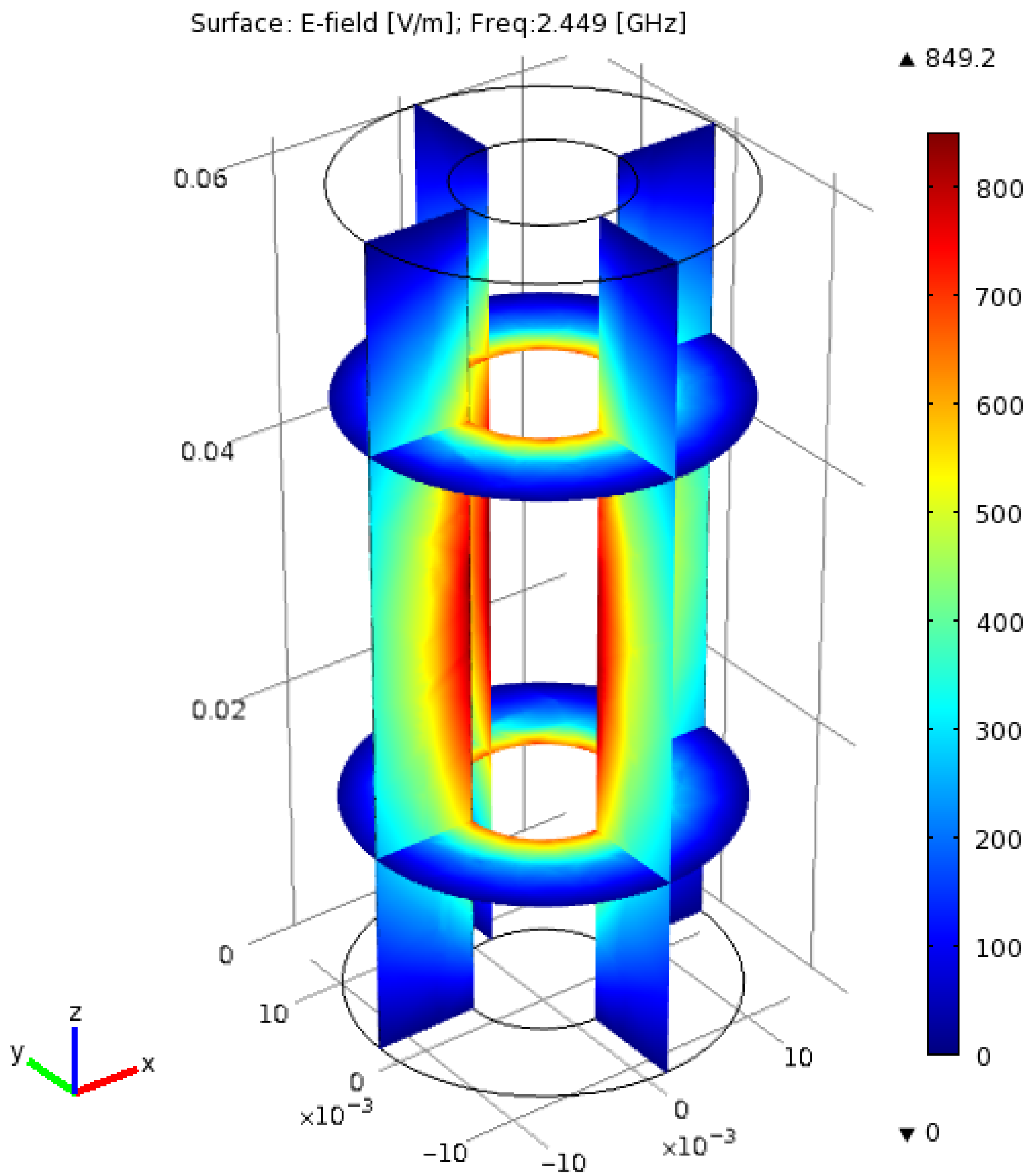

(a)

Figure 4.2.2: The first three eigenfrequencies of half wavelength coaxial cavity. (a) 2.449 GHz, (b) 4.899 GHz, and (c) 5.493 GHz.

Figure 4.2.2 (Cont'd)

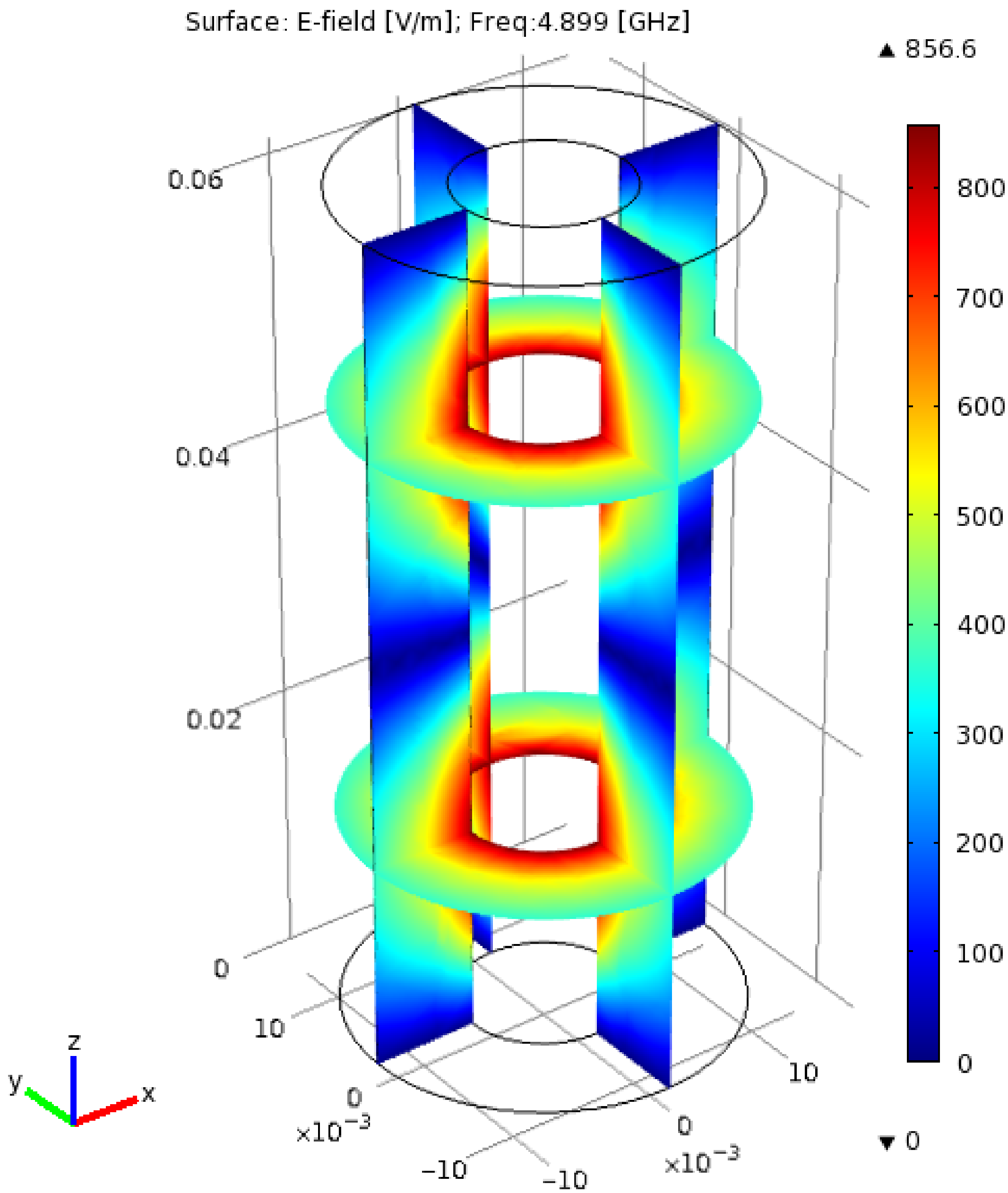

(b)

Figure 4.2.2 (Cont'd)

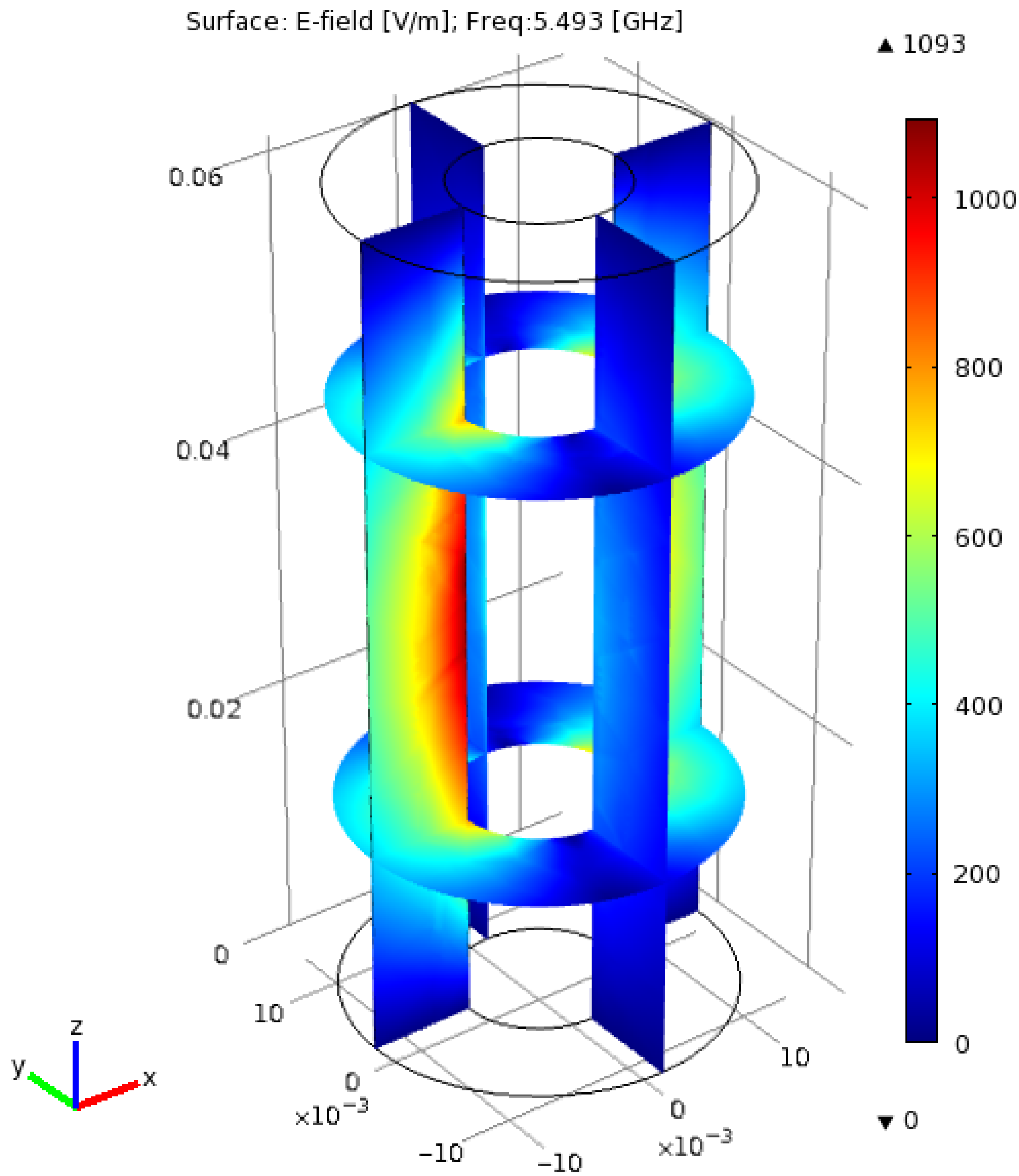

(c)

In figure 4.2.2, the electric field intensity are shown as color gradient in the slice plot. Figure 4.2.2 (a) and (b) show the half standing wave (TEM_{001}) and full standing wave (TEM_{002}) pattern of the 2.45 GHz and 4.90 GHz microwave resonant modes, respectively. The third solution converges to an eigenfrequency at 5.49 GHz as shown in figure 4.2.2(c). This resonant mode is not ϕ symmetry.

To reduce the computational cost, the cavity can be simulated in a simplified two dimensional space (2-D), instead of using the full 3-D. For this simulation, only the r-z cross section of the coaxial cavity was simulated. Moreover, due the symmetrical properties of the cavity, only a half portion of it was taken into account as seen in figure 4.2.1(b). For more accurate results, the mesh was refined so that the element dimension is approximately half the size of that used in 3-D simulation. The default mesh element type for 2-D simulation in COMSOL is the free triangular element and the maximum element size is set to $1/60^{th}$ of the wavelength. This setting is to ensure that there are at least five elements between the nearest boundaries, which in this case is the space between the inner conductor and the outer conductor wall. The total number of elements in the mesh is 242, about one order of magnitude smaller than the 3D model. All other input parameters and boundary conditions were kept the same as the previous 3D simulation and the result of this simulation is shown in figure 4.2.3.

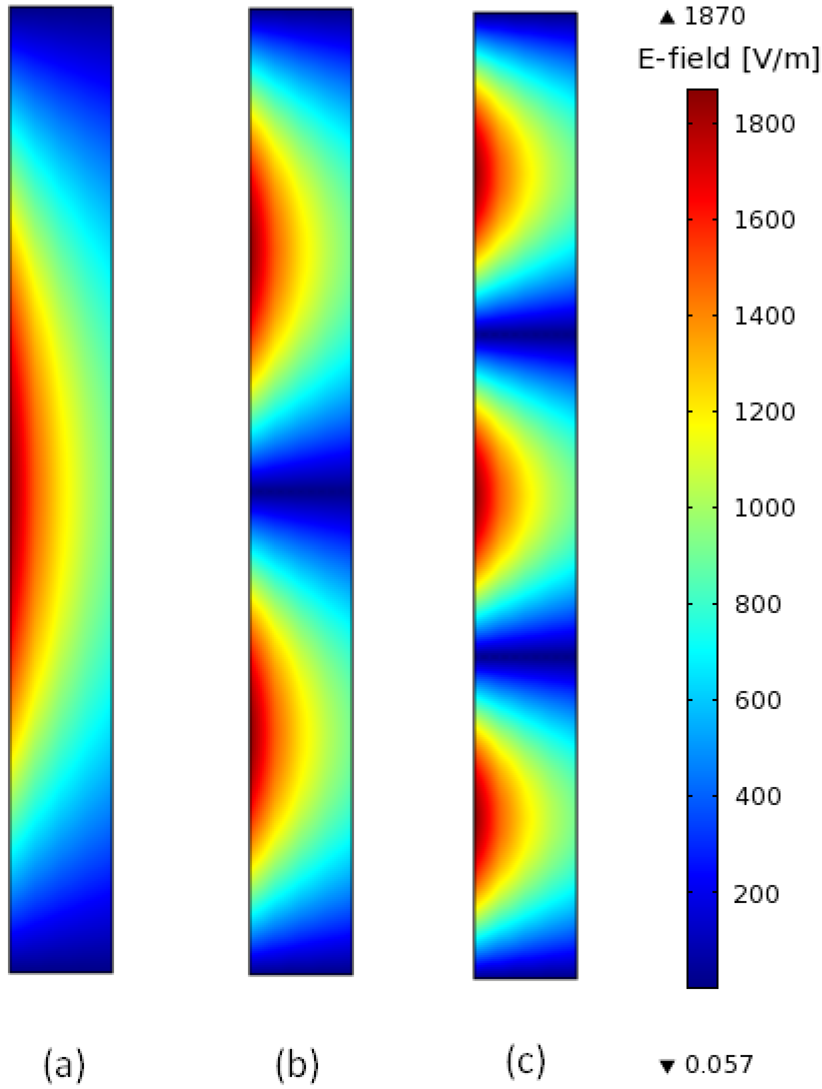

Figure 4.2.3: 2-D symmetry simulation of half-wavelength coaxial cavity. (a) 2.449 GHz (TEM_{001}), (b) 4.899 GHz (TEM_{002}), and (c) 7.349 GHz (TEM_{003}).

The first two eigenfrequencies calculated using the 2D-sym simulation, as shown in figure 4.2.3, were similar to the 3-D simulation results (figure 4.2.2(a) and (b)). The third eigenfrequency was found at 7.349 GHz. These eigenfrequencies are the first three TEM modes in a coaxial waveguide that are ϕ symmetry. From these results, it can be concluded that 2D-sym simulation can give valuable information in terms of cavity design while keeping the computational cost low as compared to the full 3-D simulation. Hence, unless there is a non ϕ

symmetry feature in the applicator structure, all of the electrodynamic and cavity simulations will be performed in 2D-sym.

4.2.2 Frequency domain analysis of an empty coaxial cavity

The eigenfrequency analysis is a useful tool to design a cavity dimension so that the driving frequency can resonate inside the cavity. However, the analysis does not include connection with the external circuit to drive the cavity. Thus, once the cavity dimension has been established, frequency domain analysis, which includes an external force calculation, can be performed.

The foreshoretened coaxial cavity applicator has a loop antenna to couple the microwave energy into the cavity as shown in figure 3.2.1. By adding this coupling structure, the cavity is no longer ϕ symmetrical. The simulation domain of the 3-D empty cavity model was modified as shown in figure 4.2.4. Four dimensionless loop wires, with radius of five mm, were inserted into the cavity one at a time. The orientation of loops 1 – 3 are normal to the ϕ direction while the orientation of loop 4 is parallel. Loops 1 and 3 are located near the bottom and the top of the cavity respectively. Loop 2 is located in the middle of the cavity. At the top of the cavity, an additional port boundary condition was created. It is 0.5 mm wide and is located between the inner conductor and the cavity top wall. Five simulations including the four loop excitation configuration and the one port excitation configuration were performed with a driving frequency of 2.45 GHz. In each simulation only one configuration was considered. As an example when the driving frequency was applied on loop 1, the input port became a PEC boundary condition and the rest of the loops were disabled.

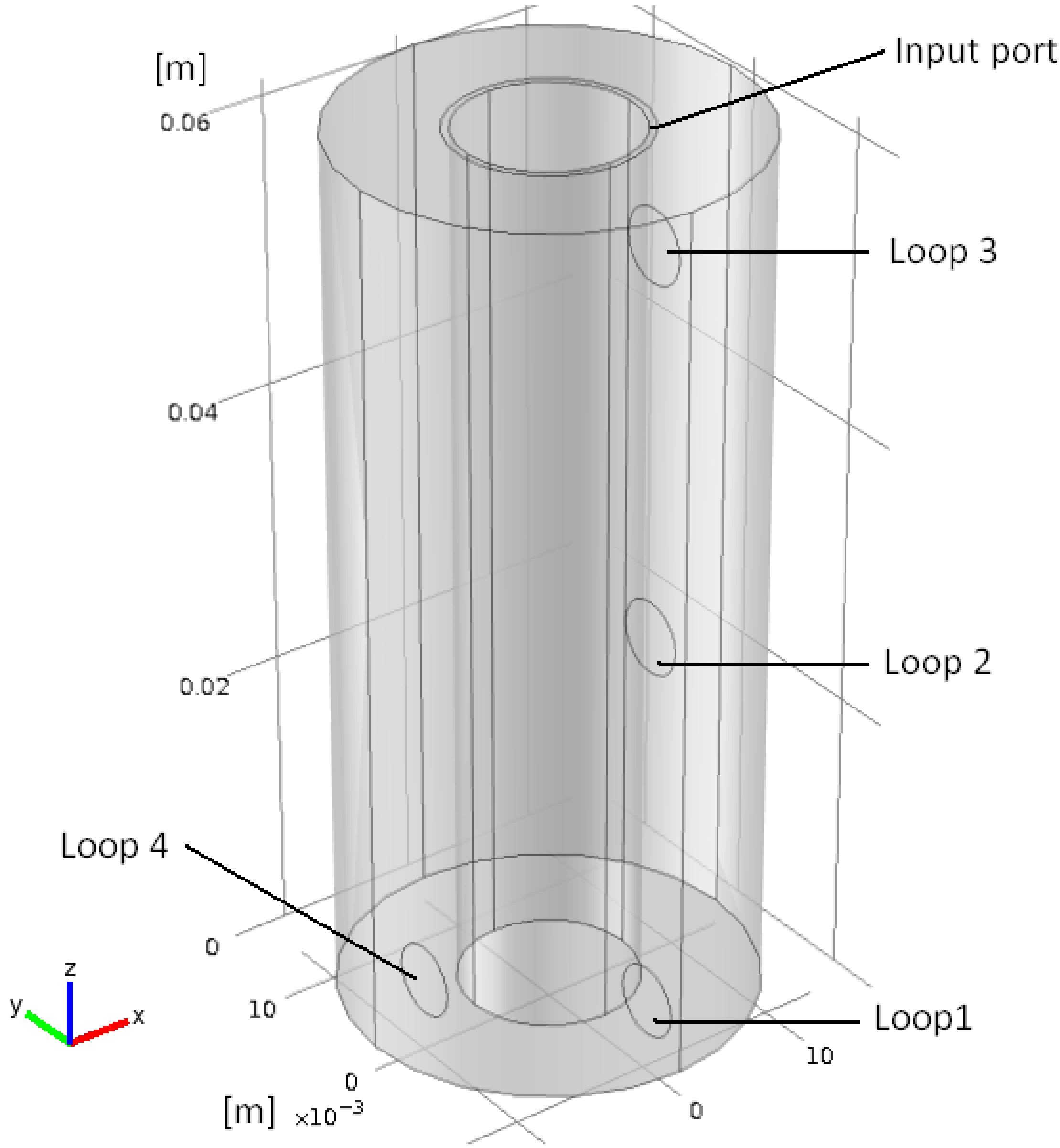

Figure 4.2.4: Simulation domain for 3D frequency driven empty coaxial cavity simulation.

As previously discussed in section 4.2.1, the size of the elements in the mesh need to be small enough to provide correct solutions. For these simulations, the complete mesh consists of 3290 elements. The semi-rigid coaxial cable was not included in the simulation domain to conserve the memory. The input parameter for the loop wire is an electric current with a magnitude of one Ampere and the input parameter of the input port is 1 W coaxial that delivers a TEM wave. Results of these simulations are presented in table 4.2.1 and figure 4.2.5.

Table 4.2.1: Frequency domain analysis result of an empty coaxial cavity driven with external circuit.

Simulation	Driving geometry	Input	Maximum E-field [V/m]
1	Loop 1	1 A	3.30×10^7
2	Loop 2	1 A	1.54×10^5
3	Loop 3	1 A	3.29×10^7
4	Loop 4	1 A	4925
5	Input port	1 W	1.31×10^4

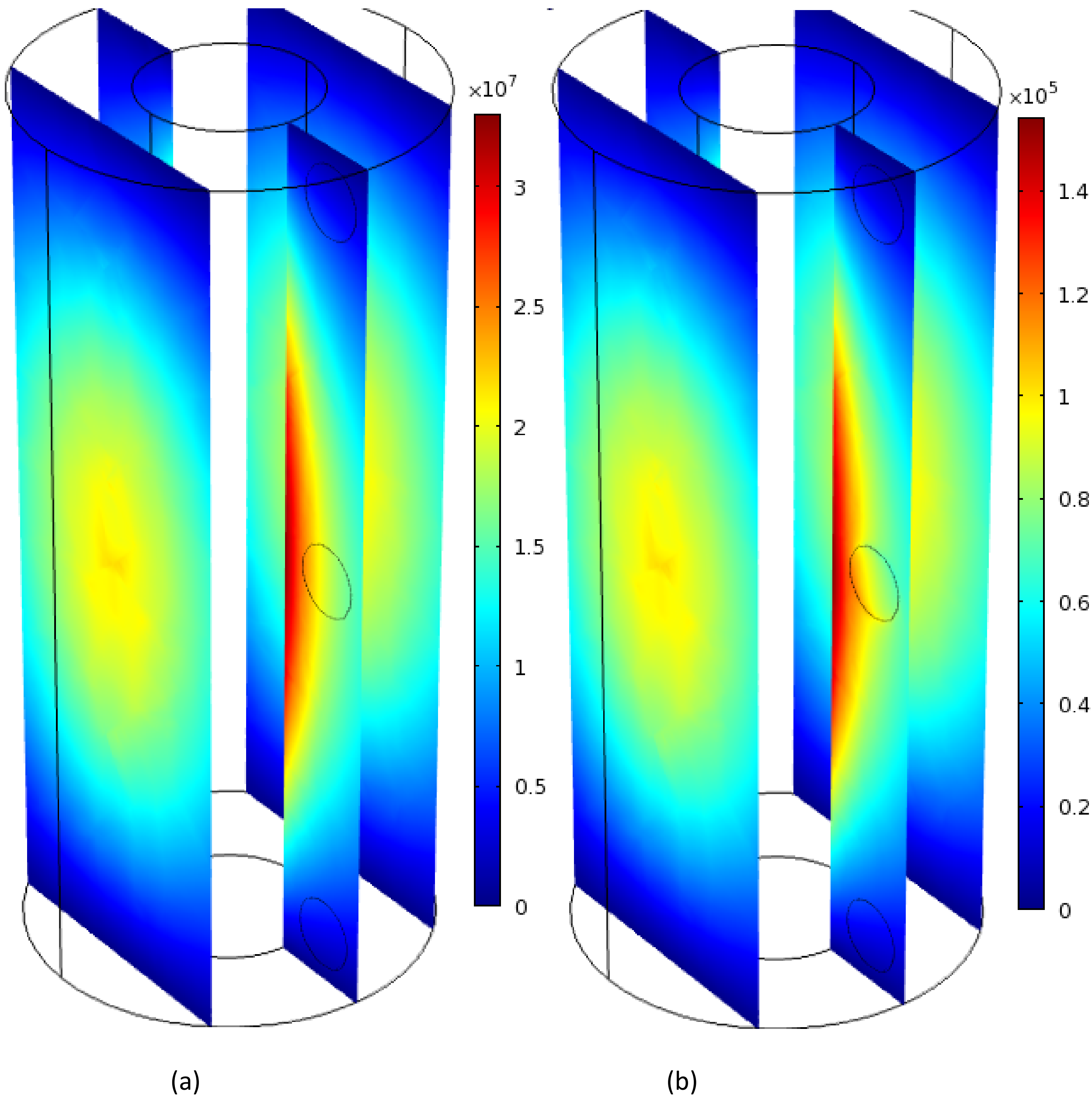

Figure 4.2.5: Electric field intensity inside an empty coaxial cavity driven at 2.45 GHz. (a - d) using loop 1 – 4 respectively, and (e) using an input port.

Figure 4.2.5 (Cont'd)

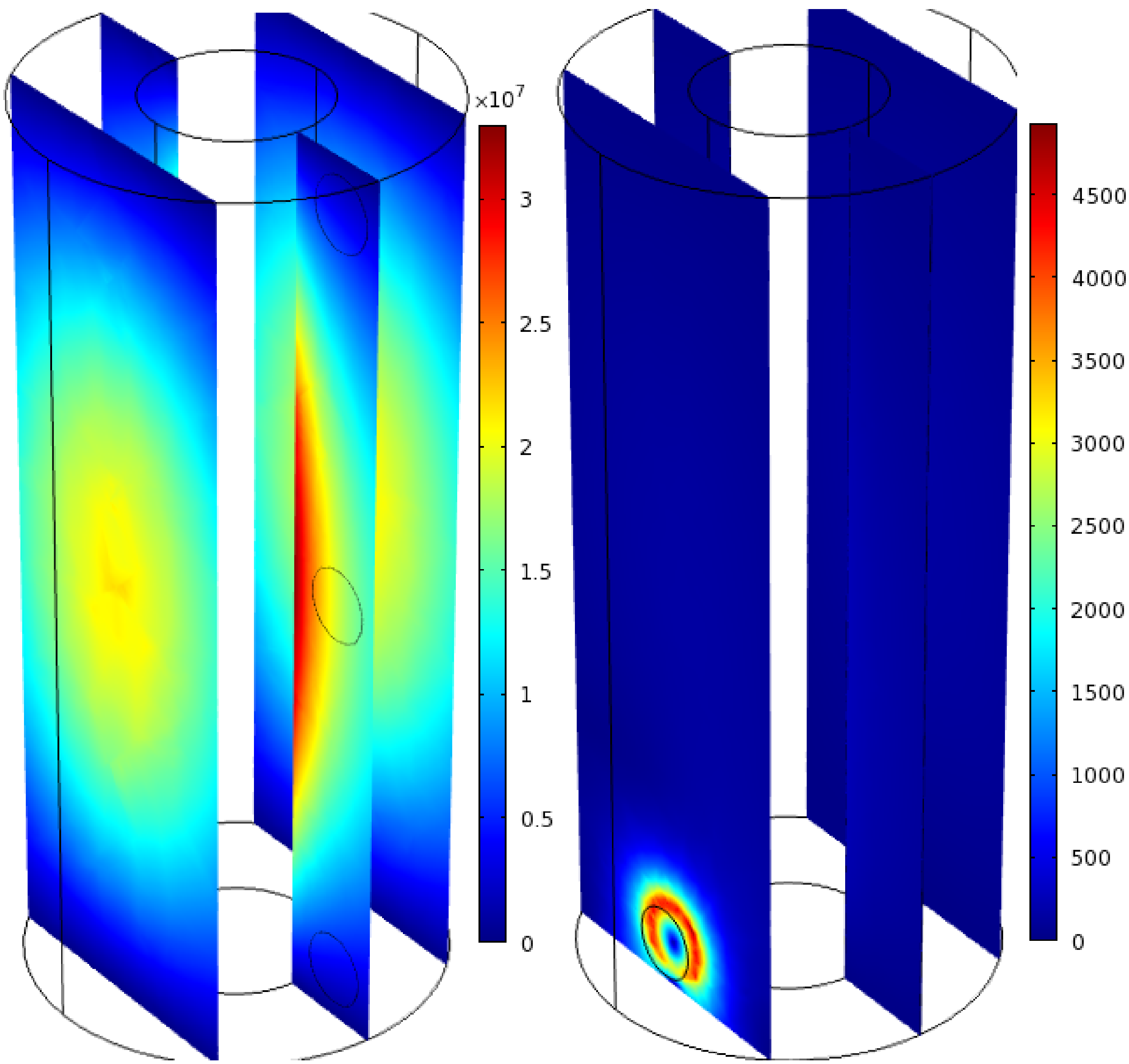

(c) (d)

Figure 4.2.5 (Cont'd)

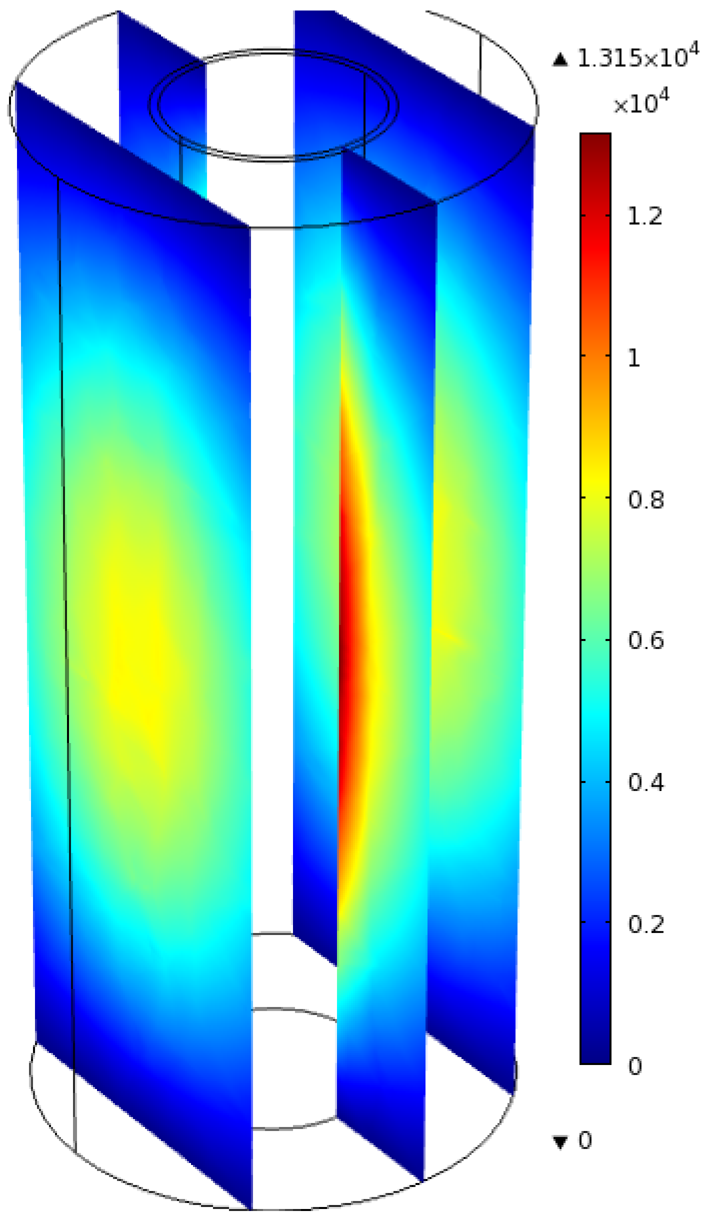

(e)

By applying external power via loop orientated normal to the ϕ direction (Loop 1 – 3), resonance was maintained. The electric field distribution was similar to the eigenfrequency simulation result at 2.45 GHZ and was similar to figure 4.2.5(a). When the loop antenna is orientated parallel to the ϕ direction, such as in Loop 4, most of the external energy is only radiated in the near field because it is not coupled into the magnetic field of the cavity, which goes in the ϕ direction. These results confirmed the previous discussion on coupling loop antenna orientation in section 3.2.

Comparing the electric field intensity between Loop 1 – 3 shows that Loop 2 coupled the external energy into the cavity the least. Loop antenna positions 1 and 2 give a larger magnetic field intensity indicating the best loop positions are near the cavity top and bottom. This result is useful in cavity adjustments for the experimental part of the research.

By creating an input port geometry as shown in figure 4.2.4, the external energy can be introduced into the cavity while still maintaining ϕ directional symmetry. The impact of making this geometry was analyzed in 3-D and the result is seen in figure 4.2.5(e). The TEM_{001} resonant mode was still maintained similarly to loop positions 1, 2 and 3. The electric field intensity starts to have meaning in table 4.2.1 when a load, such as a plasma, is present in the cavity. The use of a port also allows the reflected power from the cavity to be monitored in the simulation by using the port S-parameter, S_{11}.

This simulation of an empty coaxial cavity provides a better understanding on how to use the simulation software. It can also provide supporting evidence on cavity design theory. Substituting the loop antenna coupling probe by an input port, allows the geometry reduction in the computational model from 3-D to 2-Dsym with minimal impact to the resonant mode of the cavity.

4.2.3 Eigenfrequency analysis of an empty foreshortened coaxial cavity

A simplified model of the foreshortened coaxial cavity was simulated to find the appropriate length of the cavity (L_s) and the gap distance (L_g). The simulations were performed using the Eigenfrequency analysis in the RF module of COMSOL Multiphysics. The simulation domain is shown in figure 4.2.6. The red dashed line represents the axial symmetry of the model and the black lines are the cavity wall. The medium inside the cavity and at the gap region was set to air and the cavity walls were set to PEC material. Whereas the actual foreshortened cavity has an empty hollow inner conductor and a circular hole at the gap end of the cavity wall, the eigenfrequency analysis can only be performed for a cavity enclosed with a PEC boundary condition. When other types of boundary conditions is applied, the simulation becomes nonlinear and a special treatment is needed to avoid matrix singularity or any undefined value errors.

Iterations were performed to find L_s and L_g so that the first resonance occurs at 2.45 GHz. The mesh is free triangular that consists of 1490 elements. The cavity length must be longer than 1.5 cm to provide a space for the coupling loop antenna. The gap distance must be less than five mm to prevent a big microwave radiation leak. After a few iterations, it can be observed that by creating a larger gap distance, it will shift the resonant to a higher frequency while increasing the cavity length will shift the resonance to a lower frequency.

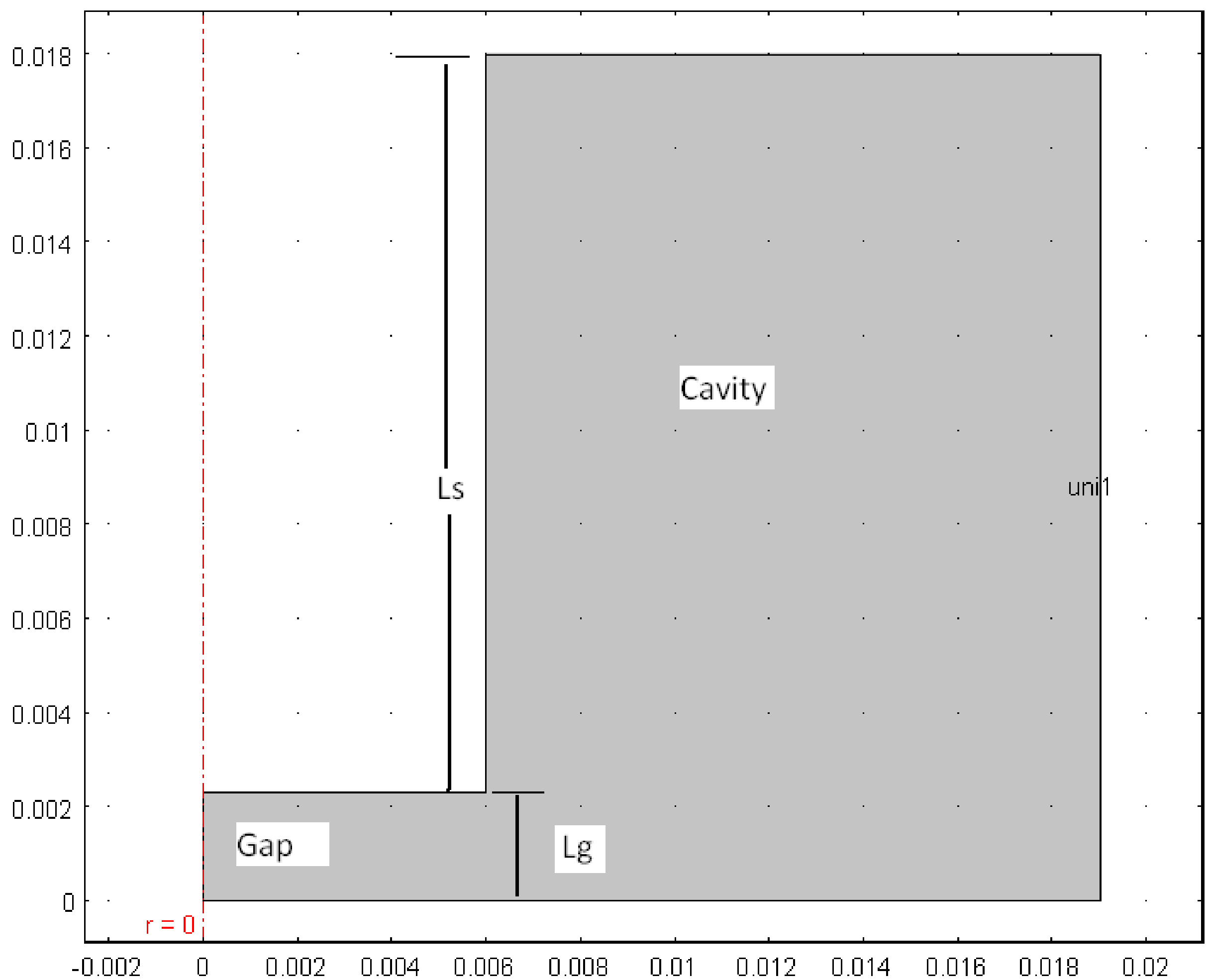

Figure 4.2.6: Simulation domain of the simplified foreshortened cavity.

The result of this simulation is shown in figure 4.2.7. One combination resulting in a 2.449 GHz resonance was with the cavity length at 1.8 cm, which is shorter than quarter-wave length, and the gap length at 2.3 mm. As seen in figure 4.2.7, the highest electric fields, which is shown in color gradient, inside the cavity are located at the corner end of the inner conductor near the gap region. A tapered inner conductor was designed so that the highest electric fields is located closer to the discharge tube.

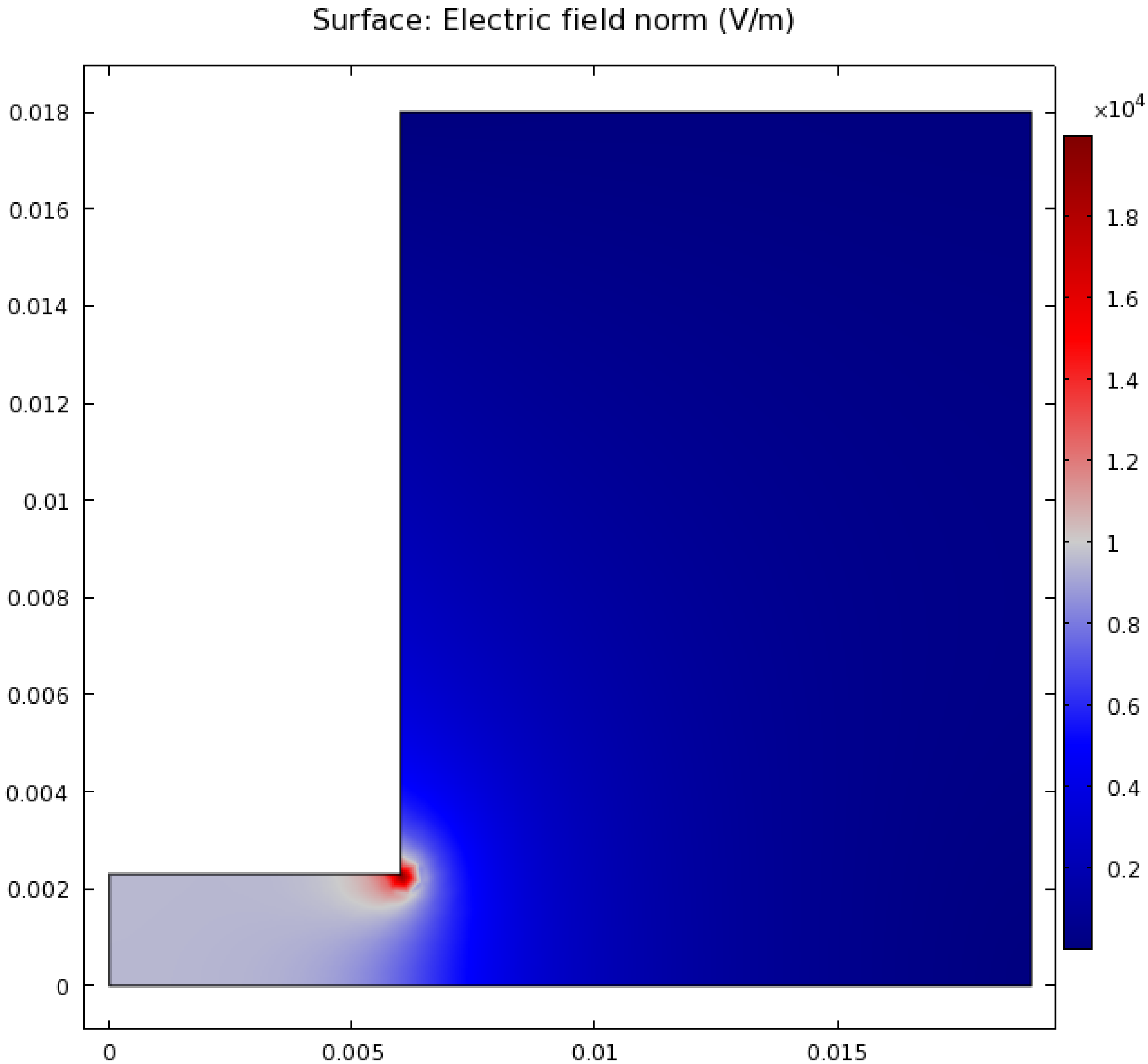

Figure 4.2.7: Simplified empty foreshortened coaxial cavity simulation result showing the electric fields distribution.

An Eigenfrequency simulation result for a foreshortened coaxial cavity with a tapered inner conductor is shown in figure 4.2.8. The highest electric field intensity can be found to be closer to the center of the gap, where the discharge tube and plasma generation is located. This tapered structure shifts the resonant frequency of the cavity slightly. Thus the cavity length and gap distance were adjusted accordingly. The new cavity structure has a length of 20.5 mm and a gap distance of 2.2 mm.

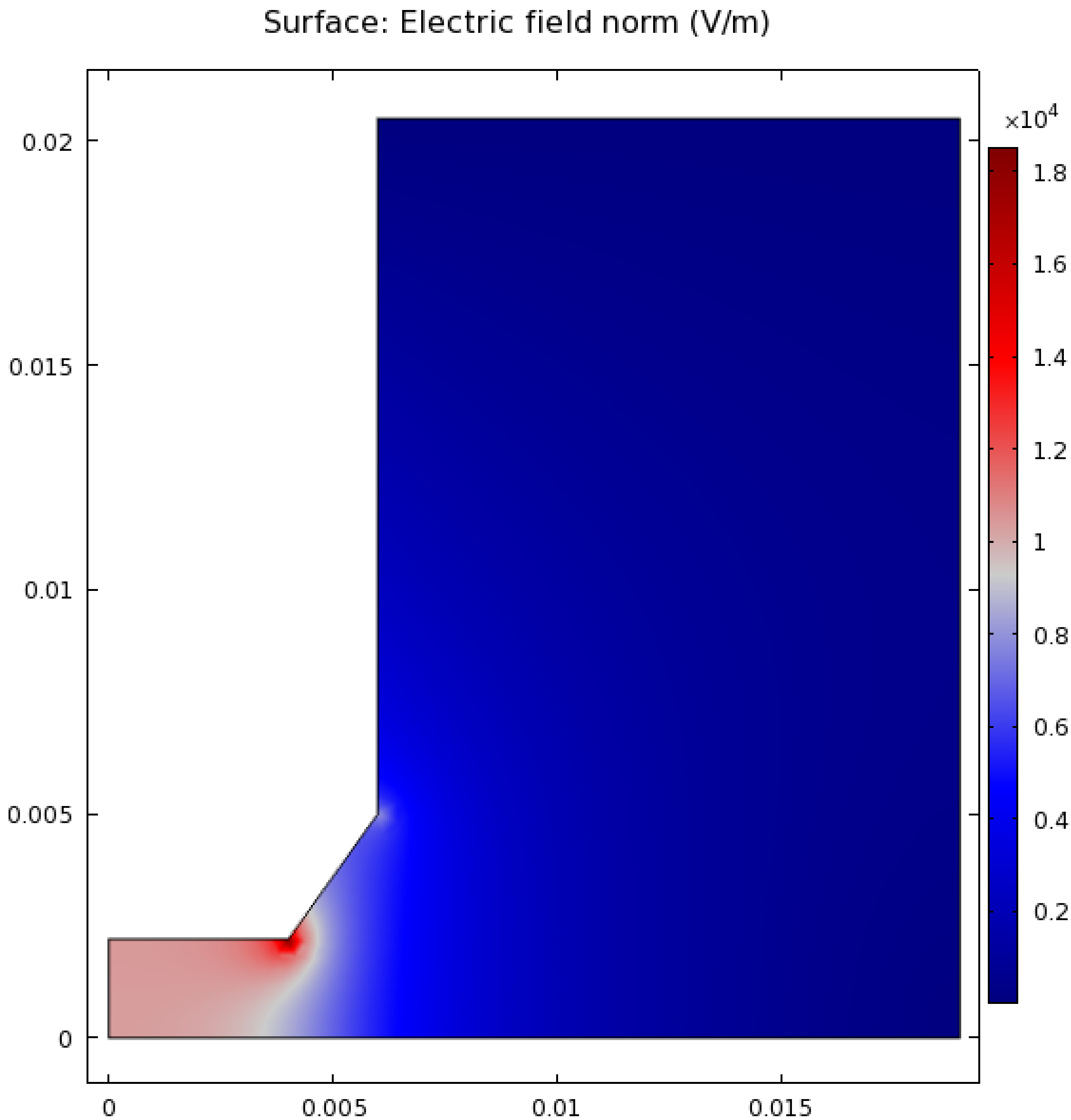

Figure 4.2.8: Electric field distribution for a foreshortened cyclindrical cavity with tapered inner conductor.

Another eigenfrequency simulation was performed for a foreshortened coaxial cavity with a complex geometry that resembles the actual cavity. The simulation was perfomed in 2D-sym and the simulation domain is shown in figure 4.2.9. The domain includes the quartz tube that runs inside the hollow inner conductor. The plasma domain, which is inside the discharge tube was set to have electrical characteristics of air ($\varepsilon_r = 1$, $\mu_r = 1$, $\sigma = 0$). All of the cavity walls were assumed to be a PEC material. Since the cavity is not completely enclosed with metal, cylindrical scattered wave boundary conditions were applied to all non-metal boundaries. A scattering boundary condition means that the boundary is transparent to an incoming wave at normal incident to the boundary. The discharge tube was made of quartz glass with relative permittivity of 4.2.

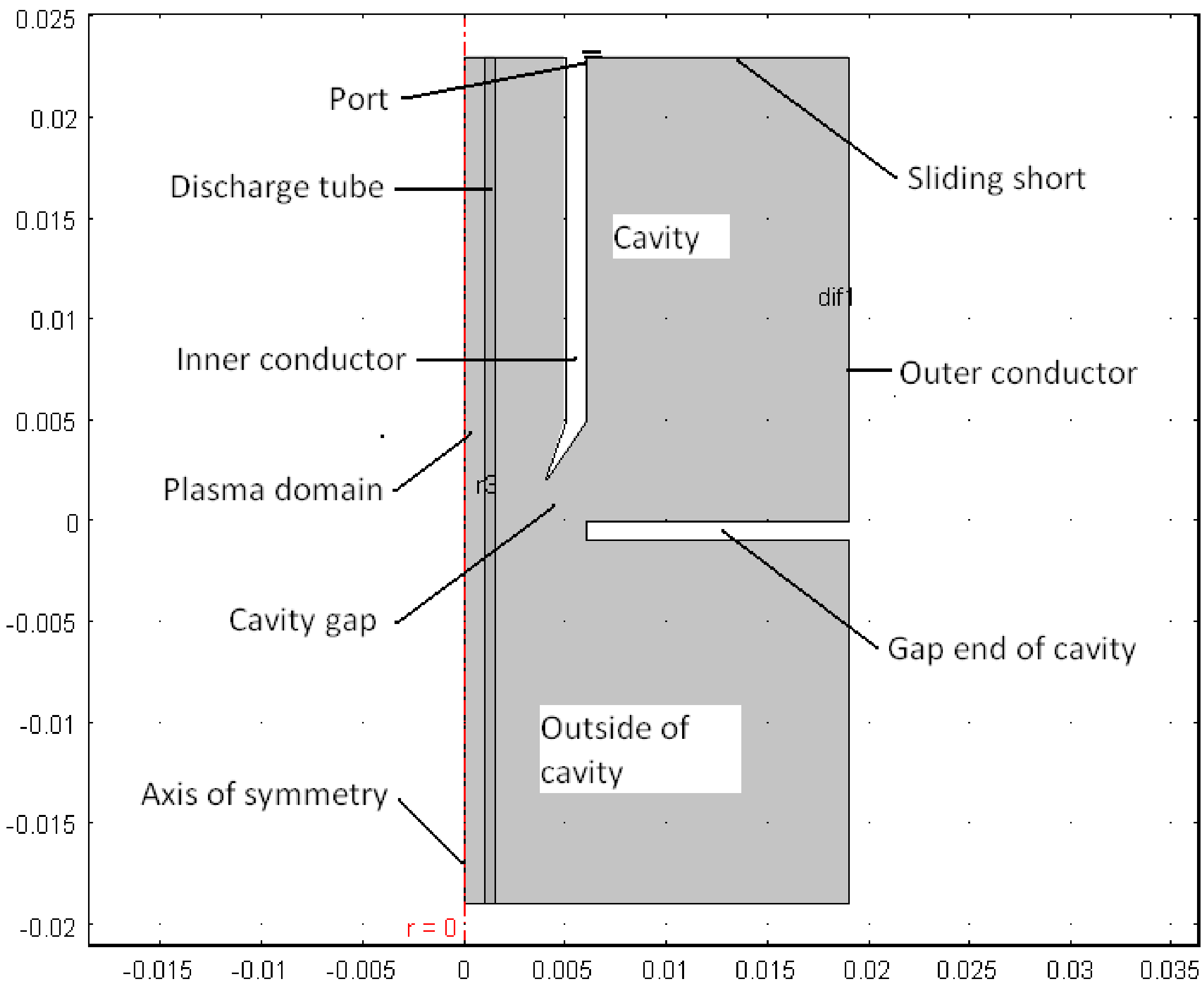

Figure 4.2.9: Simulation domain of the eigenfrequency analysis of the foreshortened coaxial cavity applicator.

The setup of this simulation can be described as follows: The complete mesh consists of

2420 elements and the quarts tube domain has a maximum element size of 4.2e^{-4} m to ensure that there were more than one element separating the walls of the tube. The eigenvalue solver was modified so that the linearization point was starting at 2.45 GHz. Using a similar iteration procedure as the previous simulation, the cavity length and the gap distance for this simulation setup were found to be 23 mm and two mm respectively. In summary, three simulations were performed using eigenfrequency analysis to determine the length of the cavity and the gap distance. Based on the simulation results, the cavity length is between 18 – 23 mm and the gap distance is between 2 – 2.3 mm.

4.2.4 Frequency domain analysis of plasma loaded foreshortened coaxial cavities

Simulations using COMSOL Multiphysics were done to find the impact of a plasma column inside the foreshortened coaxial cavity. The plasma behaves as a load in the cavity and its parameters were approximated from the previous work [53]. The charge densities (n_e) range from 10^{11} cm^{-3} to 10^{13} cm^{-3} and pressure (P) was set to 1 Torr. The feed gas is argon with flow rate set to 20 sccm. Since it is a non-magnetized plasma the effective plasma dielectric constant ($\in_p$) is [78]:

$$\epsilon_p \simeq \epsilon_0 K_p = \epsilon_0 \left(1 - \frac{\omega_{pe}^2}{\omega(\omega - j * \nu_m)}\right); \quad \omega_{pe}^2 = \frac{e^2 n_e}{\epsilon_0 m_e}; \quad \omega^2 = (2\pi f)^2 \qquad (4.2.2)$$

where, ω_{pe} is the electron plasma frequency, ω is the driving frequency, ν_m is the collision frequency, e is the elementary charge, n_e is the electron density, $\in_0$ is the permittivity of free space, and m_e is the electron mass. The collision frequency is approximated using:

$$\nu_m \approx K_{el} N \, ; \quad K_{el} \approx 10^{-13} m^3 / s \tag{4.2.3}$$

where K_{el} is the rate constant for elastic collision in argon plasma obtained from [78] and N is the density of the neutral species calculated from the operating pressure using the ideal gas law:

$$N = \frac{p}{k_B T} \tag{4.2.4}$$

where p is the pressure, k_B is the Boltzmann's constant and T is the argon gas temperature. The gas temperature is approximated from [53] which is around 800 K.

The foreshortened coaxial cavity as shown in figure 4.2.9 was simulated using COMSOL 2-D axial symmetry RF module. The mesh element type selected for the simulation was Lagrange – quadratic with the maximum element size set to 2 mm in the cavity domain and 0.3 mm in the discharge tube and plasma domains. The top of the cavity, which is the adjustable short, was set to be the excitation port for coaxial mode coupling. The frequency of operation was set to 2.45 GHz and the incident microwave power was set to one Watts. The cavity was assumed to be made of a perfect electrical conductor material thus the other cavity walls have PEC as the boundary conditions. The rest of the boundaries in the simulation domain were set as scattering boundaries, which represent no physical boundaries for the RF module. The discharge tube was made of quartz glass with relative permittivity of 4.2.

For the simulation, the top of the cavity acts as a port that delivers the coaxial mode of the microwave. The plasma was assumed to have a uniform charge density throughout the plasma column. Three different lengths of plasma columns were simulated: infinitely long, three mm, and one cm column. For the finite length plasma, the center of the column was at the bottom end of the cavity, where the highest electric field was expected. Parametric simulations were performed by varying the relative permittivity of the plasma, by sweeping the charge density, and by varying the excitation frequency. The cavity length (L_s) and the gap length (L_g) were set to 20 mm and 2.3 mm, respectively, based on the previous simulation result of the eigenfrequency analysis. The simulation results are presented in figure 4.2.10 - 4.2.15. Each of the figures show the S-parameter, S_{11}.

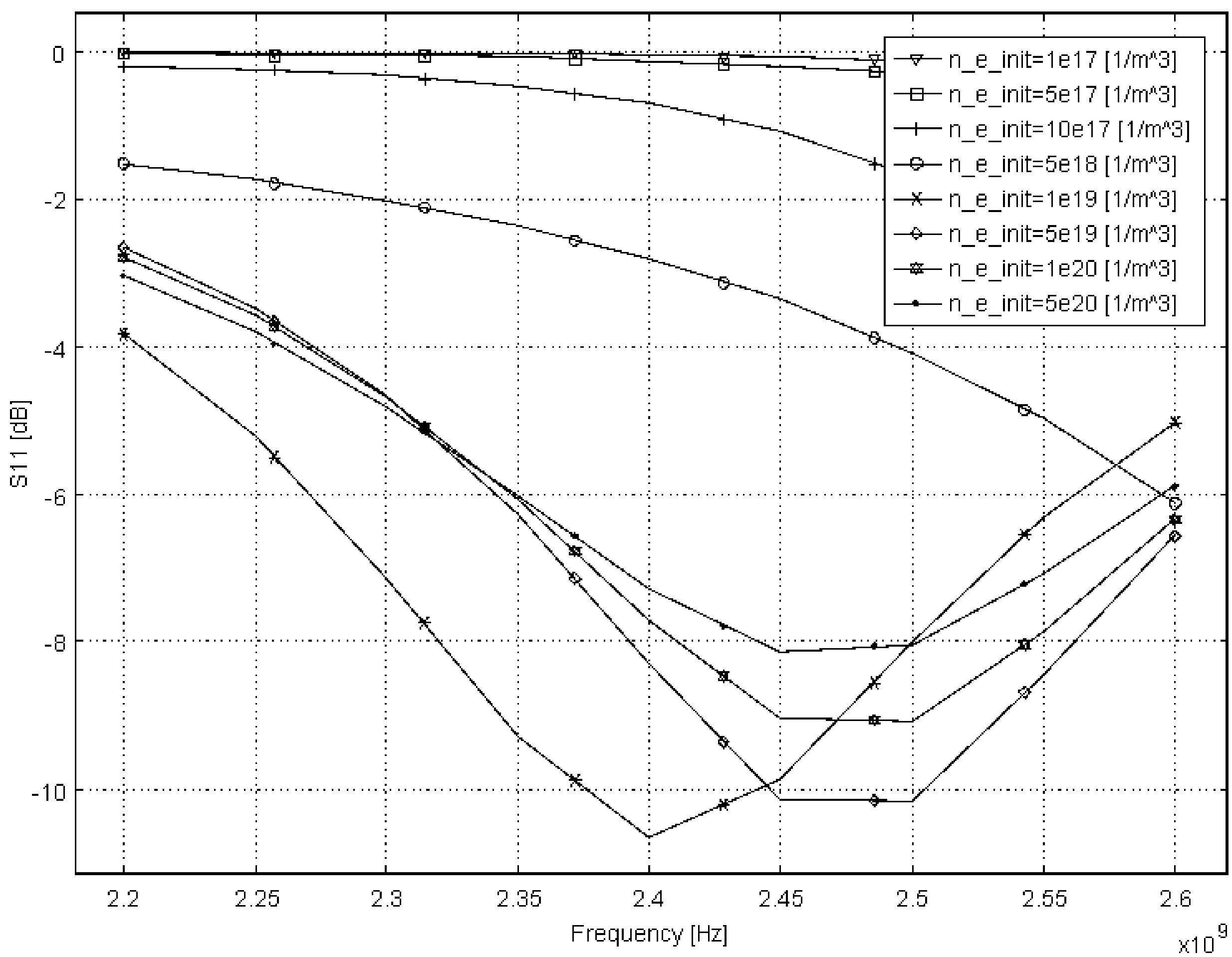

Figure 4.2.10: Frequency sweep of uniform argon plasma at various densities with an infinitely long plasma column.

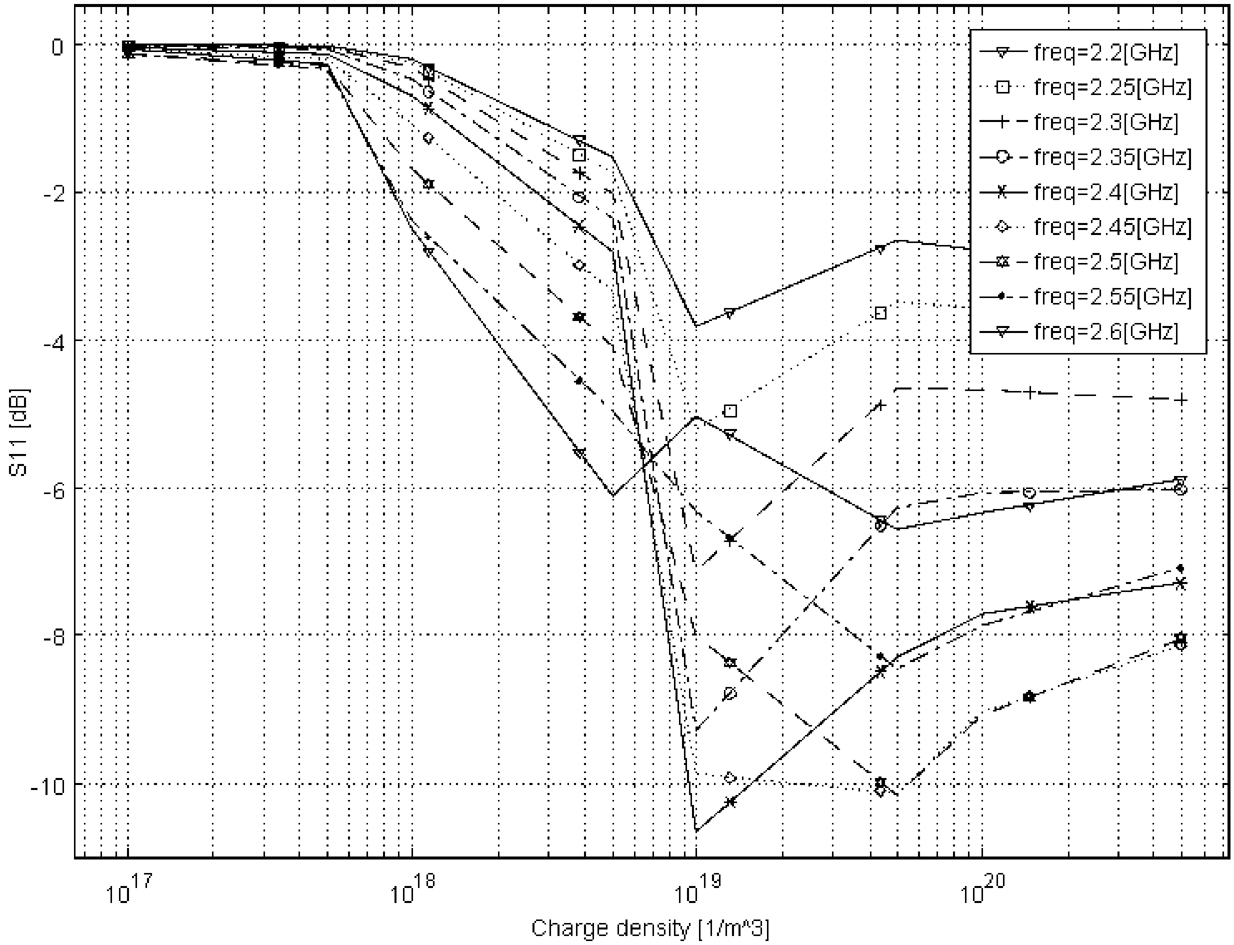

Figure 4.2.11: Charge density parametric sweep of uniform argon plasma at various excitation frequencies with an infinitely long plasma column.

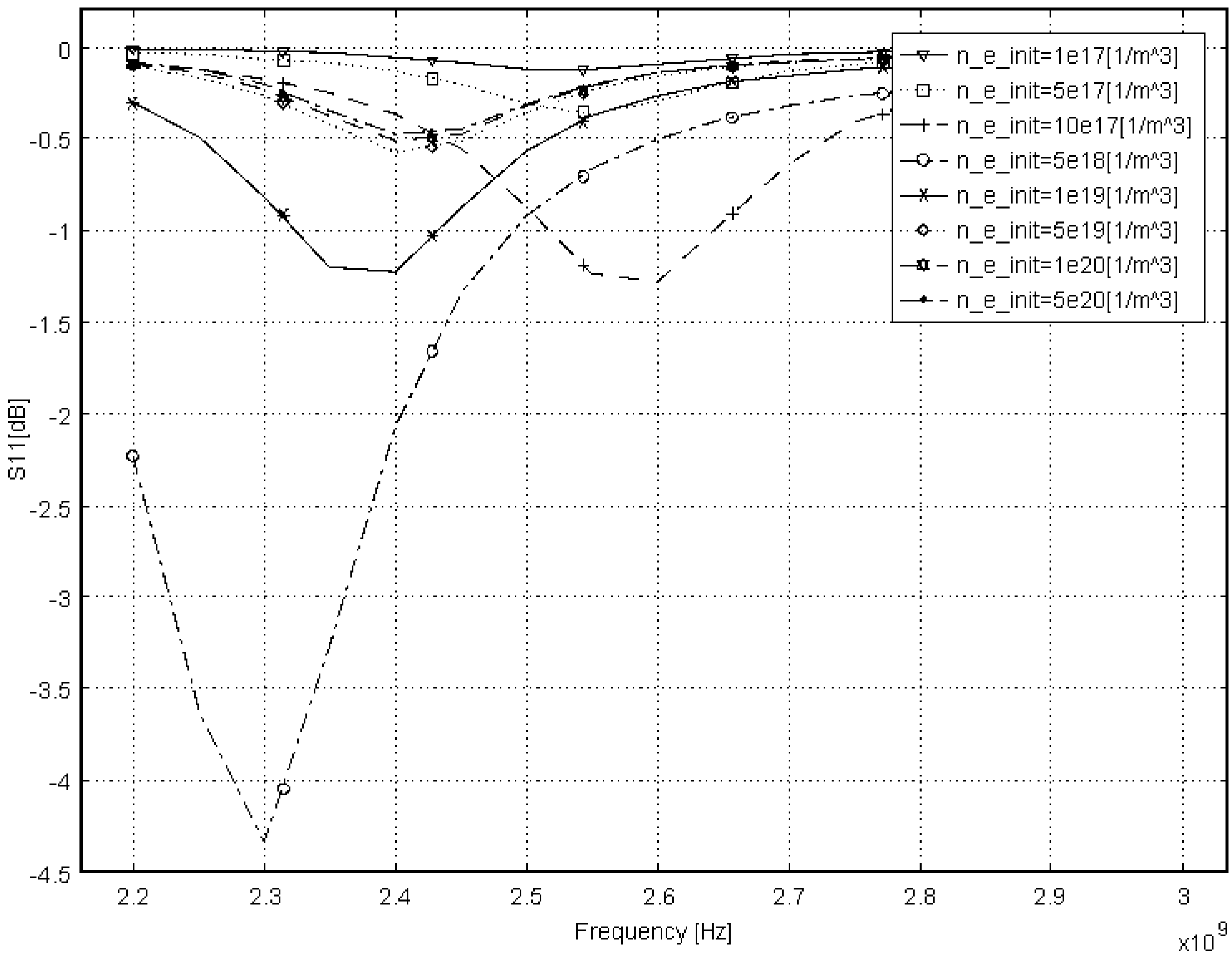

Figure 4.2.12: Frequency sweep of uniform argon plasma at various densities with one cm long plasma column.

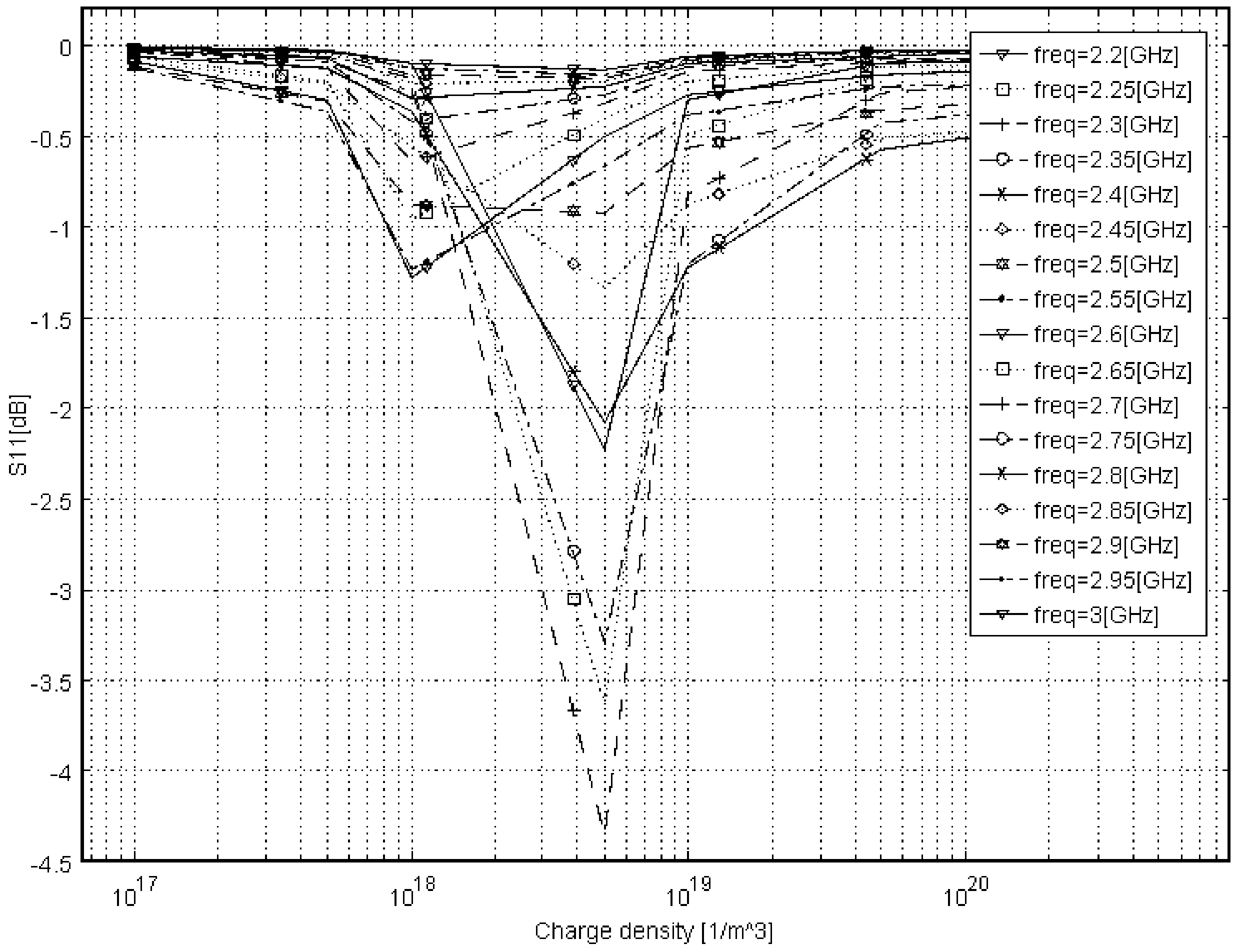

Figure 4.2.13: Charge density parametric sweep of uniform argon plasma at various excitation frequencies with one cm long plasma column.

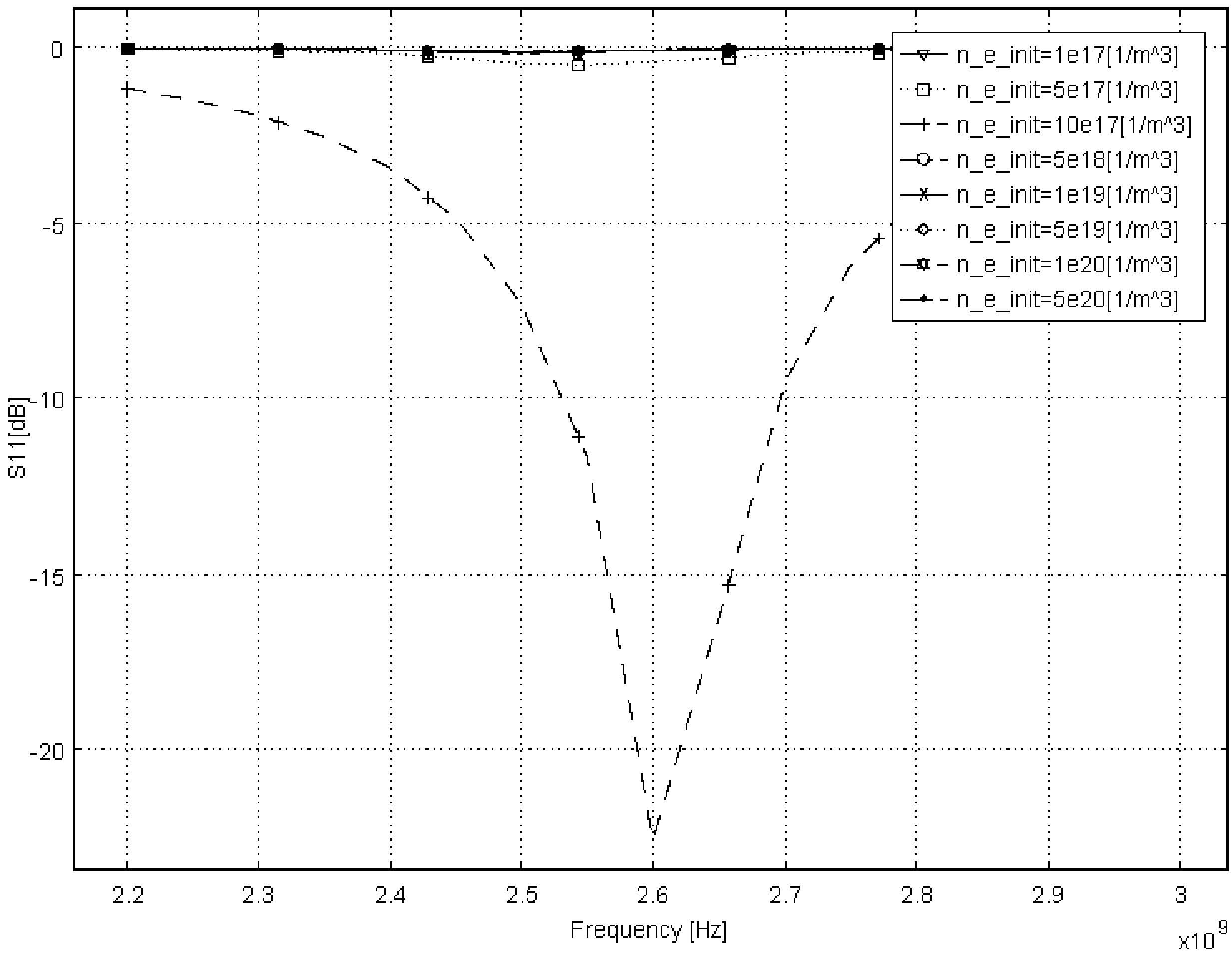

Figure 4.2.14: Frequency sweep of uniform argon plasma at various densities with a three mm long plasma column.

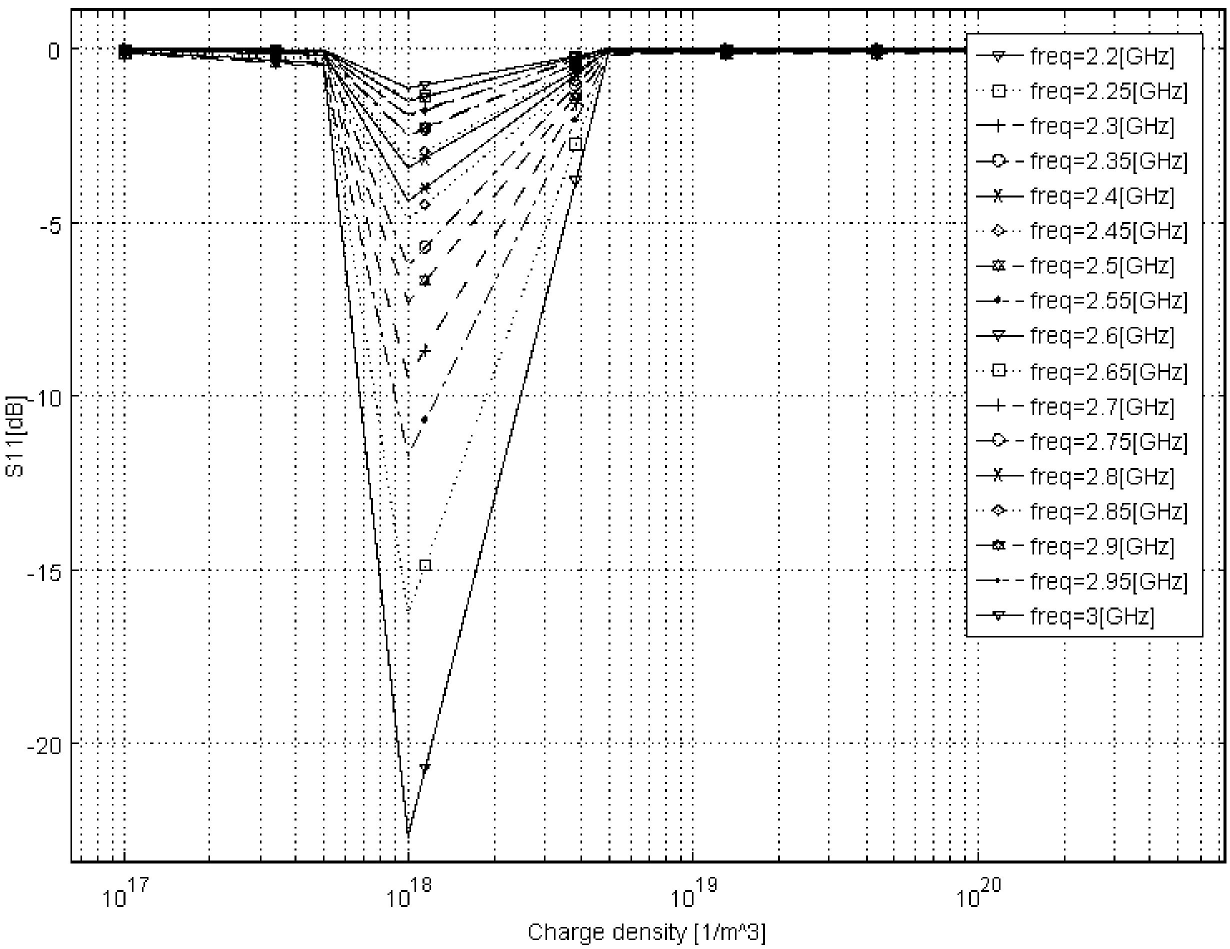

Figure 4.2.15: Charge density parametric sweep of uniform argon plasma at various excitation frequencies with a three mm long plasma column.

The simulation result shows that varying the plasma column length and the charge densities changes the resonant frequency of the foreshortened coaxial cavity. At constant cavity dimensions, in this case L_s = 20 mm and L_g = 2.3 mm, the long plasma column with charge density 10^{13} cm^{-3} and higher provides some tuning at the frequency of interest, which is 2.45 GHz. However, the resonance quality or Q-value is low as shown in figure 4.2.10 and 4.2.11. The three mm plasma load with a charge density of 10^{12} cm^{-3} provides the best matched condition for the cavity driven at 2.6 GHz, as shown in figure 4.2.14 and 4.2.15. The cavity tuning performance was poor for the one cm plasma load with L_s = 20 mm and L_g = 2.3 mm. As seen in figure 4.2.12, no resonance was found for frequencies higher than 2.4 GHz. Some microwave energy was absorbed by the plasma when the charge density was around 10^{12} – 10^{13} cm^{-3}, as shown in figure 4.2.13. In summary, the foreshortened coaxial cavity tuning parameters, when using plasma as a load, are the cavity length, the gap length, the size of the plasma, and the charge density.

A simulation was performed to tune the cavity loaded with an infinitely long plasma column with charge density on the order of 10^{12} m^{-3}. The excitation frequency was set to 2.45 GHz, cavity length and gap length were iteratively solved to find the lowest S_{11} parameter. The simulation results are presented in figure 4.2.16 – 4.2.17. The L_s and L_g value used in the figure 4.2.16 simulation result achieved a S_{11} value of -30 to -40 dB indicating a very good tuning of the cavity is possible.

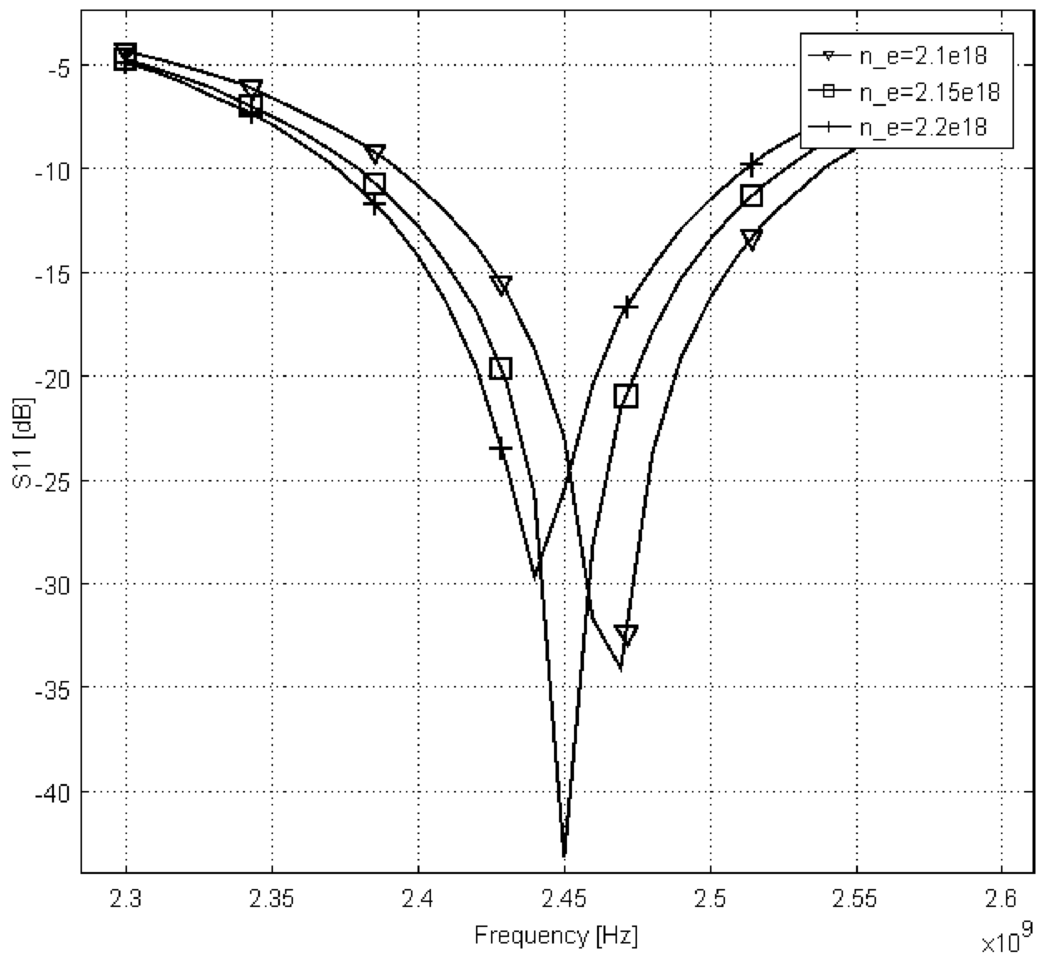

Figure 4.2.16: S_{11} plot of a foreshortened coaxial cavity loaded with an infinitely long plasma column. L_s: 24.65 mm, L_g: 2.3 mm.

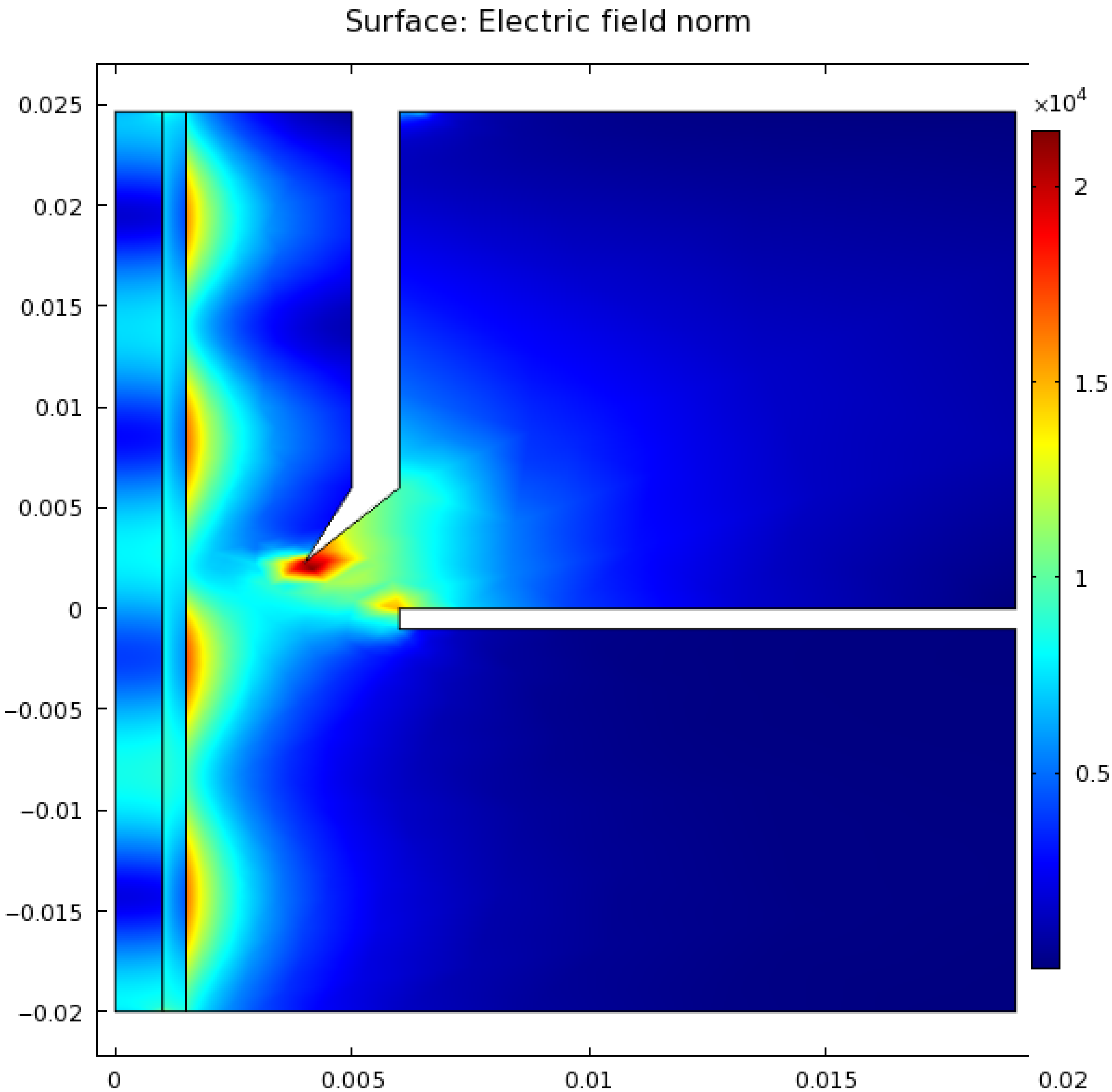

Figure 4.2.17: Electric field intensity profile of a foreshortened coaxial cavity loaded with an infinitely long plasma column. L_S: 24.65 mm, L_g: 2.3 mm, charge density: 2.15×10^{12} cm^{-3}.

For an infinitely long plasma column placed inside the hollow inner conductor of the foreshortened coaxial cavity, charge density of 2.15×10^{12} cm^{-3} provides an optimal resonant condition if the cavity length and the gap length were set to 24.65 mm and 2.3 mm as shown in figure 4.2.16. Using this setup, the electric field pattern from the simulation can be seen in figure 4.2.17. It can be observed that there were standing waves outside the quartz discharge tube and in the plasma. It is possible that the standing wave creation was the result of the scattering boundary condition, which was set in the simulation, were reflecting some of the outbound waves.

4.3 Plasma simulations

A plasma simulation model needs to be built with certain assumptions that capture the important phenomenon without being to computationally intense. An appropriate approach can be made by understanding how the model represents the operating condition of the system.

The Knudsen number (K_n) was calculated to determine the type of formulation with regard to fluid dynamics. It is a ratio between the mean free path of the gaseous particle and the physical length of the container.

$$K_n = \frac{\lambda}{L} \tag{4.3.1}$$

where λ is the mean free path and L is the physical length. For a Knudsen number that is near or greater than one, the statistical methods must be used. If the Knudsen number is less than 0.1, the continuum assumption of fluid mechanics is a good approximation.

The mean free path of argon ion-atom collisions can be estimated using the following [78]:

$$\lambda = \frac{1}{n_g \sigma} \approx \frac{1}{330\, p}\ cm, (p \text{ in } Torr) \tag{4.3.2}$$

where n_g is the gas density, σ is the collision cross section, and p is pressure. For the operating pressure condition (0.5 – 5 Torr) in the experiment, the mean free path of argon gas ranges from 6 μm to 0.6 μm. The smallest physical length of the system would be the ion grid extractor which ranges from 10’s to 100’s μm. Therefore, the Knudsen number was found to be near or smaller than 0.1. Thus, continuum mechanics formulation was used in developing the model.

Froude number (*Fr*) is used to determine whether the gravitational force is dominant in the system.

$$F_r = \frac{v}{\sqrt{gh}} \begin{pmatrix} F_r \leqslant 1 \;\; gravity\,effect \\ F_r \geqslant 1 \;\; gravity\,negligible \end{pmatrix} \tag{4.3.3}$$

where *v* is the velocity, *g* is the acceleration due to gravity, and *h* is the height of the fluid column. The discharge tube length can be used to approximate *h* = 15 cm, and the velocity can be calculated from the flow rate using:

$$Q = v\,A \tag{4.3.4}$$

where Q is the flow rate and A is the cross section of the tube. The Froude numbers are higher than one for the flow rate above 2 sccm at 5 Torr of operating pressure. Hence, the gravitational effect can be neglected.

The electron energy distribution function (EEDF) defines the kinetic processes in a discharge. For microwave generated plasma discharge below 50 Torr of operating pressure, a Maxwellian distribution can be used [128]. In summary, based on the operating condition of the micromachining system, the computational model for the plasma uses continuum mechanics approach with no gravitational effect and the electron gas has a Maxwellian EEDF.

4.3.1 Model building

For the plasma simulations of this proposed work, microwave discharges in argon are investigated. Some system parameters are set according to the experimental works. The pressure range of the discharge is between 0.5 – 10 Torr. Within these pressure range, argon reaction processes such as ionization, excitation, and collisions are considered. However, multi-body collisions and volume recombination were not included in the model. The reaction processes for argon plasma within this pressure range is listed in table 4.3.1.

Table 4.3.1: Reaction processes in argon plasma

Process	Reaction	Reaction rate	Activation Energy (ε_i)
Ground state excitation	$Ar + e \rightarrow Ar^* + e$	R_{exc}	11.56 eV
Ground state ionization	$Ar + e \rightarrow Ar^+ + 2\mathrm{e}$	R_{iz}	15.6 eV
Step-wise ionization	$Ar^* + e \rightarrow Ar^+ + 2\mathrm{e}$	R_{step}	4.14 eV
Superelastic collision	$Ar^* + e \rightarrow Ar + e$	R_{super}	-11.56 eV
Quenching to resonant	$Ar^* + e \rightarrow Ar^r + e$	$R_{quenching}$	
Metastable pooling	$Ar^* + Ar^* \rightarrow Ar^+ + Ar + e$	$R_{pooling}$	
Two-body quenching	$Ar^* + Ar \rightarrow 2\mathrm{Ar}$	$R_{quenching2}$	
Elastic scattering	$Ar + e \rightarrow Ar + e$	$R_{elastic}$	

As shown in table 4.3.1, there are four different predominant species in the reaction processes in argon plasmas within the operating pressure. They are the neutral Ar atoms (density N), electrons (n_e), Ar^+ ions (n_i), and metastable excited Ar^* atoms (n^*). Since the operating pressure is around 1 Torr, non-equilibrium conditions occur and charge neutrality between electrons and ions can be assumed. At the same time the degree of ionization is low which results in an approximately constant density of neutral Ar (N). The Ar atoms density can be approximated using the ideal gas law [104].

$$n_e(\vec{r},t) \approx n_i(\vec{r},t) \ll N \approx constant \tag{4.3.5}$$

Additionally a homogeneous temperature of heavy particles (Ar^+, Ar^* and Ar) can be assumed so that

$$T_e(\vec{r},t) \gg T_i \approx T^* \approx T_g = 0.05\,eV \tag{4.3.6}$$

Particle density of other species can be determined by the continuity equation for that particular species in the plasma. Starting with the general form of continuity equation [78]:

$$\frac{\partial n}{\partial t} + \nabla \cdot \Gamma = G - L \tag{4.3.7}$$

where *n* is the particle density, Γ is the particle flux and *G* – *L* denotes the reactions which create and destroy the particles respectively. The particle flux (Γ) depends on the mean particle velocity (***u***),

$$\vec{\Gamma} = n\boldsymbol{u} \tag{4.3.8}$$

where mean velocity (***u***) can be determined from the momentum conservation:

$$mn\left[\frac{\partial \boldsymbol{u}}{\partial t} + (\boldsymbol{u} \cdot \nabla)\boldsymbol{u}\right] = qn(\boldsymbol{E} + \boldsymbol{u} \times \boldsymbol{B}) - \nabla \cdot \boldsymbol{\Pi} + \boldsymbol{f}|c \tag{4.3.9}$$

where *m* is the particle mass, *q* is the electric charge, ***E*** is the electric field, ***B*** is the magnetic field, $\boldsymbol{\Pi}$ is the pressure tensor and ***f****/c* is collision term which can be approximated by a Krook collision operator:

$$\boldsymbol{f}|c = -\sum_{\beta} m\,n\,\nu_{m\beta}(\boldsymbol{u}-\boldsymbol{u}_{\boldsymbol{\beta}}) - m\boldsymbol{u}(G-L) \tag{4.3.10}$$

where the summation is over all other species, with $\boldsymbol{u}_{\beta}$ the mean velocity of species β and $v_{m\beta}$ is the momentum transfer frequency for collisions with species β. The last term of (4.3.10) is generally small, and taking $\boldsymbol{u}_{\beta}$ = 0 for collisions with one neutral species, the Krook collision operator can be simplified into:

$$\boldsymbol{f}|c = -m\,n\,\nu_{m}\boldsymbol{u} \tag{4.3.11}$$

In the discharge analysis, the inertial term $(\boldsymbol{u}\cdot\nabla)\boldsymbol{u}$ in the momentum conservation can often be neglected [78]. Further, for weakly ionized plasmas, pressure is assumed to be isotropic, therefore pressure gradient can be used to replace the pressure tensor. Argon plasma that is generated using the foreshortened coaxial cavity applicator is non-magnetized thus only electric field influence is considered in the Lorentz force term. Generally the time variation of $\boldsymbol{u}$ is much slower than the time scale of microwave radiation. Thus, (4.3.9) can be written as:

$$0 = q\,n\boldsymbol{E} - \nabla p - m\,n\,\nu_{m}\boldsymbol{u} \tag{4.3.12}$$

The pressure gradient can be determined using a thermodynamic equation for state which relates p to n. For a Maxwellian distribution,

$$\nabla p = k_{B} T \nabla n \tag{4.3.13}$$

Using (4.3.12) and (4.3.13) particle flux can be determined as follow:

$$\Gamma = n\boldsymbol{u} = \pm \mu n \boldsymbol{E} - D\nabla n; \quad \mu = \frac{|q|}{m\nu_m}; \quad D = \frac{k_B T}{m\nu_m} \tag{4.3.14}$$

where μ and D are the macroscopic mobility and diffusion constants. The positive sign is for positive charge and the negative sign is for negative charge.

The flux of electrons and ions out of any region must be equal such that charge does not build up. Therefore the ambipolar electric field approximation is used.

$$\boldsymbol{E}_{amb} = \frac{D_i - D_e}{\mu_i + \mu_e} \frac{\nabla n}{n} \tag{4.3.15}$$

substituting this value into (4.3.14):

$$\Gamma = -\frac{\mu_i D_e + \mu_e D_i}{\mu_i + \mu_e} \nabla n \tag{4.3.16}$$

This equation can be simplified by noting that electron mobility (μ_e) is much higher than the ion mobility (μ_i) in a weakly ionized discharge. Furthermore, $T_e >> T_i$ for the argon plasma simulated which can simplify (4.3.16) into the following:

$$\Gamma \approx \frac{-k_B T_e}{m_{Ar} \nu_{iN}} \nabla n \tag{4.3.17}$$

where ν_{iN} is the ion – neutral collision rate which can be described as follow:

$$\nu_{iN} = \sigma_{iN} \bar{v}_i N: \quad \sigma_{iN} = 5\times 10^{15} cm^2; \quad \bar{v}_i = \frac{\sqrt{8 k_B T}}{\pi m_{Ar}} \tag{4.3.18}$$

σ_{iN} is the ion – argon neutral charge exchange cross section and v_i is the ion thermal speed.

The right hand side of the continuity equation (4.3.7) depends on the reaction rates which is the product of the densities of the reactants and a temperature dependent constant.

$$R_i = \left(\prod_{j=1}^{N_{reactants}} n_j\right) \cdot K_i(T_e); \quad i = 1,2,3,... \tag{4.3.19}$$

The reaction constant are usually of an Arrhenius form:

$$K_j(T_e) = \alpha_{1j} e^{-\alpha_{2j}/T_e} \quad (cm^3 s^{-1}) \tag{4.3.20}$$

where α_{1j} is the preexponential factor and α_{2j} is the activation energy with the exception of the reaction constant for elastic scattering $K_{el}(T_e)$ that has to be approximated using a polynomial fit. However, the elastic scattering rate constant can approximated using a constant [78]:

$$K_{el}(T_e) \approx 10^{-13} m^3/s \tag{4.3.21}$$

A similar continuity equation as (4.3.7) can be written for the metastable species:

$$\frac{\partial n^*}{\partial t} + \nabla \cdot \Gamma^* = R_{exc} - R_{step} - R_{super} - R_{quenching} - 2\mathrm{R}_{pooling} - R_{quenching2}; \Gamma^* = -D^* \nabla n^* \tag{4.3.22}$$

The value for the diffusion constant for the metastable species was approximated using the diffusion constant of neutrals:

$$D^* = \frac{k_B T_g}{m_{Ar} \nu_m} \tag{4.3.23}$$

In addition to the continuity equations, the heat equation for the electrons has to also be implemented in the model to attain a self-consistent solution. The general energy conservation derived from Boltzmann's equation [78] is:

$$\frac{\partial}{\partial t}(\frac{3}{2}p)+\nabla\cdot(\frac{3}{2})(p\boldsymbol{u})+p\nabla\cdot\boldsymbol{u}+\nabla\cdot q=\frac{\partial}{\partial t}(\frac{3}{2}p)|_c \qquad (4.3.24)$$

where *3/2 p* is the energy density, *3/2 p**u*** is the macroscopic energy flux, the third term represents the heating or cooling of the fluid due to compression or expansion of its volume, *q* is the heat flow vector. For most discharges the macroscopic energy flux is balanced against the collisional processes, giving the simpler equation

$$\frac{\partial}{\partial t}(\frac{3}{2}p)+\nabla\cdot(\frac{3}{2}p\boldsymbol{u})=\frac{\partial}{\partial t}(\frac{3}{2}p)|_c \qquad (4.3.25)$$

Using the perfect gas law assumption the ratio of specific heats is *5/3*. Equation (4.3.25) can be re-written in terms of density instead of pressure and the right hand side of the equation can be expanded in to a source term and a sink term as follow:

$$\frac{\partial(n_e\frac{3}{2}eT_e)}{\partial t}+\nabla\cdot Q_e=W_{\mathrm{abs}}-W_{coll} \qquad (4.3.26)$$

where Q_e is the electron energy flux, W_{abs} is the local power density coupled from the microwave, and W_{coll} is the energy loss in the reactions.

$$Q_e=\frac{5}{2}\Gamma_e k_B T_e-K_e\nabla T_e \qquad (4.3.27)$$

where K_e is thermal conductivity of electrons in plasma. The first term of equation (4.3.27) is derived from the macroscopic energy flux term in the energy balance equation and the last term of (4.3.27) is from the microscopic energy flux term in the energy balance equation. Electron thermal conductivity can be written as [129]:

$$K_e = \frac{\pi^2 T_e k_B^2 n_e}{3 m_e \nu_{eN}} \tag{4.3.28}$$

The source term in (4.3.26) is obtained from the local power density caused by microwave:

$$W_{\text{abs}} = \frac{1}{2}\sqrt{\frac{\mu}{\epsilon}}\boldsymbol{E}\boldsymbol{E}^* \tag{4.3.29}$$

and the sink term is the energy loss over reactions

$$W_{coll} = \sum_j R_j \xi_{0\text{j}} \tag{4.3.30}$$

where ξ_{0j} is the threshold energy or electron energy loss for the j^{th} reaction.

The argon plasma is simulated in one dimension (1-D) with one end (coordinate origin) representing the center of the plasma and the other end representing the wall. For the electron continuity equation, the boundary condition at the origin was set to be symmetrical and boundary condition at the wall was set to an outward flux. The outward flux follows the Bohm sheath criterion:

$$\Gamma_s = n_s u_B \approx 0.61\, n_e \sqrt{\frac{e T_e}{M_{Ar}}} \tag{4.3.31}$$

and for the electron energy balance equation, the boundary condition is set as symmetrical at the center of the plasma and energy outward flux was set for the wall condition. The energy flux to the wall for an argon discharge is:

$$Q_w = (q_e + q_i)\Gamma_s = (2T_e + 5.2T_e)\Gamma_s \qquad (4.3.32)$$

where q_e and q_i are the energy loss at the boundary for electrons and ions. The density of the metastables vanishes at the wall, thus the boundary condition for the metastables continuity equation was set to zero at the wall and symmetrical at the origin. For the 1-D simulation, the local power density was a constant value that was set to values of 0.5 – 10 W/cm^3. The operating pressure ranges from 1 – 10 Torr and the number of elements for the mesh is 100. The simulation domain length was one mm which represents the region from the center axis to the inner radius of the discharge tube. Simulation results for 1-D argon plasma simulation are presented in figure 4.3.1 – 4.3.8.

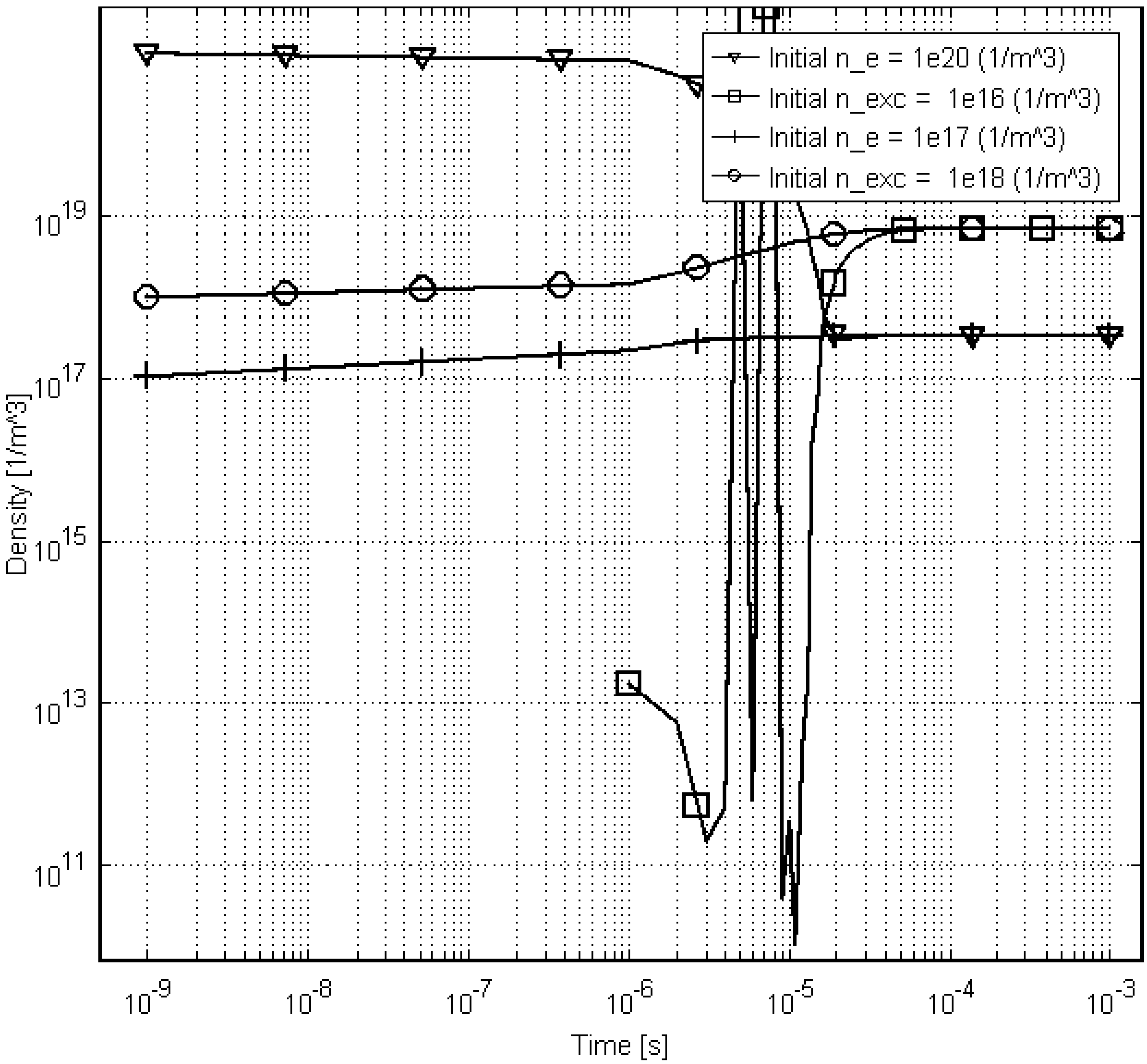

Figure 4.3.1: Time evolution of charge and metastable densities in 1-D argon plasma simulation for different initial conditions. Initial T_e = 2 eV, Power density = 1 W/cm^3.

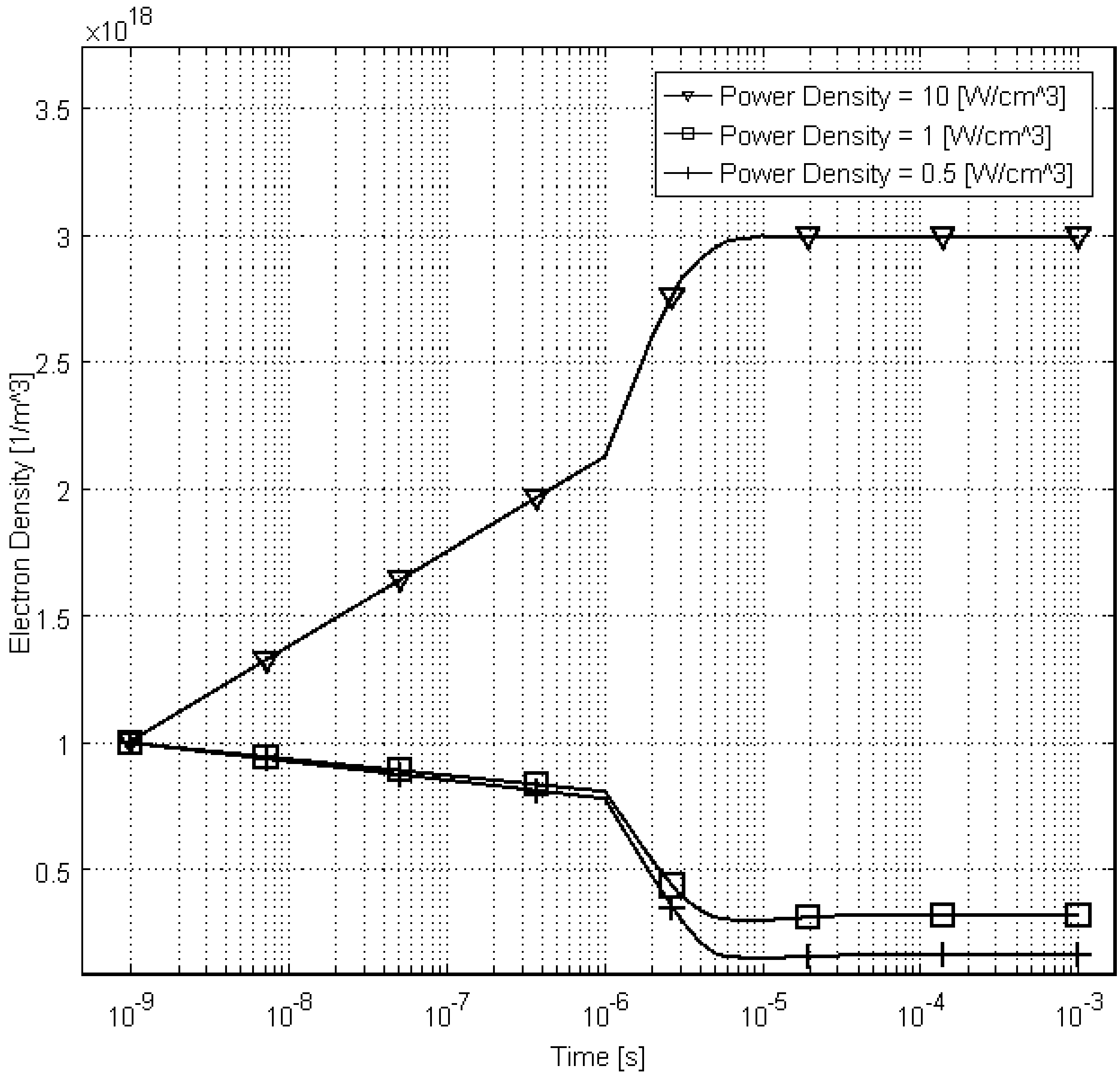

Figure 4.3.2: Electron density evolution in 1-D argon plasma simulation excited with various power density. Pressure: 1 Torr.

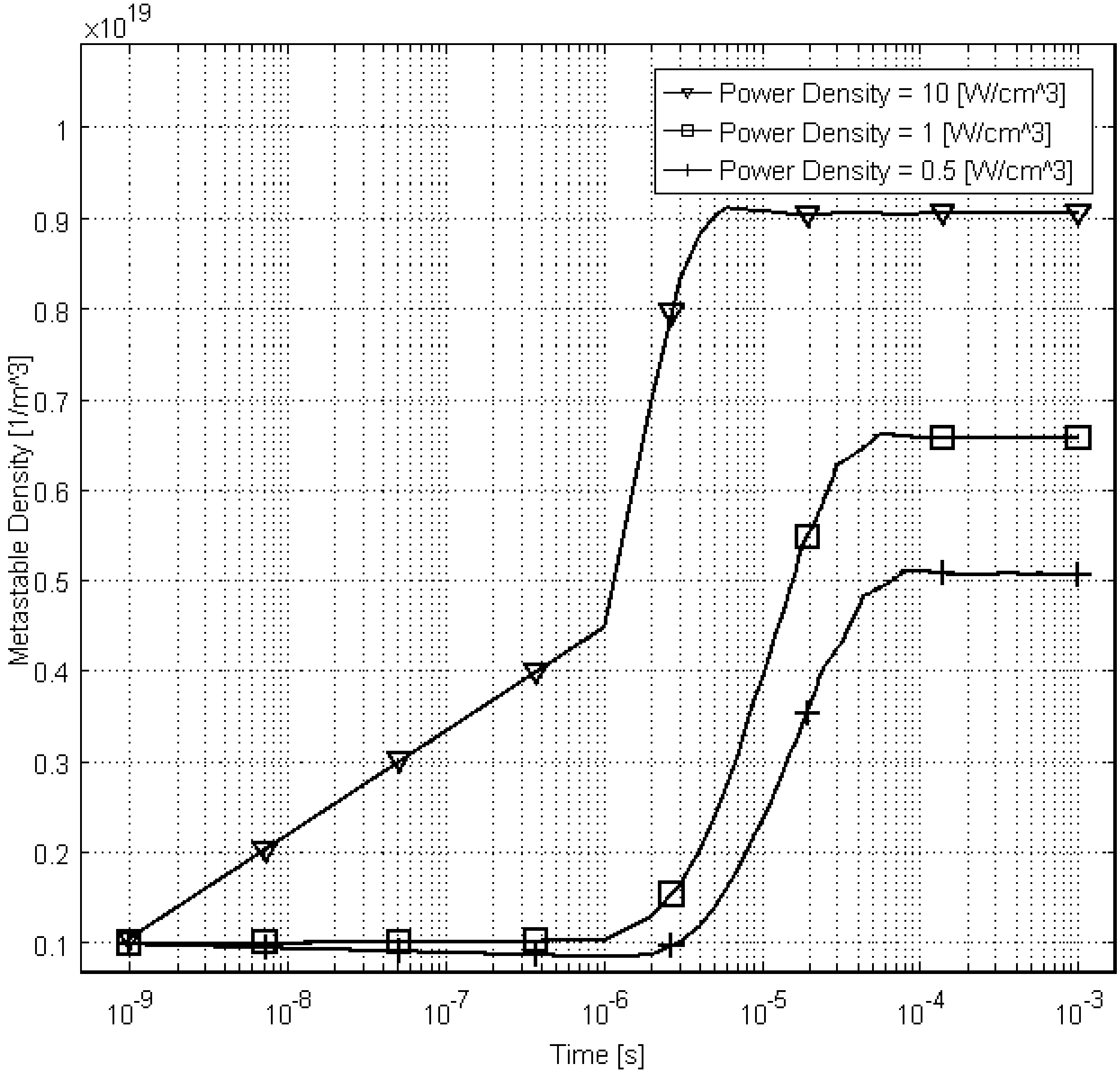

Figure 4.3.3: Metastable density evolution in 1-D argon plasma simulation excited with various power density. Pressure: 1 Torr.

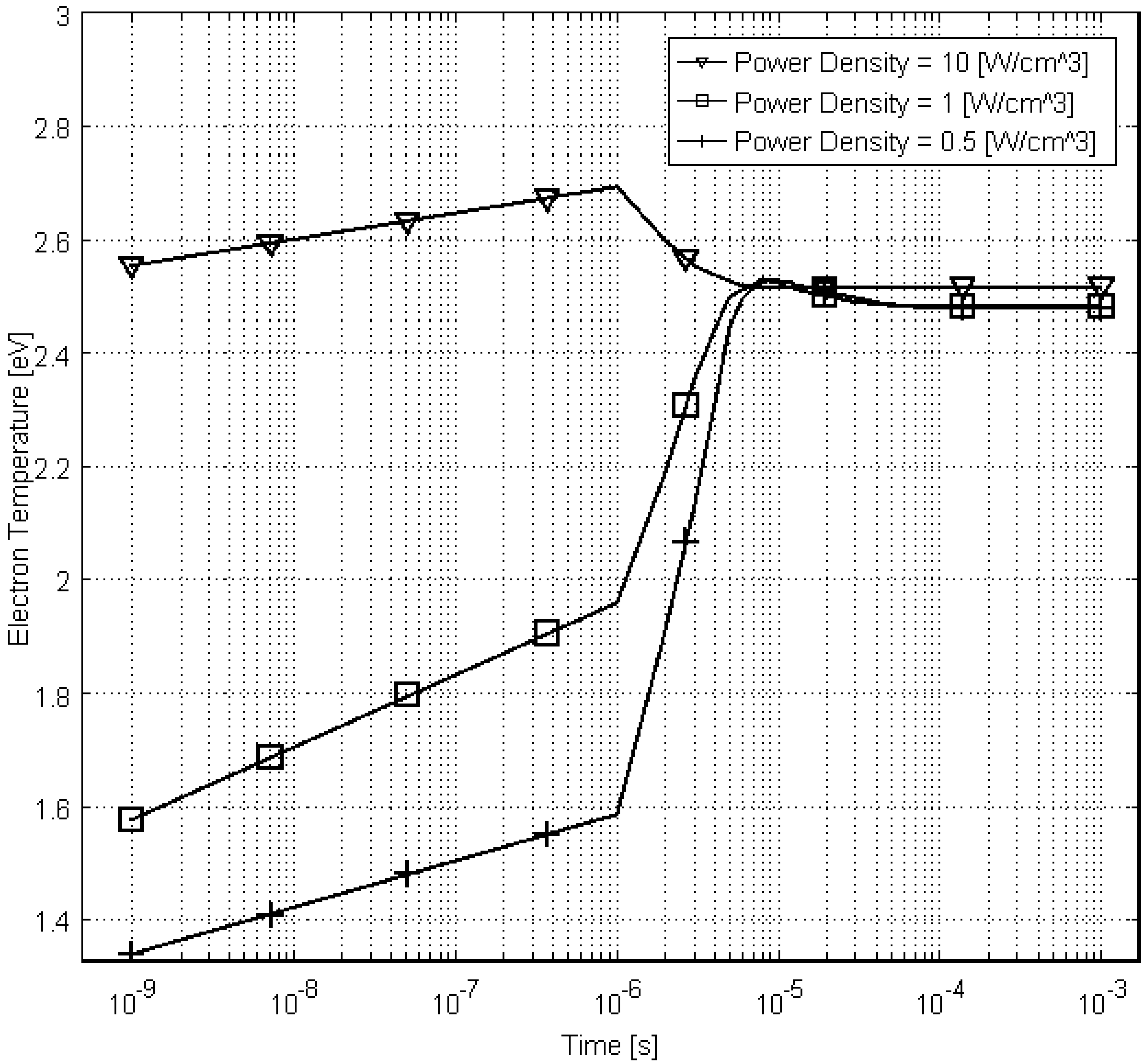

Figure 4.3.4: Electron temperature evolution in 1-D argon plasma simulation excited with various power density. Pressure: 1 Torr.

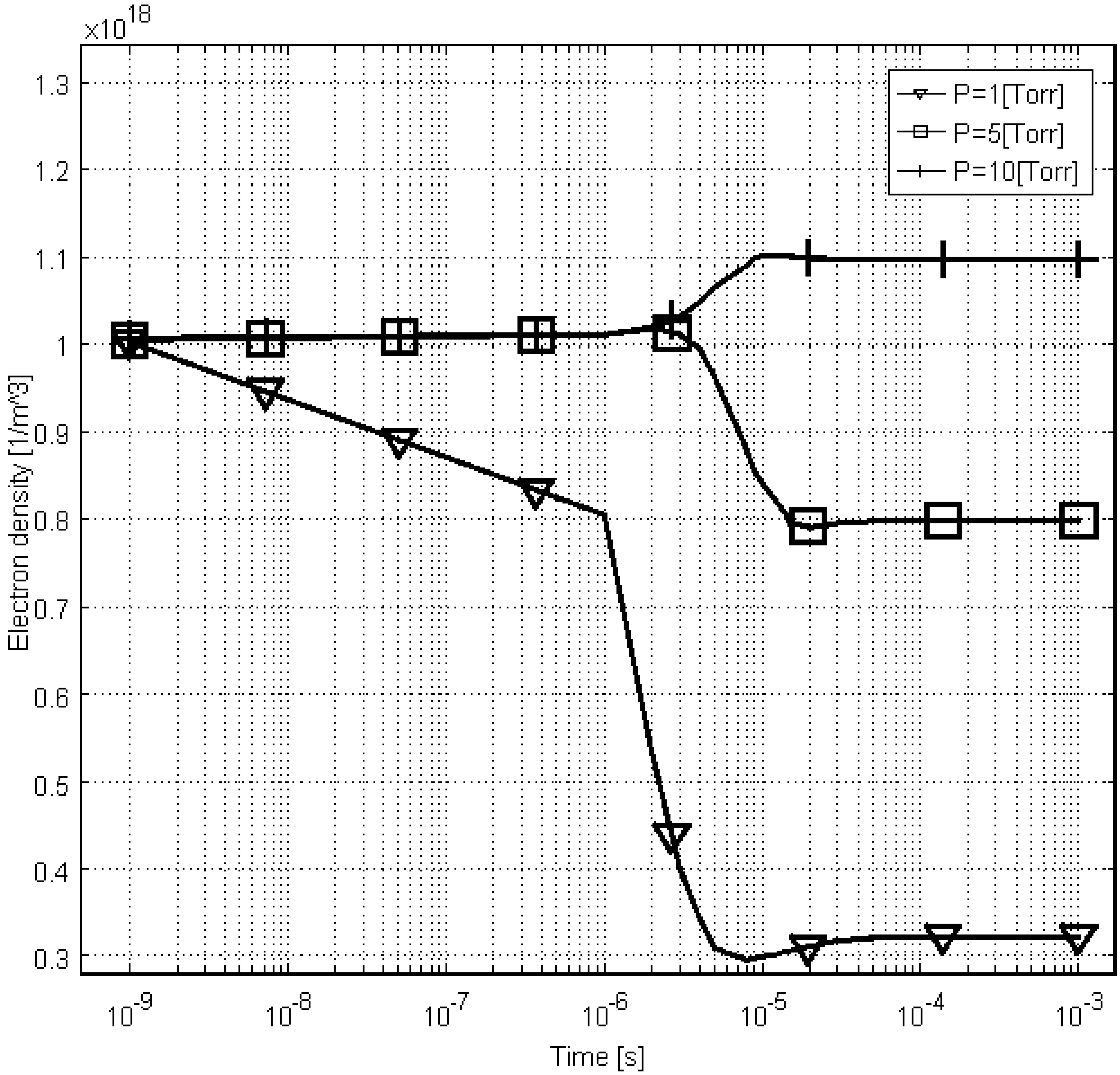

Figure 4.3.5: Electron density evolution in 1-D argon plasma simulation at various operating pressure. Power density: 1 W/cm3.

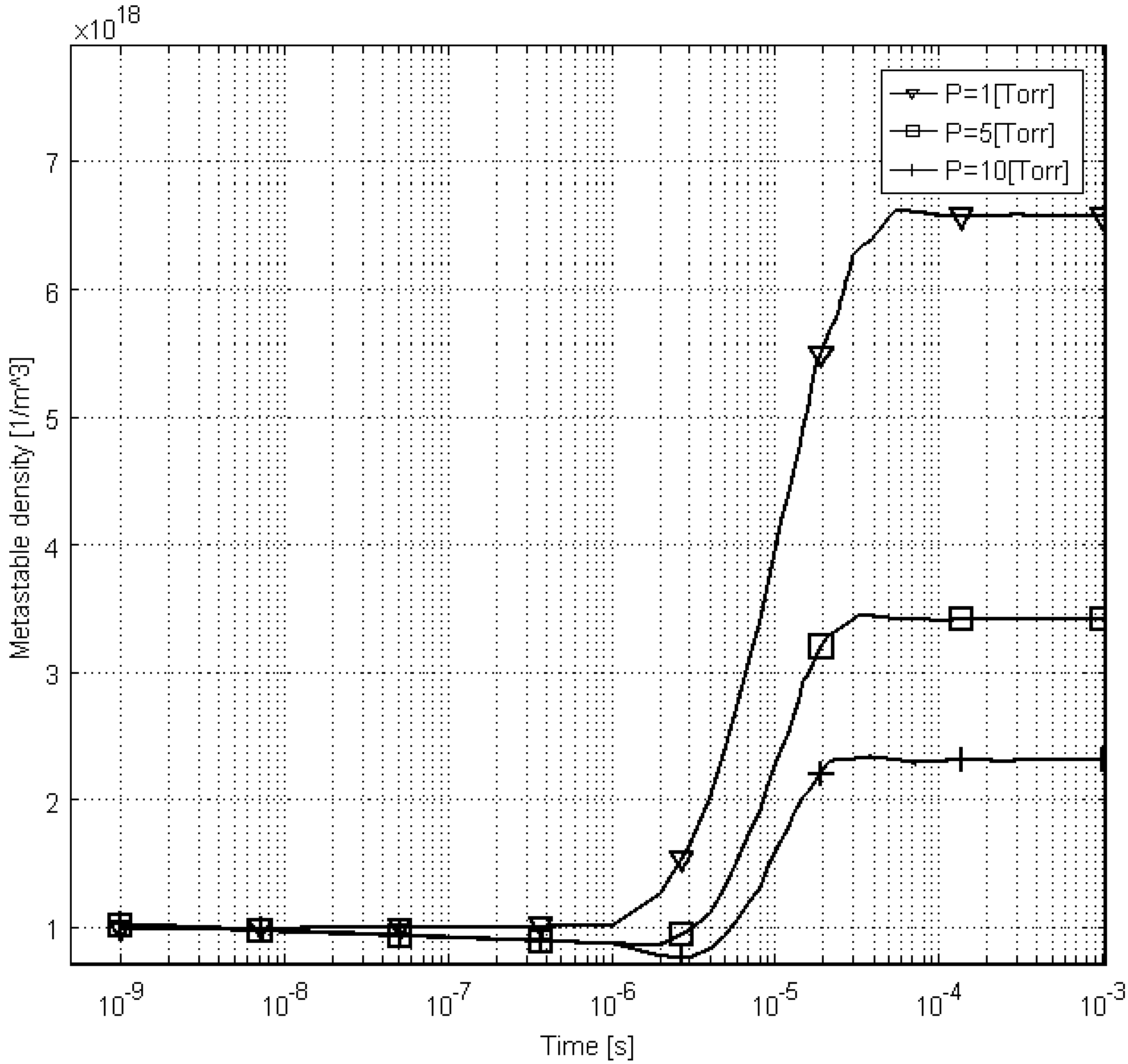

Figure 4.3.6: Metastable density evolution in 1-D argon plasma simulation at various operating pressure. Power density: 1 W/cm^3.

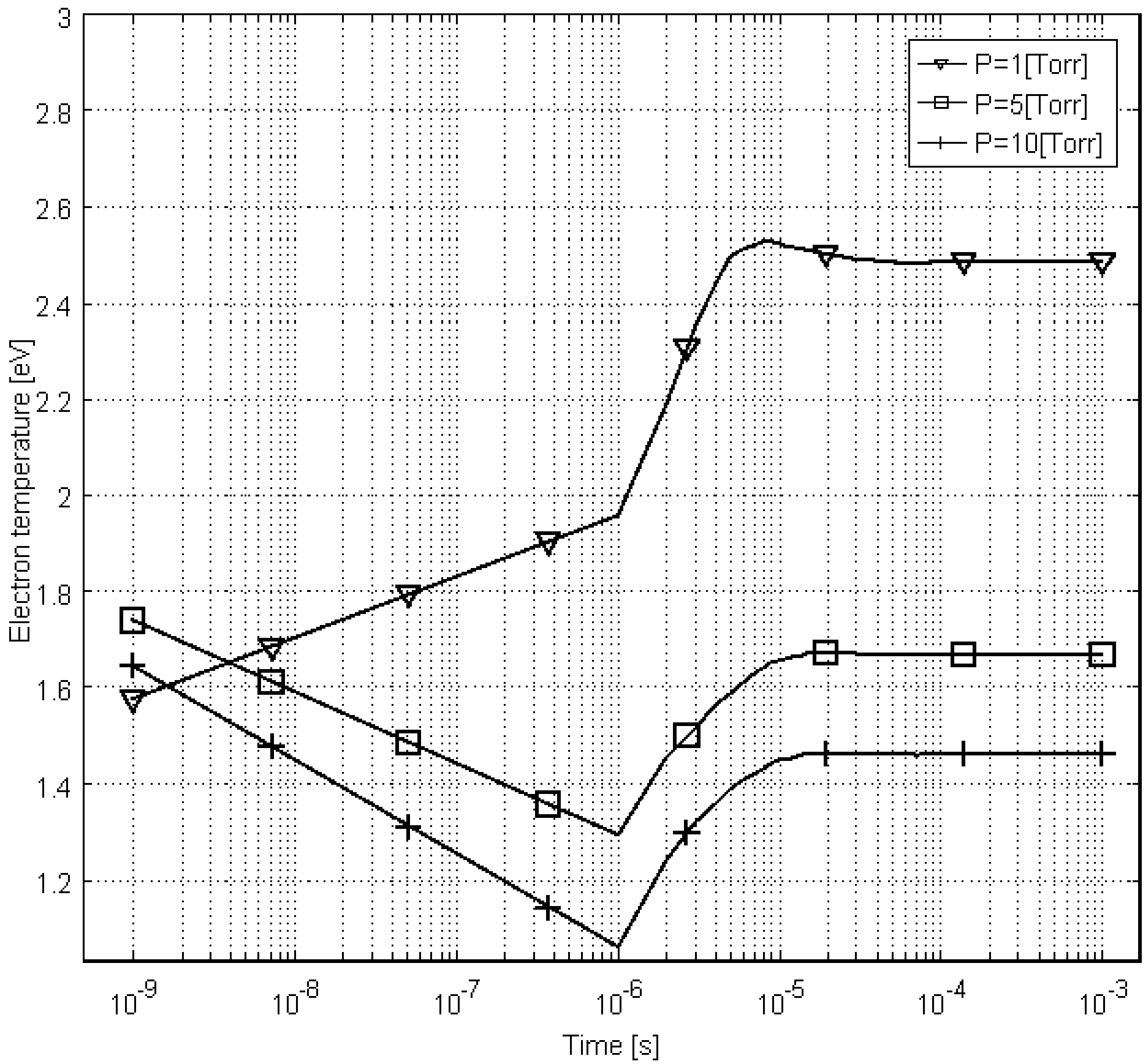

Figure 4.3.7: Electron temperature evolution in 1-D argon plasma simulation at various operating pressure. Power density: 1 W/cm^3.

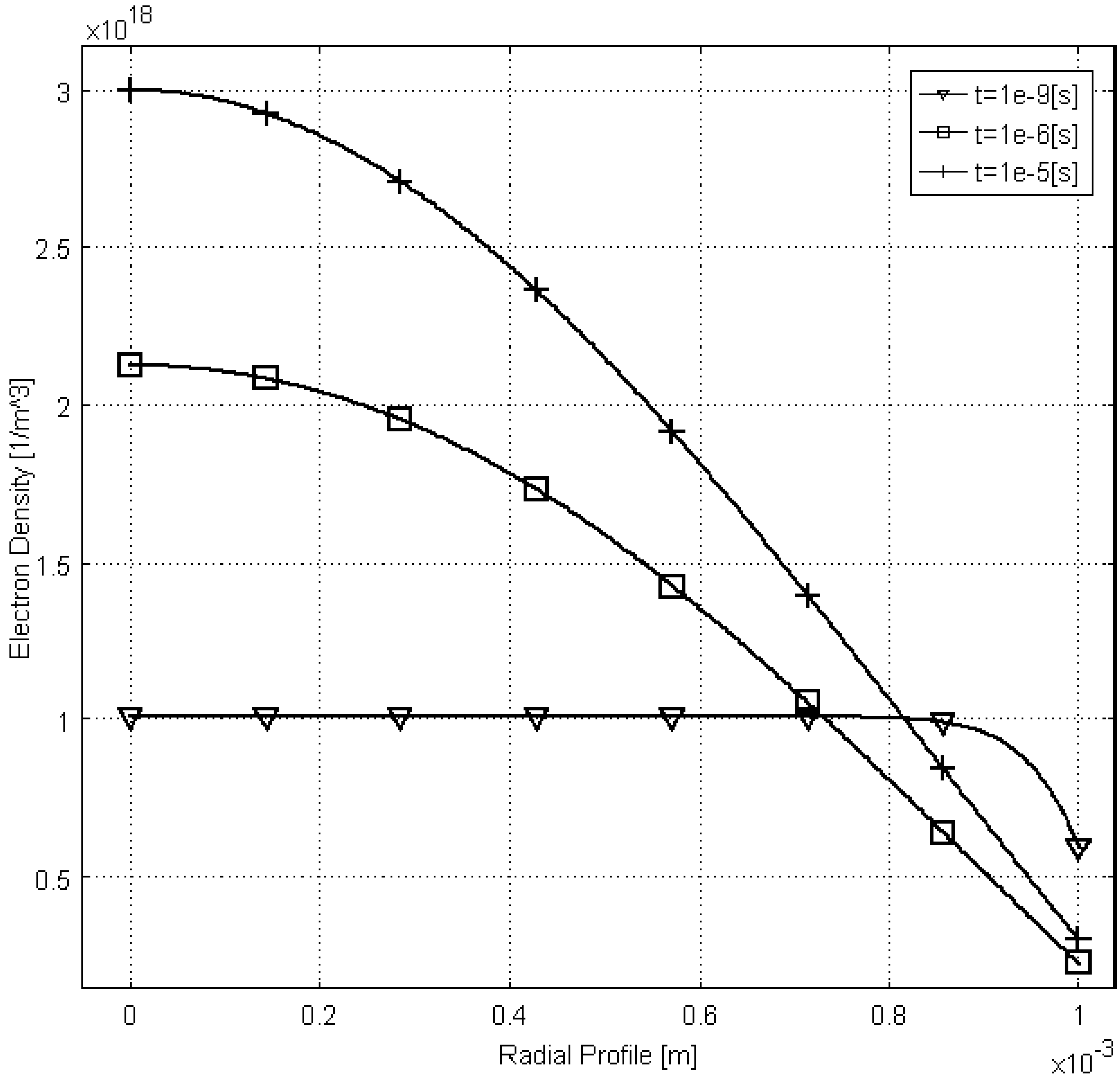

Figure 4.3.8: Radial profile of electron density in 1-D argon plasma simulation. Power density: 10 W/cm^3, pressure: 1Torr.

A good measure of building a computational model is to see its stability using different sets of initial conditions. Figure 4.3.1 shows that when the initial conditions of the electron density and the metastable density were varied, the plasma model converged to the same solutions. Thus, the plasma model is stable and the simulation result is independent from the initial conditions. The charge densities, the metastable densities and the electron temperatures data were taken from the center of the plasma (r = 0) in figure 4.3.1. The computational argon plasma model starts to converge to a stable solution around ten μs as shown in figure 4.3.2 - 4.3.7. When the local power density was increased from 0.5 – 10 W/cm^3, the peak electron and metastable density increases as seen in figure 4.3.2 and 4.3.3. However, the electron temperature, shown in figure 4.3.4, for various power density converged to around 2.5 eV. Operating pressure, on the other hand, has influence on the electron temperature. As shown in figure 4.3.7, as the pressure increased, the electron temperature decreases. The electron densities increase when the operating pressure increases. However, the metastable density decreases with increase of operating pressure. The influence of the operating pressure to the electron density and the metastable density are shown in figure 4.3.5 and 4.3.6, respectively. A typical radial profile of the electron density is shown in figure 4.3.8. The initial condition for the electron density was a flat profile. As time evolves, the density profile changes shape into a Bessel function profile.

In summary, the argon plasma computational model is stable and it converged to a solution for the input parameters of the micromachining system. The result of this 1-D simulation will be compared to the experimental results in chapter 6.

4.4 Self-consistent simulations of the micromachining system

In the previous sections, the foreshortened coaxial cavity was simulated. Using a uniform argon plasma model as a load, it was determined that the tuning parameters of the cavity include: the cavity length, the gap distance, the size of the plasma and the electron density. According to the computational argon plasma model results, the electron density was found to have a radially varying profile. In this section by combining the plasma model and the electromagnetic simulation a more in depth understanding of the system will be obtained.

The 1-D simulation of the argon plasma described in section 4.3 has power density as one of the input parameters. In the micromachining system, the foreshortened coaxial cavity provides the microwave energy coupling into the discharge. Thus, the heating mechanisms of the plasma, which is the electron energy balance, depends on the cavity tuning. The coupling of the foreshortened cavity simulation and the plasma model creates a self-consistent simulation.

Two different setups were examined for the self-consistent simulation. The first simulation setup employed an artificial high loss boundary layer for the plasma domain. The plasma domain was set to two mm long to minimize the cavity resonance perturbation by the plasma load. For the high loss boundary layer, the boundary conditions of the charge continuity equation and the energy balance equation were formulated to ignore the sheath of the plasma. This formulation means that the charge density at the wall was set to zero and the electron temperature at the wall was set to 300 K. With high loss boundary conditions, the energy supply by the microwave needed to be high. However, this high loss condition creates a more stable evolution of the charge density. With the resulting more stable plasma permittivity, cavity resonant can be maintained better. Simulation results for a self consistent simulation using an artificially high loss boundary condition are presented in figure 4.4.1 – 4.4.5.

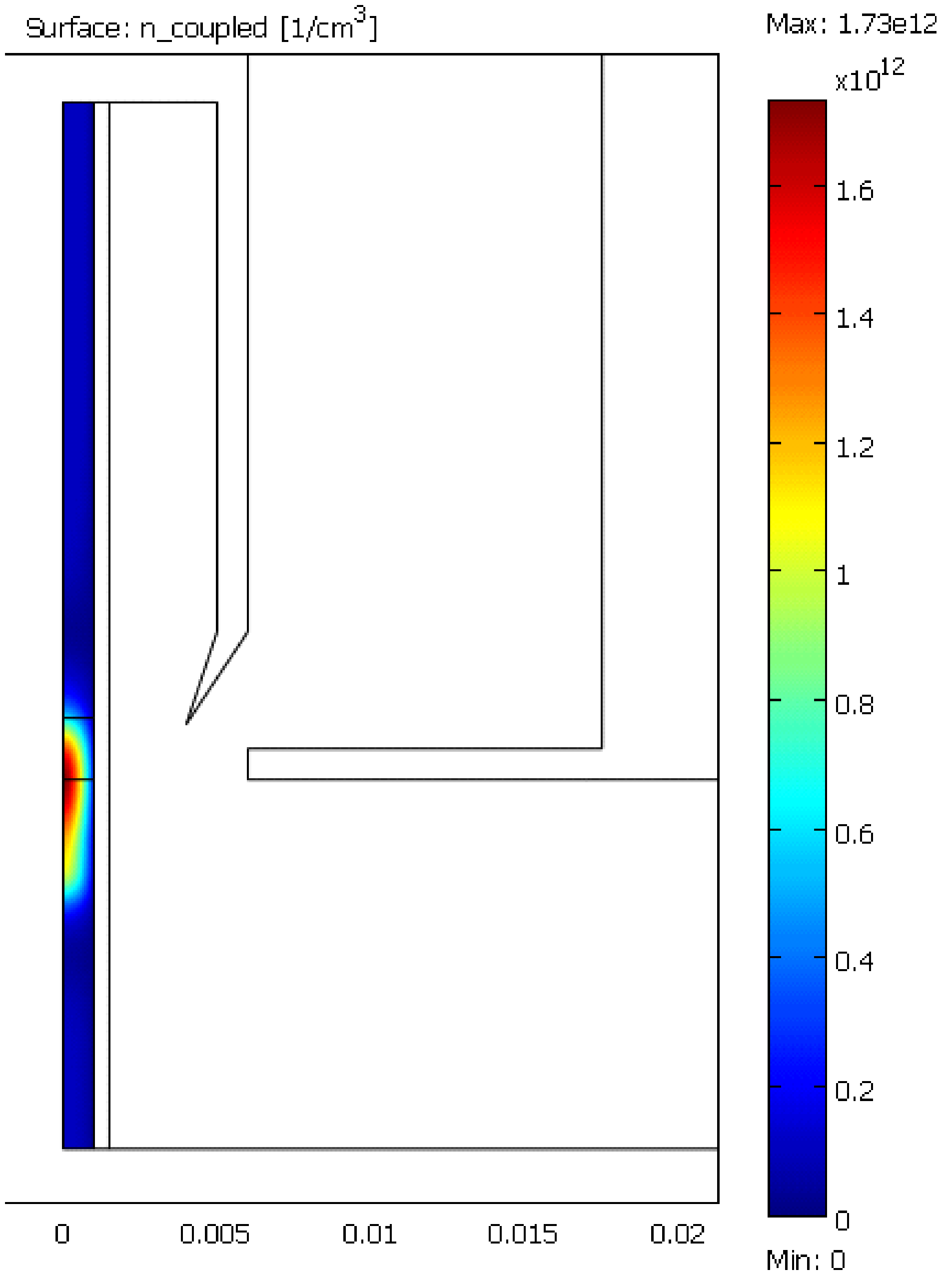

Figure 4.4.1: Electron density profile of pure argon plasma with high loss boundary after 5 μs. Pressure: 1 Torr, P_{abs}: 14 W.

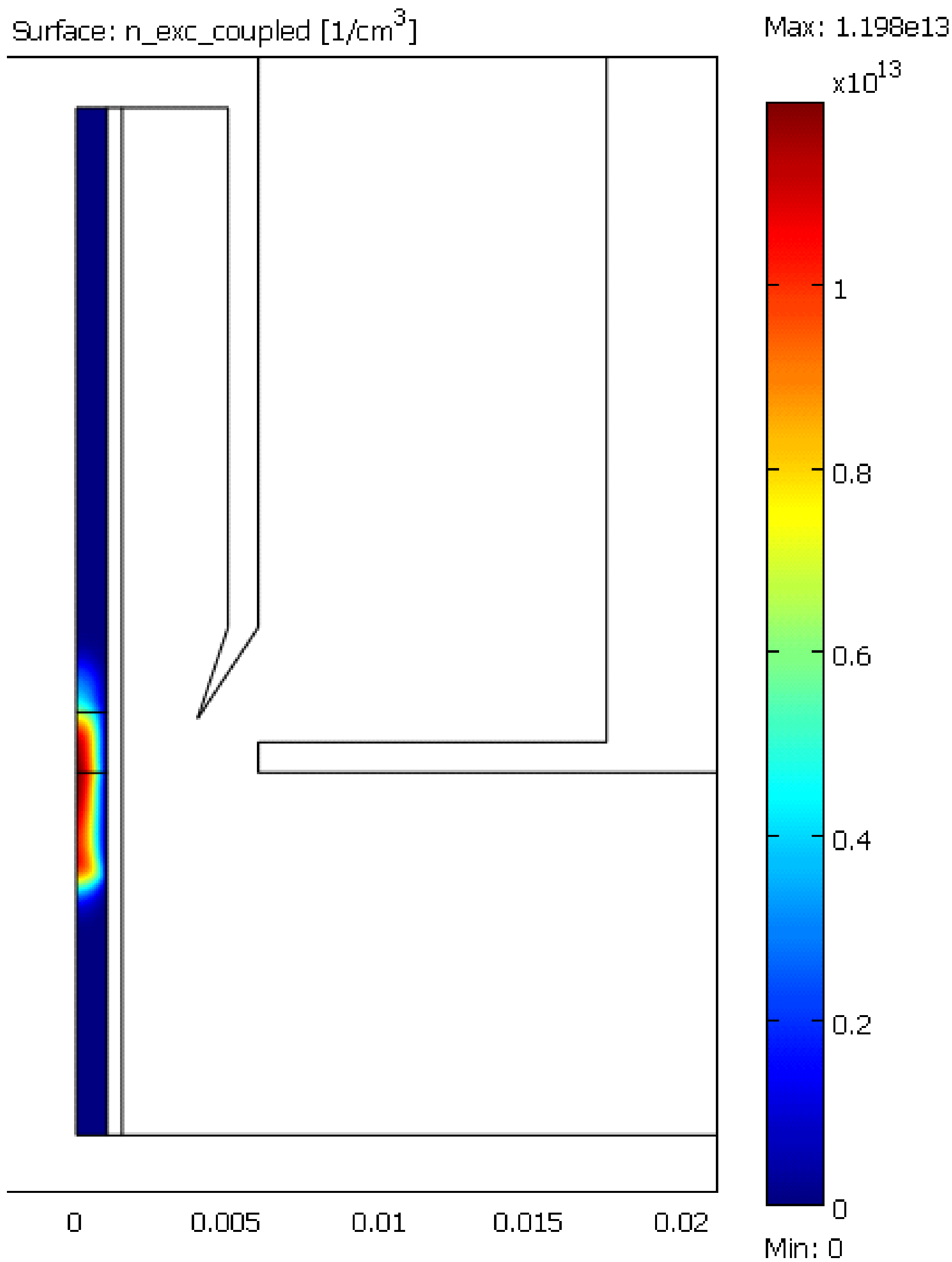

Figure 4.4.2: Metastable density profile of pure argon plasma with high loss boundary after 5 μs. Pressure: 1 Torr, P_{abs}: 14 W.

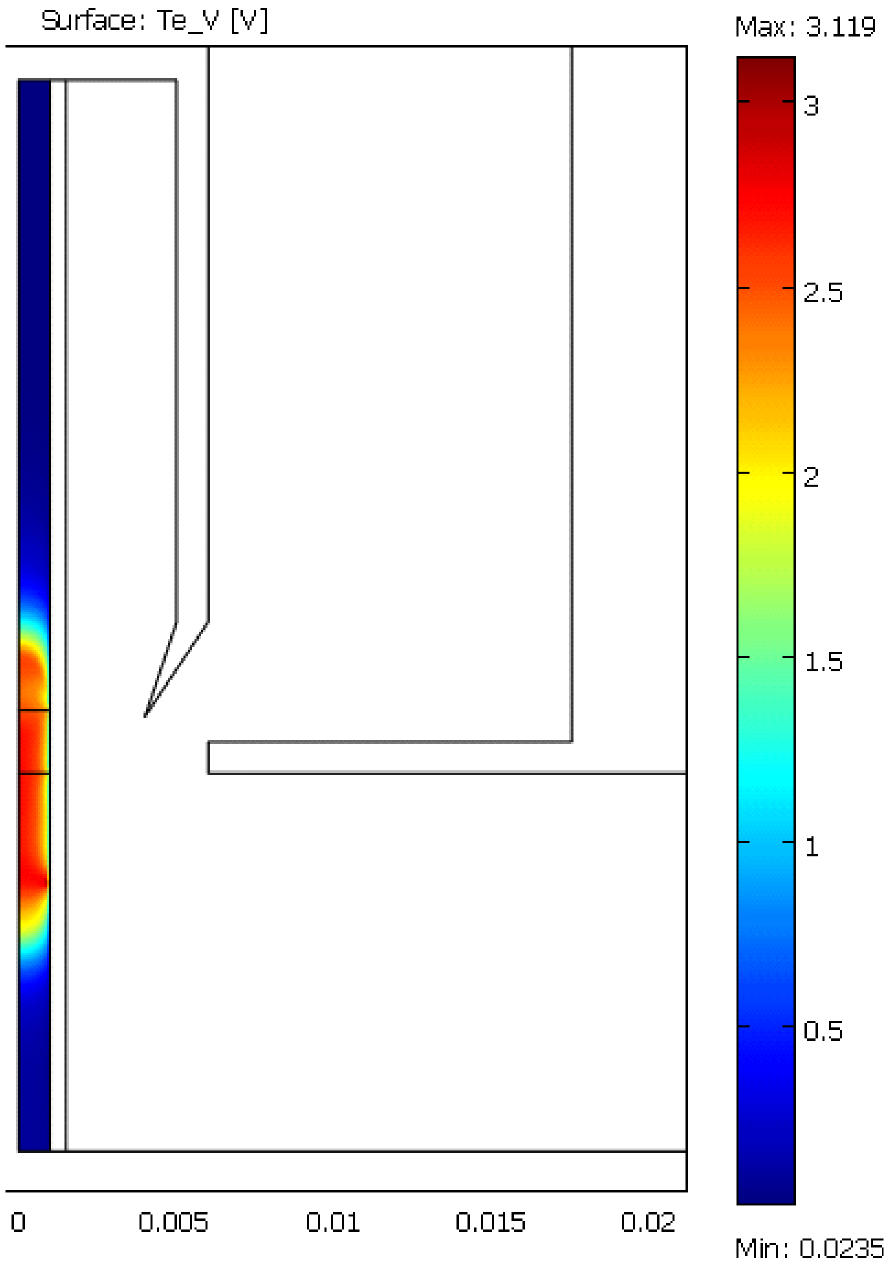

Figure 4.4.3: Electron temperature profile of pure argon plasma with high loss boundary after 5 μs. Pressure: 1 Torr, P_{abs}: 14 W.

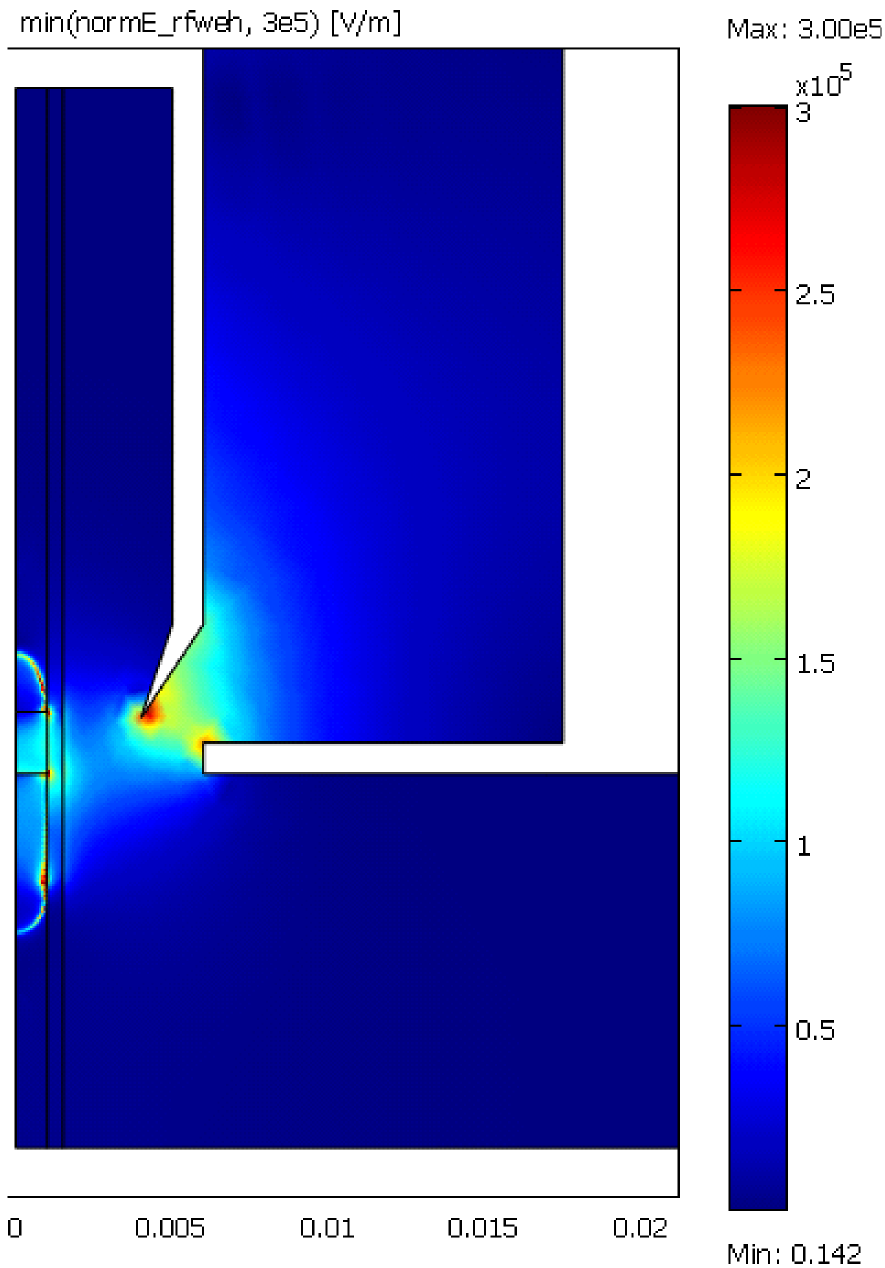

Figure 4.4.4: Electric field profile of pure argon plasma with high loss boundary after 5 μs. Pressure: 1 Torr, P_{abs}: 14 W.

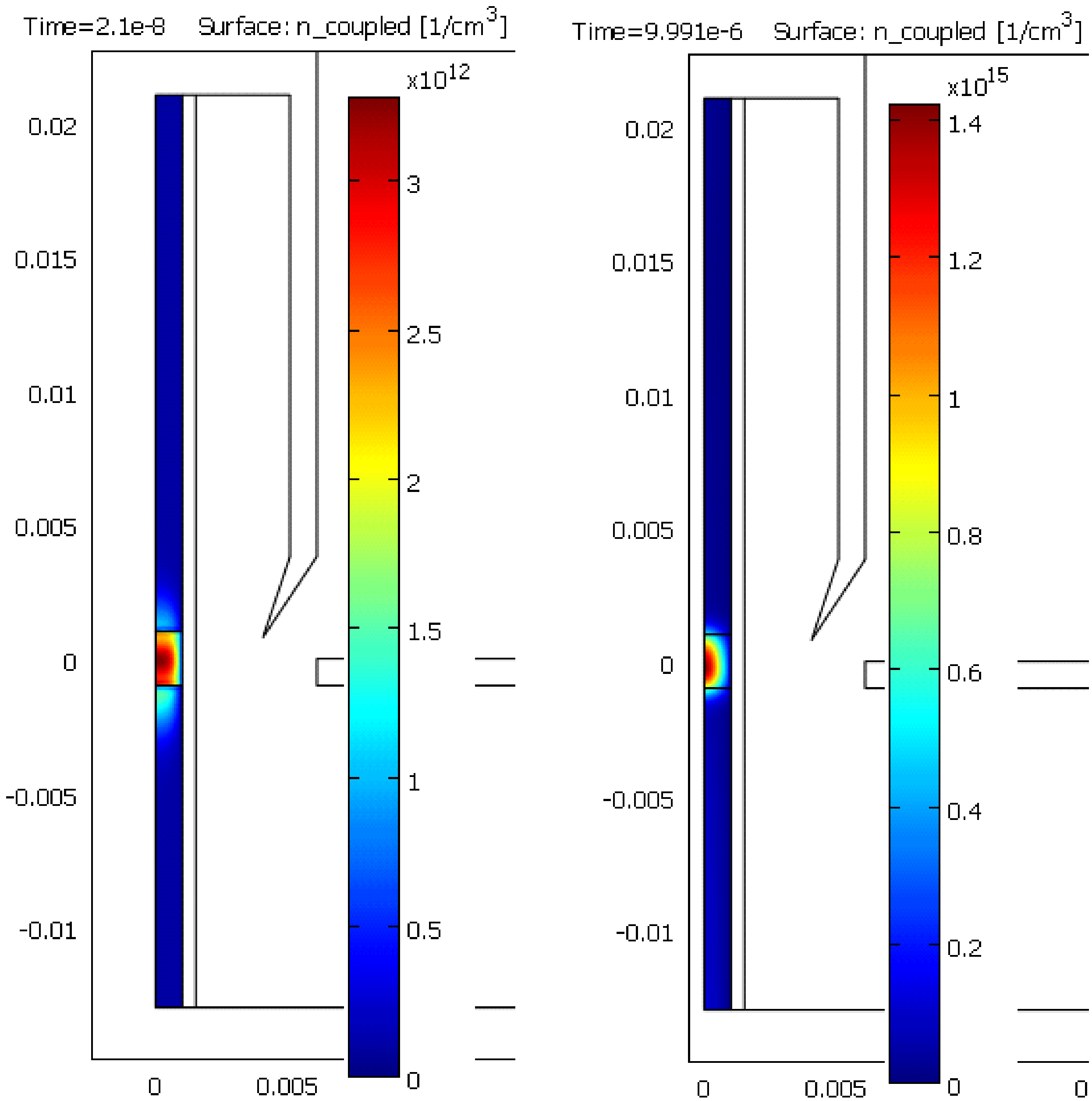

(a) (b)

Figure 4.4.5: Electron density profile of pure argon plasma with high loss boundary after (a) 20 ns and (b) 10 μs. Pressure: 10 Torr, P_{abs}: 96 W.

The initial conditions for the electron density, metastable density, and the electron temperature of the pure argon plasma were applied only at the small rectangular area inside the plasma domain. The rest of the plasma domain region initial conditions were set to have zero. As shown in figure 4.4.1 - 4.4.3, after 5 μs the charge density, the metastable density, and the electron temperature expanded outside the non-zero initial condition region. The electric field profile can be seen in figure 4.4.4. Inside the discharge tube, the highest electric field was found on the boundary of the plasma. While the plasma volume expansion can be observed, the microwave power needed to sustain the plasma was considerably high due to the artificially high loss boundary conditions. For another simulated argon plasma at 10 Torr, the microwave power supplied was 96 W.

Another self-consistent simulation was performed without the artificially high loss boundary. The simulation domain, shown in figure 4.4.6, has two different domains for the plasma. The difference of the plasma domains was the setting of the initial conditions, which are listed in table 4.4.1. Plasma was assumed to fill both of the domains to satisfy the flux boundary conditions, which depend on the charge density and electron temperature having non-zero initial conditions. Plasma domain 1 was three cm long centered at the cavity gap. The tuning parameter values for the cavity were based on the finding described in section 4.2, where the plasma was assumed to have an infinite length. For this simulation the cavity length was 24.65 mm, and the gap distance was 2.3 mm. These values were used to ensure the cavity was tuned for the initial conditions.

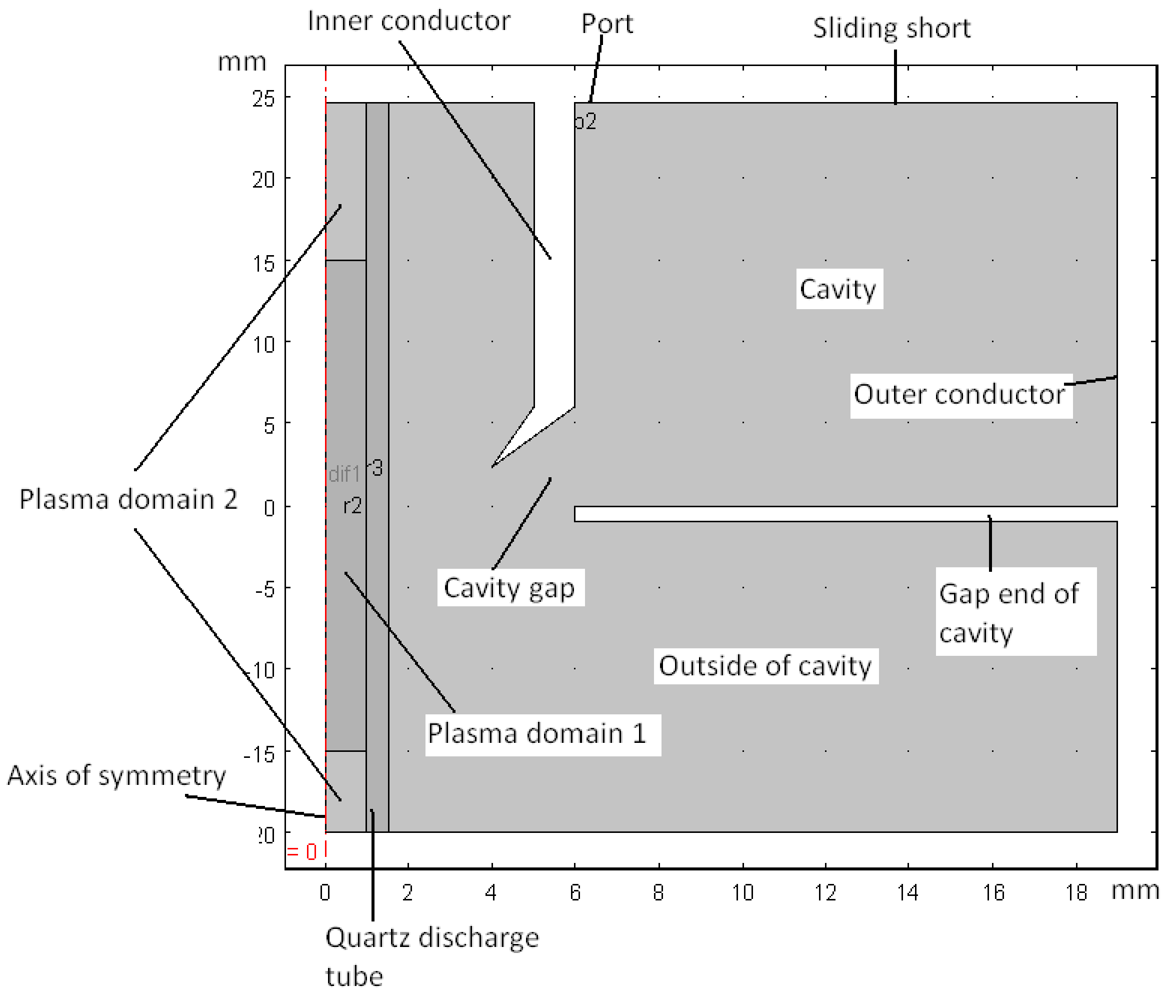

Figure 4.4.6: Simulation domain of for the self-consistent argon plasma simulation.

Table 4.4.1: Initial conditions for the self-consistent argon plasma simulation.

Initial condition	Plasma domain 1	Plasma domain 2
Electron density [cm^{-3}]	2.15×10^{12}	2.15×10^{11}
Metastable density [cm^{-3}]	10^{12}	10^{11}
Electron temperature [eV]	2	1

The maximum element size of the mesh in the cavity, quartz tube, and plasma were $\lambda/10$, 0.4 mm, and 0.35 mm, respectively. A boundary layer mesh was placed at the boundary between the plasma domain and the quartz discharge tube. The complete mesh consists of

2746 elements. The result of the simulation are presented in figure 4.4.7.

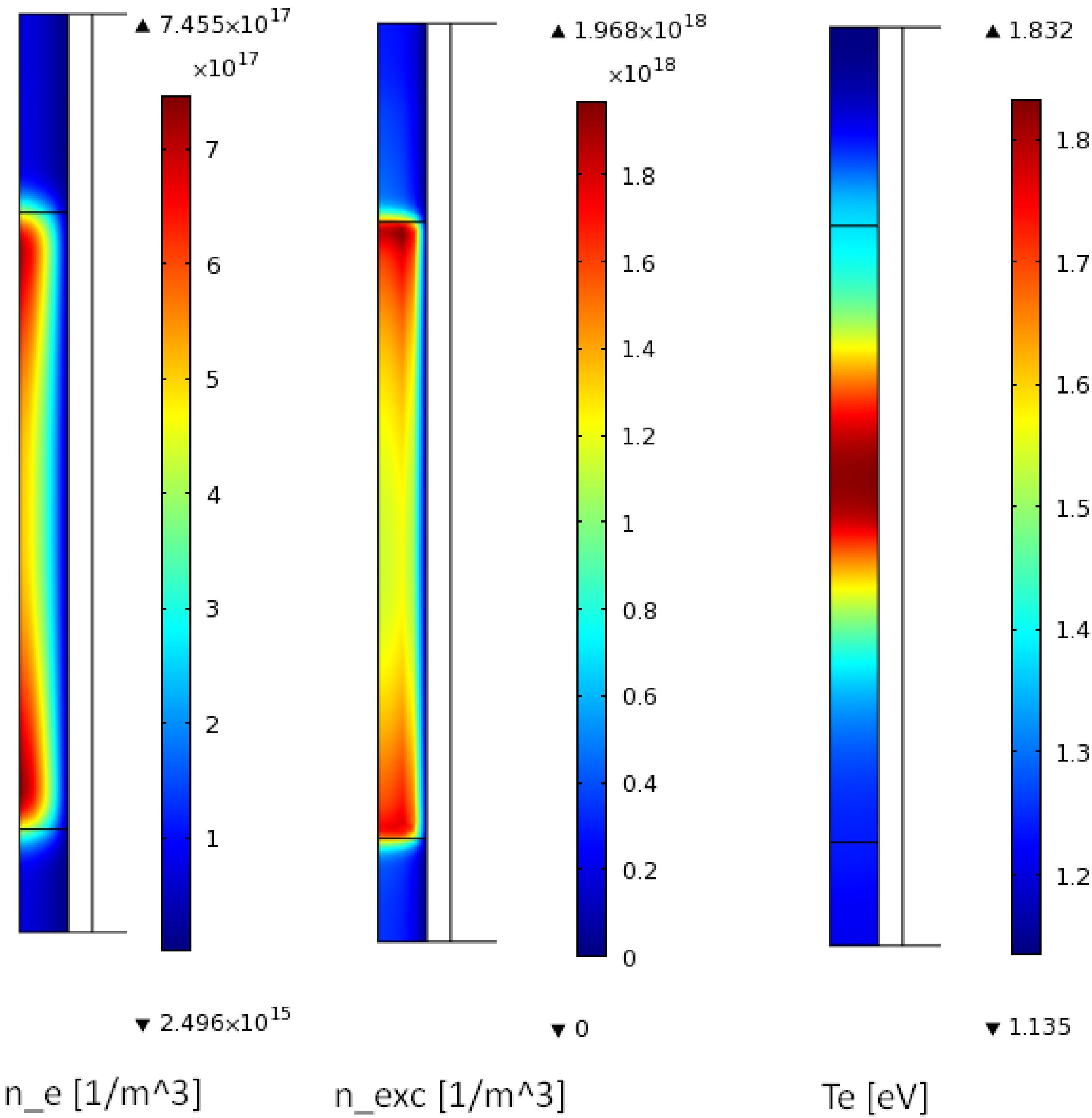

Figure 4.4.7: Simulation result of the self-consistent argon plasma at 1 Torr showing only the plasma domain. Time: 5 µs, Input power 0.5 W.

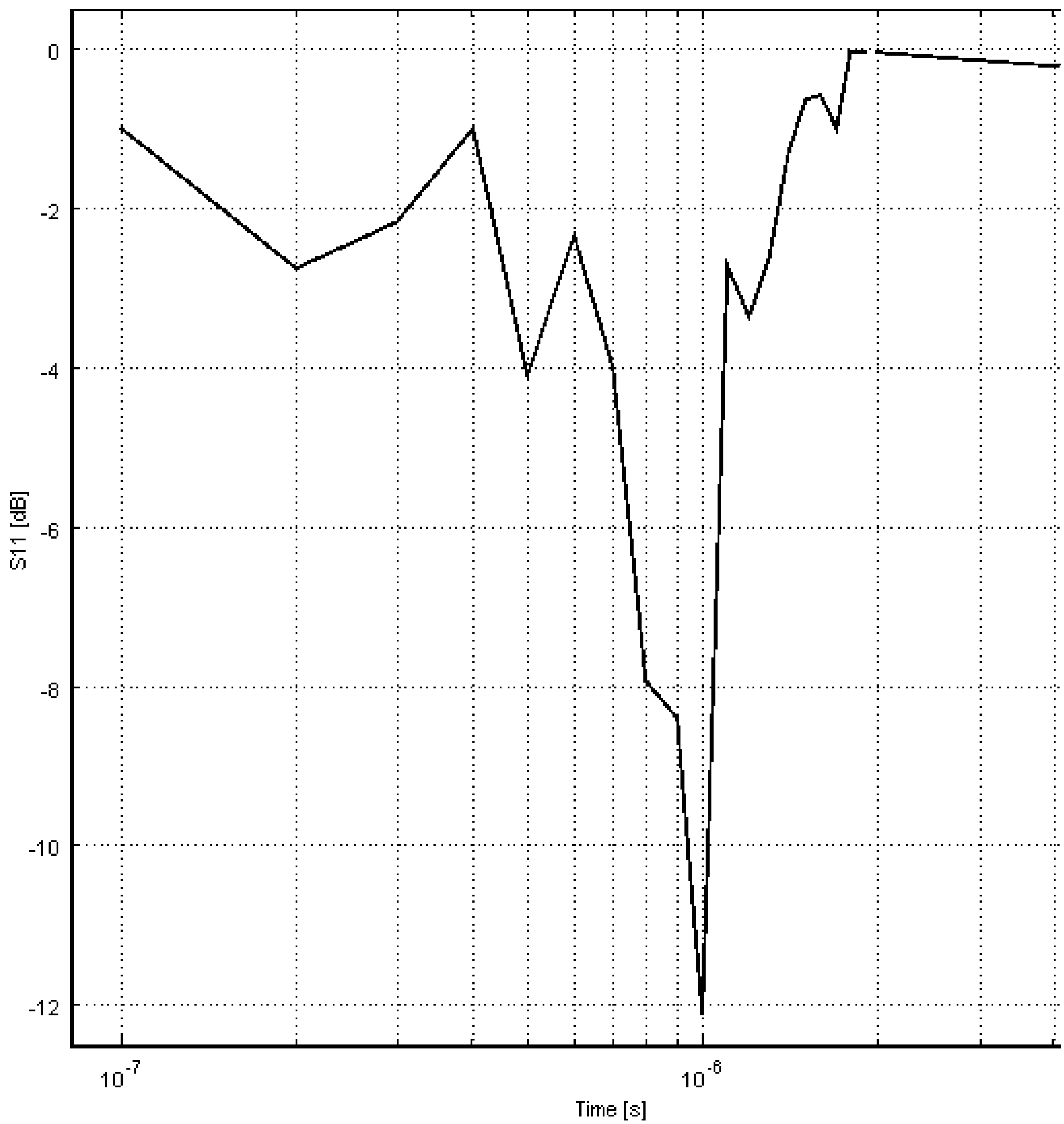

Figure 4.4.8: Evolution of S_{11} parameter of the self-consistent argon plasma simulation. Pressure: 1 Torr. Input power: 0.5 W.

This self-consistent argon plasma simulation used the foreshortened coaxial cavity. The charge density, the metastable density, and the electron temperature values, as shown in figure 4.4.7, were in a good agreement with the earlier 1-D argon plasma simulation results. However, influences from the initial conditions are still presents. This means that the simulation did not converged to a steady-state solution yet. It is possible that the simulation is not converging because the tuning or resonance frequency of the cavity changes over time. The non-steady-state behavior is indicated by the time evolution of the S_{11} parameter shown in figure 4.4.8. As S_{11} value evolves with time, the power coupled into the plasma region changes. The power coupling changes result in plasma density variations and plasma length variations. The tight coupling and non-linear interaction of the S_{11} (reflected power) parameter, plasma density, and plasma discharge length resulted in the self-consistent plasma and electromagnetic simulation not reaching a steady-state solution. Rather a transient solution as shown in figure 4.4.8 occurs.

5 Experimental Results

5.1 Introduction

In this chapter, experiments are described that demonstrate the operation of the microplasma and micromachining system. In section 5.2, the basic operating characteristics of the micromachining system is explained. First, the setup of the foreshortened coaxial cavity is explained. Second, the plasma behavior from visual inspection is described. Third, the plasma length and the power density measurements are presented. Fourth, the determination of the charge density of the plasma is presented. Section 5.3 presents demonstration results of the micromachining system operating as an ion source. In this case, the ions generated by the plasma applicator are used to locally etch silicon and polycrystalline diamond. The free radical source application of this system is explained in section 5.4. In particular, experimental work performed using oxygen plasma ashing of photoresist is described. Lastly, a light source application of the micromachining system is presented in section 5.5.

5.2 Plasma characteristics

5.2.1 Foreshortened coaxial cavity tuning

The foreshortened coaxial cavity can be tuned to resonate at a specific frequency by adjusting the cavity length (L_s) and the gap distance between the inner conductor and the gap end of the cavity (L_g) as shown earlier in figure 3.2.1. The loop antenna position inside the cavity and its orientation can also be adjusted. In a simple coaxial cavity, the resonance frequency occurs when the cavity length is $\lambda/4$. For this experiment, 2.45 GHz microwave power is used, thus the $\lambda/4$ cavity length is 3.06 cm. However, the gap and the antenna loop inside the foreshortened coaxial cavity changes the tuning behavior of the cavity. The gap acts as a capacitance thus the reactance of the cavity needs to be adjusted accordingly. Based on the COMSOL simulation, the maximum power coupling occurs when the cavity length is set to approximately 2.1 cm and the gap between the gap end of the cavity and the center conductor is 2 mm. For the experimental work, this condition is ideal to ignite the discharge using a high voltage spark. The absorbed power (P_{abs}), which is calculated by subtracting the reflected power from the input power delivered into the cavity, is maximum in this condition. However, once the plasma ignites, the gap length can be slightly adjusted to obtain a longer plasma column. As a result, this adjustment increases the reflected power.

The gap length also has a considerable effect on the discharge and coupling. Discharges can be sustained for larger gaps, as long as the loop is also moved further away from the ground plate. With larger gaps, the reflected power is larger compared to the smaller gaps. Two or three mm gaps result in power matches of 50 to 70% as compared to generally 80 to 90% for smaller gaps. Larger gaps increases the wall and radiation losses. Considering the aforementioned reason, for this experiment the gap is set to approximately 1 – 2 mm.

The excitation loop inside the foreshortened coaxial cavity also needs to be adjusted to get an optimum power coupling. The orientation of the loop antenna is set perpendicular relative to the inner conductor. With this setup, the microwave energy is coupled into the magnetic field inside the cavity in the ϕ direction. Since the strongest magnetic field inside the cavity exists at either end of the cavity, the excitation loop should be located in those areas. From the experiments, better coupling occurs when the loop antenna is placed near the gap end of the cavity.

By applying microwave power at the foreshortened coaxial cavity resonance frequency, a high electric field is formed and concentrated at the gap region. This high field breaks down the feed gas inside the discharge tube thus forming a plasma column. At low microwave power, only a short plasma column is generated in the gap region. However, with an increase of the microwave power and if the plasma density is high enough, surface waves are formed between the plasma column and the discharge tube. These waves expand along the z-axis resulting in the plasma column expanding along the z-axis as well. Typical lengths of the argon plasma column generated using the above cavity setup with a pressure of 1 Torr, flow rate of 20 sccm and absorbed microwave power of 5 Watts are around six cm. The plasma length is measured from the center of the plasma column, which is at the cavity gap, to the tip of the plasma column. Detail measurements on plasma length can be found in the next section.

5.2.2 Plasma behavior

The discharge generated using the foreshortened coaxial cavity expands along the z-axis creating a discharge column confined by the quartz tube as explained in the previous section. In the processing area where the substrate is located, the discharge becomes unconfined. A transition between confined surface wave plasma column in the discharge tube to an unconfined plasma was observed. The length of the quartz tube was shortened for this observation. With enough microwave power, the surface wave plasma will reach the processing area. Argon gas with 20 sccm of flow rate was used as the feed gas and the processing chamber pressure was varied from 0.5 Torr to 10 Torr. As seen in figure 5.2.1, microwave power delivered to the foreshortened coaxial cavity changes the length of the surface wave plasma. If the applied power is too high, the microwave energy can generate plasma outside the discharge tube.

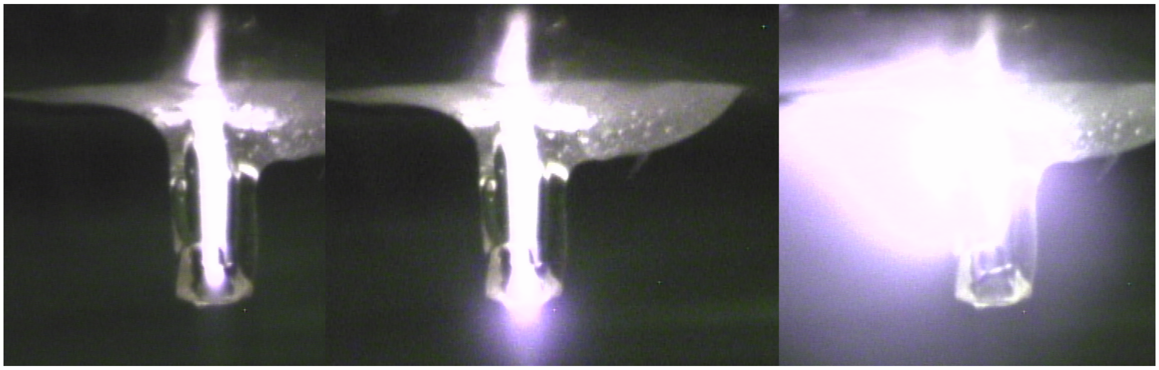

P_{in} = 10 W, P = 0.5 Torr P_{in} = 20 W, P = 0.5 Torr P_{in} = 30 W, P = 0.5 Torr

Figure 5.2.1: Argon plasmas at the tip of the discharge tube inside the processing chamber at a variation of microwave power from low (left) to high (right).

At the lower end of the pressure range, around 0.5 Torr, the discharge looked like a plasma ball protruding from the tip of the quartz tube. In this case, the mean free path of the argon gas is relatively long thus the discharge diffuses. As the pressure increases, the plasma ball volume decreases and at the high end of the pressure, it became like a plasma plume before it eventually goes out. The surface wave plasma gets shorter as the pressure increases.

The operating range of microwave power to create this plasma ball or plasma plume needs to be monitored carefully. If the microwave power is too low, the surface wave plasma will not reach the processing area. On the other hand, if the power is too high, plasma will be generated outside the discharge tube near the top of the plate. This happens because the high field generated by the foreshortened coaxial cavity radiates into the processing chamber thus breaking down the argon gas inside the chamber rather than the argon gas inside the discharge tube.

Another characterization was performed to observed the charged particles flowing out of the discharge tube on to the substrate. Two different setups are applied, first without an aperture (figure 5.2.2) and second with a 450 μm silicon aperture (figure 5.2.3).

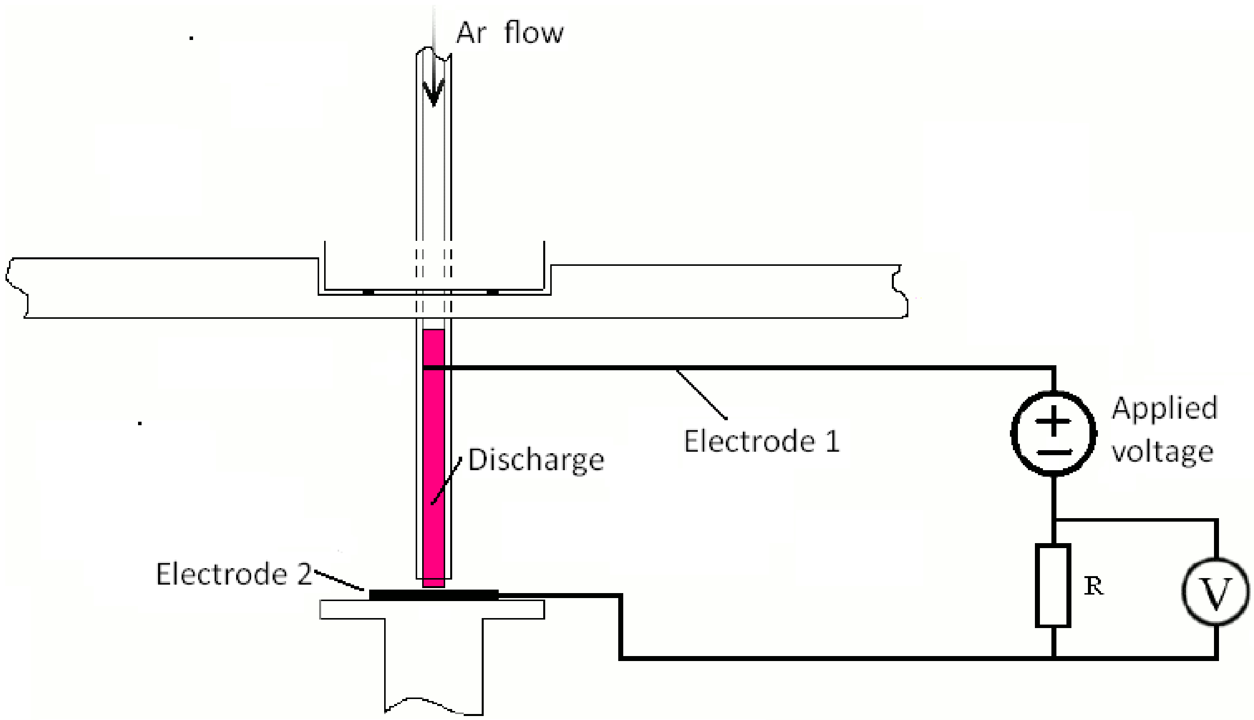

Figure 5.2.2: Schematic of charge particles observation without an aperture.

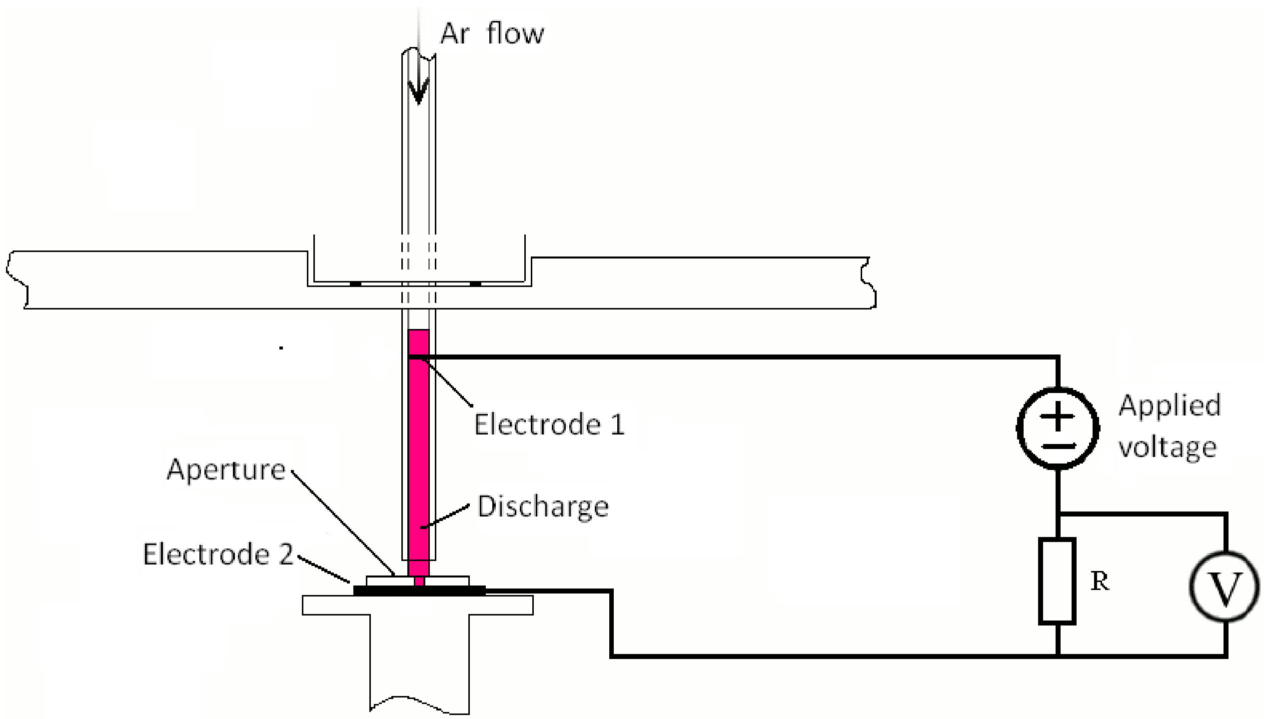

Figure 5.2.3: Schematic of charged particle observation with 450 μm Si aperture.

In both setups 20 sccm of argon gas was used and the discharge tube inner diameter was 2 mm. Pressure was set around 1.5 – 2 Torr and the absorbed microwave power was 34 W (without aperture) and 47 W (with aperture). The distance between the tip of the discharge tube and the substrate holder was around one mm. Electrode 1 is a 100 μm diameter tungsten wire exposed to the plasma column. A small hole was drilled on the discharge tube one centimeter away from the tip to insert the electrode and ceramabond was applied to patch the drilled area. Electrode 2 is the conductive substrate holder. The voltage applied between the two electrodes was varied from -70 to 70 V. The voltage drop across the 277 Ω resistor was monitored to determine the current. The circuit can be considered open unless there are charged particles within the plasma to close the circuit.

The I-V characteristics can be seen in figure 5.2.4 and 5.2.5 for charge particle observation of an open tube and for observation with a aperture, respectively. The I-V characteristics shows that current flows. Therefore, the circuit is closed and a number of charge particles reach the ion collector at the top of the sample holder. The ion current to the electrode is related to the number of charged particles and the collection area of the electrodes. However, the surface area of the tungsten wire (electrode 1) and the area of substrate holder (electrode 2) exposed to the plasma could not be determined. It is possible that for the open tube configuration, ion saturation current is larger at the wire than at the ion collector mostly because the number of charge particles inside the discharge tube is higher as compared to the number of charge particles in the substrate holder region. By adding the aperture, the saturation current at the substrate holder drops because the aperture reduced the effective collection area for the electrode 2.

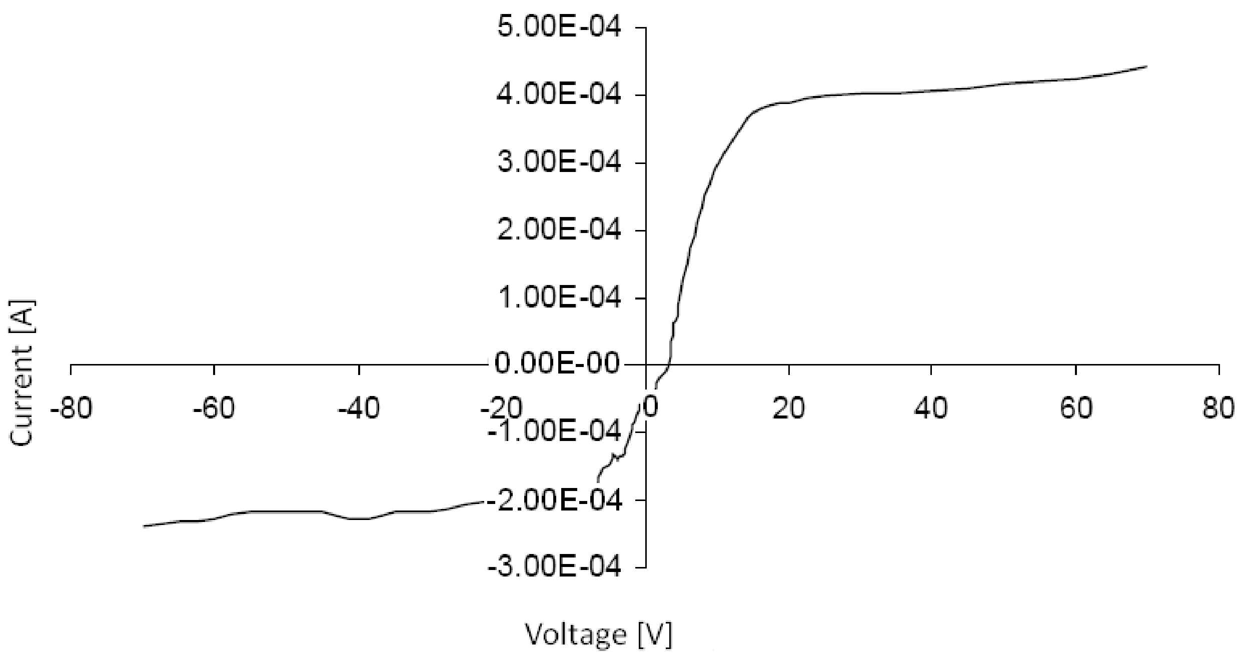

Figure 5.2.4: I-V characteristics of Ar plasma without an aperture.

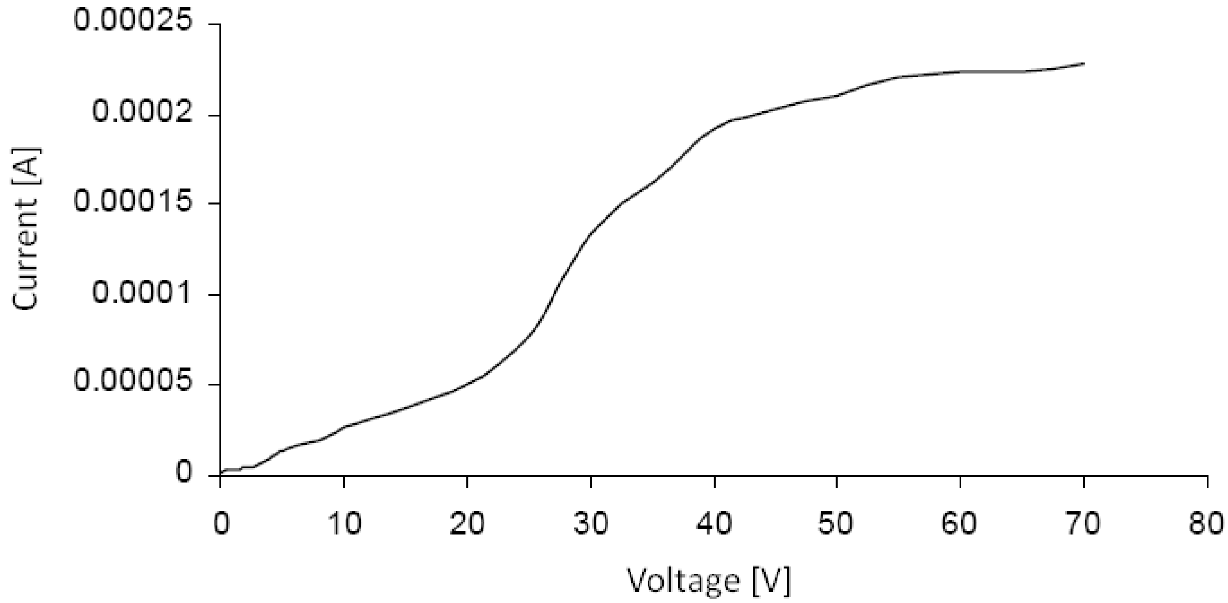

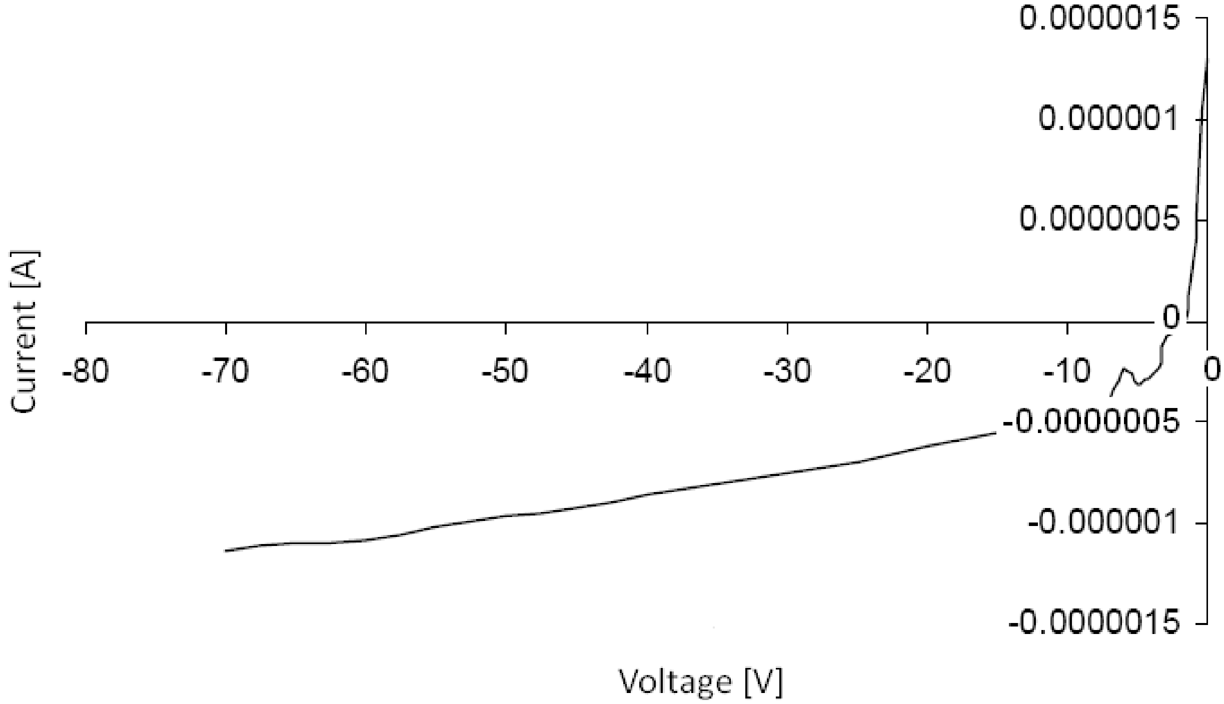

Figure 5.2.5: I-V characteristics of Ar plasma with 450 μm Si aperture.

Another test was conducted with an aperture opening size of approximately 15 μm. However, since the Debye length of the plasma is approximately few tens of μm's, and the sheath thickness of the plasma is several Debye length, as previously discussed in chapter 4, no charge carriers could be measured. In conclusion, the aperture opening must be larger than the plasma sheath so the charge particles can go through the aperture. More detailed plasma density measurements using a double Langmuir probe are presented later in section 5.2.4

5.2.3 Plasma length and power density

Plasma generated using the foreshortened coaxial cavity is confined in the radial direction by the discharge tube. The quartz tube prevents the expansion of the plasma other than along the tube length. The plasma length can be adjusted by varying the input parameters such as the input power, the gas flow rates and compositions, and the operating pressure. The length of the plasma can be defined by measuring the distance between the gap end of the foreshortened coaxial cavity applicator and the tip of the plasma column. The edge of the visible light emitted by the plasma is considered to be the plasma boundary.

The analysis of the plasma length was done for pure argon and a mixture of argon/oxygen feed gases. All of the experiments were performed using a 2 mm i.d. discharge tube. The experimental results are shown in figure 5.2.6 – 5.2.8.

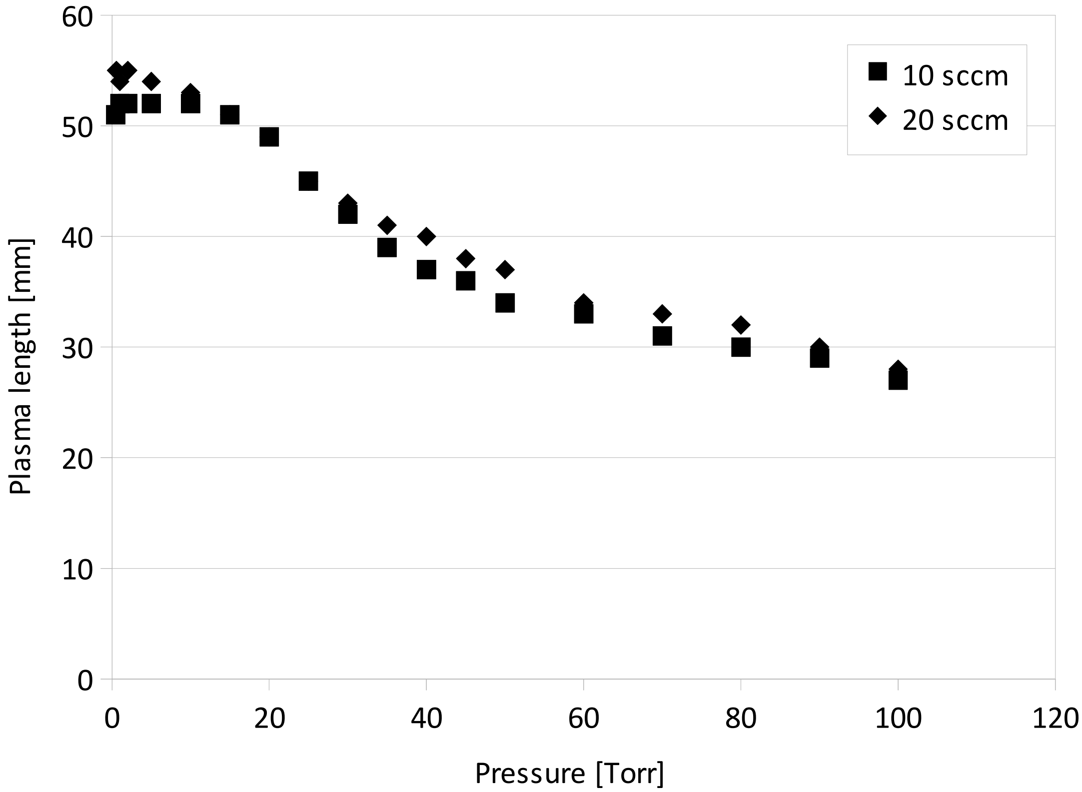

Figure 5.2.6: Variation of plasma length versus pressure for 10 and 20 sccm of pure argon feed gas. P_{abs} = 3 – 3.5 W.

From the results of the plasma length measurements shown in figure 5.2.6, it can be seen that increasing the operating pressure will shorten the plasma column. As pressure increases, the number of neutral species increases hence the collision rate between heavy particles increases as well. Increasing the pressure can also increase the volume recombination thus in order to generate a long plasma column, the operating pressure is maintained between 0.1 – 10 Torr. The effect of flow rate in plasma generation is shown in figure 5.2.6. There is no significant change in plasma length between using 10 or 20 sccm of total flow rate for pure argon plasma especially at high pressures. A careful examination at pressures lower than 5 Torr shows than using 10 sccm of argon generates a slightly shorter plasma column. The experimental system used epoxy and heat shrink as the adhesive between the discharge tube and the gas line thus the system is not entirely leak proofed. When the supply of argon species is significantly higher than the vacuum leak rate of the system, the vacuum leak can be neglected. However, when the flow rate of argon is too small, such as 3 sccm or lower, it can be observed that the color of the plasma is different. Argon rich plasma gives a purplish color while argon lean plasma gives a reddish color similar to an air plasma. From this result, all of the experiments using the micromachining system are performed using a total flow rate of 10 sccm or higher.

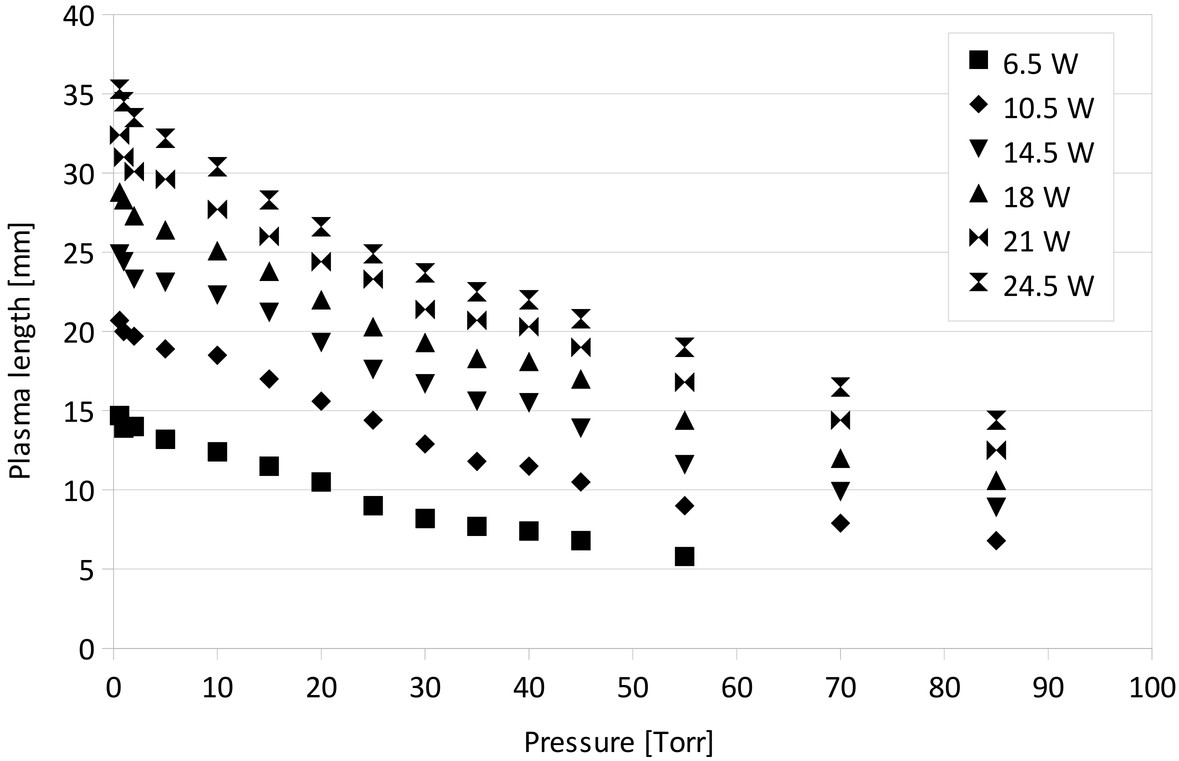

Figure 5.2.7: Variation of plasma length versus pressure for Ar/O_2 discharge. Total flow rate: 20 sccm, 98% argon, 2% oxygen. P_{abs}: 6.5 – 24.5 W.

Figure 5.2.7 shows the plasma length for an Ar/O_2 plasma at different operating pressures and absorbed powers. Increasing the power makes the plasma column longer. Ar/O_2 plasma with 98% argon and 2% oxygen can be generated with as low as 6.5 W of absorbed power.

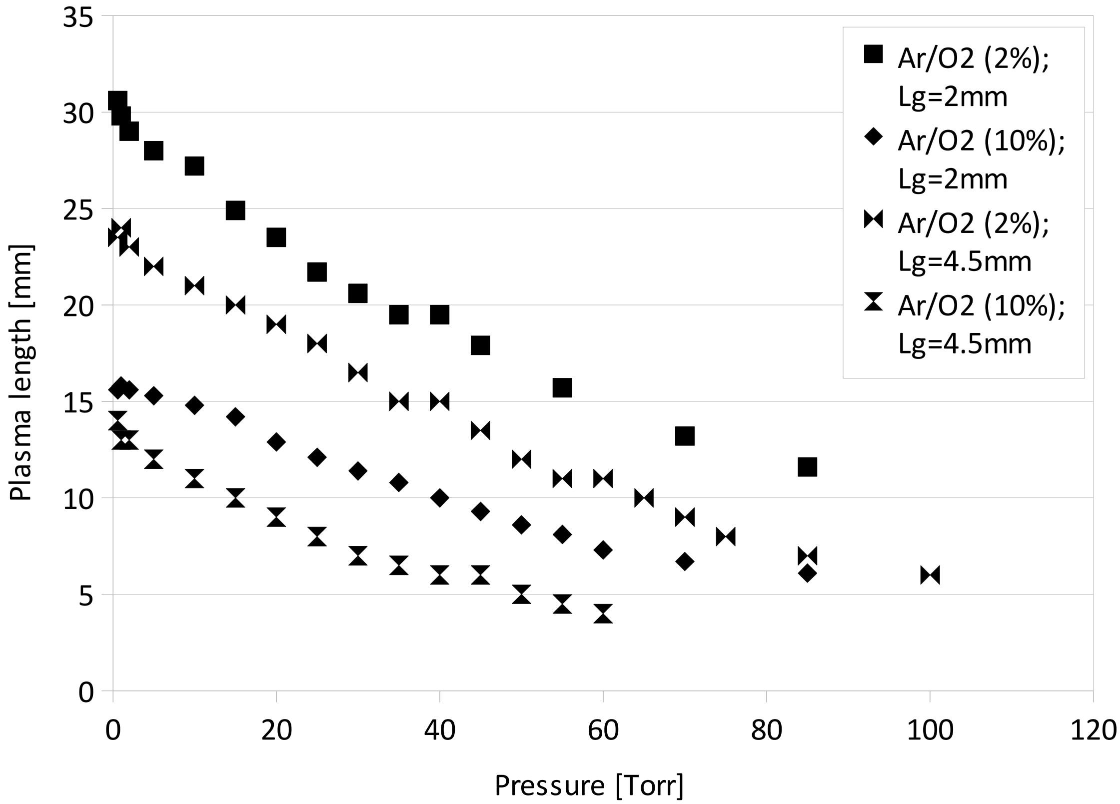

Figure 5.2.8: Variation of plasma length versus pressure for Ar/O_2 discharges with different mix ratio and cavity gap length. P_{abs}: 15 – 18 W.

The ratio of oxygen (2 – 10%) in an argon/oxygen feed gas mixture has an effect on the plasma length as seen in figure 5.2.8. A higher percentage of oxygen will reduce the plasma length. An addition of a molecular gas creates a number of additional reactions in a plasma such as two-body and three-body reactions. These reaction processes absorb the microwave energy thus the volume of the plasma is lower than a pure inert gas plasma. Figure 5.2.8 also shows a different result between setting the applicator gap length to 2 mm or 4.5 mm. Setting the gap length at 2 mm provides an adequate opening of the foreshortened coaxial cavity to make the microwave energy coupled into the plasma. However, when the gap is widened, the amount of microwave power losses to radiation is larger and the plasma length is shorter.

Power density in watts per cubic centimeter [W/cm^3] was determined by taking the ratio of the absorbed microwave power and the plasma volume. The absorbed power is the difference between the incident power that goes into the cavity and the reflected power coming out from the cavity. The incident and reflected power are measured using power meters and every component of the microwave network was calibrated to account for non plasma losses. All of the absorbed power as measured at the microwave input of the cavity is assumed to be coupled into the plasma. The radiation and wall losses inside the cavity are assumed to be negligible.

Assuming the sheath thickness is very thin compared to the overall size of the plasma, the plasma volume can be approximated using the cross sectional area of the discharge tube, that is multiplied by the overall length of the plasma column. Since part of the discharge tube is located inside the hollow inner conductor of the foreshortened coaxial cavity, the length of the SWP in this part is unknown. However, it can be assumed that SWP formed is equal length on the upstream and downstream of the discharge tube [130]. Thus the overall length of the plasma column is twice the length of the plasma, as described in plasma length measurement previously, plus the length of the gap (L_g).

The analysis of power density was done for pure argon plasma and a mixture of argon/oxygen plasma. Parameters that were varied include the gap length, the absorbed power, the operating pressure, and the gas flow rate. All of the experiments were performed using a 2 mm i.d. discharge tube. The experiment results are shown in figures 5.2.9 – 5.2.11.

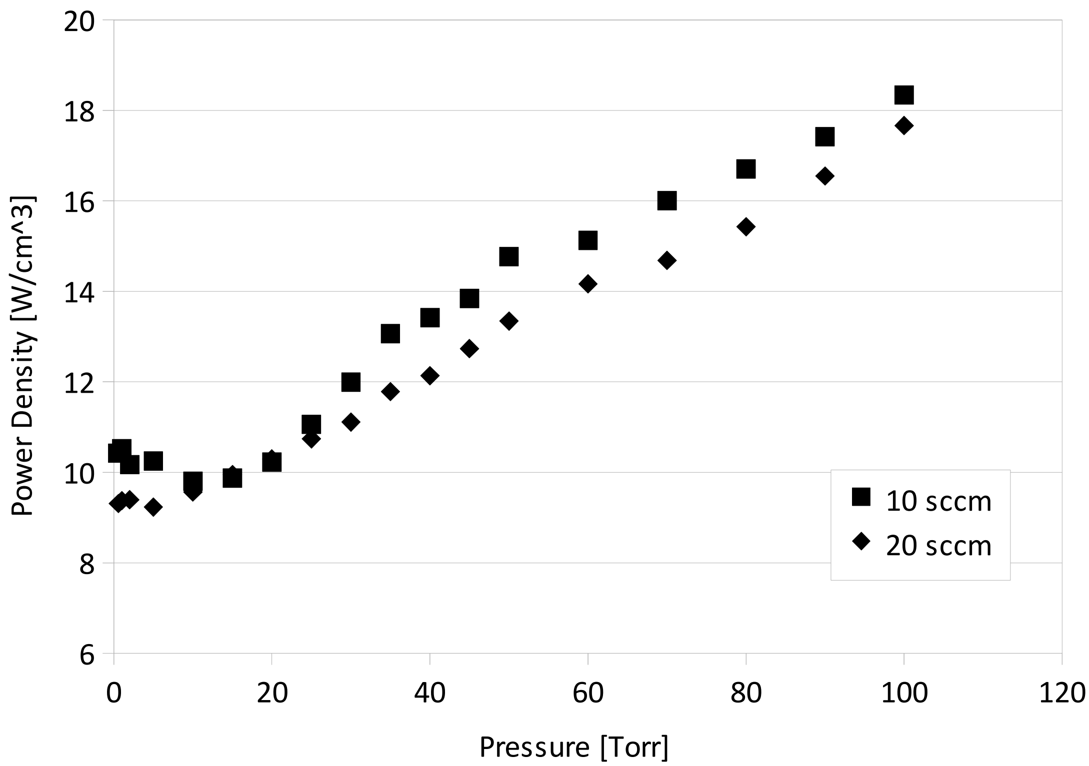

Figure 5.2.9: Variation of discharge power densities at different pressures. Feed gas: pure argon at 10 and 20 sccm, P_{abs}: 3 – 3.5 W.

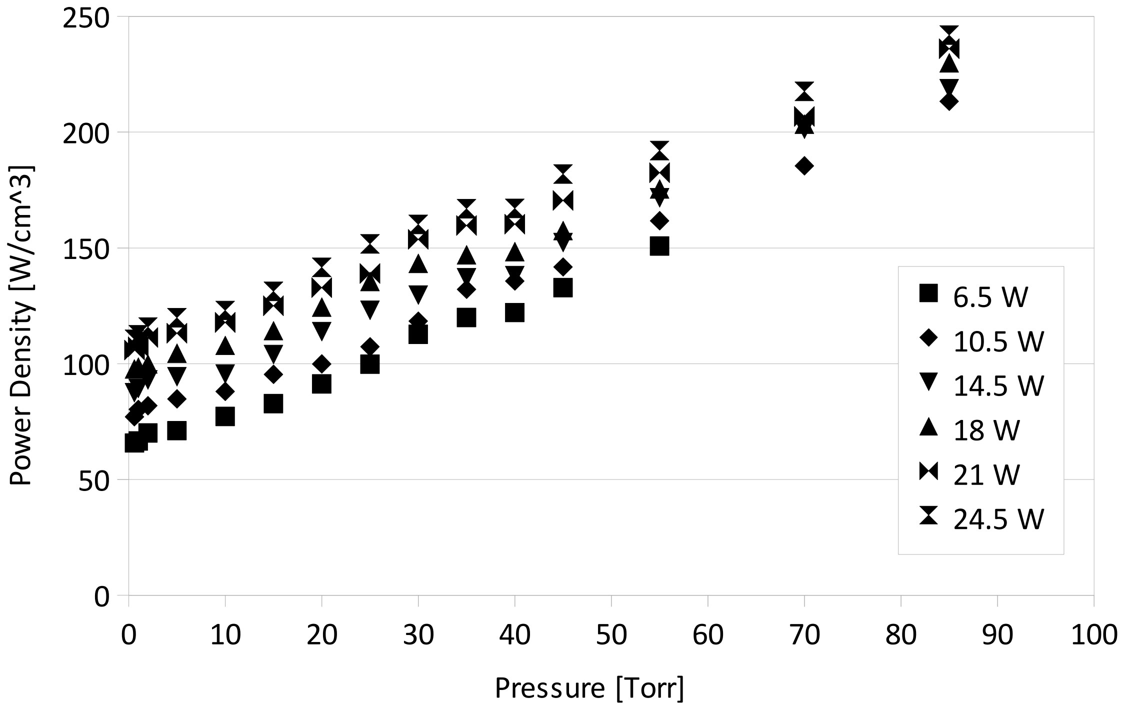

Figure 5.2.10: Variation of discharge power densities at different pressures for Ar/O_2 plasmas. Total flow rate: 20 sccm, 98% argon, 2% oxygen. P_{abs}: 6.5 – 24.5 W.

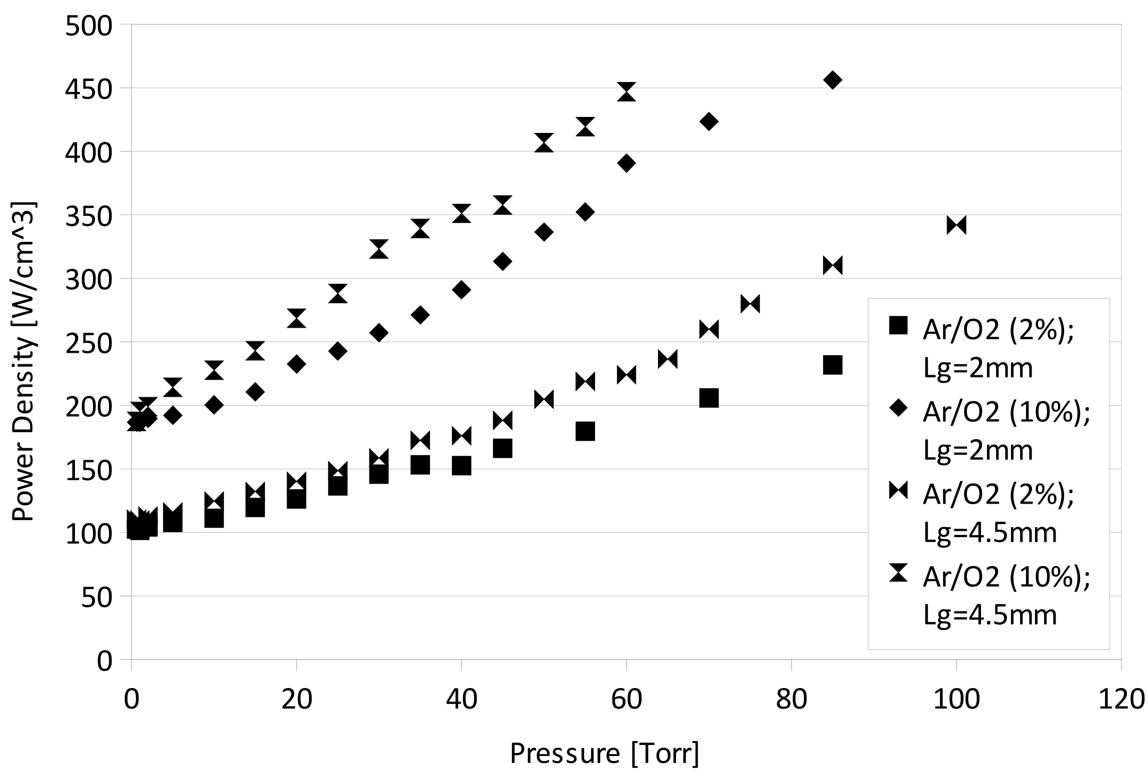

Figure 5.2.11: Variation of discharge power densities at different pressures for Ar/O_2 discharges with different mix ratio and cavity gap length. P_{abs}: 15 – 18 W.

Pure argon plasmas in the pressure range of 0.5 – 100 Torr have power densities between 9 – 18 W/cm^3 as shown in figure 5.2.9. Addition of oxygen concentration in a mixture of argon/oxygen feed gas, increases the power density. As shown in figure 5.2.10 and 5.2.11 adding 2% of oxygen increases the power density by an order of magnitude compared to the power density of pure argon plasma. In general, the power density increases as both the absorbed power and pressure increase. The argon power density measurement results are in a good agreement with a previous study by Rogers and Asmussen [130].

5.2.4 Plasma density

Langmuir probe measurements are one of the common methods to characterize a discharge. In this work, the plasma is confined in a cylindrical dielectric tube, where there is no well-defined electrical ground in the plasma, hence the Double Langmuir probe (DLP) method is used. DLP measurements were performed to determine the charge densities and electron temperatures of the argon plasmas in the micromachining system.

In DLP measurements two identical probes are inserted in the plasma. A bias voltage is then applied between the two probes and the current passing through the probe circuit is measured. From this measurement, the current – voltage (I-V) curve can be determined. Current is limited by the ion saturation current at the extreme voltage biases. In this region, ion density can be derived using the following:

$$I_{sat} = e n_s \boldsymbol{u_B} A_{eff} \tag{5.2.1}$$

Where I_{sat} is the ion saturation current, e is the elementary charge, n_s is the sheath density, $\boldsymbol{u_B}$ is the Bohm velocity, and A_{eff} is effective collection area of the probe. For argon plasmas, the sheath density is approximately 0.61 of the charge density (n_i) in the plasma. The Bohm velocity is defined as:

$$\boldsymbol{u_B} = \left(\frac{eT_e}{M}\right)^{1/2} \tag{5.2.2}$$

where T_e is the electron temperature and M is the ion mass. The equation is valid for collisionless plasmas, where the ion mean free path is longer than the discharge sheath thickness. The mean free path of ions in an argon discharge can be estimated using [78]:

$$\lambda_i = \frac{1}{330\,p} \quad cm \tag{5.2.3}$$

where p is the pressure in Torr and ion is assumed to have a low energy (T_i ~ 0.05 eV).

Assumptions regarding the electron gas characteristics are needed to simplify the equation. In this case the assumptions are that the electron distribution is Maxwellian and the electron temperature is around 2 eV. The effective collection area is essentially the surface area of the probe which is exposed to the plasma assuming that the sheath thickness of the discharge is much smaller than the probe diameter and length.

The schematic of the probe is shown in figure 5.2.12. The probe is made out of Tungsten wire with a diameter of 100 μm. Only 2.5 mm of wire is exposed to the plasma. Fused silica tubes with 220 μm ID are used as the insulating jackets. These probes are connected to a bias voltage that automatically increases the voltage from -50 to 50 Volt. The current that passes through this circuit is measured using a digital multimeter connected to a computer. The data is plotted and plasma density and electron temperature are calculated using Microsoft Excel.

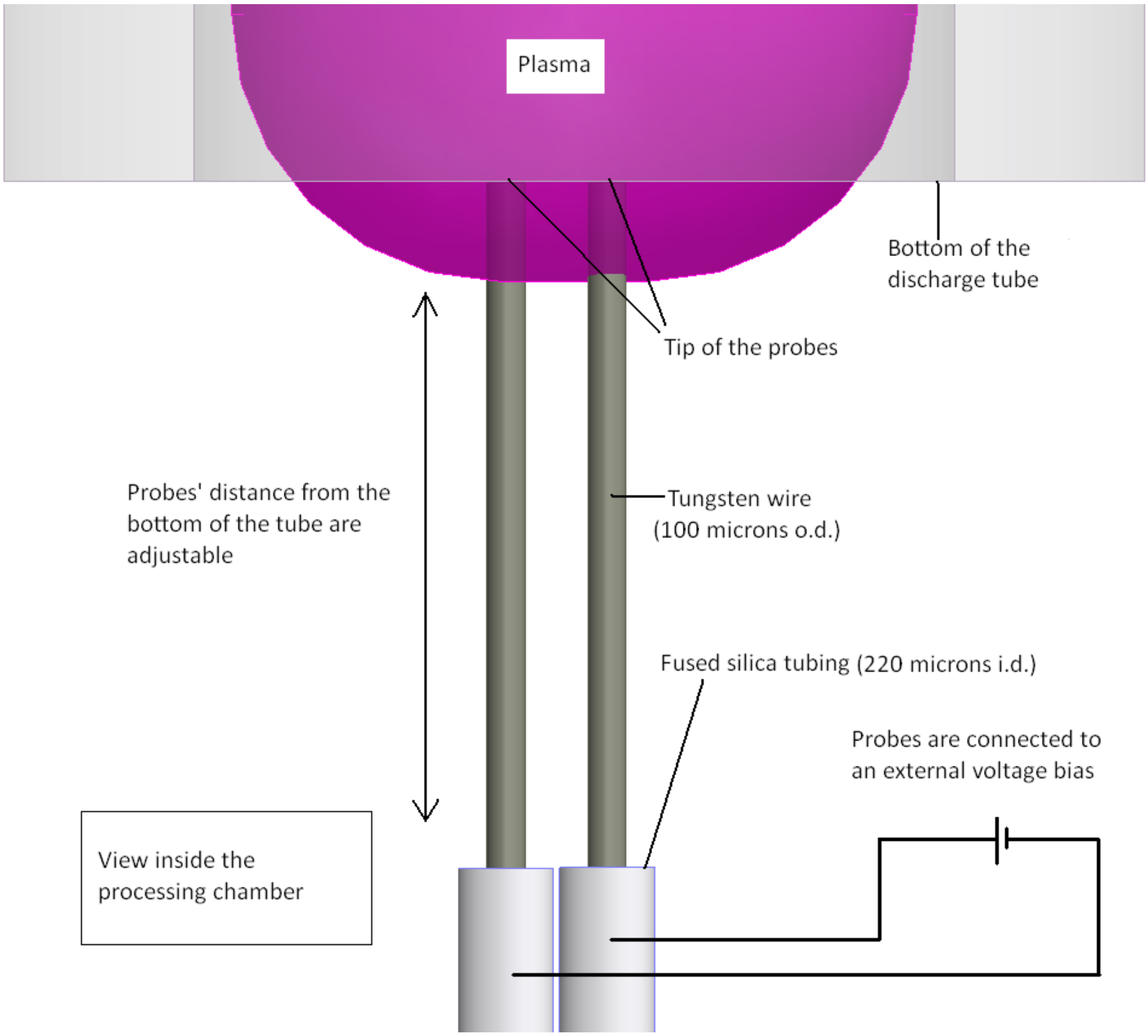

Figure 5.2.12: Illustration of the DLP measurement. Setup for experiment #2, where the tip of the probes are at the bottom of the discharge tube, is illustrated.

The I-V characteristic of a double Langmuir probe is governed by the following equation [78]:

$$\frac{I+I_1}{I_2-1}=\frac{A_1}{A_2}\exp\left(\frac{V}{T_e}\right); \quad V=V_1-V_2 \tag{5.2.4}$$

where I_1 and I_2 are the ion currents to probe 1 and 2 respectively, A_1 and A_2 are the collection areas, V_1 and V_2 are the probe potentials with respect to the plasma potential, V is the applied external potential and T_e is the electron temperature. Re-arranging equation (5.2.4) into the following form:

$$\ln\left(\frac{I+I_1/I_2-I}{A_1/A_2}\right)=\frac{V}{T_e} \tag{5.2.5}$$

it can be seen that the electron temperature can be obtain from the inverse slope of the ln(C/A) plot versus V, where

$$C=\frac{I+I_1}{I_2-I};\quad A=\frac{A_1}{A_2} \tag{5.2.6}$$

This DLP measurement characterized an argon plasma with the incident power set to 6 W, and the measured reflected power was 300 mW. The chamber pressure was set to 0.9 Torr and the argon flow rate was 20 sccm. This particular condition was chosen in order to meet the assumptions made in the previous section. Pressure was set such that the sheath is assumed to be collisionless. With the above mentioned incident power, the surface wave inside the tube has enough energy so that the tip of the plasma is extending outside the discharge tube into the processing chamber. A higher incident power will create a discharge outside the tube on the top of the processing chamber. The probes are placed on a translational stage thus the probe's height relative to the tip of the discharge tube can be varied. Four experiments were performed to measured the charge density spatially, as indicated in table 5.2.1.

A typical I-V characteristic obtained from the DLP measurements is shown in figure 5.2.13.

The charge density information can be derived from the ion saturation regions, which is governed by equation (5.2.1). In this experiment, it is assumed that all terms are equal except the charge densities. Thus, ion saturation current is proportional to the charge density. Outside the discharge tube, ions and electrons exist but their densities are low. The charge density increases as the probes penetrates into the plasma column. As seen in figure 5.2.13, the I-V curve has ion saturation current regions. The semilog plot is shown in figure 5.2.14. Based on this plot, using equation (5.2.6) electron temperature of the argon plasma can be determined. Measurement results shows that the electron temperature ranges from 1.26 – 2.62 eV. The complete results are presented in table 5.2.1.

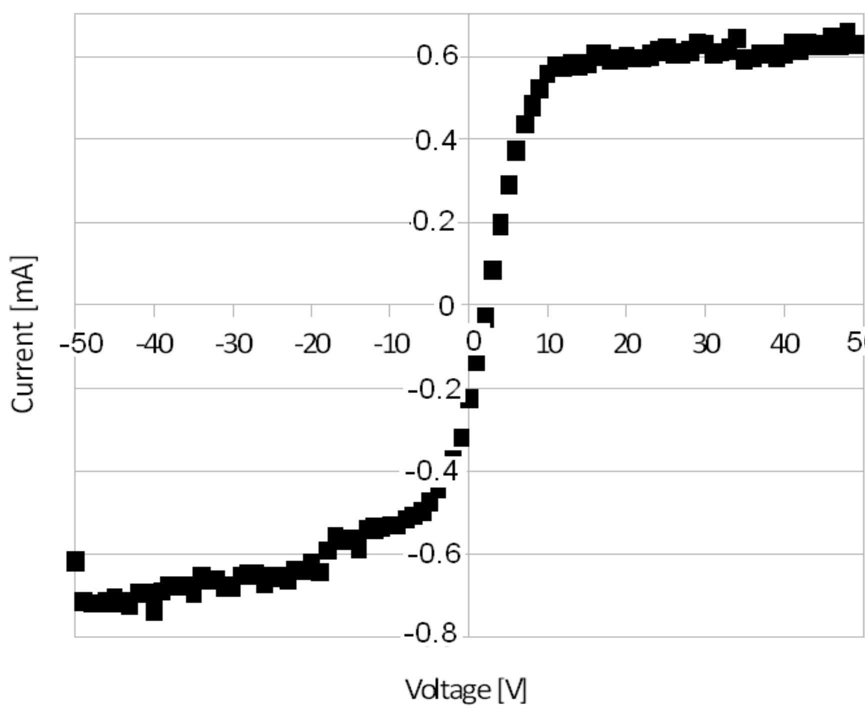

Figure 5.2.13: Typical I-V characteristics of the argon plasmas measured using DLP. Data are taken from measurement location #4 where the tip of the probes is 5 mm inside the tube.

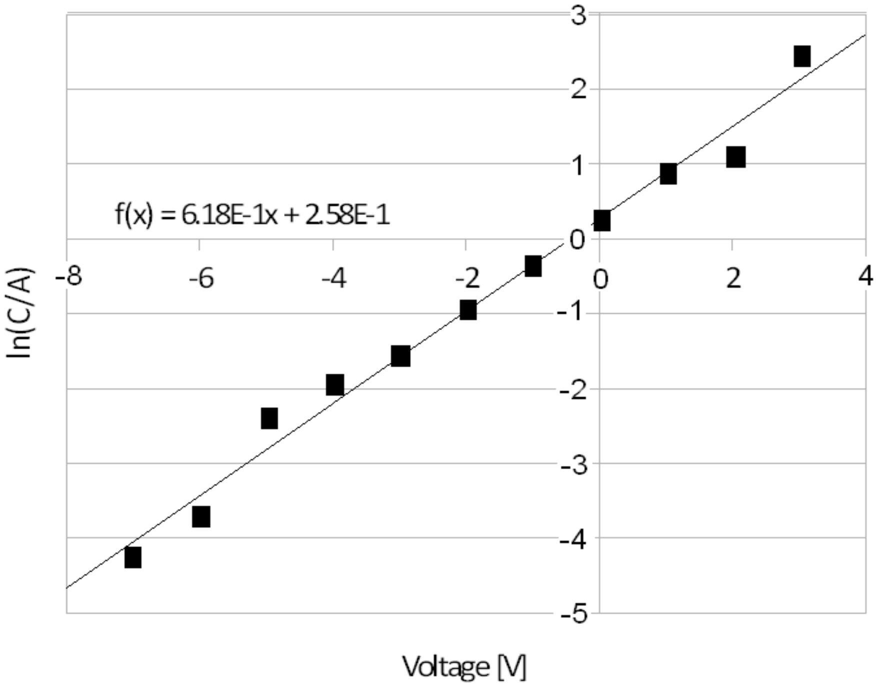

Figure 5.2.14: Log plot derived from the I-V characteristics of DLP diagnostic. $C = I+I_1/I_2-I$. $A=A_1/A_2$. Data taken from measurement #3 where the tip of the probes is 2.5 mm inside the discharge tube.

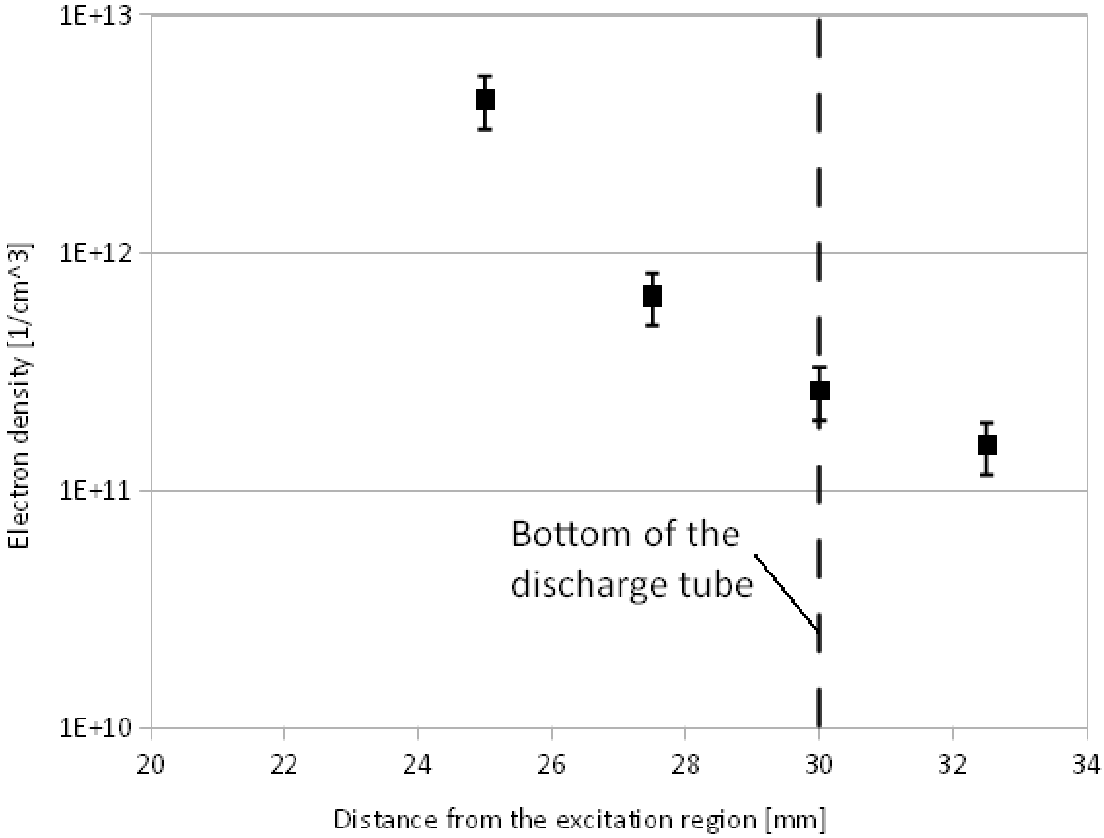

Figure 5.2.15: Axial profile of the charge density of the argon plasma. The dashed line represents the tip of the discharge tube.

Table 5.2.1: Measurement results of the double Langmuir probe diagnostics.

Probe tip location	T_e (eV)	n_e (cm^{-3})
5 mm inside the tube	1.28	$4.41 x 10^{12}$
2.5 mm inside the tube	1.62	$6.55 x 10^{11}$
At the tip of the tube	1.61	$2.63 x 10^{11}$
2.5 mm under the tip of the tube	2.62	$1.54 x 10^{11}$

Figure 5.2.15 shows the axial profile of the charge density of the plasma column. The area of the discharge tube which is located at the gap of the foreshortened coaxial cavity is denoted as the point of origin in the plot. It is shown that charge density decreases along the axis away from the microwave coupling. Near the tip of the discharge tube, charge density is measured to be in the range between 1×10^{11} – 1×10^{12} cm^{-3}. The charge density results indicate that the closer the surface to be processed is to the tip of the discharge, the faster will be the processing rate. The DLP measurement results are comparable with the argon plasma computational model simulated in 1-D and in good agreement with previous studies by Asmussen et al. [54] [55][57].

5.3 Ion source results

One of the research goals is to design an ion source based on the miniature microwave induced plasmas (mMIP's) system. Proof of concept work has been undertaken by performing localized etching of a silicon substrate and polycrystalline diamond film using Ar/SF_6 and Ar/O_2 plasmas, respectively.

5.3.1 Silicon etching

For the localized silicon etching experiments, a mixture of argon and SF_6 feed gases with flow rates of 35 sccm and 0.5 sccm, respectively, was used. The operating pressure was 1 Torr and the absorbed power was 5 W. The silicon wafer was kept at a fixed position so that the etching formed a hole on the silicon surface. Three sets of experiments were conducted. The first one was performed without any aperture thus the plasma size in contact to the substrate is similar to the cross sectional area of the discharge tube. The second one was performed with a

100 μm inner diameter (i.d) aperture. The aperture was made of Pyrex glass with 100 μm thickness. The third one was done with the silicon substrate moved creating a patterned etching. It will be explained in more detail later in this section.

Figure 5.3.1 shows the surface profile of the locally etched silicon wafer. This profile was taken using a Dektak profilometer. The duration of the etching was set to ten minutes and the deepest point of the etched profile was approximately 21 μm below the surface. The etching rate of silicon in this operating condition was roughly 2.1 μm/min. Figure 5.3.2 shows the surface profile of the second experiment that used an aperture with a 100 μm diameter hole. The duration of the etching process was only three minutes and the etched feature was approximately 0.6 μm deep. The etching rate of silicon using an aperture was approximately 0.2 μm/min. By comparing both results, it can be concluded that the addition of the aperture significantly drops the etch rate by approximately an order of magnitude. In both cases, it was noted that the plasma also damaged the inner surface of the discharge tube. The surface of the Pyrex aperture was etched as well.

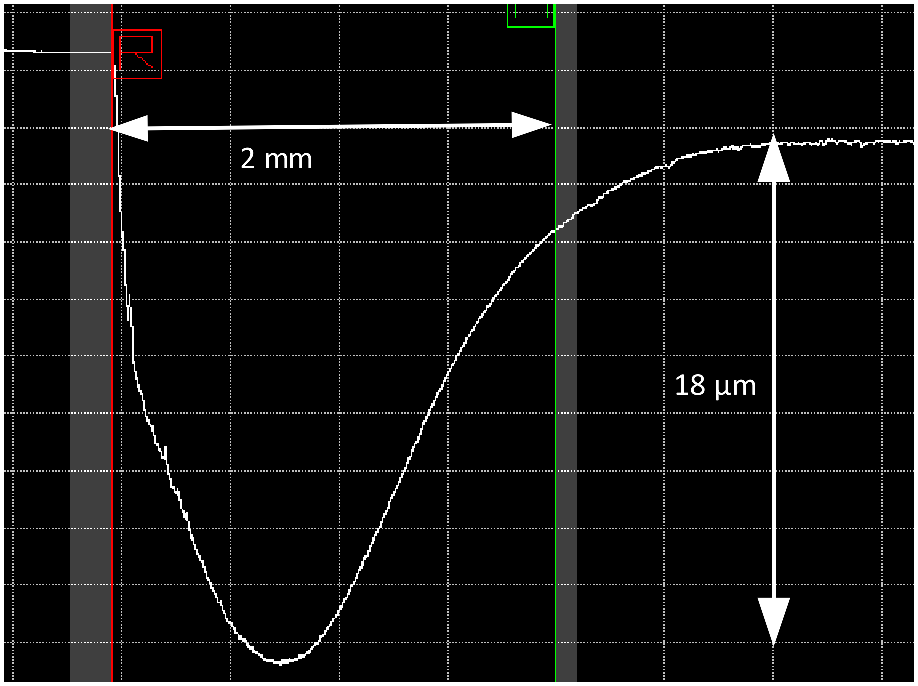

Figure 5.3.1: Surface profile of a silicon substrate after exposure to an Ar/SF_6 microplasma.

Figure 5.3.2: Surface profile of silicon after exposure to an Ar/SF_6 plasma through a 100 µm aperture.

The third experiment for silicon etching was done with the silicon substrate moved forming a square pattern. The movement was controlled by the XYZ motion stage which was connected to the substrate holder. To protect the surface of the silicon wafer from hitting the aperture when the substrate holder was moving, the distance between the bottom of the aperture and the top of the silicon wafer was kept around 500 μm. The input power was 16 W and the operating pressure was 1.35 Torr. The flow rates of the argon and SF_6 were 15 and 1.5 sccm, respectively. A 100 μm diameter Pyrex aperture were used and a voltage bias was applied between the aperture and the substrate holder. The voltage bias operated at a frequency of 4 MHz and with a 20 volt peak-to-peak voltage. The XYZ controller was given the input to stay at a fixed position for three minutes and then move to the x direction (left in figure 5.3.3) for three mm followed by moving in the y direction (up in figure 5.3.3) for three mm. And then, it was moved again in the -x direction (right) and followed by movement in the -y direction (down) forming a square perimeter of 3x3 mm. The speed was varied for each direction in the range from 100 to 500 μm/s. A result of this experiment is shown as figure 5.3.3.

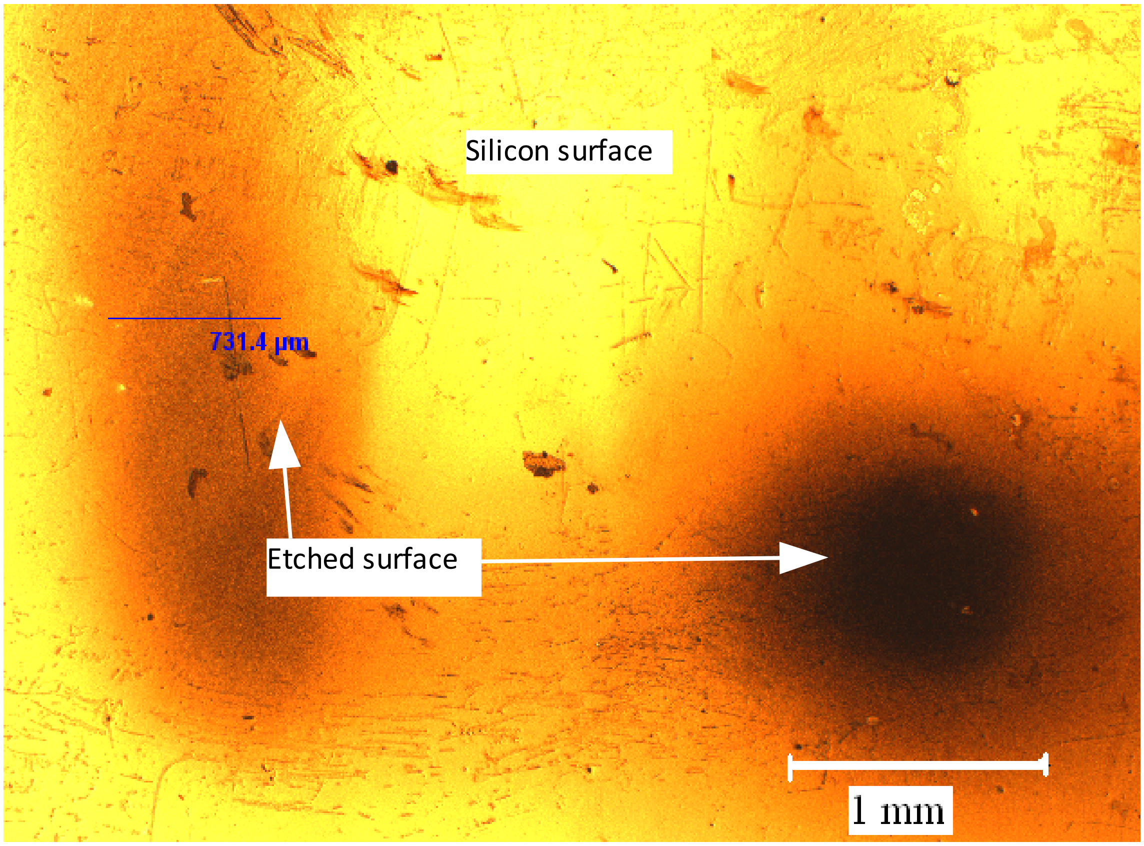

Figure 5.3.3: Optical image of localized Si etching using Ar/SF_6 microplasma.

In conclusion, etching of the silicon can be performed using an Ar/SF_6 plasma generated in the micromachining system. A high concentration of argon relative to SF_6 was needed to create a long plasma column that could reach the silicon surface and to sustain the plasma. A bias voltage was needed to accelerate the ions to the silicon surface and to reduce the quartz tube from being etched by the ion. Using a bias voltage, the Ar/SF_6 plasma can be sustained for a period longer than 15 minutes. Since the sample is around 500 μm away from the aperture, the plasma beam coming out of the aperture expands significantly due to diffusion. Thus, the etched pattern on the silicon surface has a footprint of one mm instead of 100 μm.

5.3.2 Polycrystalline diamond etching

Local area etching was also performed for ultra-nano-crystalline diamond (UNCD). The UNCD was grown on a silicon wafer using a plasma enhanced chemical vapor deposition (PECVD) process. The thickness of the UNCD layer was around 5 μm. Before every UNCD etching procedure, the substrate was cleaned inside an ultrasonic bath. The cleaning steps involve dipping the substrate in acetone for 5 min, then dipping it in methanol for another five minutes and finishing the cleaning by dipping the substrate in de-ionized water for five minutes. This sample was exposed to a mixture of argon and oxygen plasma with flow rates of 20 sccm and 10 sccm, respectively. The microwave absorbed power was 20 W and the pressure was 1.75 Torr. The substrate was kept at a fixed position from the discharge tip and the etching process was performed without using any aperture. A RF bias was applied between the substrate holder and 100 μm diameter tungsten wires, as shown in figure 3.7.9. The RF bias operate at 4 MHz with a 20 volt peak-to-peak voltage.

After 2 hours of exposure, regions of the 5 μm thick UNCD layer were totally removed leaving a clean silicon surface as shown in figure 5.3.4. Artifacts of the tungsten wires for the RF bias can be seen in the processed area. The wire placement hindered the creation of a well rounded spot. The etched region was scanned by a commercialized AFM (Dimension 3100, Veeco Inc.) to demonstrate the working process of the system. Figure 5.3.5 shows the AFM 3-D topographic image scanned in the region. It can be seen that the left part of the scanning area was smooth and had only a few diamond particles left. This result shows that the microplasma was able to effectively remove the nanocrystalline diamond coating from silicon.

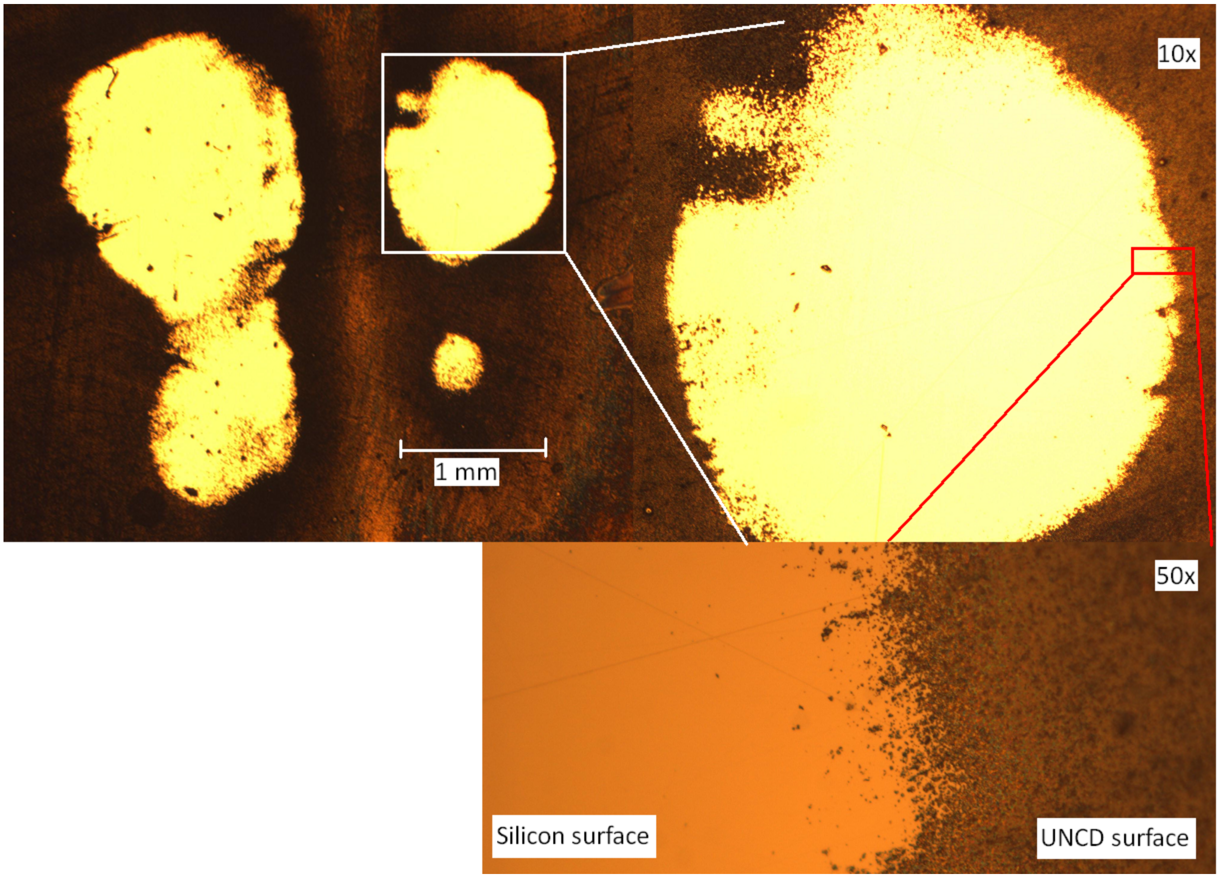

Figure 5.3.4: Optical image of silicon surface exposed after UNCD etching using an Ar/O_2 plasma.

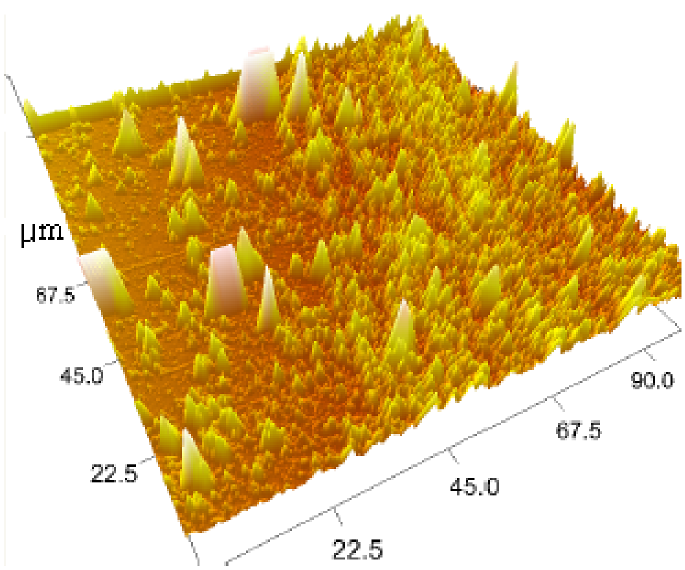

Figure 5.3.5: AFM image of traces of UNCD at the boundary of the processed area.

Total removal of UNCD layer by Ar/O_2 plasma showed that the micromachining system is capable of producing oxygen species for diamond etching. However, the etching rate is unknown and the tungsten wire blocked the ion path from the plasma to the surface. To avoid any artifacts on the processed area due to the tungsten wire, the RF bias design was modified so that the bias voltage is applied to the edge of the plasma tip inside the processing chamber and the substrate holder as shown in figure 3.7.8. An experiment was performed to etch UNCD on the Si wafer. The thickness of the UNCD layer is around 5 - 10 μm. This sample was exposed to a mixture of argon and oxygen plasma for 40 minutes with flow rates of 17 sccm and 3 sccm, respectively. The microwave absorbed power was 20 W and the pressure was 1.18 Torr. The substrate was kept at a fixed position and the etching process was performed without using any aperture. The RF bias operates at 4 MHz with 20 peak-to-peak voltage. The result of the experiment is presented in figure 5.3.6.

The UNCD surface was etched for a shorter time and with a lower percentage of oxygen in order to observe the etching rate. As seen in figure 5.3.6, the treated surface profile is a circle with a diameter of two mm, which corresponds to the discharge tube diameter. However on the outer edge of the treated surface, fringes are seen. This fringe formation is commonly known as the Newton's ring and it occurs when light is traveling through a thin film. The fringes are the result of the interference of two light paths, one is partial reflection off the top surface and the other is reflection from the flat surface below at the UNCD-silicon interface.

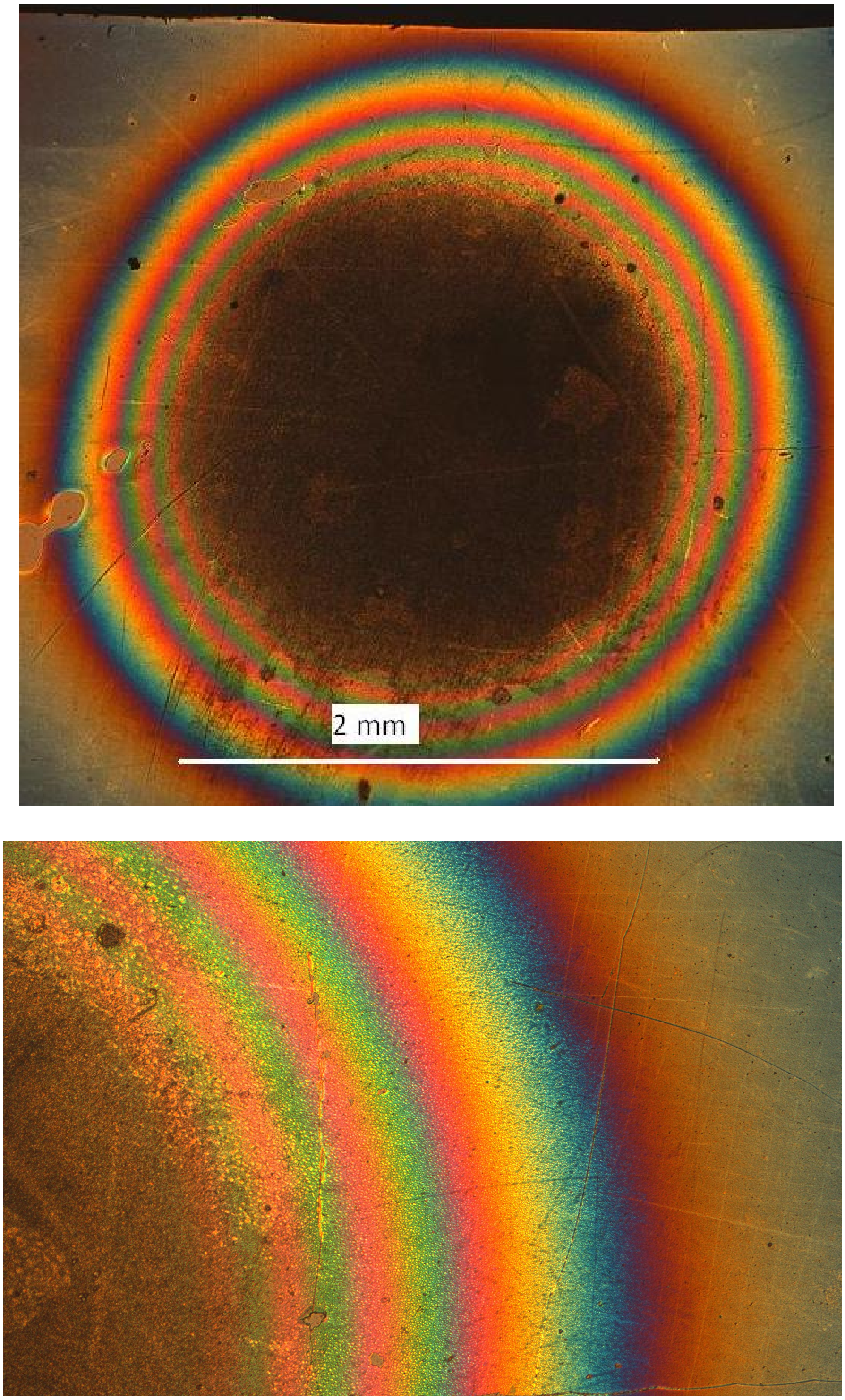

Figure 5.3.6: Image of UNCD surface etched using the micromachining system with an Ar/O_2 plasma (Top) and 10x magnification of the fringes area (bottom).

The variation in the film thickness can be approximated by counting the number of fringes of the same color. The relative vertical depth between the consecutive fringes of the same color is about 130 nm for diamond. Counting the red fringes of figure 5.3.6(b), the depth of the etched surface relative to the smooth surface of the UNCD is approximately 650 nm. Thus the etching rate is about 1 μm/hr. A more precise fringe measurement can be performed using a monochromatic light source [131].

Another set of experiments were performed to observe the impact of the aperture and RF bias on UNCD etching. A UNCD film was deposited on a silicon wafer using a PECVD system with the growth rate of 0.372 μm/hr for eight hours. The silicon wafer was cut into smaller pieces to fit the size of the micromachining system substrate holder. The initial image before the etching treatment can be seen in figure 5.3.7. The UNCD layer was not uniformly grown resulting in the occurrence of fringes on the surface. These fringes have a radial pattern and the distance between the fringes is smaller at the outer edge compared to the center of the wafer. This means that the UNCD surface is relatively uniform in thickness at the center but it changes the thickness at the edge.

The experimental setup used an absorbed power of 25 W, a chamber pressure of 0.78 Torr, and an argon and oxygen flow rate of 20 and 3 sccm, respectively. The aperture used for this experiment was the Melles-Griot pinhole aperture with 25 μm hole diameter. The RF bias setup was similar to figure 3.7.8. The aperture was installed on the floating electrode so it blocked most of the plasma coming out of the discharge tube. There were three experiments performed each with a duration of one hour. Experiment #1 (X1) was performed without any RF bias applied to the aperture, X2 with 1 MHz of RF bias, and X3 with 4 MHz of RF bias. X1 was performed on the center of the sample and X2 was performed 3 mm away from X1 toward the edge. X3 was performed near the edge of the sample and is 2.5 mm away from X2. The RF bias was set to have 20 volt peak-to-peak voltage. The result of the experiment is presented in figure 5.3.8.

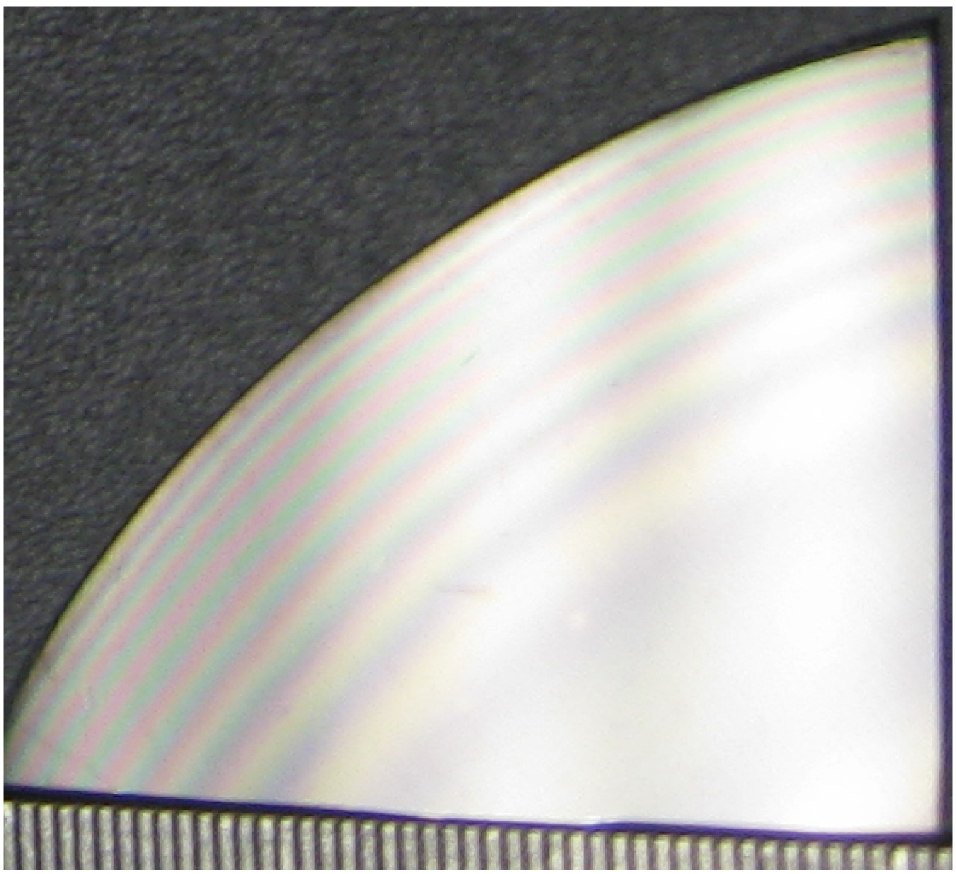

Figure 5.3.7:Image of UNCD on Si sample before the etching procedure. Distance between the ruler scale on the lower part of the image is 500 μm.

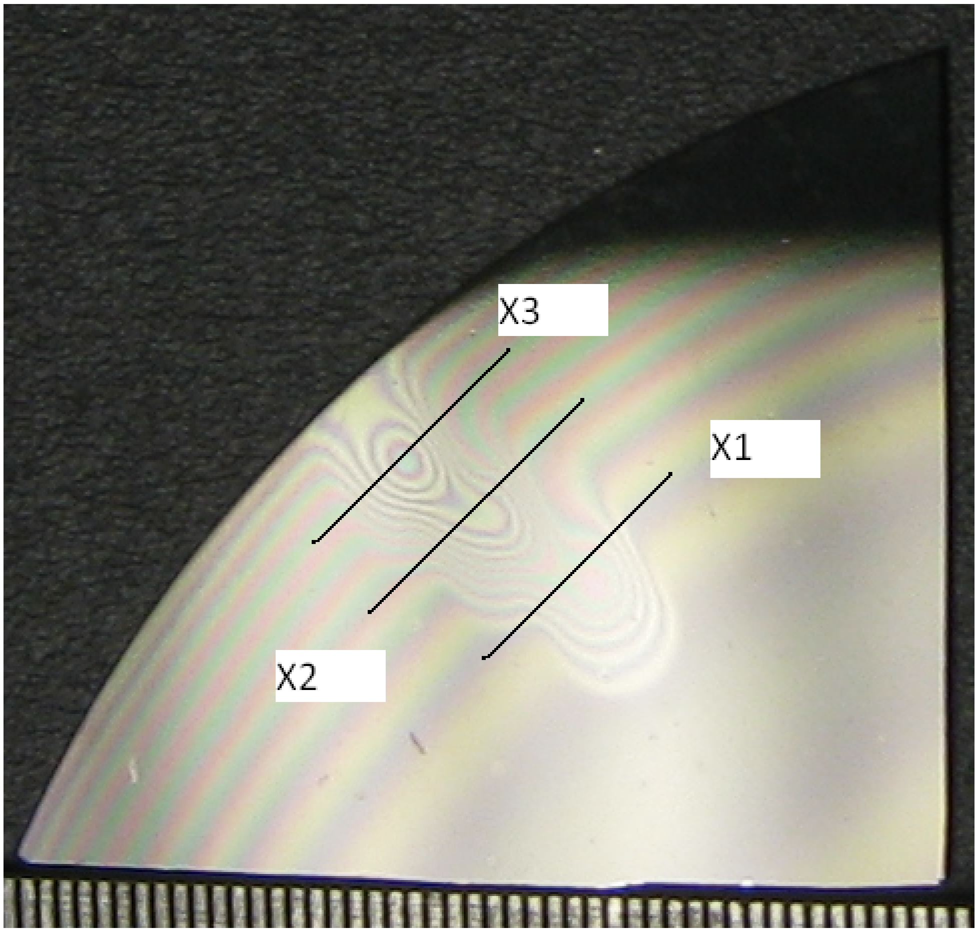

Figure 5.3.8: Image of UNCD on Si sample after the etching procedure. Distance between the ruler scale on the lower part of the image is 500 μm.

As shown in figure 5.3.8, all three etching experiments resulted in modification of the UNCD surface. Because of the non-uniformity of the surface sample before the etching procedure, depth measurement by counting the fringes was difficult to perform. Thus, Dektak profilometer were used as a comparison to the fringe counting technique for measuring the surface profile. The black lines on figure 5.3.8 correspond to the path taken by the stylus of the profilometer. Comparison between fringe measurement results and Dektak measurement results are presented in table 5.3.1.

Table 5.3.1: Measurement results of UNCD etching performed by micromachining system.

Experiment	Diameter (mm)		Depth (μm)		Etch Rate (μm/hr)	
	Fringe	Dektak	Fringe	Dektak	Fringe	Dektak
X1 (no RF bias)	1.75	1.6	0.52	0.6	0.5	0.6
X2 (1 MHz)	2	2.7	0.91	1.9	0.91	1.9
X3 (4 MHz)	2	2.5	0.78	1.7	0.78	1.7

The measurement result of X1 is comparable when comparing the fringes counting technique and the Dektak profilometer. However, when the original sample surface is not uniform, as in the case of X2 and X3, counting the fringes can create a larger margin of error. Based on the trend of the results from both measurement techniques, applying RF bias increases the etch rate. However, a RF bias with a frequency of 1 MHz gave a slightly better etching rate as oppose to a 4 MHz RF bias.

The aperture opening diameter is 25 μm in this set of experiments. However, the diameters of the etched UNCD surface were around two mm for all of the experiments. The discrepancy between the aperture opening size and the treated surface happens because during the experiment, the distance between the aperture and the top of the UNCD surface was on the order of a few hundred μm. Similar with the silicon etching experiments, once the plasma went through the aperture opening, it diffuses. Hence the larger the separation distance between the bottom of the aperture and the sample's surface, the larger the footprint of the plasma beam. This problem can be improved by implementing the substrate sensing system as mentioned earlier in section 3.7.3.

5.4 Free radical source results

Another goal of this research is to build a radical source using a microplasma system. One common example of this process is called plasma ashing. Plasma ashing is a removal process of the organic matter by an oxygen plasma. Historically, the first application was for the removal of photoresist in the microelectronics industry. Photoresist is composed of organic compounds, essentially consisting of carbon, hydrogen and oxygen. Exposure to an oxygen plasma eventually removes all the photoresist as the volatiles leave no residues unless there are inorganic contaminants in the photoresist.

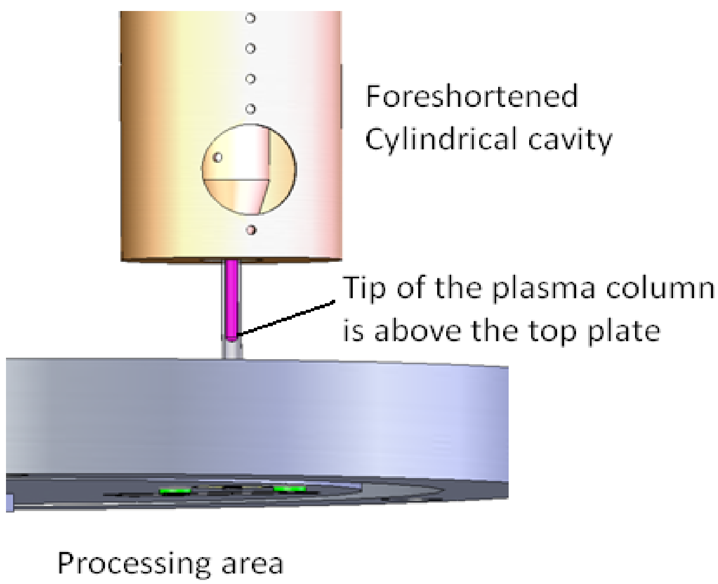

Figure 5.4.1: Illustration of remote plasma processing configuration.

For this application, a remote plasma configuration is used as shown in figure 5.4.1. In this configuration plasma is formed remotely and the desired plasma species, in this case the free radicals, are channeled to the substrate. This allows the electrically charged particles time to recombine before they reach the substrate surface. This configuration can be obtained by setting the foreshortened coaxial cavity applicator at a distance away from the top plate of the processing chamber. An Ar/O_2 plasma was excited with 34 W of absorbed microwave power at a pressure of 0.84 Torr. The argon flow rate was set to 20 sccm and the oxygen flow rate was set to 10 sccm. A 30 μm diameter aperture was used to reduce the plasma processing area. The plasma was created to locally plasma ash a line in a thin layer of Shipley 1813 positive photoresist.

The sample preparation for the plasma ashing experiment is as follow: a square silicon wafer piece (2x2 cm) was cleaned using the RCA cleaning process [132]. A layer of adhesion promoter was applied using the spinner running at 6000 rpm for 30 seconds. A layer of Shipley 1813 photoresist was applied using the spinner running at 6000 rpm for 30 seconds. A soft bake of the sample for one minute at 115 ^{o}C was done using the hot plate. This process deposited approximately 1 μm thick of photoresist layer on top of the silicon.

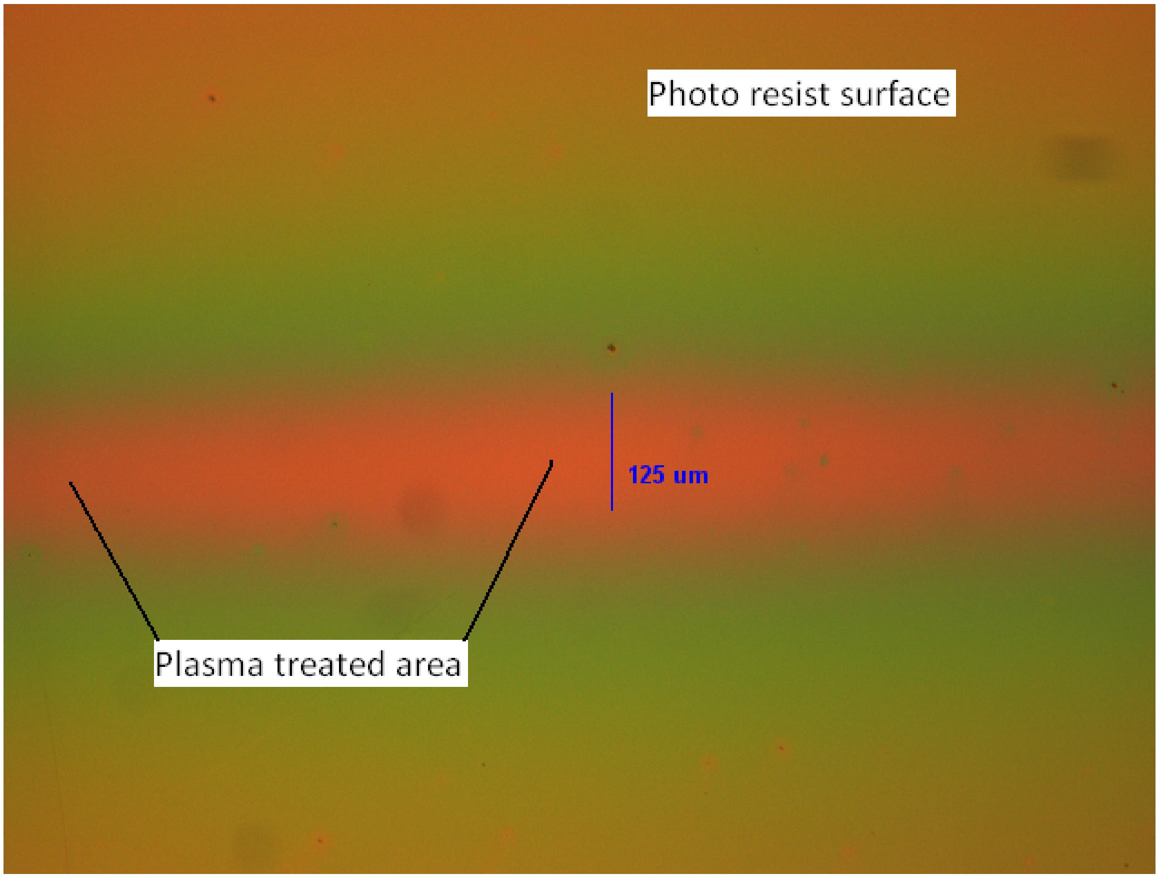

Figure 5.4.2: Optical image of the surface of a photoresist after plasma ashing performed locally by Ar/O_2 microplasma.

The result of using the microwave microplasma as a free radical source, in this case localized plasma ashing, is shown in figure 5.4.2. The substrate was moved in the x-direction (from left to right in figure 5.4.2) with a speed of 1 μm/s resulting in a line shape etched on the photoresist. The line width is approximately 125 μm, which is much larger than the aperture diameter of 30 μm. This happened because the distance between the the photoresist surface and the bottom of the aperture is relatively large, on the order of a few hundreds of microns. The pressure inside the processing chamber is lower than the pressure inside the discharge tube. This condition made the discharge diffuse once it gets outside the aperture. This diffusion will make the footprint of the etched material larger than the aperture size. This issue can be improved by implementing the substrate sensing system as mentioned in section 3.7.3.

5.5 Light source results

One of the goals of the micromachining project is to develop an Ultraviolet (UV) light source using a microplasma system. For this study, light from a surface wave microplasma generated by the microwave foreshortened coaxial cavity is used to modify a photoresist layer on top of a silicon wafer. Photoresist, commonly used in the lithography process for the IC device fabrication, is photosensitive especially in the UV spectral region. Because of this characteristic, photoresist is a good candidate to test the capability of the micromachining system to produce UV emission. Photoresist that was used for this study was Shipley Microposit S1813 positive photoresist. The absorbance spectrum of this photoresist is seen in figure 5.5.1. This photoresist can be exposed with light sources in the spectral output range of 350 nm – 450 nm according to the material data sheet.

For this experiment neon gas was used as the feed gas. Neon plasma emits numerous lines in the wavelength range of 300 – 500 nm. Some of the lines have high relative intensity according to the National Institute of Standards and Technology (NIST) database. Table 5.5.1 shows the neon lines and their relative intensities according to the NIST database [133]. The line intensities are arbitrary numbers and they depend on the excitation system and its input parameters. However, the emission lines shows that neon plasmas produce UV emission.

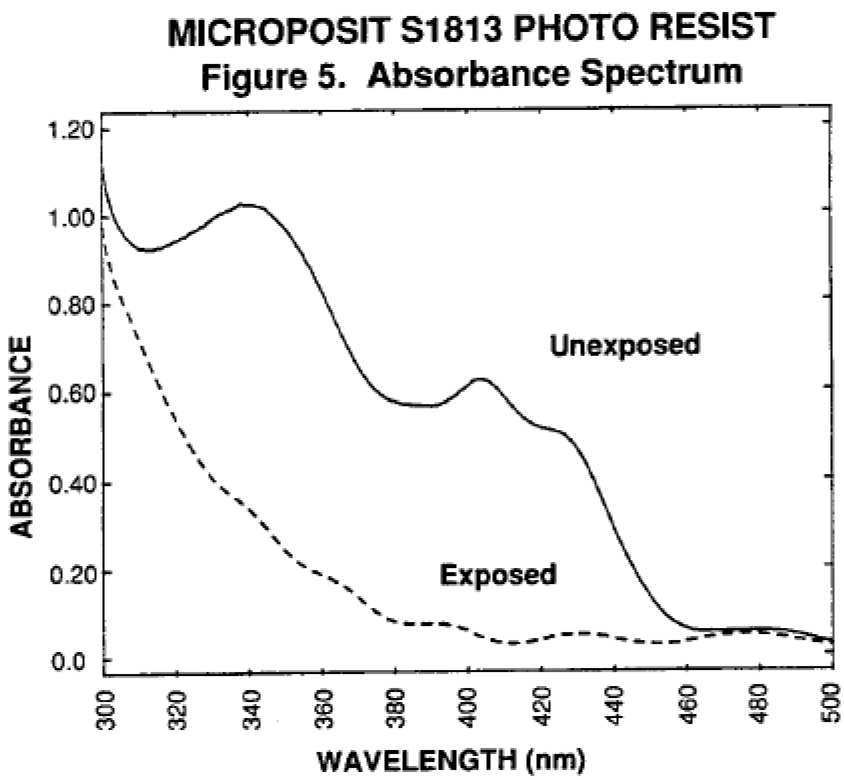

Figure 5.5.1: Absobance spectrum of the Microposit S1813 [134].

Table 5.5.1: NIST database for observed neon gas emission spectra [133]. Data presented is only for lines in the range of 340 – 413 nm with relative intensities higher than 500.

Spectrum	Observed Wavelength Air (nm)	Rel. Int. (a.u.)
Ne I	341.79	5000
Ne I	341.8	500
Ne I	342.39	500
Ne VIII	343.37	500
Ne I	344.77	2000
Ne I	345.08	500
Ne I	345.42	1000
Ne I	346.05	1000
Ne I	346.43	1000
Ne I	346.66	2000
Ne I	347.26	5000
Ne I	349.81	1000
Ne I	350.12	2000
Ne I	351.07	500
Ne I	351.52	2000
Ne I	352.05	10000
Ne II	356.85	500
Ne I	359.35	5000
Ne I	359.36	3000
Ne I	360.02	1000
Ne I	360.92	500
Ne I	363.37	1000
Ne I	368.22	1000
Ne I	368.57	1000
Ne II	371.31	500
Ne II	372.71	500
Ne I	375.42	500
Ne III	392.1	700l*
Ne III	392.1	700l*
Ne III	392.1	700l*
Ne I	404.26	500
Ne I	406.4	500
Ne I	408.01	500
Ne I	413.11	700

Shipley 1813 positive photoresist on a silicon wafer piece was used as the sample to be processed for this experiment. The substrate preparation was similar to the plasma ashing experiment mentioned in the previous sub-section. The substrate was exposed to UV light from neon microplasma through a 30 μm diameter aperture. The operating pressure of the plasma was 25 Torr and the absorbed microwave power was 14 W. The neon gas flow rate was set to 20 sccm. The substrate holder was controlled to move according to the computer-aided design (CAD) trace with the speed set to 10 μm/s. After the exposure process, the substrate was developed using the MF-319 developer solution for two minutes. The optical image of the sample after this process is shown in figure 5.5.2.

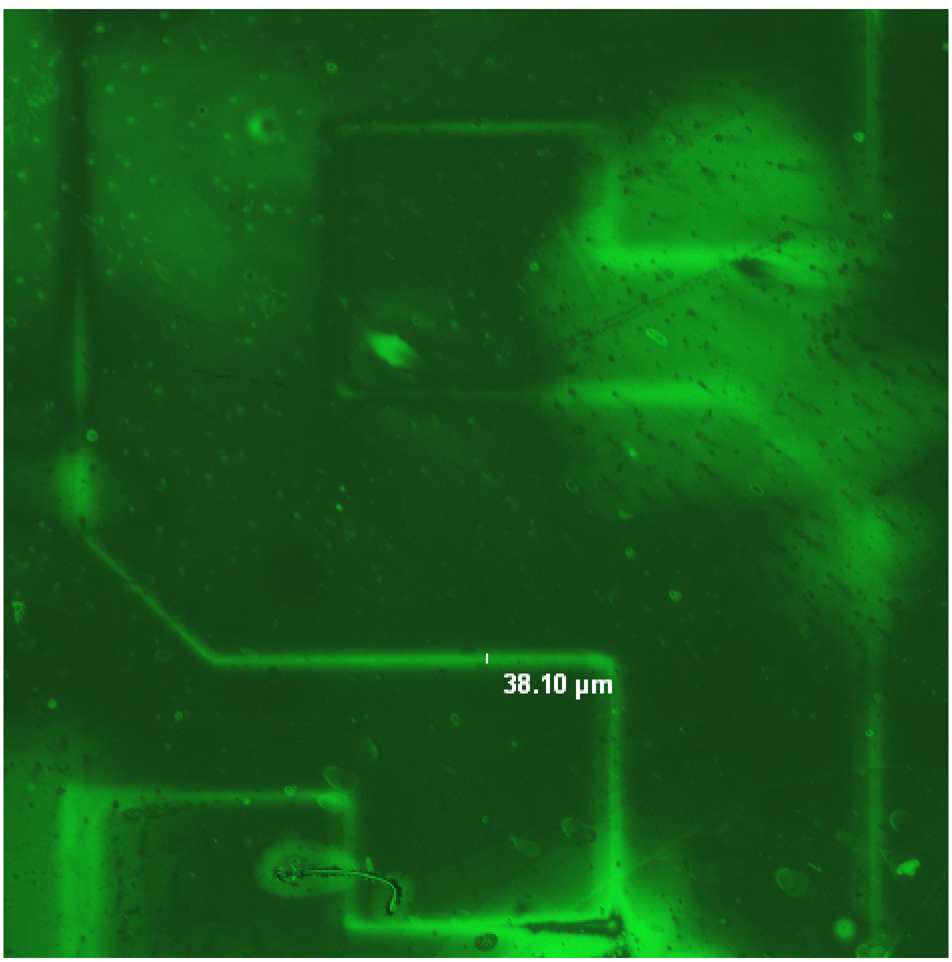

Figure 5.5.2: Optical image of the photo-resist exposed to the neon microplasma.

6 Summary of Results and Recommendations for Future Research

6.1 Summary of results

Microplasma is one of the emerging fields in today's industry with numerous research groups developing various designs and applications for microplasma. However, there is minimal research being conducted for developing miniature microwave induced plasmas (mMIP's) as a tool for material processing. This research was proposed to gain more knowledge on that topic.

Based on their large scale counterpart, mMIP's have potential to perform material processes such as etching, plasma ashing and other surface treatments. The novel aspect of this work is that material processing is performed using spatially localized microplasma sources. It means that only the processed region is exposed to the mMIP's. Applications of mMIP's as an ion source, a free radical source and a light source have been developed as a proof of concept demonstration.

To demonstrate the spatially localized material processing using microplasma concept, a micromachining system has been designed, built, and tested. A foreshortened coaxial cavity, attached to the micromachining system, was used to generate the miniature microwave plasma. Characteristics of the foreshortened coaxial cavity have been studied by experimental and modeling approaches. Basic characteristics of the microwave microplasma such as the plasma length, discharge power density, electron density, and electron temperature have been studied.

Different potential applications for the micromachining system have been demonstrated. It has been demonstrated that the micromachining system is capable to perform as an ion source, a free radical source, and a light source. As an ion source, the micromachining system is capable to perform localized etching for various substrates. As a free radical source, the system is capable to perform localized plasma ashing of a photoresist. As a light source, a pattern can be created on a photoresist by UV light exposure from the microplasma source.

6.1.1 Summary of the micromachining design

A design of local area surface treatment system has been developed. The surface treatment was done using a miniature microwave plasma generated using a foreshortened coaxial cavity. The plasma process and monitoring system is integrated inside a vacuum chamber. A detailed explanation of the system was given in chapter 3, but the general features of the micromachining system are:

- In-situ monitoring to observe the treated surface can be performed using an AFM system installed in the vacuum chamber.
- Translational stages were installed to control the location of the substrate inside the chamber by moving the substrate holder. The installation of translational stages had two purposes: (1) to move the the substrate from the plasma processing area to the AFM monitoring area, and (2) to be able to generate a pattern on the treated surface by moving the substrate under the microplasma source.
- The plasma source was mounted on a separate stage so the plasma process can be performed directly in contact with the substrate's surface or remotely.
- A variety of aperture materials and opening sizes have been designed. Material used for apertures included Pyrex glass, silicon, and steel. The opening size of the aperture ranges

from 25 – 800 μm.

- A RF bias system to draw the charged particles into the substrate was designed and implemented in the micromachining system.
- A position sensing system was designed to adjust the location of the substrate relative to the aperture.
- A computer software code was written for micromachining process automation.

Based on the possible operating range of the supporting systems such as the microwave network and the gas/vacuum system, and the demonstration results of the micromachining system, the operating parameters of the micromachining system have been established. The operating parameters are summarized in table 6.1.1.

Table 6.1.1: Operating parameters

Operating frequency	2.45 GHz
Input power	< 70 Watts
Operating pressure	0.3 – 100 Torr
Gas flow rate	1 – 50 sccm
Gases	Ar, O_2, SF_6, Ne
Discharge tube	2 mm (I.D), quartz
Aperture size	> 15 μm
RF bias frequency; voltage	$\leqslant 4\ MHz\ ;\ \leqslant 20\ V_{p-p}$
Substrate thickness	< 1 mm
Substrate maximum length	< 2.54 cm
Pattern area	< 13 mm x 13 mm

6.1.2 *Summary of the finite element method simulations*

Simulations based on computational models have been performed to get a better understanding of the microplasma system design and operation and the microwave plasma coupling mechanisms. In general, the simulation can be divided into two parts: the electromagnetic study for the foreshortened coaxial cavity and the microwave plasma study for argon gas.

In the electromagnetic study, the microwave cavity was simulated using eigenfrequency and frequency domain analysis in COMSOL. From the eigenfrequency analysis of an empty foreshortened coaxial cavity it can be found the optimal condition for resonance at 2.45 GHz can be achieved when the cavity length (L_s) is 18 – 23 mm and the gap length is 2 – 2.3 mm. A method for geometry reduction from a three dimensional to a two dimensional model to reduce the computational cost has been established using the eigenfrequency analysis.

The frequency domain analysis for the foreshortened cavity was performed with a uniform argon plasma inside a quartz tube as the load. For this study, the charge density of argon plasma was determined based on previous experimental results [53]. The quality factor value of the cavity were observed based on the S_{11} plot for different case scenarios. It was concluded that the S_{11} of the loaded foreshortened cavity is influenced by the charge density, the length of the plasma domain, the cavity length (L_s) and the gap length (L_g). The lowest value of the simulated S_{11} is around -40 dB.

A computational model of a pure argon plasma was developed to simulate 1-D plasma variations versus power density and pressure. The plasma model performed well for the range of the input parameters tested. Plasma can be generated with as little as 10 W/cm^3 as determined in the plasma length and power density measurements and the 1-D simulation shows a similar result. The charge density measurement using a double Langmuir probe measured a charge density on the order of 10^{11} – 10^{13} cm^{-3} and this is also in a good agreement with the simulation result.

Two sets of self-consistent simulation for argon plasma coupled with the foreshortened cavity was performed. Simulations with artificially high loss boundary conditions reached a steady-state solution. However, the absorbed microwave power needed to sustain the discharge was too high. Using more appropriate and realistic flux boundary conditions, a self-consistent simulation was also performed. However, strong coupling of the reflected power percentage, plasma density and plasma length (surface waves) hindered the convergence of the simulation result to a steady-state solution with the model developed.

6.1.3 Summary of the experimental results

The experimental part of the research investigated the cavity tuning, plasma characteristics, and performance of the system for ion source, free radical source, and light source applications. To couple the microwave energy optimally into the discharge, the foreshortened coaxial cavity must be tuned properly, in this case setting the cavity length (L_s) and gap distance (L_g). It was confirmed that the value of L_s and L_g gathered from the simulation is in a good agreement with the experimental result.

A set of experiments were performed to measure the number of charge particles coming out of the discharge tube into the processing chamber. The result of these experiments showed that the minimum opening diameter for the aperture must be higher than 15 μm for the operating conditions of the micromachining system.

The effect of feed gases, mixture ratio, gas flow rates, pressure, and absorbed power on plasma length and power density was evaluated for argon and Ar/O_2 plasmas. In general it was observed that inert gases such as argon produce a longer plasma column compared to other molecular gases. The plasma length decreased with increasing pressure and to smaller extent with decreasing flow rate. Power density increased with increasing absorbed power and oxygen concentration in Ar/O_2 plasma. The measured power density ranges from 10 – 450 W/cm^3, which is comparable to the previous study for a different plasma applicator based on a microstripline design[53].

Double Langmuir probe measurements were conducted for argon plasma at 0.9 Torr. The probe was inserted at the tip of the discharge tube to measure the spatial charge density variation along the plasma column. From this measurement, the charge density in the argon plasma was between 1x10^{11} – 1x10^{13} cm^{-3}. As the probe is inserted closer to the source the density is gets higher. In general the results confirmed that the plasma column is a surface wave plasma as stated by Aliev [135]. The electron temperature was around 2 – 3 eV.

Demonstration of two ion source applications, including silicon and ultrananocrystalline diamond (UNCD) etching were performed using Ar/SF_6 and Ar/O_2 plasmas, respectively. The etching rate of silicon for 1.5% SF_6 concentration was found to be 2.1 μm/min without any voltage bias nor any apertures applied. However, with an aperture, the etching rate dropped to 0.2 μm/min. The etching process is isotropic and the etched surface was rough. It was observed that the discharge tube was etched during the experiment. By using a RF bias, the ions can be directed to come out of the discharge tube thus reduce the etching of the tube. The UNCD etching rate was measured to be 0.6 μm/hr without a RF bias and in the range from 1 – 2 μm/hr with a RF bias.

The micromachining system, which includes a movable substrate holder in XYZ directions, proved to be useful for free radical and light source applications. For both applications, the substrate chosen for the study was a silicon wafer coated with photoresist. The photoresist changes its characteristics under plasma and light exposure. To minimize the influence of the gas temperature to the photoresist, plasma can be formed away from the substrate as discussed in chapter 5.

The distance between the tip of the discharge tube and the substrate is an important parameter for the local area processing. The double Langmuir probe measurement of the charge density of argon plasma shows spatial variation of the density. Higher charge density can be found near the tip of the discharge tube.

Results of 1-D simulation of the plasma model was in a good agreement with the experimental results. The charge density measured using the double Langmuir probe are on the same order with the 1-D argon plasma simulation result. The simulations were performed using a constant local power density which were approximated from the power density measurements. Thus, the computational model was valid for operating conditions of this work.

6.2 Recommendations for future research

Future work on localized surface treatments should be focused on three categories: Optimizing the overall system design, creating an enhance model for the self-consistent simulation, and optimizing the system for specific applications.

In general, the micromachining system can perform a variety of tasks. However, in order to optimize the system, improvements of the vacuum sealing of the processing chamber and the discharge tube are desirable. Ceramabond and heat shrink provides an adequate vacuum seal with minimal leak rate. However, in most applications, the concentration of feed gases is an important parameter. Even with a small vacuum leak, the mix ratio of the feed gases can be off.

The simulation part of this work provides a better insight on how to setup a microwave cavity applicator with good tuning precision either for the empty or loaded cavity. Since the load of the cavity is a plasma, it is suggested that the plasma model used for future computational work incorporate a more thorough approach such as increasing the number of reactions. Simulation should also be performed to study the spacing of the tip of the discharge tube from the substrate. Perhaps more important is improvements to the model to obtain fully self-consistent steady-state solutions of the plasma and the microwave field, that include plasma surface wave phenomenon.

A final recommendation would be to address each potential application of the micromachining system with a more in depth investigation.

REFERENCES

REFERENCES

[1] V. Karanassios, *Microplasmas for chemical analysis: analytical tools or research toys?*, Spectrochimica Acta Part B: Atomic Spectroscopy, **59**, (2004), 909-928

[2] R. Foesta, M. Schmidt and K. Becker, *Microplasmas, an emerging field of low-temperature plasma science and technology*, Int. J. Mass Spectrom., **248**, (2006), 87-102

[3] K. H. Becker, K. H. Schoenbach and J. G. Eden, *Microplasmas and applications*, J. Phys. D: Appl. Phys., **39**, (2006), R55-R70

[4] J. Asmussen, J. Hopwood, and F. C. Sze, *A 915 MHz/2.45 GHz ECR plasma source for large area ion beam and plasma processing*, Rev. Sci. Instrum. , **61**, (1990), 250

[5] A. Ohl, *Fundamentals and limitations of large area planar microwave discharges using slotted waveguides*, Journal de Physique IV, **08**, (1998), Pr7-83

[6] Y. Yasaka, *Control of power deposition profile for uniform plasma production in microwave and radio frequency ranges*, Journal de Physique IV, **08**, (1998), Pr7-165

[7] C. Boisse-Laporte, N. Bénissad and S. Béchu , *Large microwave plasma reactor based on surface waves*, Journal de Physique IV, **08**, (1998), Pr7-187

[8] T. Lagarde, J. Pelleteir and Y. Arnal, *Recent developments in DECR plasmas*, Journal de Physique IV, **08**, (1998), Pr7-121

[9] T. Ito and K. Terashima, *Generation of micrometer-scale discharge in a supercritical fluid environment*, Appl. Phys. Lett., **80**, (2002), 2854-2856

[10] Z. Lj. Petrovic, N. Skoro, D. Maric, C. M. O. Mahony, P. D. Maguire, M. Radmilovic-Radenovic and G. Malovic, *Breakdown, scaling and volt-ampere characteristics of low current micro-discharges*, J. Phys. D: Appl. Phys., **41**, (2008), 194002

[11] K. H. Scoenbach, R. Verhappen, T. Tessnow, F. E. Peterkin and W. W. Byszewski, *Microhollow cathode discharges*, Appl. Phys. Lett., **68**, (1996), 13

[12] M. Moselhy, W. Shi, R. H. Stark, and K. H. Schoenbach, *Xenon excimer emission from pulsed microhollow cathode discharges*, Appl. Phys. Lett., **79**, (2001), 1240

[13] K. H. Becker, P. F. Kurunczi, M. Moselhy, and K. H. Schoenbach, *Vacuum ultraviolet spectroscopy of microhollow cathode discharge plasmas*, Proc. SPIE, **4460**, (2002), 239

[14] I. Petzenhauser, L. D. Biborosch, U. Ernst, K. Frank, and K. H. Schoenbach, *Comparison between the ultraviolet emission from pulsed microhollow cathode discharges in xenon and argon*, Appl. Phys. Lett., **83**, (2003), 4297

[15] G. Bauville, B. Lacour, L. Magne, V. Puech, J. P. Boeuf, E. Munoz-Serrano, and L. C. Pitchford, *Singlet oxygen production in a microcathode sustained discharge*, Appl. Phys. Lett., **90**,

(2007), 031501

[16] S. J. Park and J. G. Eden, *13–30 micron diameter microdischarge devices: Atomic ion and molecular emission at above atmospheric pressures*, Appl. Phys. Lett., **81**, (2002), 4127

[17] D. D. Hsu and D. B. Graves, *Microhollow cathode discharge stability with flow and reaction*, J. Phys. D: Appl. Phys., **36**, (2003), 2898-2907

[18] Y. Yin, J. Messier, and J. A. Hopwood, *Miniaturization of inductively coupled plasma sources*, EEE Trans. on Plasma Science, **27**, (1999), 1516-1524

[19] J. Hopwood, O. Minayeva, and Y. Yin, *Fabrication and characterization of a micromachined 5 mm inductively coupled plasma generator*, J. Vac. Sci. Technol. B., **18**, (2000), 2446-2451

[20] F. Iza and J. Hopwood, *Influence of operating frequency and coupling coefficient on the efficiency of microfabricated inductively coupled plasma sources*, Plasma Sources Sci. Technol., **11**, (2002), 229-235

[21] O. B. Menayeva and J. Hopwood, *Emission spectroscopy using a microfabricated inductively coupled plasma-on-a-chip.*, J. Anal. At. Spectrom., **17**, (2002), 1103-1107

[22] O. B. Menayeva and J. Hopwood, *Langmuir probe diagnostic of a microfabricated inductively coupled plasma on a chip.*, J. Appl. Phys., **94**, (2003), 2821-2828

[23] T. Ichiki, T. Koidesawa and Y. Horiike, *An atmospheric-pressure microplasma jet source for the optical emission spectroscopic analysis of liquid sample*, Plasma Sources Sci. Technol., **12**, (2003), S16-S20

[24] E. Stoffels, A. J. Flikweert, W. W. Stoffels and G. M. W. Kroesen, *Plasma needle: a non-destructive atmospheric plasma source for fine surface treatment of (bio)materials*, Plasma Sources Sci. Technol., **11**, (2002), 383-388

[25] I. E. Kieft, E. P. v d Laan and E. Stoffels, *Electrical and optical characterization of the plasma needle*, New J. Phys., **6**, (2004), 149

[26] E. P. van der Laan, E. Stoffels and M. Steinbuch, *Development of a smart positioning sensor for the plasma needle*, Plasma Sources Sci. Technol., **15**, (2006), 582-589

[27] E. Stoffels, Y. A. Gonzalvo, T. D. Whitmore, D. L. Seymour and J. A. Rees, *A plasma needle generates nitric oxide*, Plasma Sources Sci. Technol., **15**, (2006), 501-506

[28] Y. Sakiyama, D. B. Graves and E. Stoffels, *Influence of electrical properties of treated surface on RF-excited plasma needle at atmospheric pressure*, J. Phys. D: Appl. Phys., **41**, (2008), 095204

[29] H. Yoshiki and Y. Horiike, *Capacitively coupled microplasma source on a chip at atmospheric pressure*, Jpn. J. Appl. Phys., **40**, (2001), L360-L363

[30] H. Yoshiki, A. Oki, H. Ogawa and Y. Horiike, *Inner wall modification of a poly(ethylene terephthalate) (PET) capillary by 13.56 MHz capacitively coupled microplasma.*, Thin Solid Films, **407**, (2002), 156-162

[31] S. Okazaki, M. Kogoma, M. Uehara and Y. Kimura, *Appearance of stable glow discharge in air, argon, oxygen and nitrogen at atmospheric pressure using a 50 Hz source*, J. Phys. D: Appl. Phys., **26**, (1993), 889-892

[32] M. Miclea, K. Kunze, G. Musa, J. Franzke, K. Niemax, *The dielectric barrier discharge — a powerful microchip plasma for diode laser spectrometry*, Spectrochim. Acta Part B., **56**, (2001), 37-43

[33] K. Kunze, M. Miclea, G. Musa, J. Franzke, C. Vadla and K. Niemax, *Diode laser-aided diagnostics of a low-pressure dielectric barrier discharge applied in element-selective detection of molecular species*, Spectrochim. Acta Part B, **57**, (2002), 137-146

[34] M. Miclea, K. Kunze, J. Franzke and K. Niemax, *Plasmas for lab-on-the-chip applications*, Spectrochim. Acta Part B., **57**, (2002), 1585-1592

[35] C Penache, M Miclea, A Bräuning-Demian, O Hohn, S Schössler, T Jahnke, K Niemax and H Schmidt-Böcking, *Characterization of a high-pressure microdischarge using diode laser atomic absorption spectroscopy*, Plasma Sources Sci. Technol., **11**, (2002), 476-483

[36] X. P. Lu and M. Laroussi, *Temporal and spatial emission behaviour of homogeneous dielectric barrier discharge driven by unipolar sub-microsecond square pulses*, J. Phys. D: Appl. Phys., **39**, (2006), 1127-1131

[37] A. El-Dakrouri, J. Yan, M. C. Gupta, M. Laroussi and Y. Badr, *VUV emission from a novel DBD-based radiation source*, J. Phys. D: Appl. Phys., **35**, (2002), L109-L114

[38] E. E. Kunhardt, *Generation of large-volume, atmospheric pressure, nonequilibrium plasmas*, IEEE Trans. Plasma Sci., **28**, (2000), 189-200

[39] A. D. Koutsospyros, S. Yin, C. Christodoulatos and K. Becker, *Plasmochemical degradation of volatile organic compounds (VOC) in a capillary discharge plasma reactor*, IEEE Trans. Plasma Sci., **33**, (2005), 42-49

[40] N. Mericam-Bourdet, M. Laroussi, A. Begum and E. Karakas, *Experimental investigations of plasma bullets*, J. Phys. D: Appl. Phys., **42**, (2009), 055207

[41] A. M. Bilgic, U. Engel, E. Voges, M. Kückelheim and J. A. C. Broekaert, *A new low-power microwave plasma source using microstrip technology for atomic emission spectrometry*, Plasma Sources Sci. Technol., **9**, (2000), 1-4

[42] A. M. Bilgiç, E. Voges, U. Engel and J. A. C. Broekaert, *A low-power 2.45 GHz microwave induced helium plasma source at atmospheric pressure based on microstrip technology*, J. Anal. At. Spectrom., **15**, (2000), 579

[43] U. Engel, A. M. Bilgiç, Oliver Haase, E. Voges and J. A. C. Broekaert, *A Microwave-Induced Plasma Based on Microstrip Technology and Its Use for the Atomic Emission Spectrometric Determination of Mercury with the Aid of the Cold-Vapor Technique*, Anal. Chem., **72**, (2000), 193-197

[44] S. Schermer, N. H. Bings, A. M. Bilgiç, R. Stonies, E. Voges, J. A. C. Broekaert, *An improved microstrip plasma for optical emission spectrometry of gaseous species*, Spectrochimica

Acta Part B, **58**, (2003), 1585-1596

[45] I. J. Zapata, P. Pohl, N. H. Bings and J. A. C. Broekaert, *Evaluation and application of argon and helium microstrip plasma for the determination of mercury by the cold vapor technique and optical emission spectrometry*, Anal. Bioanal. Chem., **388**, (2007), 1615-1623

[46] J. Pollak, M. Moisan and Z. Zakrzewski, *Long and uniform plasma columns generated by linear field-applicators based on stripline technology*, Plasma Sources Sci. Technol., **16**, (2007), 310-323

[47] F. Iza and J. Hopwood, *Split-ring resonator microplasma: microwave model, plasma impedance and power efficiency*, Plasma Sources Sci. Technol., **14**, (2005), 397-406

[48] J. Hopwood, F. Iza, S. Coy and D. B. Fenner, *A microfabricated atmospheric-pressure microplasma source operating in air*, J. Phys. D: Appl. Phys., **38**, (2005), 1698-1703

[49] F. Iza and J. A. Hopwood, *Low-power microwave plasma source based on a microstrip split-ring resonator*, IEEE Trans. Plasma Sci., **31**, (2003), 782-787

[50] F. Iza and J. A. Hopwood, *Rotational, vibrational, and excitation temperatures of a microwave-frequency microplasma*, IEEE Trans. Plasma Sci., **32**, (2004), 498-504

[51] F. Iza and J. A. Hopwood, *Self-organized filaments, striations and other nonuniformities in nonthermal atmospheric microwave excited microdischarges*, IEEE Trans. Plasma Sci., **33**, (2005), 306-307

[52] T. A. Grotjohn, J. Asmussen and A. Wijaya, *Microwave stripline applicators*, US Patent #6,759,808, 2004

[53] J. J. Narendra, T. A. Grotjohn and J. Asmussen, *Microstripline applicators for creating microplasma discharges with microwave energy*, Plasma Sources Sci. Technol., **17**, (2008), 035027

[54] R. M. Fredericks, *An experimental and theoretical study of resonantly sustained plasma in microwave cavities*, Ph.D. Dissertation, Michigan State University, 1971

[55] J. R. Rogers, *Properties of steady-state, high pressure, argon microwave discharges*, Ph.D. Dissertation, Michigan State University, 1982

[56] M. L. Brake, *A theoretical and experimental investigation of the chemical kinetics of an oxygen microwave discharge*, Ph.D. Dissertation, Michigan State University, 1983

[57] M. Brake, J. Rogers, M. Peters, J. Assmusen, and R. Kerber, *Electron density measurements of argon surface-wave discharges*, Plas. Chem. and Plas. Processing, **5**, (1985), 255-261

[58] K. W. Hemawan, C. L. Romel, S. Zuo, I. S. Wichman, T. A. Grotjohn and J. Asmussen , *Microwave plasma-assisted premixed flame combustion*, Appl. Phys. Lett., **89**, (2006), 141501

[59] C. I. M. Beenakker, *A cavity for microwave-induced plasmas operated in helium and argon at atmospheric pressure*, Spectrochim. Acta. Part B., **31**, (1976), 483-486

[60] C. I. M. Beenakker, B. Bosman, P. W. J. Bouwmans, *An assessment of microwave-induced plasma generated in argon with a cylindrical TM010 cavity as an excitation source for emission spectrometric analysis of aerosols.*, Spectrochim. Acta. Part B., **33**, (1978), 373-381

[61] M. Moisan, G. Sauve, Z. Zakrzewski and J. Hubert, *An atmospheric pressure waveguide-fed microwave plasma torch: the TIA design*, Plasma Sources Sci. Technol., **3**, (1994), 584-592

[62] Z. Zakrzewski and M. Moisan, *Plasma sources using long linear microwave field applicators: main features, classification and modelling*, Plasma Sources Sci. Technol., **4**, (1995), 379-397

[63] H. Nowakowska, Z. Zakrzewski, M. Moisan and M. Lubanski, *Propagation characteristics of surface waves sustaining atmospheric pressure discharges: the influence of the discharge processes*, J. Phys. D: Appl. Phys., **31**, (1998), 1422-1432

[64] T. Fleisch, Y. Kabouzi, M. Moisan, J. Pollak, E. Castaños-Martínez, H. Nowakowska and Z. Zakrzewski, *Designing an efficient microwave-plasma source, independent of operating conditions, at atmospheric pressure*, Plasma Sources Sci. Technol., **16**, (2007), 173-182

[65] R. Stonies, S. Schermer, E. Voges and J. A. C. Broekaert, *A new small microwave plasma torch*, Plasma Sources Sci. Technol., **13**, (2004), 604-611

[66] A. M. Bilgic, C. Prokisch, J. A. C. Broekaert, E. Voges, *Design and modelling of a modified 2.45 GHz coaxial plasma torch for atomic spectrometry*, Spectrochim. Acta Part B, **53**, (1998), 773-777

[67] S. P. Kuo, D. Bivolaru, H. Lai, W. Lai, S. Popovic and P. Kessaratikoon, *Characteristics of an arc-seeded microwave plasma torch*, IEEE Trans. Plasma Sci., **32**, (2004), 1734-1741

[68] S. P. Kuo, D. Bivolaru, S. Williams and C. D. Carter, *A microwave-augmented plasma torch module*, Plasma Sources Sci. Technol., **15**, (2006), 266-275

[69] Q. Jin, C. Zhu, W. Borer, G. M. Hieftje, *A microwave plasma torch assembly for atomic emission spectrometry*, Spectrochim. Acta Part B., **46**, (1991), 417-430

[70] H. S. Uhm, Y. C. Hong and D. H. Shin, *A microwave plasma torch and its applications*, Plasma Sources Sci. Technol., **15**, (2006), S26-S34

[71] J. Asmussen, T. Grotjohn, N. Xi and T. P. Hogan, *Process and apparatus for modifying a surface in a work region*, US Patent #7,262,408, 2007

[72] J. Xue and J. Hopwood, Particle trapping by dusty microplasmas, Conf. Proceeding, IEEE International Conf. on Plasma Sci., (2006)

[73] Y. Takao and K. Ono, *A miniature electrothermal thruster using microwave-excited plasmas: a numerical design consideration*, Plasma Sources Sci. Technol., **15**, (2006), 211-227

[74] T. Takahashi, Y. Takao, K. Eriguchi and K. Ono, *Microwave-excited microplasma thruster: a numerical and experimental study of the plasma generation and micronozzle flow*, J. Phys. D: Appl. Phys., **41**, (2008), 194005

[75] M. Teschke, J. Kedzierski, E. G. Finantu-Dinu, D. Korzec and J. Engemann, *High speed photographs of a dielectric barrier atmospheric pressure plasma jet*, IEEE Trans. Plasma Sci.,

33, (2005), 310-311

[76] J. Shi, F. Zhong, J. Zhang, D. W. Liu and M. G. Kong, *A hypersonic plasma bullet train traveling in an atmospheric dielectric-barrier discharge jet*, Phys. Plasmas, **15**, (2008), 013504

[77] S. Harris, *An Introduction to the theory of Boltzmann Equation*, New York: Dover, 2004

[78] M. A. Liebermann and A. J. Lichtenberg, *Principle of Plasma Discharges and Materials Processing*, New York: Wiley, 1994

[79] S. Ichimaru, *Basic Principles of Plasma Physics - A Statistical Approach*, Reading, MA: W. A. Benjamin, 1973

[80] B. M. Penetrante, J. N. Bardsley and L. C. Pitchford, *Monte Carlo and Boltzmann calculations of the density gradient expanded energy distribution functions of electron swarms in gases*, J. Phys. D: Appl. Phys., **18**, (1985), 1087-1100

[81] H. Risken, *The Fokker-Planck equation : methods of solution and applications*, New York: Springer-Verlag, 1984

[82] V. I. Kolobov, *Fokker-Planck modeling of electron kinetics in plasmas and semiconductors*, Comput. Materials Sci., **28**, (2003), 302-320

[83] T. Farouk, B. Farouk, D. Staack, A. Gutsol and A. Fridman, *Simulation of dc atmospheric pressure argon micro glow-discharge*, Plasma Sources Sci. Technol., **15**, (2006), 676-688

[84] T. Farouk, B. Farouk, D. Staack, A. Gutsol and A. Fridman, *Modeling of direct current micro-plasma discharges in atmospheric pressure hydrogen*, Plasma Sources Sci. Technol., **16**, (2007), 619-634

[85] A. Chirokov, S. N. Khot, S. P. Gangoli, A. Fridman, P. Henderson, A. F. Gutsol and A. Dolgopolsky, *Numerical and experimental investigation of the stability of radio-frequency (RF) discharges at atmospheric pressure*, Plasma Sources Sci. Technol., **18**, (2009), 025025

[86] G. J. M. Hagelaar and L. C. Pitchford, *Solving the Boltzmann equation to obtain electron transport coefficients and rate coefficients for fluid models*, Plasma Sources Sci. Technol., **14**, (2005), 722-733

[87] E. Muñoz-Serrano, G. Hagelaar, Th. Callegari, J. P. Boeuf and L. C. Pitchford, *Properties of plasmas generated in microdischarges*, Plasma Phys. Control. Fusion, **48**, (2006), B391-B397

[88] K. Makasheva, E. Muñoz Serrano, G. Hagelaar, J-P. Boeuf and L. C. Pitchford, *A better understanding of microcathode sustained discharges*, Plasma Phys. Control. Fusion, **49**, (2007), B233-B238

[89] Y. Lagmich, Th. Callegari, L. C. Pitchford and J. P. Boeuf, *Model description of surface dielectric barrier discharges for flow control*, J. Phys. D: Appl. Phys., **41**, (2008), 095205

[90] J. P. Boeuf, Y. Lagmich, Th. Unfer, Th. Callegari and L. C. Pitchford, *Overview of the different aspects in modeling moderate pressure H2 and H2/CH4 microwave discharges*, J. Phys. D: Appl. Phys., **40**, (2007), 652-662

[91] T. A. Grotjohn, *Numerical modeling of a compact ECR ion source*, Rev. Sci. Instrum., **63**, (1992), 2535-2537

[92] T. A. Grotjohn, W. Tan, V. Gopinath, A. K. Srivastava, and J. Asmussen, *Modeling the electromagnetic excitation of a compact ECR ion/free radical source*, Rev. Sci. Instrum., **65**, (1994), 1761

[93] V. P. Gopinath and T. A. Grotjohn, *Three-dimensional electromagnetic PIC model of a compact ECR plasma source*, IEEE Trans. Plasma Sci., **23**, (1995), 602-608

[94] W. Tan and T. A. Grotjohn, *Modeling the electromagnetic excitation of a microwave cavity plasma reactor*, J. Vac. Sci. Technol. A, **12**, (1994), 1216-1220

[95] T. A. Grotjohn, *Modeling the electron heating in a compact electron cyclotron resonance ion source*, Rev. Sci. Instrum., **67**, (1996), 921-923

[96] K. Hassouni, T. A. Grotjohn and A. Gicquel, *Self-consistent microwave field and plasma discharge simulations for a moderate pressure hydrogen discharge reactor*, J. Appl. Phys., **86**, (1999), 134

[97] K. Hassouni, G. Lombardi, X. Duten, G. Haagelar, F. Silva, A. Gicquel, T. A. Grotjohn, M. Capitelli and J. Röpcke, *Overview of the different aspects in modelling moderate pressure H2 and H2/CH4 microwave discharges* , Plasma. Sources. Sci. Technol., **15**, (2006), 117-125

[98] K. Yee, *Numerical solution of inital boundary value problems involving maxwell's equations in isotropic media*, IEEE Trans. Antennas Propag., **14**, (1966), 302-307

[99] A. Taflove and M. E. Brodwin, *Numerical solution of steady-state electromagnetic scattering problems using the time-dependent Maxwell's equations*, IEEE Trans. Microwave Theory Tech., **23**, (1975), 623-630

[100] A. Taflove, *Application of the finite-difference time-domain method to sinusoidal steady state electromagnetic penetration problems*, IEEE Trans. Electromagnetic Compatibility, **22**, (1980), 191-202

[101] A. taflove, *Computational Electrodynamics: The Finite-Difference Time-Domain Method*, Boston: Artech House, 1995

[102] G. K. Grubert, D. Loffhagen and D. Uhrlandt, Two-fluid modelling of an abnormal low-pressure glow discharge, Conf. proceeding, COMSOL Conf., (2005)

[103] H. Nowakowska, M. Jasinski and J. Mizeracyk, Electric field distributions and energy transfer in waveguide-based axial-type microwave plasma source, Conf. Proceeding, COMSOL Conf., (2008)

[104] C. Hunyar, E. Rauchle, L. Alberts, R. Emmerich, M. Graf, M. Kaiser, K-D. Nauenburg, Numerical study of surface waves in plasma, Conf. Proceeding, COMSOL Conf., (2007)

[105] D. L. Bitzer, H. G. Slottow and R. H. Wilson, *Gaseous display and memory apparatus*, U. S. Patent#3559190, 1971

[106] D. Alpert and D. L. Bitzer, *Advances in computer-based education*, Science, **167**, (1970),

1582-1590

[107] L. F. Weber, *History of the plasma display panel*, IEEE Trans. Plasma Science, **34**, (2006), 268-278

[108] A. Sobel, *Plasma displays*, IEEE Trans. Plasma Science, **19**, (1991), 1032-1047

[109] T. Shinoda and K. Awamoto, *Plasma display technologies for large area screen and cost reduction*, IEEE Trans. Plasma Science, **34**, (2006), 279-286

[110] J. G. Eden, S.-J. Park, N. P. Ostrom and K.-F. Chen, *Recent advances in microcavity plasma devices and arrays: a versatile photonic platform*, J. Phys. D: Appl. Phys., **38**, (2005), 1644-1648

[111] J. G. Eden and S.-J. Park, *Microcavity plasma devices and arrays: a new realm of plasma physics and photonic applications*, Plasma Phys. Control. Fusion, **47**, (2005), B83-B92

[112] S-J Park, J D Readle, A J Price, J K Yoon and J G Eden, *Lighting from thin (<1 mm) sheets of microcavity plasma arrays fabricated in Al/Al2O3/glass structures: planar, mercury-free lamps with radiating areas beyond 200 cm2*, J. Phys. D: Appl. Phys., **40**, (2007), 3907-3913

[113] K. S. Kim, S.-J. Park and J. G. Eden, *Self-patterned aluminium interconnects and ring electrodes for arrays of microcavity plasma devices encapsulated in Al2O3*, J. Phys. D: Appl. Phys., **41**, (2008), 012004

[114] T. A. Grotjohn, *Ion sources for microfabrication*, Rev. Sci. Instrum., **65**, (1994), 1298-1303

[115] A. K. Shrivastava, J. Asmussen, T. Antaya and K. Harrison, *The study of a 2.45 GHz plasma source as a plasma generator for the SCECR electron cyclotron resonance ion source*, Rev. Sci. Instrum., **65**, (1994), 1135-1137

[116] Y. Matsubara, H. Tahara, S. Nogawa and J. Ishikawa, *Development of microwave plasma cathode for ion sources*, Rev. Sci. Instrum., **61**, (1990), 541

[117] M. Liehr, R. Trassl, M. Schlapp and E. Salzborn, *A low power 2.45 GHz ECR ion source for multiple charged ions*, Rev. Sci. Instrum., **63**, (1992), 2541-2543

[118] R. Trassl, P. Hathiramani, F. Boetz, J. B. Greenwood, R. W. McCoullough, M. Schlapp and E. Salzborn, *Characterization and recent modification of a compact 10 GHz electron cyclotron resonance (ECR) ion source for atomic physics experiments/*, Physica Scripta, **T73**, (1997), 380-381

[119] E. Galutschek, R. Trassl, E. Salzborn, F. Aumayr and H. P. Winter, *Compact 14.5 GHz all-permanent magnet ECRIS for experiments with slow multicharged ions*, J. Phys.: Conf. Ser., **58**, (2007), 395-398

[120] L. T. Sun, H. W. Zhao, X. H. Guo, X. Z. Zhang, Z. M. Zhang, P. Yuan, W. L. Zhan, B. W. Wei, X. H. Cai, J. Y. Li, Y. C. Feng, W. He, Y. Cao, M. T. Song, X. X. Li, H. Wang, B. H. Ma, W. Lu and T. Jin, *First results from the recently developed, high-performance next-generation 18GHz ECRIS-SECRAL*, J. Phys.: Conf. Ser., **58**, (2007), 435-438

[121] S. K. Hahto, S. T. Hahto, Q. Ji, K. N. Leung, S. Wilde, E. L. Foley, L. R. Grisham and F. M.

Levinton, *Multicusp ion source with external rf antenna for production of protons*, Rev. Sci. Instrum., **75**, (2004), 355-359

[122] D. Boonyawan, N. Chiraphatpimol and T. Vilaithong, *Characteristics of a 13.56 MHz radio-frequency-driven multicusp ion source*, Plasma Sources Sci. Technol., **11**, (2002), 389-396

[123] Y. Dawei, L. Xiaoqian, W. Yu and L. Yongchang, *The gridless plasma ion source (GIS) for plasma ion assisted optical coating*, Plasma Sci. & Technol., **6**, (2004), 2416-2418

[124] M. G. Mlynczak and B. T. Marshall, *A reexamination of the role of solar heating in the O2 atmosperic and infrared atmospheric bands*, Geophys. Res. Lett., **23**, (1996), 657-660

[125] M. L. Kaplan and P. G. Kelleher, *Oxidation of a polymer surface with gas phase singlet (1Δg) oxygen*, Science, **169**, (1970), 1206-1207

[126] H. W. Hermann, I. Henins, J. Park and G. S. Selwyn, *Decontamination of chemical and biological warfare (CBW) agents using an atmospheric pressure plasma jet*, Phys. Plasmas, **6**, (1999), 2284-2289

[127] K. W. C. Lai, J. J. Narendra, N. Xi, J. Zhang, T. A. Grotjohn and J. Asmussen, *Development of Plasma Nanomanufacturing Workcell*, J. Manuf. Sci. Eng., **132**, (2010), 031003

[128] S. K. Nam and J. P. Verboncoeur, *Effect of electron energy distribution function on the global model for high power microwave breakdown at high pressures*, Appl. Phys. Lett., **92**, (2008), 231502

[129] P. S. Shternin and D. G. Yakovlev, *Electron thermal conductivity owing to collisions between degenerate electrons*, Phys. Rev., **74**, (2006), 043004

[130] J. Rogers and J. Asmussen, *Standing waves along a microwave generated surface wave plasma*, IEEE Trans. on Plasma Sci., **PS-10**, (1982), 11-16

[131] H. D. Espinosa, B. Peng, B. C. Prorok and N. Moldovan, *Fracture strength of ultrananocrystalline diamond thin films - identification of Weibull parameters*, J. Appl. Phys., **94**, (2003), 6076-6084

[132] B. Wright, *Standard operating procedure for RCA Clean*, http://www.egr.msu.edu/erc-cleanroom/sop/SOP_for_RCA_Clean.pdf, 2009

[133] Y. Ralchenko, A.E. Kramida and J. Reader, *NIST: Atomic spectra database ver. 3*, http://physics.nist.gov/PhysRefData/ASD/index.html, 2009

[134] Shipley Data Sheet, *Microposit S1800 series photo resists*, http://www.nanophys.kth.se/nanophys/facilities/nfl/resists/S1813/s1800seriesDataSheet.pdf, 2009

[135] Y. M. Aliev, *Guided-Wave-Produced Plasmas*, Berlin: Springer, 2000